UNIVERSITY OF
BIRMINGHAM

Design Improvements of Micro-Tubular Solid Oxide Fuel Cells for Unmanned Aircraft Applications

by

Katie Sarah Howe

A thesis submitted to
The University of Birmingham
for the degree of

Doctor of Philosophy

Centre for Hydrogen and Fuel Cell Research
School of Chemical Engineering
University of Birmingham
Edgbaston
Birmingham
B15 2TT

September 2013

UNIVERSITY OF
BIRMINGHAM

University of Birmingham Research Archive

e-theses repository

This unpublished thesis/dissertation is copyright of the author and/or third parties. The intellectual property rights of the author or third parties in respect of this work are as defined by The Copyright Designs and Patents Act 1988 or as modified by any successor legislation.

Any use made of information contained in this thesis/dissertation must be in accordance with that legislation and must be properly acknowledged. Further distribution or reproduction in any format is prohibited without the permission of the copyright holder.

ABSTRACT

This work contributes to the development of a micro-tubular solid oxide fuel cell (μSOFC) stack for use in a small unmanned aerial vehicle. Fuel cells offer cleaner, quieter operation than combustion engines. Solid oxide fuel cells were chosen due to their higher efficiency and hydrocarbon fuel tolerance. Micro-tubular cells were chosen due to their simpler sealing requirements and stronger cycling properties. 250 W power is required, necessitating the use of many cells.

Cathode manufacture was considered and various changes to current techniques suggested. Dip-coating was tested as an alternative to brush-painting. The acetone-based ink was unsuitable for dip-coating so a novel, lower cost, water-based ink was developed and a patent application registered.

Cell power, transient and cycling performances were investigated. Dynamic studies are a significant addition to the literature, improving understanding of μSOFC behaviour. Brush-painted cells take under half a second to adjust to current changes, without voltage overshooting. Dip-coated cells showed weaker performance, potentially due to lower porosity inhibiting mass transport.

A six-cell module was built, using modelling to optimise manifold design, and its power and transient performance assessed. Interconnections present significant issues for μSOFCs. Despite power density decreasing with increasing diameter, fewer, larger tubes were used to reduce this problem. A new interconnection approach was developed.

ACKNOWLEDGEMENTS

I have had several academic supervisors over the course of this project, and would like to thank all of them. My thanks go to Professor Kevin Kendall for his enthusiasm and initiative in getting this project going, as well as securing EPSRC funding, and to Professor Stephen Decent for his help with the modelling and dealing with my first paper submission in the first year. Dr Waldek Bujalski was the key academic for the European project to which this PhD contributed and also my supervisor for nearly a year before losing his battle with cancer. His positivity and determination were an inspiration. Professor Robert Steinberger-Wilckens' help in tying up loose ends and pulling together my research into a coherent thesis was invaluable. Dr Aman Dhir's practical guidance in the laboratory throughout the project and, more recently, supervision have also been a great help.

I benefitted from collaboration with and sponsorship from EADS Innovation Works, and would like to thank Sarah Nash, Caroline Turner and Tom Owen for their support. I also want to thank Pierre Tantot, Eric Georges and Jacques Chapuis of SurveyCopter who welcomed me for a placement. I am grateful for the guidance and encouragement I received from Erich Erdle, and also to Phil Robbins and Bushra who kindly allowed themselves to be persuaded to read over a chapter. Thanks also go to my examiners, Dan Brett and Tim Button, for their helpful comments and suggestions.

Finally, I would like to thank my family, friends and colleagues for their support. Tom, JC, Dub, T, Dan, Anna and the rest of the fuel cell group have all helped to prevent me from being devoured by the Dreaded Write-Up. Particular thanks go to Dad, Fiona and the long-suffering and overly-tall Ewan for reading sections for me and telling me it would be okay, honest, and to James for putting up with living with me and reminding me not to panic too often.

TABLE OF CONTENTS

Contents

Nomenclature and Abbreviations

Some of the most common abbreviations used throughout the thesis are defined below.

Fuel cells used			**Most common materials**	
SOFC	Solid Oxide Fuel Cell		LSM	Lanthanum strontium manganite
µSOFC	Micro-tubular SOFC		YSZ	Yttria-stabilised zirconia
AMI-5.5 µSOFC	µSOFCs used initially; 5.5cm long		LSCF	Lanthanum strontium cobalt ferrite
AMI-15.2 µSOFC	µSOFCs used later in the project; 5.5cm long		SDC	Samaria doped ceria
Cell descriptions and testing				
OCV	Open circuit voltage (cell voltage when no current is drawn)		I-V curve	Current-voltage or polarisation curve; a standard measure of fuel cell performance
TPB	Triple Phase Boundary		EIS	Electrochemical Impedance Spectroscopy

List of Figures

List of Tables

1. INTRODUCTION

1.1 Rationale for Developing Sustainable Technology

The scientific evidence for global warming is now very strong [1] and, with the Intergovernmental Panel on Climate Change reports [2] stating that "Greenhouse gas forcing has *very likely* caused most of the observed global warming over the last 50 years", backed up by evidence from various other scientists [3-5], it would be foolish to ignore this issue. The Stern Review [1] details the expected costs that will be incurred if global warming is allowed to continue on its present trajectory unchecked, and the expenses necessary to ensure it does not. The Review's conclusion is that "the benefits of strong, early action on climate change outweigh the costs" but persuading companies to change currently profitable practices to give unproven savings in the future is challenging.

Besides global warming, there is also the aspect of "peak oil". At present, the rate at which fossil fuels are formed on earth is negligible in comparison to the rate at which they are used. As such, seeing how heavily they are relied upon, they must be treated as a precious and finite resource. The 2009 BP Statistical Review of World Energy [6] states that, "Our data confirms that the world has enough proved reserves of oil, natural gas and coal to meet the world's needs for decades to come", but these reserves will become more expensive as exploration and technological advances are needed to find more sites, and to get more out of those already known. Prices will be forced to rise. Looking beyond cost limitations, the question remains of what happens once those few decades' resources are exhausted.

A few more optimistic analysts suggest that peak oil will not be a supply-side phenomenon, but rather a gradual reduction in our demand for oil as people shift to renewable energy generation and electric vehicles etc. [7, 8]. They expect oil production rates to start to fall by 2020, as use decreases due to use of alternative energy resources. A Deutsche Bank report along these lines suggests that peak oil demand will occur in 2016 [7].

These issues raise the pivotal question – what are the alternatives? At the simplest level, there are two options:

1. Reduce consumption to align with natural production of fossil fuels.
2. Increase utilisation of renewable resources so current consumption levels, and the predicted increases, are sustainable.

Reducing consumption where possible is sensible, and is supported by government grants for home insulation, for example. However, with an ever-expanding population and high levels of power demand for modern life, this is insufficient to keep energy usage rates below or at generation rates. A combination of the two options is therefore the only practical route. Wind, solar, tidal and biomass energy are all examples of renewable resources now being exploited, but a great deal more renewable energy is required to meet sustainability targets, so a lot more research and development is needed.

To become sustainable in terms of energy consumption, radical changes are required in all aspects of life. A great deal of research has gone into potential routes to sustainable energy economies, such as the Roads2HyCom project [9], but the impetus to bring these ideas into effect is widely lacking. In order to get public and industrial support for new, cleaner

technology, the research community has to visibly demonstrate that the technology is viable, both in terms of performance and of cost.

The role of this PhD project is to aid in the development of an early market product that can demonstrate the benefits of sustainable technology for transport, and reassure investors and the general public that this is the way forward, not blue-sky research.

Only 13.1% of the world's energy (19.5% of electricity) came from renewable resources in 2009 [10], only a 1% increase from 2006 [11]. This includes generation from waste materials, which still releases carbon dioxide (CO_2) into the atmosphere, and, as such, may not be classed as environmentally sustainable if this CO_2 release is not balanced by carbon capture. The main sources of renewable energy are hydroelectric (16% of electricity generation), solar, wind, geothermal, tidal power.

Energy storage for use later or in mobile applications is another important issue. With renewable energy sources such as wind, supply cannot be matched to demand directly as the supply depends entirely on the weather conditions at the time. To make best use of the turbines, therefore, a method of energy storage must be used so the excess energy generated at off-peak times does not go to waste. Mobile energy storage must also be available for transport applications, among others, so stationary systems such as hydro-electric pumped storage alone are insufficient. Batteries are one option, and renewably-generated hydrogen gas is under consideration as another [12], due to its zero point-of-use CO_2 emissions.

Currently known sustainable options for transport are pure electric (battery and ultra-capacitor) or fuel cell/fuel cell-battery hybrid systems. Although pure electric systems are very good for short range systems, Thomas [13] states, "...for any vehicle range greater than 160 km (100 miles) fuel cells are superior to batteries in terms of mass, volume, cost, initial greenhouse gas reductions, refuelling time [and] well-to-wheels energy efficiency". Fuel cell power systems are therefore the subject of this research.

1.2 What is a Fuel Cell?

Fuel cells are devices for extracting electrical energy from hydrogen-rich fuels electrochemically. The basic principle was discovered by Christian Friedrich Schönbein [14] and demonstrated by Sir William Grove in 1839 [15]. Since then, huge improvements have been made in the designs and materials used, and fuel cells are now seen by many as the energy generation method of the future [12, 16, 17]. As the perceived priority of environmental concerns in industry is increasing, the case for fuel cells is getting stronger [18]. Lifetime, reliability and cost are the three main issues that need to be addressed for large-scale commercialisation [19].

Fuel cells resemble batteries in many ways, but, unlike batteries, they are not limited by their internal capacities. For as long as reactants are supplied from an external pipe or reservoir, the fuel cell will give power. As they use an externally supplied fuel, these cells can also be compared to gas, oil or coal-burning generators. Traditional generators burn the fuel, so are limited by the Carnot efficiency for heat engines, due to the second law of thermodynamics. Hydrogen fuel cells do not burn the fuel, however, so are not limited to the Carnot efficiency. As such, potential efficiencies of fuel cell generators are much higher

than those of traditional generators, at around 50-60% [20] (as compared to coal-fired power generation, which has an electrical efficiency generally under 40% [21]) . Fuel cells are modular in nature, with stacks of cells being built up to meet the power requirements of the relevant application. The size of individual cells can also be increased to raise the power per cell, although limiting factors such as heating rates and current path resistance can reduce the efficacy of this approach. This adaptability, along with their clean and quiet operation, makes them a very attractive option for a wide range of applications [15, 22].

Figure 1 shows the key features and basic operating principles of a hydrogen fuel cell. The direction of ion flow through the electrolyte, and so the type of ion, depends on the type of fuel cell. The ions are generally H^+, O^{2-} or CO_3^{3-}. Sealing of cells, interconnections between cells in stacks and choices of material and catalyst are active areas of research. More detail will be given later for the type of fuel cell chosen.

When fuel cells are operated on pure hydrogen, the only waste product is water. Fuel cells therefore have the potential to offer very clean energy generation, but the hydrogen has to be produced. At present, a lot of the hydrogen used comes from reforming of fossil fuel sources; although this may give better use of the energy content due to the higher efficiencies, this is not sustainable. Production of hydrogen by electrolysis can be sustainable if renewable electricity is used to power the electrolyser. This has the added advantage that hydrogen generation can be used for energy balancing [23]. Renewable energy sources such as wind and solar are notoriously unreliable, which can cause grid instability [24]; hydrogen offers one method of storing the energy until it is needed.

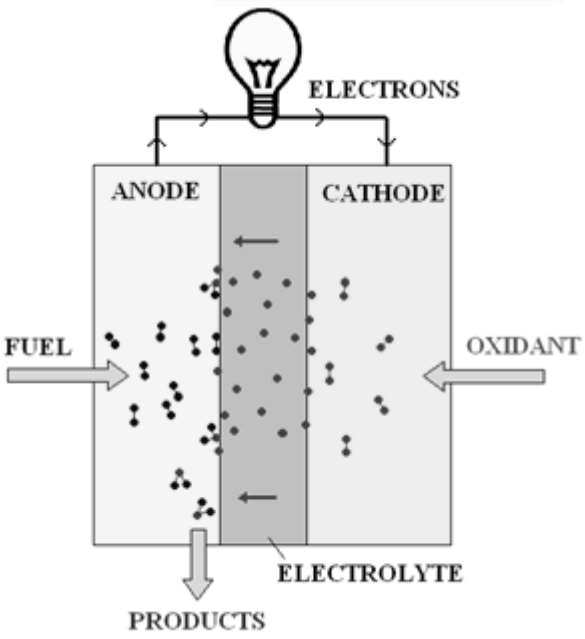

Figure 1 - Schematic of a fuel cell with flow of negatively charged ions (O^{2-}) across the electrolyte, with hydrogen (H_2) fuel at the anode and oxygen (O_2) at the cathode

The electrochemical reactions occur at the electrodes. For the direction of ion transport shown in Figure 1, the generalised reactions are:

Anode: Fuel + Ions → Product + Electrons e.g. $H_2+O^{2-} \rightarrow H_2O+2e^-$ …(Eq. 1.1)

Cathode: Oxidant + Electrons → Ions e.g. $O_2+4e^- \rightarrow 2\ O^{2-}$ …(Eq. 1.2)

For the reverse direction of ion transport, the generalised electrode reactions are:

Anode: Fuel → Electrons + Ions e.g. $H_2 \rightarrow 2H^+ +2e^-$ …(Eq. 1.3)

Cathode: Oxidant + Electrons + Ions → Product e.g. $½O_2+2e^-+2H^+ \rightarrow H_2O$ …(Eq. 1.4)

The overall reaction is the same in both cases: Fuel + Oxidant→Product (H_2 + ½ O_2→H_2O). The electrons transferred in the course of this reaction drive the circuit and provide the electrical power.

The Nernst equation (Eq. 1.5) for this overall reaction of a fuel cell can be derived [25] considering the changes in the Gibbs free energy of formation of the product (in this case water) from the reactants (hydrogen and oxygen) and treating the hydrogen, oxygen and steam as ideal gases. Assuming the system has no losses, the electrical work done is equal to the amount of Gibbs free energy released (Δg_f), giving proportionality between Δg_f and the electromotive force, E.

$$E = E^0 + \frac{RT}{2F} ln\left(\frac{a_{H_2} a_{O_2}^{1/2}}{a_{H_2O}}\right) \quad \text{....(Eq. 1.5)}$$

In Equation 1.5, E is the theoretical electro-motive force (EMF) of the fuel cell, E^0 is the EMF at standard pressure and temperature (STP), R is the gas constant, T is the temperature, F is Faraday's constant, and a_X is the activity of substance X. 2F is the constant of proportionality between Δg_f and E, as this is the charge transferred per mole of hydrogen reacted, 2 being the number of electrons transferred per molecule of hydrogen.

At 25°C and atmospheric pressure (STP), E=1.23 V. In the ideal case, this electromotive force can be seen and measured as the Open Circuit Voltage (OCV – voltage at zero net current) of the fuel cell. In reality, the OCV is usually slightly below this level due to increased

temperatures and small amounts of cross-over of gas, for example, and various other losses in voltage are seen with increasing current, as discussed later.

1.3 Choice of Product

The intended application must be known in order to make an informed decision on which fuel cell technology is the most suitable. As the technology becomes more advanced and affordable, fuel cells should expand into the domestic, automotive and aerospace sectors. As the cost is currently relatively high, early market applications must have requirements not met by alternative technologies to make fuel cells the technology of choice. Fuel cells are already in use in some niche areas, including back-up power supplies and "green" stationary generation [26], power for camper-vans [27] and factory floor fork-lift trucks [28, 29], where better environmental credentials than combustion engines and improved duration as compared to batteries are required.

Unmanned aerial vehicles (UAVs) are the chosen commercial technology for this project because this is an expanding market (see Figure 2) with well-defined system requirements (payload, flight time, range and mission profile capabilities), for which the fuel cell advantages of extended range, low point of use emissions, reliability, efficiency and silence of operation are key.

Fuel cells have proven capable of more than doubling the maximum possible flight times for small UAVs [30] as compared to battery-powered flight, so giving significant added value to

the customer in allowing longer ranges and mission profiles. The lack of pollution as compared to internal combustion engines makes them more suitable for polar surveys, for example, where protecting the environment is crucial.

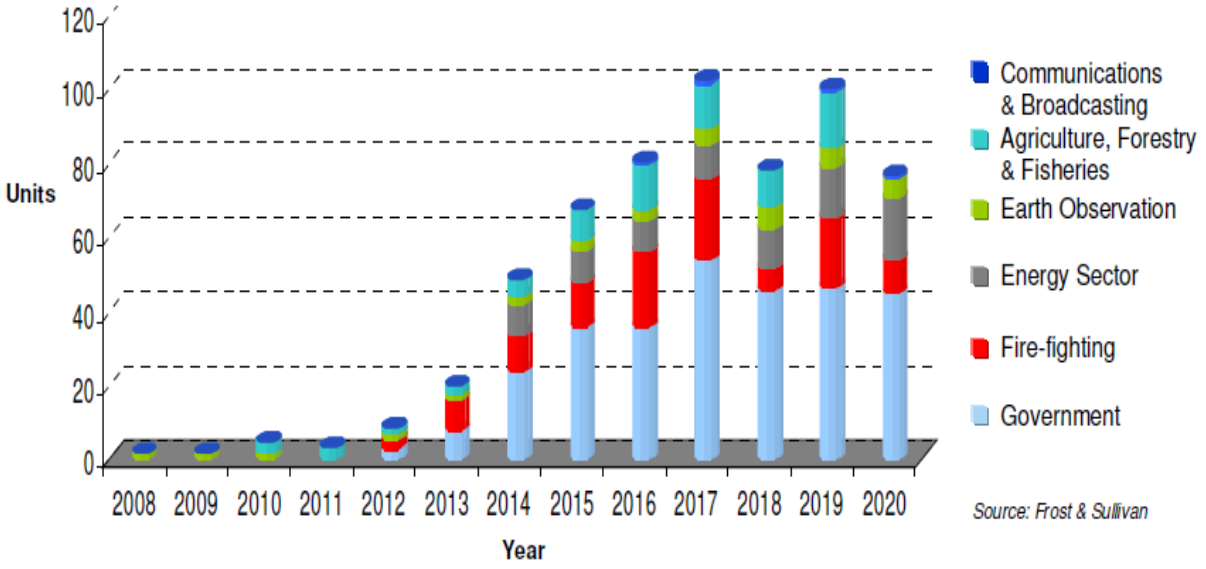

Figure 2 - Actual and projected growth of the European civil and commercial UAV market [31]

In these niche markets, customers are much less cost-sensitive, so it is ideal for developing new, and therefore currently expensive, technologies. Collaboration with EADS (world leaders in drone manufacture) gives access to state-of-the-art design specifications and technical ability.

Once proof of concept has been provided and publicised through this project, the market should increase and the same technology can be expanded to other applications with similar power requirements. UAVs have the potential to be an early-market fuel cell product, due

to the investment and dedication of various companies and SMEs. They represent a promising starting point with a substantial potential market if the project is successful [32].

1.4 Fuel Cell UAVs

Unmanned Aerial Vehicles (UAVs) have many possible uses, both civilian and military. To date, nearly all UAVs have been internal combustion engine or battery powered. Internal combustion engines have the disadvantages of being loud and producing significant exhaust fumes. Batteries offer the advantage of clean and silent operation, which is especially useful for stealth purposes. They lack the range or flight time required for more demanding missions, however, and have reduced payload carrying capacity [33]. Recent advances in battery technology have given significant increases in flight time [34], but battery size and weight is still a limiting factor.

Battery powered mini-UAVs generally have maximum flight durations of around two hours; using a fuel cell-battery hybrid power system can increase this to around eight to ten hours, depending on the system. This increases the possible range of the UAV significantly, and can open up different mission possibilities.

Although publicly available information on these UAVs is limited due to obvious military and commercial concern over state-of-the-art technology, published information on 37 fuel cell powered UAVs was found and tabulated (See Appendix I: Fuel Cell UAVs).

There are three main manufacturers of fuel cell-based UAV power systems, and their products are used in the majority of fuel cell UAVs tabulated. These companies are Ultra Electronics – AMI, Horizon Fuel Cell Technologies and Protonex. EnergyOr Technologies Inc. also advertises a fuel cell UAV system, although they are less well known. All four use fuel cell-battery hybrids. These companies often do not make the UAV platforms themselves, but are suppliers to other companies. Two different types of fuel cells are used by these companies – Solid Oxide Fuel Cells (SOFCs), which operate at high temperatures, and Polymer Electrolyte Membrane Fuel Cells (PEMFCs), which operate at lower temperatures. The temperature ranges and other advantages and disadvantages of fuel cell types will be addressed later.

Having contacted all three PEMFC UAV power-pack suppliers, EnergyOr was the first to respond, and the most forthcoming. Despite the dimensions being listed as, "Fully configurable depending on UAV airframe" [35], approximate dimensions for the unit are classed as proprietary information. They quoted a price of CAD $29,500 (US $29,219) for a test unit, not including the refilling station (email correspondence). Horizon provided a quotation of US $20,000 for a single, standard AEROPAK evaluation unit with two fuel cartridges. It then costs $500 per like-for-like fuel cartridge re-fill exchange (thus $500 per flight, not including depreciation, as at present the cartridges cannot be stopped and started). They estimated a year for system adjustment and integration. Protonex did not provide any information beyond that on the website, suggesting a lack of commercial readiness.

None of the companies gives much information on how best to integrate the power pack with an existing UAV system (control and feedback system/any need for air vents, etc.), as this is still a key area of development. Table 1 compares and contrasts the available information on these fuel cell systems.

The lack of published information on the Ultra Electronics-AMI system (the Amie50) makes a direct comparison of extant SOFC and PEM systems hard, although its ability to use off-the-shelf fuels is a key advantage. Protonex claim to be developing a new SOFC system for portable applications (again based on the small tubular design), but data on this are not yet available. EnergyOr do not state a volume for their product, so a size comparison is not possible. In terms of energy storage for its size, the UAV-C250 is stronger than the AEROPAK Type I; its peak power is lower, however, and weight higher. The EPOD series' claimed peak powers are impressively high, but there is no external verification of their capabilities publically available (no published evidence of collaborations with known companies or universities).

These values were compared to the requirements for UAVs produced by SurveyCopter (confidential information, not recorded here). Only the lowest power UAV they produce could have its average power demand covered by any one of these fuel cell power packs, and even then more battery storage would be needed for the high peak power requirement for take-off. Size restrictions would be a strict limitation here; reducing the fuel cartridge to "only" double the stored energy (instead of more than tripling it, as any of the listed systems

would) would reduce the volume required, but an increase would probably still be needed as compared to the currently used batteries.

Table 1 - Comparing extant UAV power-packs [35-42]

	Horizon Fuel Cell		Ultra-AMI	Protonex	EnergyOr		
	AEROPAK Type I	**AEROPAK Type II**	**Amie50**	**UAV - C250**	**EPOD-310**	**EPOD-210**	**EPOD-210-XLE**
Fuel Cell Type	PEMFC	PEMFC	SOFC	PEMFC	PEMFC	PEMFC	PEMFC
Volume (m^3)	0.0034	0.0049	+	0.0036	+	+	+
Volume without Fuel Cartridge (m^3)	0.00103	0.00103	+	0.00135	+	+	+
Weight without Fuel Cartridge (kg)	0.47	0.47	+	1.2	+	+	+
Weight - dry (kg)	1.26	1.65	*	3.00**	3.95*	2.95*	3.65*
Weight - hydrated (kg)	2.00	3.50					
Peak Power (W)	600	600	+	500	1000	850	
Continuous Output Power (W)	200	200	50	250	310	210	
Voltage for this power (V)	21	21	26	24	between 32 and 45+	between 30 and 45+	
Energy (Wh)	900	2125	+	1500	1790	990	1665
Guaranteed lifetime (hours)	500	500	"hundreds"	500	1000	500	
Fuel Flexibility			☑				

*hydration irrelevant, **hydration relevant but unspecified, +unspecified

To comfortably meet the continuous power requirements of the more power-hungry UAVs, two to three of these power packs would be required, although a single fuel cartridge would suffice for a very significant increase in net energy stored. The peak power would be near-impossible to match for the same airframe, given the volumetric increase required for additional fuel cells. More reasonably, this peak power gap could be filled by additional battery storage.

1.5 Requirements for the Power Unit

A crucial requirement for an early market product is that it runs on a fuel which is readily available and easily affordable today (a strategic fuel). As such, although a "green" fuel cell system would ideally run on pure hydrogen (or bio-gas if some point-of-use CO_2 emissions are accepted [43]), the use of propane is considered here. High temperature SOFCs therefore need to be used, as PEMFCs require pure hydrogen as fuel. The higher efficiency (up to 60% electrical efficiency demonstrated with methane [18]) of SOFCs means that this would make more efficient use of the energy in the propane than an internal combustion engine would. Switching to hydrogen would reduce system complexity (removing need for as pre-reformer) once that is more widely available. Propane provides low weight and good energy density[1] for the UAV tank. A list of the main requirements is given below:

- Strategic fuel
- Rapid start-up (≤20 minutes)
- Cycling capability (reduction-oxidation cycling should not happen, but the system must be tolerant of multiple thermal cycles)
- Lifetime suitable for application (≥600 hours of flight time)
- Good efficiency and range, giving longer flight-time than possible with current battery UAVs (here fuel cells have distinct advantages over traditional batteries, see Figure 3)
- Rapid recharging (e.g. re-filling or exchanging the propane canister)
- Ease of adaptation to alternative fuels in the future (e.g. bio-hydrogen)

[1] The gravimetric energy density of propane, 46 MJ/kg, is lower than the 120 MJ/kg for hydrogen, but volumetrically, hydrogen only gives 10 MJ/m^3 (NTP), as compared to 85 MJ/m^3 for propane. A smaller tank of propane can therefore be used to contain the same energy, at a given pressure.

Any new technology is also required to be economically competitive with current equivalents, and to prove equal to the same challenges.

Figure 3 - Comparing fuel cell and battery UAVs - Horizon AEROPAK [41]

With the choice of product in mind, a hybrid battery-fuel cell power system is the sensible option to give good efficiency and performance. The batteries provide instantaneous response to changes in load and the fuel cell system extends the range of the UAV by adding additional power to the system and recharging the batteries when the system is not operating at maximum load. The advantages of hybrid systems have been discussed repeatedly in the literature [13, 44-46]. The two key points are that a fuel cell capable of providing enough power for take-off would be under-utilised for the remainder of the flight (hence "wasting" weight, which is very limited), and that although the dynamic response of fuel cells to load changes can be very good [47], limitations in the systems [48] usually give significantly longer lead times than the near-instantaneous change possible with batteries.

1.6 Choice of Fuel Cell Type

Fuel cells are characterised by the type of electrolyte used. There are five main types of fuel cell, and these can be split into three groups according to their temperatures of operation. These main types and their key advantages and disadvantages are listed in Table 2.

The two most widely used types, mentioned briefly earlier, are:

1. Polymer Electrolyte Membrane fuel cells (PEMFCs)
2. Solid Oxide fuel cells (SOFCs)

Polymer Electrolyte Membrane fuel cells are often seen as the most attractive option due to high power density and lower temperature requirements, and are generally the design of choice for vehicles to date [49]. They are very easily poisoned by impurities in the fuel, however, and so require very pure hydrogen (around 99.999% purity required - draft international standards, ISO 14687, in preparation [50]).

Solid Oxide Fuel Cells (SOFCs) are more efficient and can use hydrocarbon fuels directly, so are a sensible choice for early market products. This facilitates the use of currently more familiar and easily available fuels such as propane for the initial development and manufacture, changing to hydrogen in the future as supply chain dynamics alter and make this economically viable. This helps to avoid the “chicken-and-egg” problem of industries being unwilling to make a vehicle before the fuel to power it is widely available, and unwilling to invest in infrastructure before the vehicles exist to use it. Although the high operating temperatures of SOFCs can be a disadvantage, due to heating and insulation requirements, this heat can be used in combined heat and power applications, making

SOFCs very versatile [51, 52]. The high temperature is also what allows the increased fuel flexibility of SOFCs – CO and hydrocarbons can all be used as fuels [52].

Table 2 - Different types of fuel cells - summary

Temp.	Type	Advantages	Disadvantages
Low (50-100°C)	Polymer Electrolyte Membrane	• High power density • Low weight and volume • Quick start-up (warm-up times)	• Requires very high purity hydrogen* • Electrolyte must be kept hydrated • Require precious metal catalyst
	Alkaline	Good performance due to quick reactions	Very easily poisoned by CO_2 (which converts the KOH to potassium carbonate (K_2CO_3)), so they have to be operated on pure oxygen rather than air
Medium	High-temperature PEM	Improved kinetics, impurity tolerance and heat and water management as compared to PEM [53]	Increased thermal stresses in materials
	Phosphoric Acid	• More tolerant of CO than PEM cells • One of the most mature types in terms of technological development	• Safety: Requires use of very high temperature acid. • Heavier and larger for the same power as other cell types • Requires precious metal catalyst
	Molten Carbonate	• Can use hydrocarbon fuels directly (internal reforming) • Can use non-precious metal catalysts	Generally poorer durability due to the combination of high temperature and the electrolyte being corrosive
High (500°C+)	Solid Oxide (SOFC)	• Can use hydrocarbon fuels directly (internal reforming) • High-temperature heat • Can use non-precious metal catalysts • Most tolerant of sulphur [54]	• Safety concerns and material and energy costs increased due to high operating temperatures • Slower start-up†
*A variant operates on methanol; high purity again needed †Micro-tubular solid oxide fuel cells have shorter start up times than the planar design			

Micro-tubular solid oxide fuel cells (µSOFCs) running on catalytically reformed propane are a strong candidate based on the requirements listed in Section 1.5 Requirements for the Power Unit. The high purity of hydrogen required for PEMFCs could not be obtained through on-board reforming given the space and weight restrictions of the small UAV chosen, and planar or larger-tube SOFCs would not heat up within the required 20 minutes for "rapid" start-up.

Although their power density to date has been typically lower than that for planar arrangements, they have less stringent sealing requirements [55] (the tubes can extend out of the highest-temperature area, allowing seals to be at lower temperatures), can survive steeper temperature gradients [56] (due to the smaller size and avoidance of rigid high-temperature seals) and have a shorter start-up time (2-20 minutes, depending on size, rather than 2-6 hours for planar cells [56]). Details of µSOFC design and operation will be discussed in the following chapter.

Stack design is another key consideration for this project. The number of required cells and interconnects determines the complexity of the design, and also contributes to the total weight. Obviously, both should be minimised within the constraints imposed by the operational requirements of the UAV.

1.7 PhD Objectives

The overall aim of this project is to contribute to the development and building of a 300 W µSOFC stack, weighing less than 1.5 kg, for use in a small UAV. This work provides some

contribution to the Solid oxide fuel cell Unmanned Aerial Vehicle (SUAV) FCH JU project [57], for which other areas of stack and system design required are assigned to other partners[2]; for example, the development of gas reformers and a sulphur filter to pre-treat the propane before it is used inside the cell. Figure 4 shows the main areas to be tackled in this PhD project. The two key areas for research were characterisation and improvement of the individual cells and development of new interconnections for cylindrical cells. The niche market area, i.e. customer requirements and what is already available, was also investigated thoroughly.

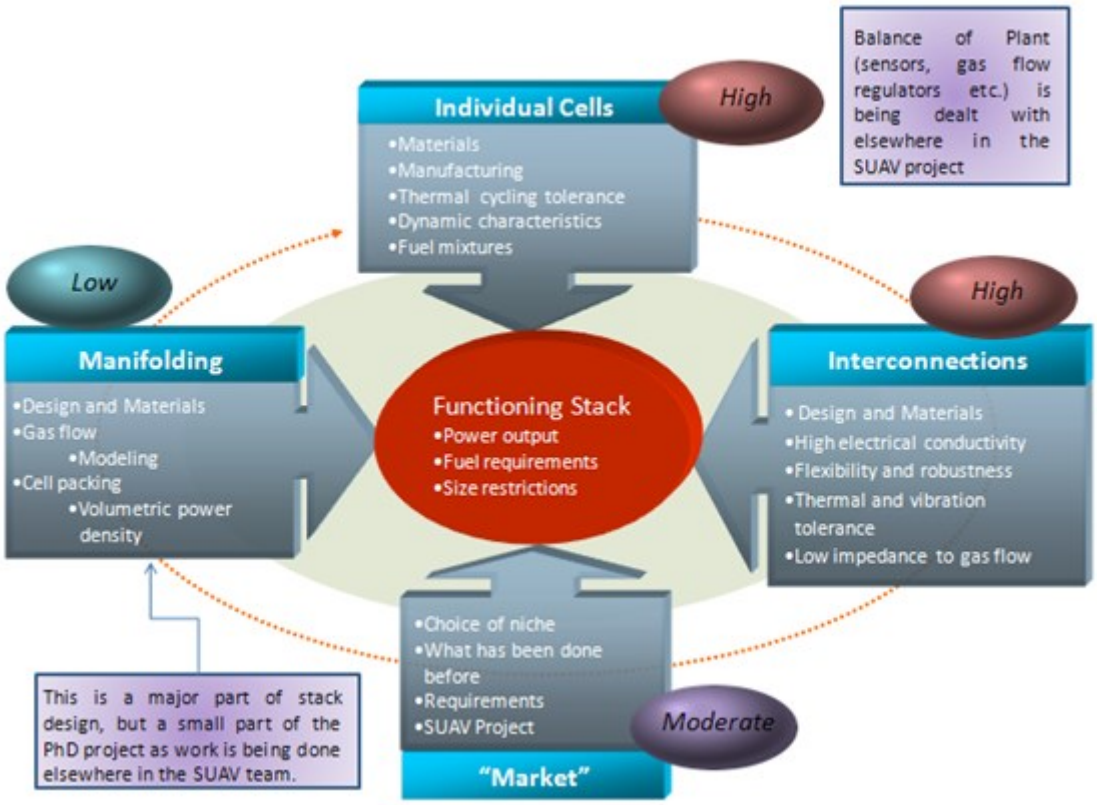

Figure 4 – Overview of activities and areas covered

[2] Hygear, Adelan, Catator, CNR, EADS Innovation Works, efceco, SurveyCopter and ZUT

2. LITERATURE REVIEW – µSOFC CELLS AND STACKS

In this chapter (sections of which have previously been published [3]), the properties and performance of various micro-tubular solid oxide fuel cells from a number of research groups are compared and the differentiating factors discussed. Combining these individual cells into stacks is necessary to obtain useful power outputs, so stack designs reported in the literature are then compared. Issues of fluid and heat transfer within large stacks are critical, so the use of computational modelling as a design tool is also highlighted. A further review of the literature, focused on cell interconnections, is given later in this work (see Chapter 5).

The best recorded power density in the literature to date is 1.3 W/cm^2 for a single cell (a 1.2 cm long µSOFC tested at 550°C with humidified hydrogen [1]), with anode microstructure and current collection technique emerging as the two foremost factors influencing electrical performance of cells. The use of hydrocarbon fuels instead of pure hydrogen, and methods for reducing the resultant carbon deposition, are key areas of research. Performance on thermal and reduction-oxidation (RedOx) cycling is also a critical issue for cell durability and lifetime.

[3] **Relevant Publications:**
Howe, K. S.; Kendall, K. Microtubular SOFCs - Review of Properties and Performance, Proceedings of the 9th European Solid Oxide Fuel Cell Forum, Lucerne, 2010.

Howe, K. S.; Thompson, G. J.; Kendall, K., Micro-tubular solid oxide fuel cells and stacks. Journal of Power Sources 2011, 196, (4), 1677-1686.

Tubular solid oxide fuel cells were pioneered in the 1960s [2], becoming more commercially viable in the 1970s, when Westinghouse began to use an electrochemical vapour deposition technique for their fabrication [3, 4]. This design reduced the problems of sealing as compared to planar cells, but still required a heat up time of four to six hours (Siemens Westinghouse 100 kW system consisting of 1152 tubes of 2.2 cm diameter and 150 cm length [5]). Whilst their performance was fairly good, they did not have a very high power density (around 0.1 W/cm^2). With optimised materials and sufficient fuel, the surface area available for reactions becomes the limiting factor for power generation. For stacked tubular cells, smaller diameters allow more surface area to be fitted into the same volume; theoretically, the narrower the tubes, the better the volumetric performance. This observation led to the invention of micro-tubular SOFCs (μSOFCs) by Kendall in the early 1990s [6] and the following review is entirely focused on this design, as it is the design chosen for this project.

These tubes generally have diameters of less than 1 cm and lengths of 1-15 cm, unlike the 2.5 cm diameters and 1-2 m lengths of their predecessors. μSOFCs have the advantage that they have shorter start-up times (on the order of a few seconds for a single cell) and stronger thermal cycling tolerance [7] than both the planar and tubular designs, due to their small size, and maintain the less stringent sealing requirements of the tubular cells. Interconnects and current collection provide new problems here, however, especially when assembling stacks. As such, there are still issues to be resolved. A comprehensive review of the advantages and issues of these micro-tubular cells, as compared to other SOFC designs, has recently been presented by Kendall [8]. The purpose of this chapter is to compare

performances of different µSOFCs and review the progress that has been made since their inception, as a background to the research subsequently reported.

In addition to the discussion of individual cells, this chapter goes on to summarise progress in stack design. As the output from a single µSOFC cell is currently below 10 W, even at the larger end of the size range [9], these must be combined into stacks of various sizes to meet application demands. Very soon after Kendall's invention of the micro-tubular fuel cells [6], he and his group demonstrated 200-cell [10] and 1000-cell [11] stacks. Since then, new stack and interconnect configurations have been designed and tested by various groups, as discussed below and extended in Chapter 5. Lower operating temperatures and higher power densities are the two main targets of research.

2.1 µSOFC Design

The first µSOFCs, made in the early 1990s, were based on extruded tubes of yttria stabilised zirconia (YSZ) [6]. These tubes were up to 5 mm in diameter, with wall thicknesses in the range of 100-200 µm. YSZ was the electrolyte material, and anode and cathode layers were then added to this supporting electrolyte tube. A schematic of such an electrolyte-supported cell is shown in Figure 5a.

Other designs of µSOFC have also been investigated with anode-supported cells (YSZ and nickel cermet anode tube – schematic in Figure 5b) emerging as strong competitors for the original electrolyte-supported model [12].

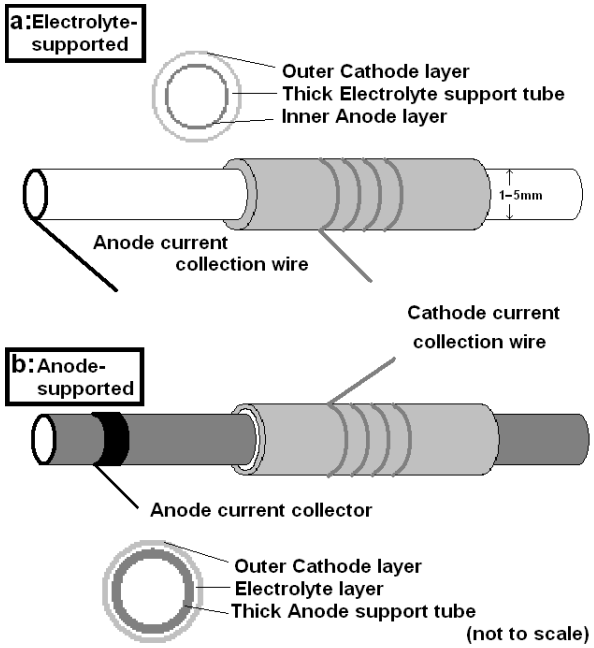

Figure 5 - µSOFC designs (a) Electrolyte supported and (b) Anode-supported. (tube length ~ 1 to 15 cm) [13]

Electrode support allows for a thinner electrolyte (3-30 µm, the work of Tan *et al*. [14] having one of the thinnest), and therefore lower Ohmic resistance. Cathode-supported designs have also been investigated [15-17] (similar to the Siemens-Westinghouse design), but are not common in the literature as it is more difficult to prepare a dense electrolyte on the porous cathode than it is to do so on the anode due mainly to sintering temperature differences [15]. Most µSOFC research in the last few years has therefore used anode-supported cells [18].

In nearly all designs, the support tube is longer than the active cell length. The first tube segment provides a gas inlet tube and the outlet section can be used as a combustor tube, in which the fuel (hydrogen, short-chain hydrocarbons, etc.) and oxidant (oxygen or air) combine.

Co-extrusion to form multi-layer tubes has been demonstrated [19]. This enables better matching of thermal expansion coefficients by changing from e.g. 100% YSZ (electrolyte) to the 90% nickel, 10% YSZ anode in several steps, reducing the risk of cracking on thermal cycling still further.

2.2 Materials Used

Current state-of-the-art materials used for each component of µSOFCs are listed in Table 3. These are by no means the only materials used, and some other choices will be discussed in more detail later. The review of Jacobson [20] discusses these materials in some detail, with a focus on materials suitable for the lower temperature range of SOFC operation (around 450°C). The required properties for the electrolyte and electrodes are described below.

Table 3 – Typical µSOFC materials

Materials for µSOFC components	
µSOFC Component	Material Used
Anode	YSZ and Nickel cermet (with added pore-formers/dopants)
Electrolyte	Yttria-stabilised Zirconia (8 or 10 mole% yttria; 8YSZ or 10YSZ respectively)
Cathode	Lanthanum Strontium Manganite [LSM] (LSM/YSZ composite more recently)
Anode current collector	Nickel
Cathode current collector	Silver

Electrolyte: The three main requirements for the µSOFC electrolyte material are:

- Pure ionic conductivity
- Stability (both at high temperatures and in reducing and oxidising environments)
- Gas tightness

The theoretical operation of SOFCs requires transport of oxygen ions (O^{2-} anions) only through the electrolyte. Passage of electrons, or hydrogen ions (H^{+} cations), through this material would result in short circuiting or combustion, respectively. In addition, the material chosen must have a high ionic conductivity and a very low electronic conductivity over a wide range of temperatures and oxygen partial pressures. This shortens the list of suitable materials significantly.

Some other materials (for example Bi_2O_3 and CeO_2) show higher oxygen ion conductivity then YSZ, but are thermodynamically unstable in reducing environments [21]. They become unstable at low oxygen partial pressures (i.e. on the anode side), leading to some electronic conductivity [22]. Stability at low oxygen partial pressures and on thermal cycling are both critical to cell performance and therefore to material suitability. Sahibzada *et al*. [23] made some progress in using gadolinium to stabilise ceria at low oxygen concentrations.

This stabilisation of ceria allows GDC (Gadolinia-doped Ceria) electrolytes to be used [24]. This has the problem that GDC is a mixed electronic and ionic conductor, so the electronic conductivity needs to be blocked for successful operation. Operating at lower temperatures (500-600°C) offers some improvement, as the electronic conductivity increases with temperature [25]. The use of bilayer electrolytes has also been investigated for this purpose [26, 27]. Yamaguchi *et al.* [26] used scandia-stabilised zirconia as the interlayer, forming the bilayer by a cosintering technique. This yielded good, stable performance. Ahn *et al.* [27] used ESB ($[(Bi_2O_3)_{1-x}(Er_2O_3)_x]$–Ag) as the second part of the bilayer with GDC. This gave a

significant improvement in both resistance and power density as compared to a single GDC layer electrolyte.

The main draw-back of YSZ is the high temperature requirement. Research into materials with good oxygen ion conductivity at lower temperatures has been performed, resulting in the use of Lanthanum Strontium Gallate Mangnesite (LSGM) and Samaria-Doped Ceria (SDC) as electrolytes [28, 29]. LSGM is a good oxygen ion conductor, and, at 800°C, gives performance comparable to that of YSZ at 1000°C [30, 31]. At lower temperatures, the improvement becomes more noticeable - Figure 6 shows the I-V curves obtained for LSGM, SDC and YSZ electrolytes at 500°C.

Use of the anode-supported design allows for a thinner electrolyte (on the order of 10 µm). This can improve performance due to the reduced Ohmic resistance, but care must be taken to avoid the formation of pin-holes, ensuring that the layer is gas tight [32].

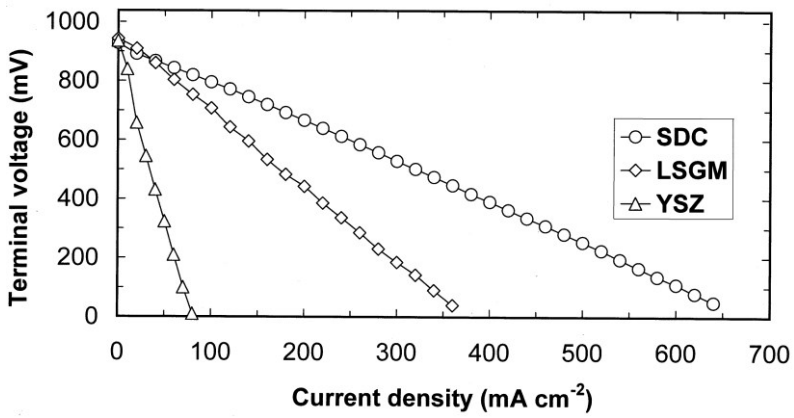

Figure 6 - I-V curves from single-chamber SOFCs using SDC, YSZ, and LSGM electrolytes with a thickness of 0.50 mm electrolyte at 500°C, fuelled with a mixture of ethane and air [28]

Anode: The main requirements for the μSOFC anode material are:

- High porosity (for transport of gases)
- Ionic and electronic conductivity
- Stability at high temperatures in a reducing environment

The oxidation of fuel for current generation occurs at the anode, so the anode's role is to facilitate this reaction. This reaction occurs at the three-phase boundary (TPB), where electronic conductor, reactants and ionic conductor meet. Porosity and mixed conduction are therefore vital for performance – in a nickel-YSZ cermet anode, reactions can occur anywhere that YSZ (ionic conductor), Ni (electronic conductor) and gas are in contact (assuming sufficient conductivity through the anode matrix). This allows the TPB to extend into the electrode, rather than just being the electrode/anode interface. Experiments have been performed to test various pore-formers (for example in the work of Haslam *et al*. [33]) and a porosity of around 50% is found to be preferable to maximise gas transport without compromising conductivity and structural integrity.

The presence of YSZ in both the anode and the electrolyte helps to match thermal expansion coefficients, and so reduce cracking on thermal cycling. The YSZ also inhibits sintering of the nickel particles, which would degrade cell performance. Adding a dopant such as ceria helps to improve performance on temperature and RedOx cycling [34] (as well as increasing the sulphur tolerance [35]). Ceria improves thermal cycling tolerance because it helps to match the thermal expansion coefficient of the cermet to that of the pure zirconia more closely, reducing thermal stresses on cycling. Doping with ceria increases the electrical conductivity of the anode, allowing lower loadings of nickel to be used [36]. Oxidation and reduction

increase the likelihood of the nickel particles agglomerating and sintering, reducing the available surface area for reaction. Ceria helps to stabilise the nickel particles [37], so reducing this effect on RedOx cycling. Careful control of YSZ particle size and anode porosity also helps to improve the stability under RedOx conditions [38, 39], with the more porous structures (tested up to 34% porosity) being most stable [38]. Suzuki [39] found that using a nickel particle size below 100 nm made the microstructure more porous and improved cycling performance.

Cathode: The main requirements for the μSOFC cathode material are the same as for the anode, although stability in an oxidising environment replaces the need for stability in a reducing environment (except for in the case of single chamber operation). Cathode optimisation is critical as the oxygen reaction occurring here is often the rate limiting factor, so various different materials and layered designs are being researched [40-42]. The use of various interlayers has become the subject of much research, with such a layer often being placed between the cathode and electrolyte to reduce the occurrence of unwanted chemical reactions [24, 43]. For example, when a lanthanum strontium cobalt ferrite (LSCF) cathode is in contact with a YSZ electrolyte, not only does the thermal expansion mismatch cause stresses on heating [43], but also $SrZrO_3$ can form at the interface during operation, decreasing ionic conductivity [44]. A GDC or SDC interlayer is used to reduce or avoid these problems.

LSM is not a good mixed conductor, however; other materials therefore seem likely to replace it as the standard. More recently, an LSM/YSZ mixture has been used. With this

mixture, a 50:50 mass ratio and a fairly large LSM grain size in the outer cathode collection layer has been found to be optimal [45]. Examples of other such materials for replacing LSM include mixed conducting perovskites such as lanthanum strontium ferrite (LSF) and lanthanum strontium cobalite (LSC) [43, 46, 47]. Mai *et al*. found that $La_{1-x-y}Sr_xCo_{0.2}Fe_{0.8}O_{3-\delta}$ (LSCF) cathodes gave much better current densities that those based on manganite, with a high strontium content giving a very noticeable positive effect [43]. The recent review of Sun *et al*. [48] examines material and microstructure options in more detail.

Research at Forschungszentrum Jülich [49] found LSCF cathodes to have higher degradation (up to 1.5%/1000 hours of operation at 800°C and 0.7 V) than the LSM equivalents (less than 1%/1000 hours [50]), but the power densities were higher by almost a factor of two, especially at lower temperatures [43, 49, 51]. LSCF lowers the activation polarisation of the reaction [51], allowing this reduction in operation temperature. The A-site deficiency in the $La_{0.58}Sr_{0.4}Co_{0.2}Fe_{0.8}O_{3-\delta}$ structure has been shown to play a very important role in performance due to the effect on ionic conductivity [49]. Having more Sr^{2+} cations on the A-sites, rather than La^{3+} has also been shown to increase the surface exchange of oxygen, which can also improve performance [52].

The thermal expansion coefficient increases as the concentration of Sr increases, however, which can cause mechanical problems [53]. Another advantage of using LSCF for the cathode is that it has a lower electronic resistance than LSM [51], so reduces the Ohmic

losses and power drop in connections. Overall, LSCF is shown to give higher electrical and electrochemical performance at lower temperatures than LSM [49, 54], with precise values depending on the LSCF A-site compositions (see Figure 7), but the long-term stability still needs some improvement [43, 49].

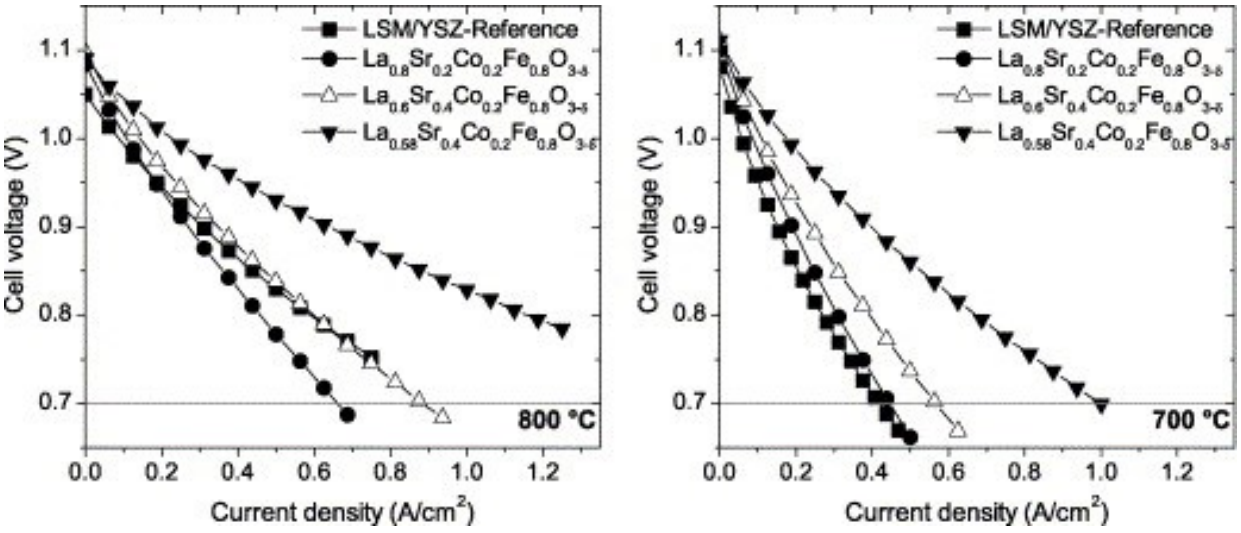

Figure 7 – I-V curves at 800°C and 700°C of single cells with various LSCF cathodes compared to cells with LSM/YSZ cathodes [49]

For this work, ~1% degradation/1000 hours is acceptable, as a total stack lifetime of 600 hours of operation is the target, in line with current expectations for similar UAVs powered by batteries [4]. The advantages of higher power density at lower temperature more than compensate for this slightly higher degradation rate, as the reduced required volume for both the stack itself and the insulation is a major benefit aerodynamically. As such, although the initial work in this PhD used LSM-based cathodes, the cells eventually selected for the SUAV project have LSCF-based cathodes.

[4] Communication with SurveyCopter

To take full advantage of the lower temperature operation of LSCF, changes need to be made to the electrolyte to allow oxide ion conduction at lower temperatures. Thin-film ceria electrolytes have proved useful in the 500-600°C range [54], and also offer the advantage over YSZ of chemical compatibility with LSCF, avoiding the need for a barrier layer between the electrolyte and cathode. The cells used in this work have YSZ electrolytes, so the ideal operating temperature remains relatively high, at 750°C.

2.3 Current Technology Status

There are three main aspects of fuel cell "performance" when looking at power generation. These are power density (areal or volumetric), efficiency and durability. Various definitions of efficiency and fuel utilisation exist, as discussed in Section 2.4.2. Appendix II: Calculations of Fuel Utilisations shows the methods and values used to calculate the utilisation values tabulated here. Reported areal power densities (Wcm^{-2}) in the literature in the last few years are given in Table 4, and durability will be discussed in Section 2.4.1.

The following standard abbreviations are used in Table 4:

GDC: Gadolinia-doped Ceria

LSCF: Lanthanum strontium cobalt ferrite (La-Sr-Co-Fe-O)

LSM: Lanthanum Strontium Manganite

YSZ: Yttria-stabilized Zirconia

It should be noted that the vast majority of recent work on µSOFCs uses the anode-supported design; all of the cells listed in Table 4 are anode supported.

Table 4 – Overview of reported anode-supported single cell µSOFC performance

Ref.	Year	Power Density[a] (Wcm^{-2})	Temp. (°C)	Cell external diameter (mm)	Anode Material	Electrolyte Material	Cathode Material	Fuel	Fuel Utilisation[b] (%)
Sammes et al. [1]	2011	1.3	550	1.6	Ni-GDC	GDC	LSCF-GDC	H_2	
Sammes et al. [55]	2009	1.02	570	0.8	Ni-GDC	GDC	LSCF-GDC	H_2	~54
		0.84	550	0.8	Ni-GDC	GDC	LSCF-GDC	H_2	~43
Suzuki et al. [39]	2009	1.1	600	1.9	Ni-Sc-Zr, Ce-doped Zirconia (10Sc1CeSZ)	10Sc1CeSZ	LSCF-GDC	H_2	~3.4
		0.5	550	1.9	Ni-Sc-Zr, Ce-doped Zirconia (10Sc1CeSZ)	10Sc1CeSZ	LSCF-GDC	H_2	~2
Suzuki et al. [24]	2007	1.017	550	0.8	Ni-GDC	GDC	LSCF	H_2	~56
		0.628	500	0.8	Ni-GDC	GDC	LSCF	H_2	~33
		0.273	450	0.8	Ni-GDC	GDC	LSCF	H_2	~14
Suzuki et al. [56]	2012	0.57	700	1.93	Ni-YSZ	ScSZ - GDC	LSCF-GDC	H_2	~40
Jin et al. [57]	2007	0.645-0.848	800	8	Ni-YSZ	YSZ	LSM	H_2	~4
Yang et al. [58]	2010	0.78	800	1.5	Ni-YSZ(-SDC)	YSZ	LSM–YSZ(–SDC)	H_2	~11
Droushiotis et al. [59]	2012	0.7	600	<1	Ni-GDC	GDC	LSCF	H_2	17
Lee and Kendall [60]	2007	0.7	850	2.5	Ni-YSZ	YSZ	LSM/ YSZ[c]	CH_4	
Dhir and Kendall [61]	2008	0.425	850	2.3	Ni-YSZ	YSZ	LSM	CH_4	79
Galloway and Sammes [62]	2007	0.3	450	1.8	Ni-GDC	GDC	LSCF-GDC	H_2	~30
Akhtar et al. [63]	2009	0.122	750	2	Ni-YSZ	YSZ	LSM	CH_4	<11.4

[a]Values taken directly from paper where possible; geometric cathode area used

[b]Values calculated from data given in paper; approximate only, simplistic assumptions made - methods given in appendix

[c]Two layers with different LSMs: $La_{0.5}Sr_{0.5}MnO_3$ and $La_{0.82}Sr_{0.18}MnO_3$

Only the main materials for the major cell components are listed in this table – details of binders and pore-formers used, as well as further information on how the cells were produced, can be found in the referenced papers. All of the anodes listed here are nickel cermets, with various dopants, particle sizes and pore-formers. There is more variety in the choices of electrolyte and cathode materials.

In addition to the many research groups working on μSOFCs, there are also several companies, at different stages of commercialisation, which manufacture them. These include Ultra Electronics AMI [64] (from whom the cells used in this PhD project have been purchased), eZelleron [65], KoMiCo [66] and CoorsTek [67], amongst others. Of these, KoMiCo is unusual in being willing to provide a datasheet for the cells [68], including I-V curves, without requiring a Non-Disclosure Agreement (NDA). This suggests more commercial readiness on the part of KoMiCo. Figure 8 is an extract from this, and shows that the peak power at 760°C is just under 0.5 W/cm^2. This is in line with the values given by other research groups, especially when the total cathode surface area (3.4 cm^2) of the KoMiCo cell is considered, as this is larger than many of the cathodes tested by the groups listed in the table above, and power density often decreases as cathode area increases due to the interconnection regimes used (discussed further in Chapter 5).

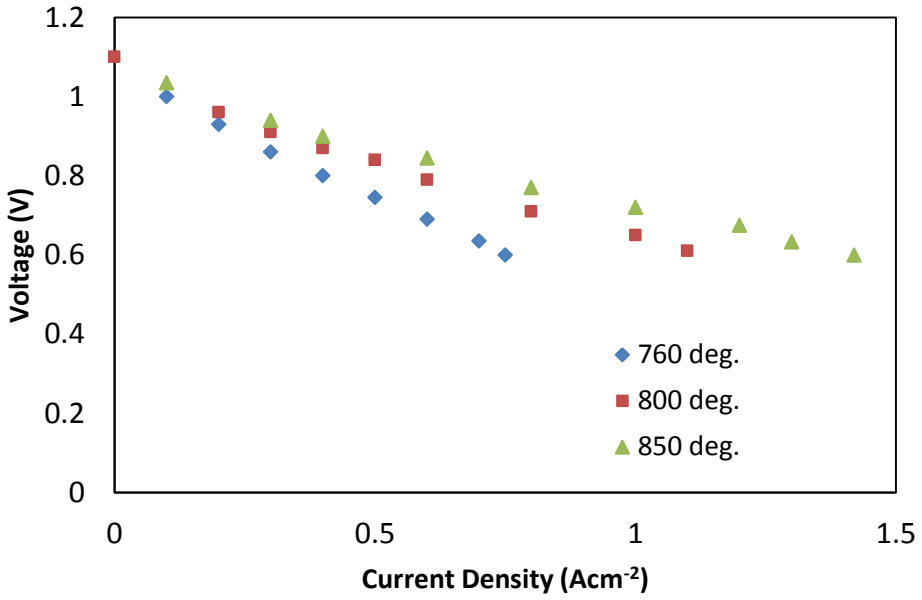

Figure 8 - KoMiCo tube characteristics (points extracted from datasheet image provided by KoMiCo on request [68])

2.4 Key Aspects

Fuel cells are complex systems, with performance determined by the interplay of many different physical and chemical processes. Particular key issues have been identified by researchers, however, and summaries of their findings for SOFCs are given below.

2.4.1 Durability

There are three separate aspects of durability; firstly the gradual performance drop with time during continuous operation on hydrogen, secondly the tolerance of the cell to fuel impurities and carbon deposition, and thirdly the level of degradation the cell suffers on thermal and Reduction-Oxidation (RedOx) cycling.

Performance Drop with Time

Performance drop is usually defined by either % degradation or mV drop per thousand hours when it comes to "commercial" fuel cells. In their review of SOFC technologies for micro-

combined heat and power [69], Hawkes and Leach state that, "Current large-scale tubular SOFC technology has been proven to operate for approximately 40,000 h with less than 0.2% voltage degradation per 1000 operating hours". Many laboratory tested μSOFCs would struggle to reach 1000 hours of testing, however. Galloway and Sammes [62] reported a 40% drop in power after two weeks (<340 hours), for example, and Calise *et al.* [70] reported a 16.1% voltage drop over 6 days (132 hours of testing). The worst degradation is normally seen during the first few hours of operation [62, 70], and the power is generally seen to stabilise after that point. A likely cause of this more rapid initial decline is nickel coarsening in the anode, as porosity is often seen to drop [62].

This anode densification, which reduces fuel flow to the Triple Phase Boundary (TPB), is one identified cause of degradation [62, 71, 72]. The type of wire used for the anode interconnection also has an effect, with Ni wires being shown to be more resilient than Ag wires [62]. Loss of contact of the wire interconnections is hypothesised to dominate the degradation observed when using pure hydrogen as fuel by Calise *et al.* [70], who also suggest micro-cracking of the cells as another cause of degradation. Micro-cracking, and subsequent delamination of the electrode-electrolyte-interconnection layers, is a more significant issue when thermal and RedOx cycling occur (see later), as these cause differential expansion and contraction, leading to stresses between layers. Microstructural characterisation and stress analysis have shown that these stresses are a very likely cause of failure for the YSZ matrix [73]. Stresses at Ni-YSZ interfaces were found to sometimes exceed the yield strength of the nickel, suggesting that stress may be released by plastic

deformation (or possibly deleterious delamination) at such boundaries in Ni-YSZ anodes during thermal cycling [73].

Operating conditions also have a significant effect on performance drop. Operating at lower temperatures can reduce degradation of the cell and interconnect materials [62]. Using excess fuel or operating the cell at higher voltages (lower currents) helps to ensure that the anode is not damaged by oxidation.

Operation on Hydrocarbon fuels

SOFCs operate at a high enough temperature for endothermic reforming of short-chain hydrocarbons, such as methane, ethane and butane, to occur within the anode material (internal reforming) [74]. SOFCs can therefore directly use such hydrocarbons as fuel [61, 75], but rapid degradation is seen with any hydrocarbons with a carbon-carbon bond (with nickel-based anodes, there is often a several-hour offset between the start of exposure to methane and the onset of coke formation [76]). Running directly on hydrocarbon fuels results in carbon deposition on the anode surface, which has a negative impact on cell performance. The deposited carbon blocks catalytic sites and destroys the anode structure [70]. Calise *et al*. found that their cells failed after only a few hours of operation on carbon-containing fuels (H_2-CO and H_2-CH_4 mixtures) as a result of this deleterious deposition [70]. With methane, it is possible to adjust operating conditions to minimise carbon deposition, and this deposition can be reversible (the carbon deposits can be removed if the cell is then fuelled with pure hydrogen, returning cell performance to its original level) [77].

The heat output from SOFCs can be used, along with a catalyst, to pre-reform the hydrocarbon before it enters the cell [78-81], or for internal steam reforming if steam is co-fed to the cell along with the hydrocarbon fuel. Bessler's 2008 review [82] compares and contrasts direct oxidation and internal reforming. Pre-reforming has been shown to reduce carbon deposition, but the catalysts used can be expensive, with that developed by Chen *et al.* [79] being 1% platinum by weight. Although nickel is catalytically active for the reformation of hydrocarbon fuels and often used, precious metals have been shown to be more effective [83].

There are three known techniques for minimising carbon deposition at the anode for direct hydrocarbon utilisation. These are using various anode-dopant combinations, such as Ni/YSZ with molybdenum or ceria [84-86] (or indeed avoiding the use of nickel entirely [87]), using catalyst or barrier layers [88-90] and modifying the anode reduction technique [61, 91]. The principles here are the same for any geometry of SOFC.

The drawback of nickel-based anodes is that nickel acts as a catalyst for the formation of carbon when the ratio of steam to carbon on the anode side is low (a steam:carbon ratio of 3-5:1 is generally required to avoid coke formation with methane [92]). This solid carbon can severely degrade cell performance. Materials including electronically conductive perovskites and copper based cermets have been suggested as alternatives [87]. McIntosh *et al.* [93, 94] investigated the use of $Cu/CeO_2/YSZ$ anodes, and found that using precious metal catalysts would help to increase the OCV of the cell when hydrocarbon fuels are used.

The use of various anode materials and dopants is discussed in the review of Jiang and Chan [95] who conclude that using materials with mixed ionic and electronic conductivity helps to improve operation on both hydrogen and methane. Zhang *et al.* [85] conclude that, "Although the carbon deposition was not suppressed absolutely [by the use of samaria-doped ceria additions to the Ni/YSZ anode], some deposited carbon was beneficial for performance improvement". Dhir and Kendall [61], Mallon and Kendall [91] and Latz *et al.* [96] similarly observed an improvement in performance when using methane fuel instead of hydrogen in cells modified to minimise problematic carbon deposition (see examples of methods below).

Lin *et al.* [88] used an inert, porous layer as a barrier between the anode and fuel stream with the aim of reducing coke formation. They conclude that their results using this technique "demonstrate that diffusion barrier layers increase the stable operating parameter range of Ni-YSZ anode-supported SOFCs operating directly with methane". At 800^{o}C, they found that use of such a barrier layer reduced the current density required to avoid coke formation threefold. This is thought to be due to the barrier layer increasing the product (H_2, H_2O, CO, and CO_2) concentration and decreasing the methane concentration in the anode. Zhan and Barnett [89] looked at the use of a ruthenium-ceria catalyst layer. This was found to enable partial oxidation of propane at temperatures above 500^{o}C without carbon formation at the anode (a propane-air mixture was used). This is a marked improvement as carbon deposition would be expected at temperatures of up to 773^{o}C for this gas composition. Resultant gas diffusion limitations were found to limit the high temperature performance, however. Yoon *et al*. [90] used a coating layer of samaria-doped

ceria in the anode pores to improve cell performance with methane fuel. This was also shown to reduce carbon deposition and nickel sintering.

Dhir and Kendall [61] investigated the effect of anode reduction technique on cell performance with methane fuel. They found that reduction at a constant, reasonably low (650^{o}C), temperature was optimal. This is thought to produce fine, evenly sized nickel particles. The conductivity is relatively low, as the connectivity of the nickel particles is not high. Graphitic carbon deposition is thought to aid conductivity by producing conducting "bridges" between the particles, increasing connectivity and so conductivity (Figure 9).

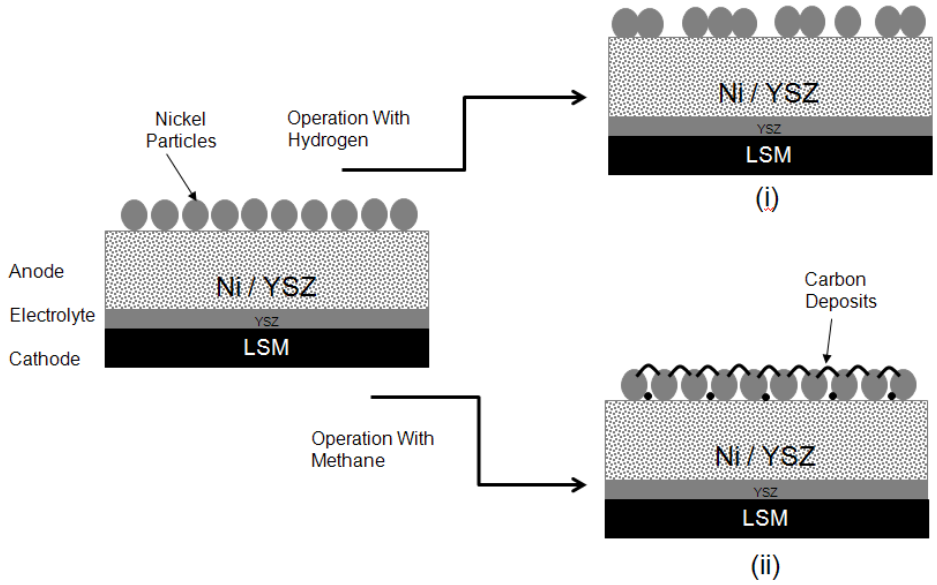

Figure 9- Proposed anode structure after constant temperature reduction in hydrogen with the cell then operated on i) hydrogen and ii) methane [61]

The performance of these cells was notably better for methane than for hydrogen fuel; this was attributed to the carbon deposition from the methane obstructing the sintering of nickel and so helping to preserve the anode microstructure during use, as well as the

afore-mentioned bridging properties. In longer-term testing, periods running the cells on hydrogen may be needed to remove excess deposited carbon.

McIntosh *et al.* [97] had previously observed similar improvements in performance due to hydrocarbon deposits, in their case using copper instead of nickel as the metallic component of the anode. They likewise concluded that this was due to the carbon deposits improving connectivity and so conductivity of the metallic anode components. They found the performance to be most dramatically improved when the metal made up less than 20% of the anode by weight.

Use of a large enough flux of O^{2-} ions through the electrolyte to remove the carbon as the deposits form on Ni-based anodes has also been investigated, with some success [98, 99]. In addition, Kendall *et al.* [100] showed that diluting methane with carbon dioxide or inert gas allowed for more stable operation by shifting the equilibrium point of the carbon deposition reaction. For methane fuel, they found that such a mixture could be fed directly into the cell, with the optimal mixture being around 30% methane, 70% carbon dioxide – this is an example of dry reforming.

Thermal and RedOx cycling

During their periods of use, µSOFCs will be subjected to cycling of both temperature and electrochemical conditions. These processes can both cause microstructural defects in the cell, leading to a reduction in cell performance. Cycling of SOFCs damages the cells in two distinct ways.

Firstly, the temperature gradient leads to degradation during thermal cycling, with microcracks opening up in the anode [101]. These separate the nickel particles, and so increase resistance, giving a corresponding worsening of performance. This was investigated in detail in the REAL SOFC project [102] and is discussed elsewhere in the literature [8, 103]. A relationship similar to those for mechanical fatigue has been established.

A summary of observed thermal cycling capabilities of μSOFCs is given in the review of Lawlor *et al.* [104]. Du *et al.* [105] found single μSOFCs to have very good thermal shock resistance, withstanding temperature changes of 550^{o}C per minute. They also found that stacks could be started up within five minutes, and could withstand over fifty thermal cycles. With single cells, 0% power degradation was seen after 150-338 cycles. The work of Bujalski *et al.* [7] showed that their microtubular cells used could be comfortably raised to their operating temperature of around 800^{o}C within ten seconds, and also cooled rapidly. This allows many hundreds of cycles to be performed in quick succession. For these cycles, the temperature was cycled up and down every ten minutes to 800^{o}C from room temperature. The first few cycles were found to be the most damaging, with a drop in current of about 1% per cycle. The deterioration slowed down after that, however.

Secondly, RedOx cycling (where the fuel flow is turned off then back on again, either deliberately or due to a fault, with temperature remaining constant) was shown to lead to increased damage [106]. This is due to the nickel in the anode oxidising then reducing; the repeated expansion and contraction helps to extend the microcracks. If the cell is cooled rapidly [7] (falling to below 300^{o}C in a matter of seconds) the time for which the cell

temperature is high enough for this deleterious reaction to occur is reduced, improving RedOx durability. This is in opposition to the gentle temperature gradients preferred for thermal cycling durability. As such, the choice of heating or cooling rate must be a trade-off between these two concerns [8], leading to the existence of an optimal temperature ramp rate for a given μSOFC.

2.4.2 Efficiency & Fuel Utilisation

Many different definitions of efficiency for fuel cells exist, and values must be treated with caution unless the definition used is clearly stated [107]. Is the heat useful or wasted? Should parasitic powers required for heating the cell or stack and blowing air around, if required, be included? Should the heat produced by any burned-off fuel be counted? Is the Higher or Lower Heating Value (HHV or LHV, respectively) of the fuel used?

The electrochemical efficiency of the cell can be defined according to Equation 2.1, where V_{cell} is the cell operating voltage, and $V_{rev.}$ is the difference between the standard reduction potentials at the anode and cathode (temperature and fuel dependent; usually a little above 1 V). Practically, even the OCV is always below this value, as it is impossible to eliminate every irreversibility [108].

$$\eta_{electrochem.} = \frac{V_{cell}}{V_{rev.}} 100\% \quad \text{...(Eq. 2.1)}$$

Using a high fuel flow rate, flooding the cell with fuel, maximises the electrical performance at the expense of fuel utilisation. Considering the electrochemical efficiency alone gives a skewed view of fuel cell "efficiency" in this case as hydrogen wastage is not considered – hence use of a fuel utilisation coefficient is important for fuel cell efficiency values. Larminie and Dicks [107] suggest the following definition of fuel cell efficiency, η:

$$\boldsymbol{\eta = U_f \frac{V_{cell}}{1.48} 100\%} \quad \text{...(Eq. 2.2)}$$

Here U_f is the fuel utilisation coefficient (discussed below) and the factor of 1.48 is the ideal EMF that would be obtained from the cell were all the energy value of the hydrogen fuel converted into electrical energy (Equation 2.3, below) where Δh_f is the enthalpy of formation for the reaction $H_2 + 1/2O_2 \rightarrow H_2O_{(L)}$, as this is with respect to the HHV).

$$\boldsymbol{EMF = \frac{-\Delta h_f}{2F}} \quad \text{...(Eq. 2.3)}$$

The importance and definition of fuel utilisation are addressed in the literature [62, 63, 109] with two potential definitions given. In brief, the two options are:

i) $$\boldsymbol{U_f = \frac{I}{nFv}} \quad \text{...(Eq. 2.4)}$$

Where *I*, *n*, *v* and *F* are the current (A) drawn from the cell, the number of electrons transferred in the reaction between hydrogen and oxygen (*n* = 2 for hydrogen), the flow rate of fuel (moles/second) and Faraday's constant, respectively. This is used by Galloway and Sammes [62] amongst others.

ii) $$\boldsymbol{U_f = 1 - \frac{\dot{m}_{out} \times \Delta h_{out}}{\dot{m}_{in} \times \Delta h_{in}}} \quad \text{...(Eq. 2.5)}$$

Where *ṁ_out* and *ṁ_in* are the masses of flow rate fuel leaving and entering the cell (kg s^{-1}), respectively, and *Δh_in* and *Δh_out* are the specific enthalpies associated with completely oxidising the inlet and outlet fuel (kJ kg^{-1}), respectively.

There are advantages and disadvantages of each method; the first only considers the amount of fuel converted into externally useable electrical energy; the effective utilisation calculated will therefore be slightly smaller than the amount of hydrogen reacted due to various losses incurred in the cell, with the current collection efficiency having a significant

effect. Current dropped across the wires or interconnect-SOFC interfaces is lost. The large amounts of thermal energy released by any burning of the fuel at the outlet are also ignored. It has the advantage, however, that it is easily calculable. The second equation accounts for thermal and other losses, but is perhaps less intuitive, and is much harder to find experimentally. For these reasons, (i) is generally more popular, and is the definition of choice in this review (as used in Table 4)

With hydrocarbon fuels, it has been found [60] that increasing the fuel flow rate (and thereby decreasing the utilisation) can have a negative impact on cell performance beyond a certain point due to increasing carbon deposition on the anode. For this reason, the optimal performance is seen at a higher percentage fuel utilisation when the fuel contains carbon. The theoretical discussion in the review of McIntosh and Gorte [87] also suggests that higher percentages of fuel conversion will give better results when a hydrocarbon is used than when hydrogen is used, as the hydrocarbons were seen to act as a buffer, reducing changes in oxygen partial pressure. This buffering effect increases with hydrocarbon chain length, and allows a higher theoretical thermodynamic efficiency for fuel cells operating on hydrocarbons instead of hydrogen. They point out that the dilution effect from the increased mole ratio of products to reactants may limit the advantage of increasing utilisation with hydrocarbon use.

Suzuki *et al.* [39] found that increasing linear fuel velocity of hydrogen improved performance up to a point, but that gas diffusion then became the limiting factor. Microstructural porosity then becomes vital.

2.4.3 Porosity

Electrode porosity is essential to maximise the area of the three-phase boundary, however there must be an upper limit on optimal porosity for conductivity and structural stability to remain sufficiently high. Jin *et al.* [57] found that porosity should be less than 55% to avoid raising the resistivity of the anode too much. They also point out that pore size is crucial, with larger pores being detrimental to mechanical strength. Suzuki *et al.* [39] investigated anode microstructure, concluding that, "the electrochemical performance of the cell was extensively improved when the size of constituent particles was reduced so as to yield a highly porous microstructure". They found the best performance when the Ni particles of the anode had diameters below 100 nm.

The cells with the best performance recorded in the literature to date (Suzuki *et al.* [39]) had an anode porosity of 54% (before reduction). This represents a balance between porosity to aid gas flow and interconnectivity of the nickel to aid conductivity.

It is obvious that an increase in porosity will yield a lower mechanical strength. The effects of volume percentages of pore-formers used [110] and the type of material used as the pore-former [33, 57, 111] have been investigated, for both anodes and cathodes. As most µSOFCs are anode-supported, the strength-mass transport trade-off is most critical for the anode.

Roy *et al.* [110] quantified the mechanical weakening of the cell for three pore-former volume percentages (40%, 50% and 60%) in the anode, seeing a drop of approximately 26% in average burst strength for each 10% volumetric increment of pore-former. This average

burst strength was 11.7±7.5 MPa for the test tubes with 60% pore-former by volume; this should be sufficient in most cases, but this negative effect of increased porosity must be a consideration where hard-wearing cells are required.

Jin *et al.* [57] investigated the use of flour as an anode pore-former, as well as the more standard graphite. They found that the flour showed more significant shrinkage on sintering, leading to a number of larger pores big enough to be problematic in terms of cell strength. Flour decomposes by a violent burning reaction, and this led to an uneven pore distribution, as well as the size variation mentioned. The graphite pore former was found to be preferable due to the even spread of smaller pores giving good gas permeability and a large surface area without overly compromising cell strength. Hu *et al.* [112] had some success developing a composite anode pore-former comprised of flour and activated carbon. Wang *et al.* [111] found magnesium oxide to be preferable as a pore-former in their silver-impregnated $Ce_{0.8}Sm_{0.2}O_{1.9}$ anode.

Graphite, carbon black, rice starch and corn starch have been used as LSCF cathode pore-formers [113, 114]. Graphite was found to be more effective than rice or corn starch for cathodes prepared by tape-casting [114], but this can be very dependent on material and fabrication method.

2.4.4 Current Collection

Overall cell resistance increases with increasing Ohmic resistance, causing the electrical performance to decrease. The length and resistance of the current collection path is therefore critical. Experimentation [57] has shown a 24% decrease in power density when the distance of the cell from the anode current collection point was increased by a factor of seven. Interconnections to the external circuit, and between cells when several are stacked together, are therefore a very important issue.

Whilst collecting the anode current along the whole electrode length would be ideal, the small tube size and need for good gas flow to the anode surface make this difficult. Cui *et al.* [115] found that having a current collection point at both the inlet and the outlet of the cell has a significant positive impact on cell performance as opposed to a single collection point. Suzuki *et al.* found that using this "double terminal" current collection method reduced the electrical losses two- to four-fold as compared to single terminal collection [116] (these results were confirmed by in-house experimentation [13]). Decreasing electrode length and increasing its conductivity were also shown to improve performance. The cell length again emerged as a crucial factor in later work of Suzuki *et al.* [117], with a clear relationship being seen between performance loss and cell length due to increased current collection resistance (Figure 10).

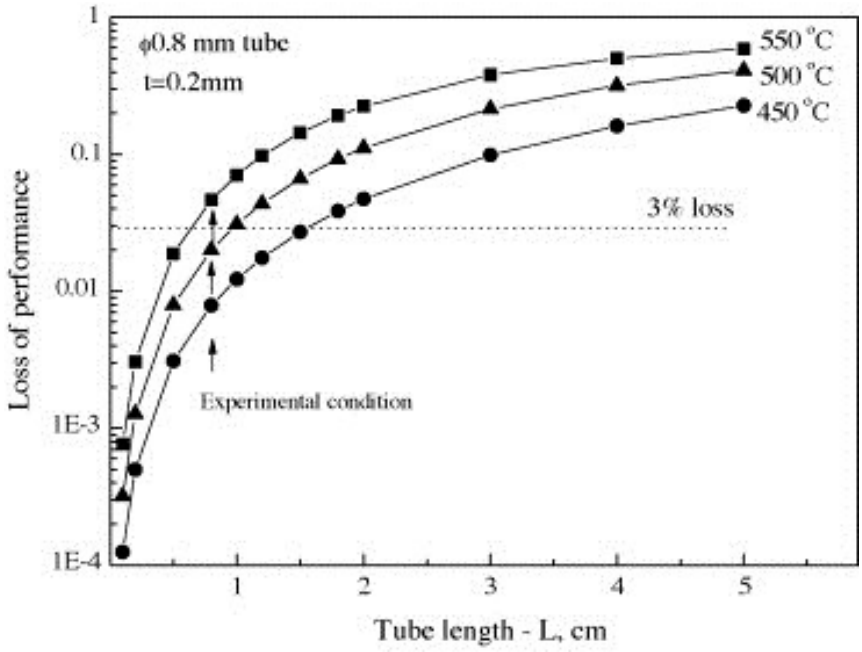

Figure 10 - Effect of tube length on cell performance [117]

Zhu and Kee [118] developed a mathematical model to assist with current collection design for anode-supported tubular SOFCs. They found that the resistance and placement of current collection materials can have a notable effect on local temperature and species distributions, as well as on overall performance (fuel utilisation and power density being key examples). They found that more current collection points should be used on the cathode than on the anode. These principles also apply to the micro-tubular cells.

It has been observed that minimising the cell length maximises the performance per unit area; the length of the current collection path is thought to be the responsible factor [57]. Various interconnection designs have been tested; these are described and compared later in Section 5.2 Interconnection Design. An extended review of current collection techniques can also be found in that section.

2.5 Single Cells: On-going Developments

As previously mentioned, the volumetric power density of µSOFC stacks depends on the inverse of the cell diameter. Making yet narrower tubes is therefore a promising line of research. Work has been done on YSZ hollow fibre tubes, with outside diameters of around only 1.6 mm, and sub-millimetre inside diameters [119-121]. The fabrication processes were carefully controlled to give open and interconnected pores on the external and internal surfaces, giving a high internal surface area for the electrodes, and a thin dense gas-tight central layer giving low Ohmic resistance. There is a great deal of ongoing research in into µSOFCs with diameters of around 1 mm to obtain higher power densities [24, 59, 122, 123]. Dual-layer hollow fibre cells have been fabricated [123] with maximum power densities of 0.042 W cm^{-2} and 0.08 W cm^{-2} at 450 °C and 550 °C, respectively. There is still a lot of work to be done to optimise these designs, but the concept has been shown to work and manufacturing techniques and resultant microstructures should improve with further research.

Work has also been done to improve the RedOx stability of anode materials [124]. The idea is that by dispersing the nickel more finely in the anode structure, less can be used to give the same performance as the conductive percolation paths and active surface area are maintained. This means there is less nickel around to be oxidised and then re-reduced, decreasing the damage done by this process. Ouweltjes et al. [124] observed a drop in current density at 0.7 V of 10% after 50 RedOx cycles and 23% after 100 with their cells utilising highly dispersed nickel.

2.6 Stack Designs

The development of stack designs is also critical to the commercial adoption of μSOFCs. The power provided by an individual cell is too small for most applications so intensive research into stack design is receiving a great deal of interest, both for modelling and experimental work [104, 125-128].

The first μSOFC stack designs [10, 11] consisted of modular combinations of sets of cells in individual racks used to build up to the required power output. The 1000-cell stack, shown in Figure 11, had cells arranged in 40 racks of 25 tubes with the aim of supplying 30 kW of water heating and 500 W of electrical power [11]. This modular arrangement helps to facilitate even gas distribution throughout the stack – each rack had a tubular gas distribution manifold to help ensure uniformity [11]. In this instance, the tubes were connected in parallel and the racks in series to provide the voltage and current desired.

Although this stack produced only 0.082 Wcm^{-2} (155 W total electrical output) at 850^{o}C, this served as proof of concept for μSOFC stacks. This arrangement has another advantage in that the modules can be removed and replaced individually in case of failure, without losing the entire stack; this feature is popular in more recent designs.

Figure 11 - 1000 cell µSOFC stack [11]

2.6.1 The Use of Modelling

The fuel cell provides a complex modelling challenge due to the number of different physical processes involved. These include heat and mass transfer by various mechanisms, chemical and electrochemical interactions, macro-scale fluid dynamics and micro-scale molecular interactions. In addition to these issues, certain fundamentals of the electrochemical reaction mechanisms in SOFCs are not yet fully understood.

Many models in the literature have a strong focus on one particular aspect, with fewer actually incorporating all aspects as would be required for a model aimed to have predictive power. Nonetheless, these models all provide valuable insight as detailed below. Reviews such as that of Kakac *et al.* [129] give an overview of the key assumptions and equations

used in SOFC modelling to date. Here, results are summarised, not the modelling techniques.

Computational modelling has greatly helped understanding of fluid flow and heat transfer in stacks, amongst other phenomena. This is discussed in Lawlor's review [104]. Notable work discussed there includes that of Lockett *et al.* [125] who describe the results from a single μSOFC alongside their work on thermal distributions and heat use in a stack of twenty cells. The main problem for single cells highlighted by this work is that the temperature varies significantly from the optimum even along a relatively short active length. Despite this temperature variation, Cui and Cheng [130] found that the main source of thermal stress in μSOFCs is the mismatch of material expansion coefficients between layers, not thermal gradients within each layer. They conclude from their model and analysis that matching coefficients of thermal expansion is the most important factor in ensuring cell reliability.

Serincan *et al.* [131] looked at the effects of operating conditions on cell performance, and more specifically at the temperature dependence of current leaks across the GDC electrolyte. They conclude that current leakage due to GDC reduction does not have a significant effect below 500^{o}C; unfortunately this is below the range of most SOFCs at present. An increase in temperature results in better cell performance overall, however, due to increased catalytic activity and ionic conductivity. They also note that a change in pressure has more effect at the cathode side than at the anode side due to the slow reaction kinetics of the cathode.

Izzo *et al.* [132] highlight the importance of diffusion within the anode layer for cell performance. The gas and voltage distributions along the tube were found to vary significantly when a diffusive anode layer was incorporated into their model, extending the TPB into the electrode rather than assuming it to be the geometric area of the tube's interior.

Cui *et al.* [115] investigated the efficacy of different current collecting methods with varying tube length for μSOFCs. They found collecting current from the anode at both the inlet and the outlet of the cell more efficient than from the inlet or outlet individually by a factor of ~2-6. Creating good contacts on the inside and outside of a small tube is not simple, making current collection one of the primary concerns of developers. Collecting current at the outlet only does however give a much more uniform electrochemical reaction distribution in the cell.

More recent modelling work by Funahashi *et al.* [133] looked specifically at a module-type μSOFC stack as discussed in more detail in the following section. Air flow, Joule heat and temperature distribution were the main focuses. A temperature difference of 100^{o}C across the 1 cm^{3} stack was a striking illustration of the necessity of optimising the design to give an even temperature distribution. Thinner tubular cells were found to lead to lower air pressure loss in the cathode matrix. Their simulation confirmed that the Joule heat caused by the anode tube and cathode matrix resistances was negligible as compared to that from the internal cell resistance (smaller by a factor of 1000). As such, this can be safely ignored for the purposes of most simulations.

Kattke *et al.* [134] presented a model of a highly integrated cylindrical 66 cell stack, with a focus on thermal management (Figure 12). This model is unusual in that it has "the goal of increasing system efficiencies by optimizing the thermal coupling between BoP and the SOFC stack" – the Balance of Plant (BoP) is often not considered in modelling work.

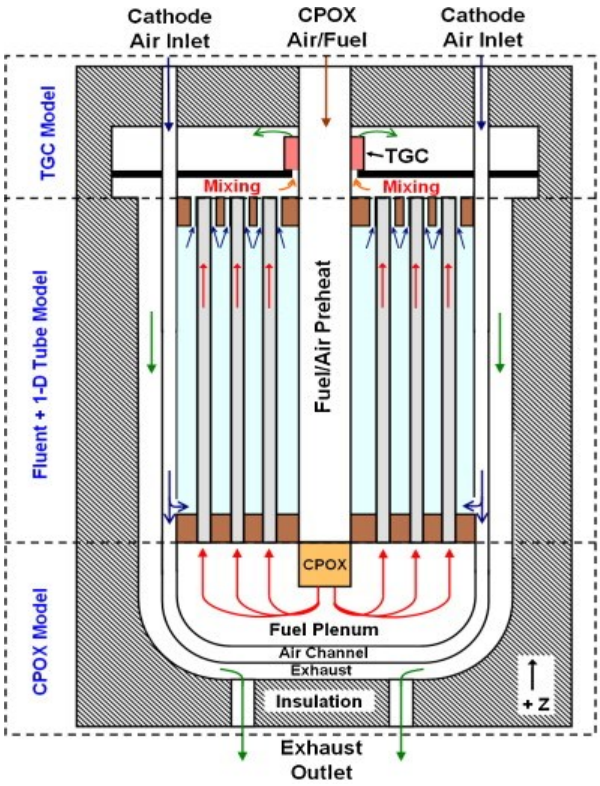

Figure 12 - Cylindrical stack design [134]

Mulone *et al.* [135] developed a CFD stack-design tool; this uses a modular design with an optimised manifold design. The air distributor is the support-frame, with a honeycomb arrangement of tubes within this. The spacing between tubes larger than the tube diameter gave the best performance of the three arrangements tried. Comparisons were made with single tube experimental data, but a full stack experiment was not performed. Adaptation of this model to two similar designs discussed in the next sub-section [126, 128] would be an interesting addition.

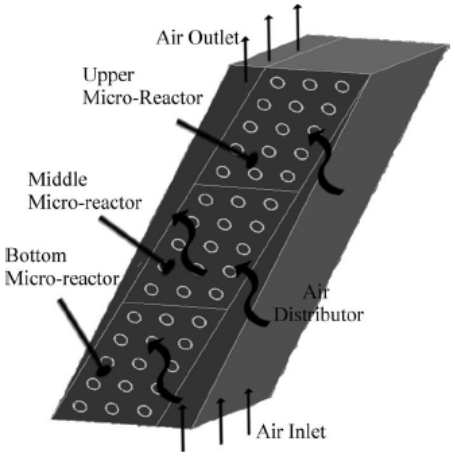

Figure 13 - Modular assembly of three micro-reactors [135]

Yang [136] and Tade [137] both focus on identifying model parameters rather than stack design itself. They highlight the importance of temperature variations, which were found to have a much stronger effect on performance than pressure variations in the electrochemical model [136]. These models can therefore be used as tools to estimate the effect of a geometry change, for example.

As yet, there is no off-the-shelf stack design model available, and indeed single cell models with good predictive power are still notably lacking. Nonetheless, this can be a very useful design tool.

2.6.2 Experimental Stacks in the Literature

In 2008, Suzuki *et al.* [128] created an µSOFC stack with a volume of 1 cm^3, which they operated at 500°C. This gave a maximum power output of 1.5 W. Each module was composed of three cells, held in place by a shaped block of the cathode mixture (as shown in

Figure 14). These stacks could then be combined to make up larger stacks for higher-power applications. Further testing of this design, but with 0.8 mm diameter tubes replacing the previous 2 mm diameter tubes, was also performed [122]. This gave a power density of 2 Wcm^{-3} at an operating temperature of 550°C, and various configurations were examined [138].

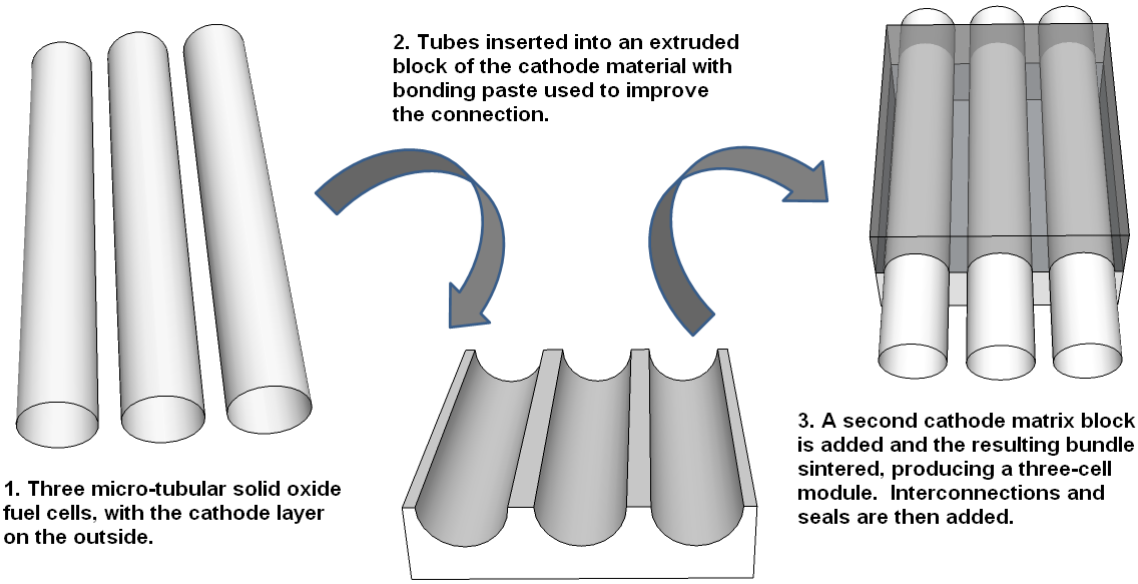

Figure 14 - µSOFC stack design in a cathode matrix block [128]

Yamaguchi, Suzuki *et al.* [126] also looked at the possibility of using a honeycomb arrangement for an µSOFC stack (see Figure 15). This design had been postulated for tubular cells in 1999 [139], and the µSOFC version showed a promising power density (0.6 Wcm^{-3} at 600°C with a tube diameter of around 1.6 mm) as compared to this. Like the shaped support for the previously mentioned design, the honeycomb was made from the cathode material and metallic interconnects were used. More recently, they used a similar design with larger cells of 4 mm diameter and 40-50 mm length [140], obtaining a power of 7.5 W from twelve cells in series at 630°C.

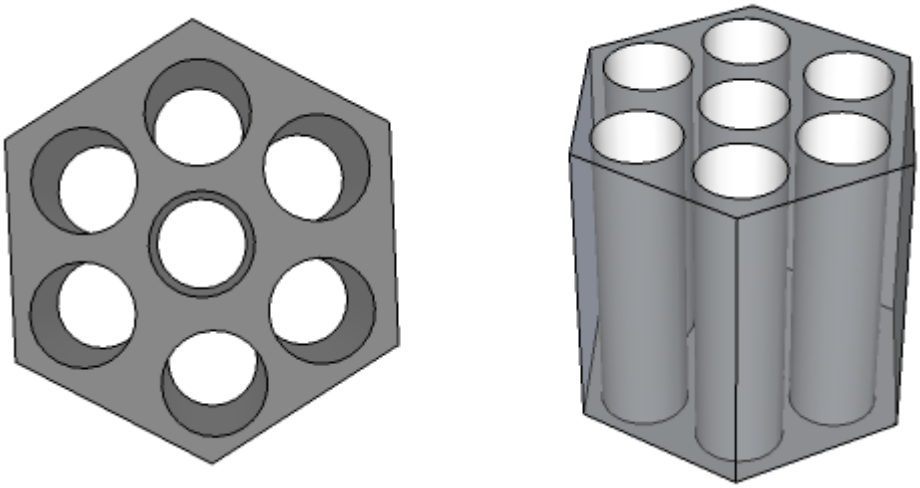

Figure 15 - Honeycomb cathode matrix µSOFC stack design [126]

Funahashi *et al.* [127] used a magnesium oxide matrix to support their stack design instead of extruded cathode material as seen in the two designs previously mentioned, and obtained a power density of over 0.6 Wcm^{-3} at 500°C. Sufficient air for the cathode could flow through this MgO matrix. The design was otherwise very similar to that shown in Figure 14, although the "bundles" were stacked on top of each other instead of side-by-side, giving a more cubic stack. In other work [141], a similar design was used but with the porous matrix made from the cathode material. The effect of the spacing of tubes within such bundles was investigated by Suzuki *et al.* [142]. They discuss the trade-off between densely-packed tubes giving a higher surface area per unit volume and the corresponding loss in performance due to reduced gas flow and extended current paths. A power density of 2.5 Wcm^{-3} at 550°C was obtained with a tube diameter of 0.8 mm.

Sammes *et al.* [143, 144] used a similar "planar multicell array" arrangement as for the modules of Suzuki *et al*. (Figure 14), and obtained a power of 100 W with 40 cells. The cells

used had diameters of 1.32 cm and lengths of 11 cm, however. As such, the volumetric power density is much lower (~0.13 Wcm^{-3} at most). Lee *et al.* [145] similarly used cells of around 1 cm diameter for their 700 W stack, which consisted of 36 cells, each of length 20 cm. Again, these 36 cells were arranged into bundles (of six), giving the stack a modular nature.

Wang *et al.* [146] built a two cell stack with a co-sintered ceramic anode interconnection. They saw a 20% drop as compared to the total performance expected for two cells separately. They used a novel bi-layered $La_{0.4}Sr_{0.6}TiO_3/La_{0.8}Sr_{0.2}MnO_3$ interconnector which also prevents H_2 and O_2 cross-over. The requirements of being "completely dense, sufficiently conductive, and quite stable in both oxidizing and reducing atmospheres" were met, but the ideal operating temperature for this is quite high (900°C). The maximum power density obtained was 0.353 W/cm^2, which is reasonable for cells of 1.12 cm diameter.

Liu *et al.* [147] took a different approach, using cone-shaped tubular cells to make a segmented in-series stack, as shown in Figure 16. This gave just under 0.5 W/cm^2 at 600°C, using dense silver paste as both interconnection and seal at the join between adjacent cells. The conical shape of the cells facilitates this style of connection, but similar would be possible with cylindrical cells.

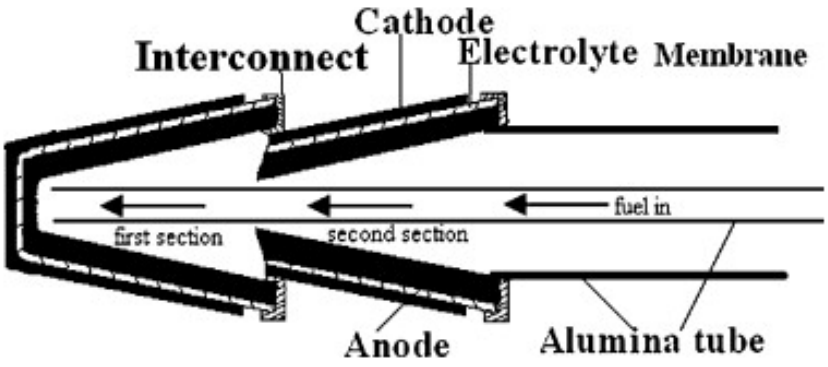

Figure 16 - Segmented-in-series stack [147]

Du *et al.* [105] tested NanoDynamics' (later, "ndEnergy") microtubular stacks and found very promising results including start-up within five minutes and good thermal cycling characteristics. Unfortunately the stack design used here is not publically available information.

2.7 Summary

Resistance to thermal and RedOx cycling degradation, fuel utilisation, electrode porosity and current collection have been identified as the four main differentiating factors of fuel cell performance from the point of view of cell design. A summary of recent findings and the theoretical reasoning behind them was given. Material choices were discussed to a small extent, although materials and manufacture are not considered in detail. These two issues are covered more fully by Mizutani's review [148], which focuses on Japanese research and development. In terms of stack power densities; the maximum found in the literature was 2.5 Wcm^{-3} at 550°C [142], although balance of plant volumes will also need to be taken into account for industrial applications.

Micro-tubular SOFCs provide an active research area, as demonstrated by the number of papers published in recent years. With research areas such as materials suitable for lower temperatures of operation [149] and better interconnections [150], it promises to remain a productive area in the near future.

3. MATERIALS, MANUFACTURING AND CHARACTERISATION TECHNIQUES

In this chapter, the experimental methods used in fabricating and testing the µSOFCs are discussed. Many of these are "tried and tested" in-house methods and are not changed. New methods (such as dip-coating for cathode preparation) are discussed later.

3.1 Micro-tubular fuel cell manufacture

3.1.1 Anode and Electrolyte

Anode-supported anode and electrolyte tubes were supplied by Adaptive Materials Inc. (AMI, image shown in Figure 17 below), the electrolyte being a thin coating (14±4 µm) on the exterior of the thicker anode tube (240±10 µm). These nickel oxide/yttria stabilised zirconia tubes are 5.5 cm long and 2.3 mm in diameter (internal) and were commercially available from AMI at the start of the project. These cells are subsequently referred to as AMI-5.5 µSOFCs.

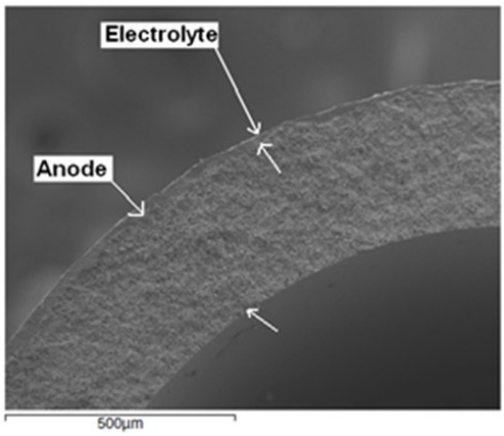

Figure 17 - AMI 5.5 µSOFC (scanning electron microscope image)

The preparation techniques detailed in this chapter were used for these cells throughout the remainder of the work, except when explicitly stated otherwise. Part way through the project, AMI stopped manufacturing the AMI-5.5 µSOFCs in favour of a larger design. Using fewer, larger µSOFCs for the same total power facilitates interconnections and manifolding, at the cost of volumetric power density. The new cells, described in more detail in Chapter 5, are 15.2 cm in length and 5.5 mm in diameter (internal). These are referred to as AMI-15.2 µSOFCs; a visual comparison of the two types is shown in Figure 18.

Figure 18 - Comparing AMI µSOFCs: (A) AMI-5.5 µSOFCs, which are provided as unreduced anode and electrolyte tubes, and (B) AMI-15.2 µSOFCs, which are provided ready for use, bar application of interconnections

These cells were supplied ready-prepared, fully reduced and with cathodes already added, therefore in-house preparation steps were no longer needed beyond adding the interconnections. The remainder of this chapter focuses on the AMI-5.5 µSOFCs. Interconnection design and application for the AMI-15.2 cells is discussed in Chapter 5.

3.1.2 Cathode

The cathode is applied as an ink to the external electrolyte surface of the AMI-5.5 µSOFCs. It consists of two layers prepared according to an in-house recipe that has been used in many research projects at the University of Birmingham [203, 204]. The compositions of each of the two inks used are given in Table 5. These ingredients were measured out to accuracies of ±2 mg and placed inside milling bottles, with the exception of the Terpinol. The two

bottles were carefully sealed and packaged into a third container to be milled for 24 hours in a vibro-milling machine. After 24 hours, the Terpinol was added to ink 2, before returning the container to the vibro-mill for a further ten minutes to ensure complete mixing.

Table 5 - Cathode ink compositions

Component	**Cathode ink 1 (active cathode)**	**Cathode ink 2 (current collector)**
LSM ($La_{0.82}Sr_{0.18}MnO_3$ - Merk)		20 g
LSM ($La_{0.5}Sr_{0.5}MnO_3$ - SSC)	6.5 g	
YSZ (TZ8Y - TOSCH)	6.5 g	
Hypermer KD2	0.25 g	0.4 g
Acetone	16 ml	14 ml
Glycerol Triolate Triolien	0.2 g	
#Milling beads used	13	16
Terpinol		2 g

The inks were then applied to the tube using a brush-painting technique. Cathode ink 1 was painted on to the desired length (30 mm for the first batch), and the cells were then left to dry overnight before application of the second layer (Cathode ink 2), which acts as a current collection layer.

Dip-coating was also used to coat later batches of cells. This was a new technique to the University of Birmingham, although previously used in the literature quite widely [78]. The dip-coater used was a KSV Compact Dip Coater, shown in Figure 19 below. Thread seal tape was used to seal the lower end of the tube during dipping. Various cathode ink recipes and dipping speeds were tested, as discussed in Chapter 6.

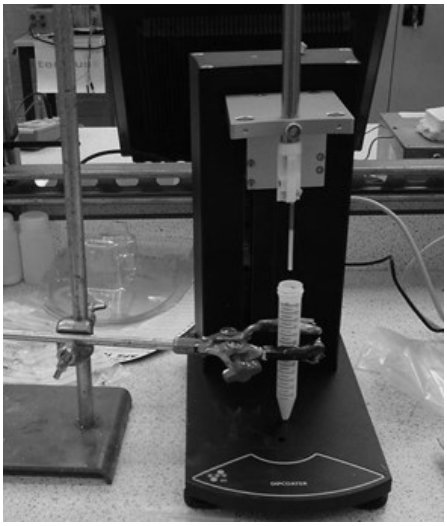

Figure 19 - KSV dip-coater used

The cells were then sintered in a Carbolite™ furnace, in air. The furnace was set to a programmed temperature-time profile as shown in Figure 20. The furnace's cooling becomes insufficient to match the desired rate at around 100°C, so the furnace door is opened, allowing slow cooling to continue.

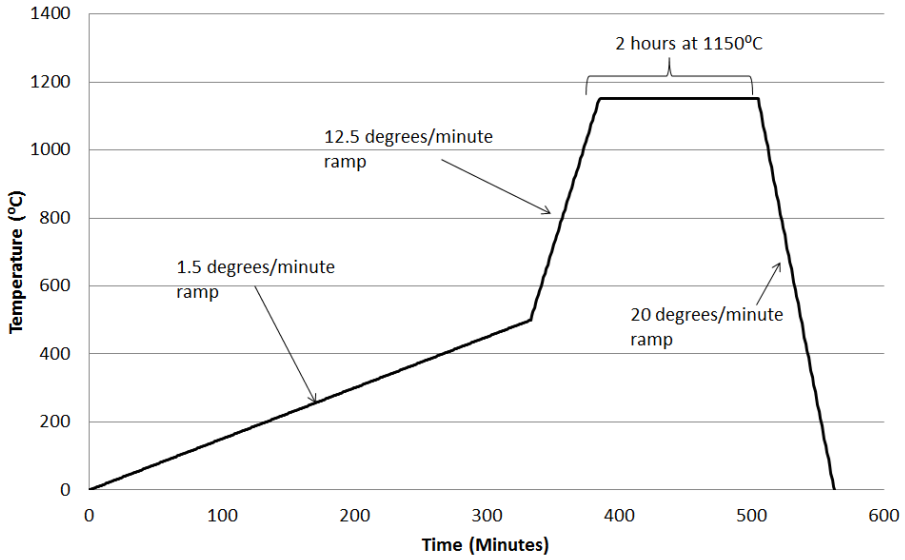

Figure 20 - Temperature profile for sintering µSOFCs

3.1.3 Reduction

Previous work [115] found reduction at a constant temperature to give better results than reduction during a temperature ramp when carbon-containing fuels are used. As operation on propane is the end goal, constant temperature reduction was used. The temperature profile used is shown in Figure 21, and a picture of a reduced cell given in Figure 22.

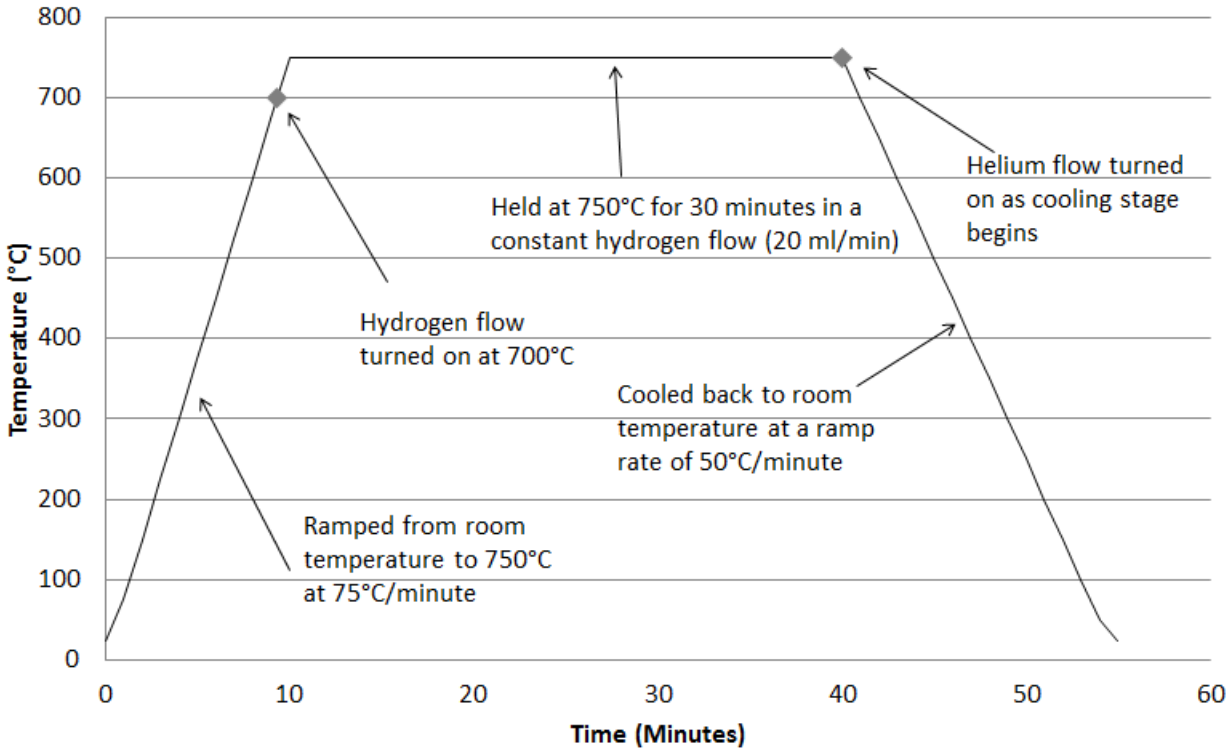

Figure 21 – Temperature profile of reduction for µSOFCs

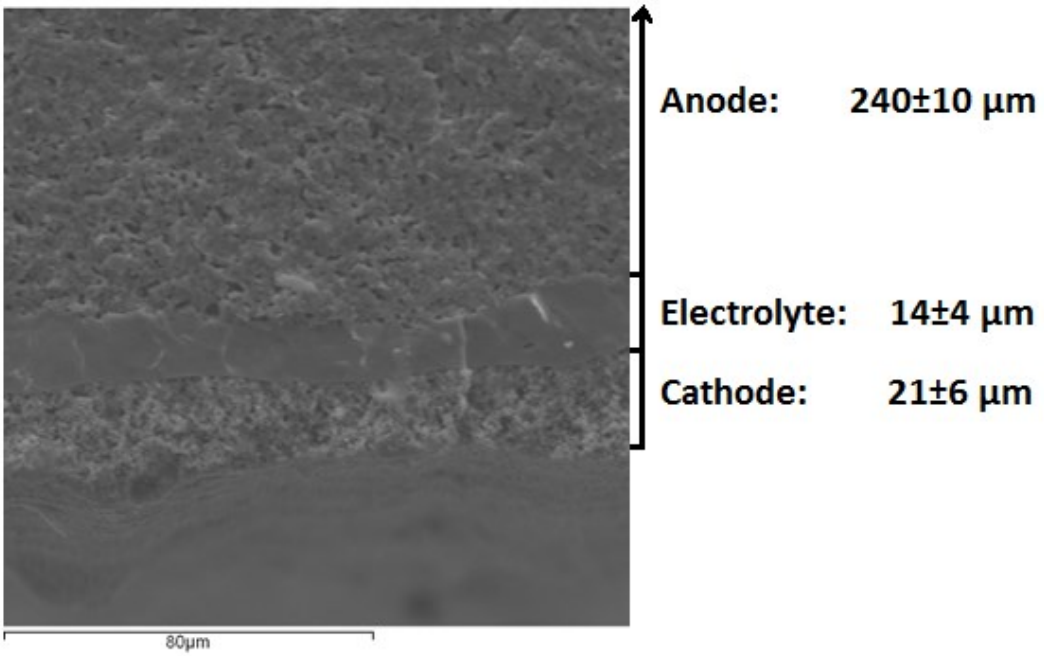

Figure 22 - Cross-section of a reduced µSOFC

The cells were placed inside a quartz glass reactor in batches of not more than five and positioned in the middle of the furnace. The hydrogen (99.999% pure) flow of 20 ml/minute was turned on at 700°C to ensure the system was flooded with hydrogen by the time it reached the set temperature. The hydrogen flow was left on and a helium flow added to the mixture during cooling to prevent oxidation of the reduced tubes. Below around 100°C in the cooling ramp, the insulation of the furnace is too good to allow continued cooling at the desired rate, so the furnace lid is tilted and then removed completely to help the measured actual temperature remain near the set temperature. Photographs of a batch of cells at three key stages are shown below in Figure 23.

Figure 23 - Preparation of dip-coated cells (hand-painted cells are treated in the same way, but avoid the necessity of having one end covered for dip-coating)

3.1.4 Current Collection

The optimisation of interconnects for individual cells and especially for stacks remains a large area of research. The methods used in this work represent a combination of cheap and simple technology and previous research findings.

The anode current collection point was made on the exterior of the cell by removing a small section of the electrolyte layer near (but not touching) the edge of the cathode using a metal file. This technique has advantages of simplicity and reliability as compared to using an internal mesh and wire, as described by Dr Dhir in his PhD thesis where this exterior connection technique was developed [203].

A band of ~3 mm width is scraped away around 4 mm from the end of the cathode. This proximity provides a short current path whilst still avoiding the possibility of short circuits. The anode layer is duller than the electrolyte layer, so the colour change means it is easy to ascertain when the correct layer has been reached. Silver ink (varieties discussed later) is then used to paint on the connections. These consist of one band on the etched area for the anode connection, and a number of bands of silver ink for the cathode, connected by a strip along its length. These bands are ~2.5 mm in width, and evenly spaced along the cathode. The number and spacing of these is kept constant. The cells are then left to dry overnight.

The current collection wires consist of 50 cm of 0.25 mm diameter silver wire. The majority of this is wrapped around the cathode, with a set number of turns on each band (three for most of the work done), and a set number of loops between bands (one in each direction for most of the work done). Again, this must be kept constant when not the variable under test. The remainder of the wire is wrapped around the anode collection point. The wire ends are tightly twisted together to minimise resistance.

Platinum would be preferable to silver in terms of melting point, as pure silver melts at 961^{o}C, which is not dissimilar to the required operating temperature (700-850^{o}C). By contrast, pure platinum does not melt below 1773^{o}C, but its cost makes use of it uneconomical. Silver also has a higher electrical conductivity, and Ohmic resistance is critical to cell performance.

Cement (Fortafix) is used to cover the anode current collector – this helps to protect the exposed anode from oxygen during high temperature operation. Figure 24 shows a finished cell.

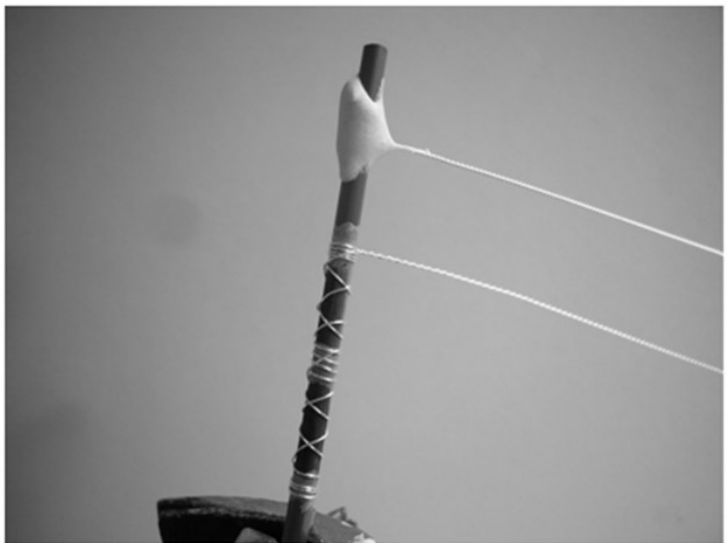

Figure 24 - A fully-prepared µSOFC (photograph courtesy of Wing Kung)

This method of current collection is simple and effective, but labour-intensive and results in having a large number of wires present. Alternative methods of current collection have been tested, as discussed in Section 5.2.

3.2 Preparation for Testing

The desired method of fuel injection must be chosen, and the cell set up accordingly. For the simplest method of using an injector tube, the cell slots neatly over the thinner section of the injector tube and is positioned in the testing furnace. The silver wire connections to the external current help to keep it balanced in place. This is shown in Figure 25.

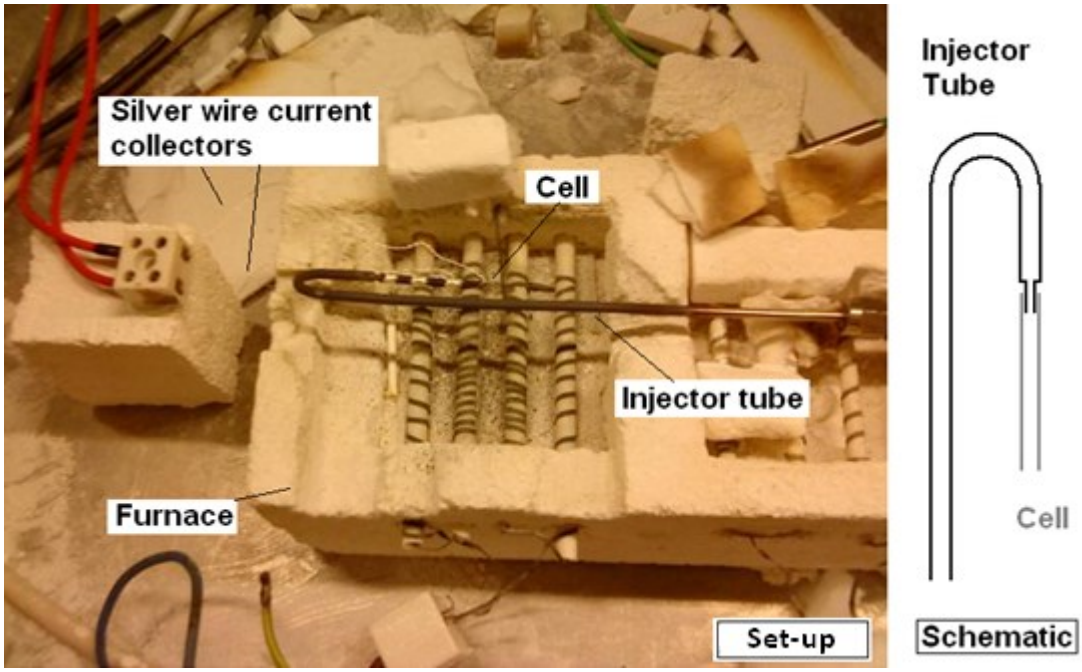

Figure 25 - µSOFC test rig

This has the advantages of speed and simplicity, but the seal is not gas tight, so some hydrogen may escape without passing through the cell (insufficient to be a hazard). Also, an early section of the cell active area may be covered if there is an insufficient length of unused tube for the injector. There is unlikely to be much backflow, so this wastes a section of the fuel cell.

The second method involves cementing the micro-tubular cell to an injector block. This has the advantages of providing a gas-tight seal and ensuring the full length of the cell is used. The disadvantages are the time taken to make and set the cement and the difficulty of removing the cell from the block after use. The cement used needs to be strong and resistant to high temperatures, but its strength means that removing the cell after use risks breaking it.

Clamps were used to hold the cell in place as the cement dried. The silver wires that provide the anode current collection point were also covered with cement to protect the silver wire [203].

3.3 Cell Testing Apparatus and Methods

The test rig consisted of a furnace, temperature controlling apparatus and a Solartron™ analytical 1400 Cell Test System connected to a computer where purpose-built programmes were run using Cell Test™ (v 5.2.0) software. The furnace used for cell testing allows the cell to be raised to the desired operation temperature and held there for the duration of the test before the temperature is again lowered. It was constructed from Thermal Ceramics insulating fire blocks, with the heating elements (visible previously in Figure 25) consisting of Nichrome ribbon (Advent Ni80/Cr20 1.5 mmx0.13 mm) wound around ceramic rods. This furnace was not newly built for this project as it had been successfully used for many previous in-house tests. This is connected to a Eurotherm™ 2404 controller which allows programmed temperature profiles to be set, and shows the desired and actual temperature.

The silver wire current collectors are secured into the external circuit with screws, and a load programme set for the Solartron™ using Cell Test™ software. Voltage, current and time data for each test can be easily collected in this way.

The fuel gas, hydrogen, was not pre-heated, but the first section of the delivery tube is inside the furnace, before the cell is reached, which will provide some heating. Atmospheric air was used as the oxidant; again this was not preheated but, being inside the furnace, will be at a similar temperature to the cell.

Many µSOFC researchers humidify the hydrogen used. Humidification has been seen to protect the anode from cracking in some cases [205], although the differences in performance are generally small when the fuel is hydrogen [206] (addition of steam is strongly beneficial when hydrocarbon fuels are used as it facilitates internal reforming). As the target application is an Unmanned Aerial Vehicle (UAV), with very limited space and weight allowance for a power pack, the extra balance of plant required for that would present a problem. As such, the hydrogen used was not humidified. Anode off-gas recycling is one potential option for introducing some steam without a large amount of extra balance of plant, but this still adds system complexity so was not implemented in this project.

3.4 Electrical Analysis Techniques

The majority of the analysis is based on Solartron™ data, i.e. analysis of voltage and current with time, under different conditions.

3.4.1 Current-Voltage Characterisation

Fuel cells are usually characterised by plots of voltage against current density (IV curves, see Figure 26). For a single cell operated on pure hydrogen at around 750°C, the voltage at zero current (Open Circuit Voltage) should always be around 1 V, with lower voltages indicating problems such as cracking of the electrolyte or a short circuit. At the same temperature and fuel flow rate, the voltage and output power depend very strongly on the current. The point of peak power (at around 1.7 A/cm^2 in the graph given in Figure 26) depends strongly on cell type and the fuel used. Running at peak power is not always practical, however, as this does not give the flexibility to increase output on demand, and can cause damage to the cell if the voltage is too low. With changes in load, the output current and voltage move along the IV curve. Changing the temperature and/or the fuel flow rate changes the shape of the IV curve.

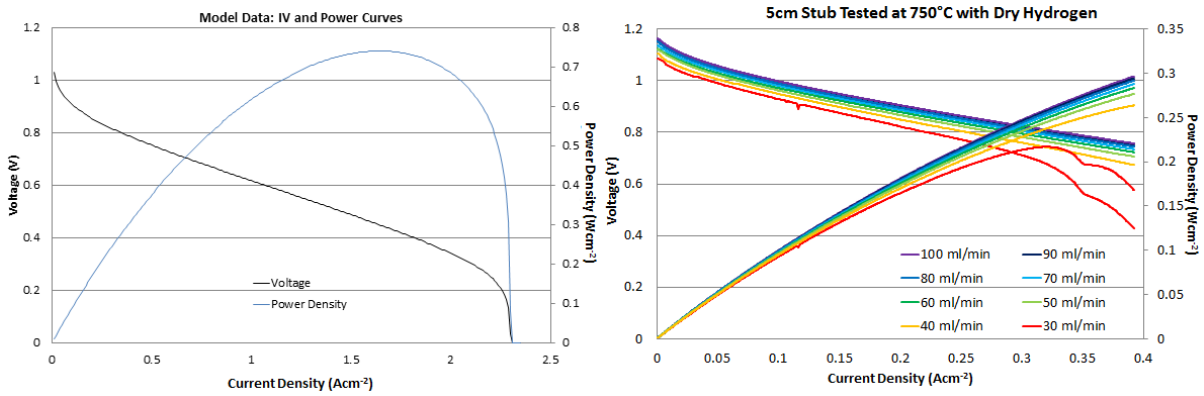

(a) (b)

Figure 26 - Standard fuel cell characteristics (a) model data and (b) varied flow rates experimental data

IV curves have three distinct sections, as shown in Figure 27; at very low currents there is a sharp drop in voltage due to activation energy losses, there is then an approximate straight line section where Ohmic losses dominate, and finally, at high currents, a rapid voltage (and

hence power) drop due to mass flow limitations. Which of these losses is most important depends strongly on the cell design and operating conditions.

In the literature, µSOFCs are often compared using peak power densities [207-209], so this approach was taken for most of the comparative studies in this work. There can be issues with using peak power densities, however, as these can occur at very high current densities, which can damage the cells if too little fuel remains and areas of the anode oxidise.

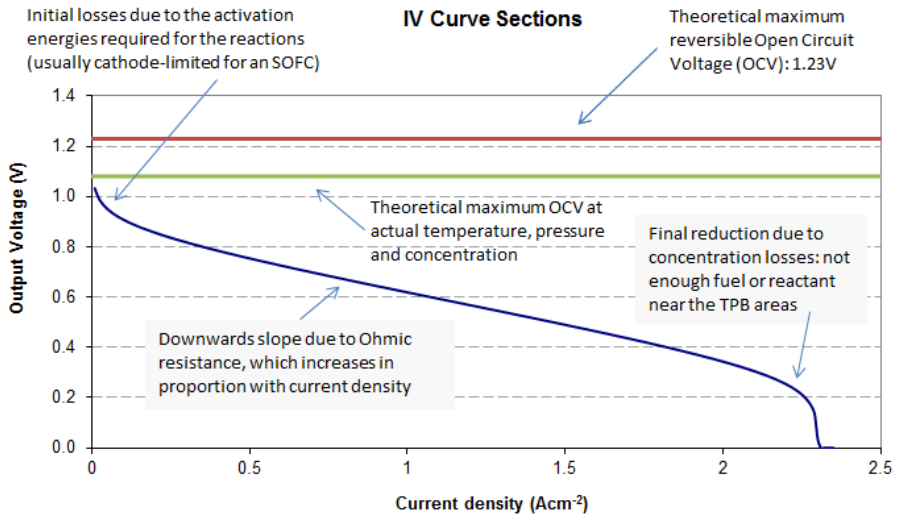

Figure 27 - Losses visible in I-V curves

This is not believed to be a problem in this work for two reasons:

1. An excess of fuel is used, so mass-limited regions are not reached (there were a couple of exceptions to this rule when mass flow effects were being analysed, but peak powers were not used in these cases)
2. A voltage cut-off is set in the programme; if the voltage drops too low, the programme is terminated

Nonetheless, this method was checked against comparing current densities at 0.7 V (see Chapter 6) to confirm that the comparison point chosen did not significantly affect the trends seen. The results were the same within errors, increasing confidence in the technique chosen for the remainder of the work.

3.4.2 Electrochemical Impedance Spectroscopy

Although various electrochemical techniques can be used for fuel cell analysis, e.g. cyclic voltammetry which is very popular in Proton Exchange Membrane (PEM) cell analysis [210], Electrochemical Impedance Spectroscopy (EIS) is by far the most popular such technique for SOFCs [211, 212]. EIS entails applying a small magnitude AC voltage perturbation to the fuel cell system, and measuring the current response [213]. This can be compared to the response that would be obtained from a predetermined model of the system which is related to the known physical processes. In this way, an idea of the relative importance of various phenomena can be obtained, and effects of changes to the cell or stack analysed.

The first step in EIS is to create an equivalent circuit model of your system. This can become very complex, as fuel cells involve a large number of interdependent processes. Sample sections of equivalent circuits for parts of an SOFC are shown in Figure 28 and Figure 29. These two differing approaches [214, 215] illustrate the fact that this is a developing field – there is not a single, standard equivalent circuit for ion transport in an SOFC, let alone for the whole cell or even stack. A good understanding of the processes involved is required to make a reasonably accurate model. Standard circuit elements are combined to mimic the expected effects of system components, and the data are then interpreted according to this model.

Figure 28 - SOFC diffusion: equivalent circuit [214]

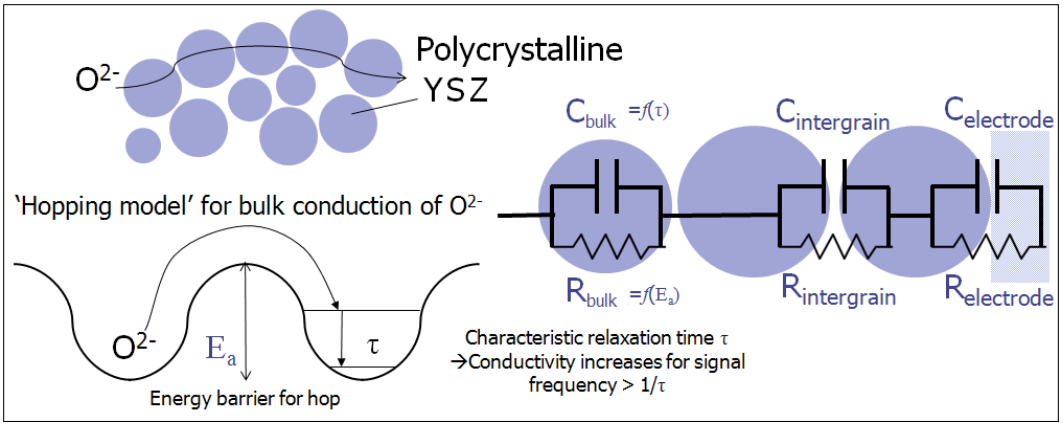

Figure 29 - SOFC ionic conductivity: equivalent circuit [215]

As the AC voltage perturbation applied is chosen to be sinusoidal, it can be written $V=V_o sin(\omega t)$, where V_o is the magnitude of the voltage and ω is the frequency of the perturbation. The current is expected to follow this shape, but with a different magnitude and a phase shift, φ, giving $I=I_0 sin(\omega t+\varphi)=I_0 cos(\omega t+\phi)$. Euler's equation (*Equation 3.1*) allows sine and cosine functions to be written in terms of complex exponentials:

$$e^{ix} = \cos(x) + isin(x), \qquad i = \sqrt{-1} \qquad \text{...(Eq. 3.1)}$$

The above voltage and current can then be re-written as $V=V_0 e^{i\omega t}$ and $I=I_0 e^{i\phi} e^{i\omega t}$, meaning that the impedance ($Z=V/I$) becomes $Z=(V_0/I_0)e^{-i\phi}$, where $-\phi$ gives the phase difference between the voltage and the current. This impedance can then be split into real and imaginary components (Z' and Z'', respectively).

Various graphs can be used for data analysis; plotting the imaginary component (Z") of the impedance, *Z*, against its real part (Z') for a variety of frequencies of the perturbation gives a Nyquist plot. The Z' value decreases (towards zero) with increasing frequency, so higher-frequency arcs are on the left-hand side of such a plot, and vice versa. The expected plot for the process shown in Figure 29 is given in Figure 30. Each RC pair should give a semicircle in this plot – the diameter gives the relevant resistance, R. The capacitance, C, can be found from *Equation 3.2*.

$$\omega(at\ \max -Z") = {}^{1}/_{CR}, \qquad C = {}^{1}/_{\omega R} \qquad \text{...(Eq. 3.2)}$$

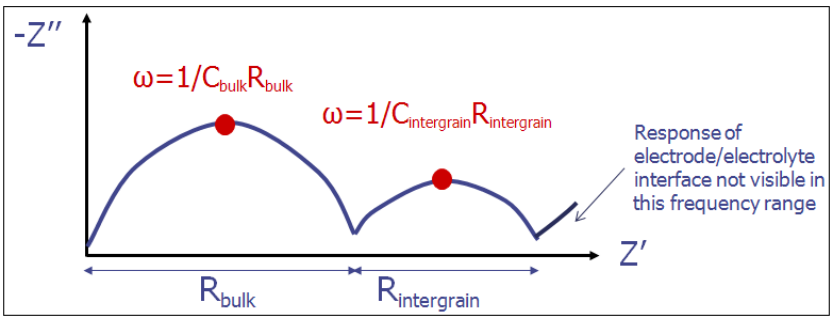

Figure 30 - Nyquist plot [215]

If there were a resistance, R_2 in series with the equivalent circuit shown above, e.g. to represent Ohmic resistance of the metal interconnections, this plot would be shifted along the real axis to the right by R_2. More complex circuit elements, such as Warburg impedances (invented to model transmission lines, but found to be a good model for diffusion [215]) and Constant Phase Elements can also be used when the semi-circles are flatter than desired to give a better fit, although their physical meaning is sometimes doubtful [215].

Specific experimentation is needed to ascertain which peak corresponds to which RC pair, or other circuit element, in the equivalent circuit. When the product, RC, for different sections

is very similar, the semicircles overlap, so data analysis becomes more complicated. The more detailed and accurate the model is, the better the fit and the more useful the analysis. However, the use of too many set parameters that are not properly justified can give a good fit without useful physical meaning.

This technique is quick, non-destructive and only requires a small perturbation of the system, whilst still giving insights into all aspects of fuel cell performance. It provides a very useful tool for identifying where problems lie in poorly-performing cells, and for assessing changes to electrode microstructure, for example. These benefits make it very powerful despite the complicated modelling and data analysis required. Some analysis can be performed without the need for an equivalent circuit [216], but a very good understanding is still required to avoid misinterpretation.

A simple SOFC equivalent circuit model was chosen for this work, as shown in Figure 31, with the aim of analysing the most significant processes without spending large amounts of time modelling all processes so as to obtain a perfect fit. Series resistors represent the simple Ohmic resistances from the connections and circuit (which can be almost eliminated in four-point tests) and from the electrolyte. Parallel RC pairs are used to represent each electrode. The electrode capacitance is mainly “double layer capacitance”. At the interface between the electrode and the electrolyte, there is some charge separation – charges separated by an insulator (in this case simply a few nanometres of empty space) form a capacitor; the value of this double layer capacitance is dependent on many factors including temperature, electrode potential, ionic concentrations, surface roughness and impurities. The resistance

is mainly charge transfer resistance for the electrons and ions separating and dissolving into the relevant conductors; this resistance depends on temperature, the kind(s) of reaction, the concentration of reactants and reaction products and the electrode potential. As series circuit elements are simply added to obtain the total impedance, the simplified circuit shown in Figure 31 B is equivalent to A; giving exactly the same plot in the complex plane.

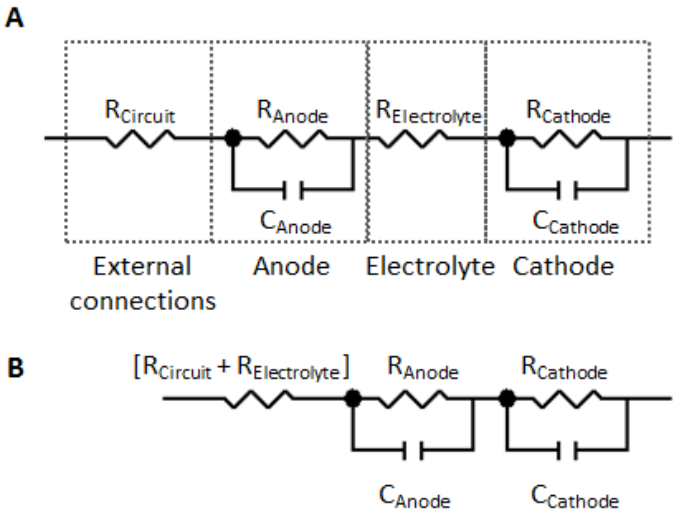

Figure 31 - Basic fuel cell model chosen (A) and the simplified equivalent circuit (B)

This equivalent circuit has been used in the literature [148] to compare usage of different fuels. Impedance spectra were taken at various current densities on both H_2 and n-butane, and the resultant Nyquist plots are shown in Figure 32. The Ohmic resistance, attributed to the electrolyte, is shown to be unaffected by the change of fuel, as would be expected. One of the two arcs changes dramatically with the change of fuel, suggesting that this is the anode polarisation arc, as the cathode is unlikely to be as strongly affected.

Much larger resistances were seen with n-butane than with hydrogen at the lower current densities, although performance was more similar when current density was higher. This

suggests that there is an activation polarisation for n-butane that, once overcome, allows the performance on the two fuels to be similar [148].

This is an example of how a simple model can be used effectively to identify useful trends and draw conclusions. This technique is used in Chapter 5.

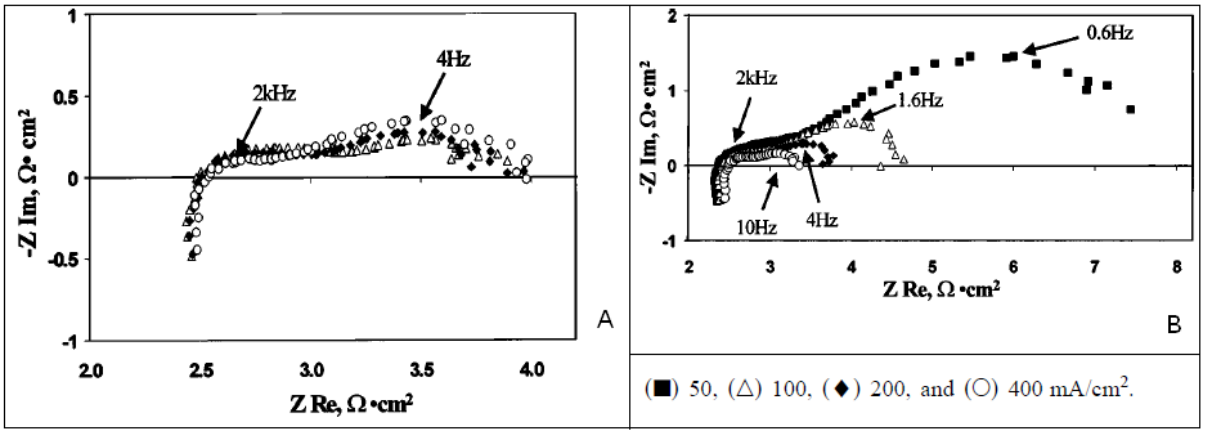

Figure 32 - Nyquist plots on (A) hydrogen and (B) n-butane [148] (note the differences in axis scales)

3.5 Material Characterisation Techniques

The various techniques used are listed and their application to the work presented here is described. More detail of the operating principles of some of these techniques can be found in Appendix III.

3.5.1 Scanning Electron Microscopy

Electron microscopy was used extensively throughout this thesis. A photograph of the Scanning Electron Microscope (SEM) used (Philips XL30) is shown in Figure 33 [217].

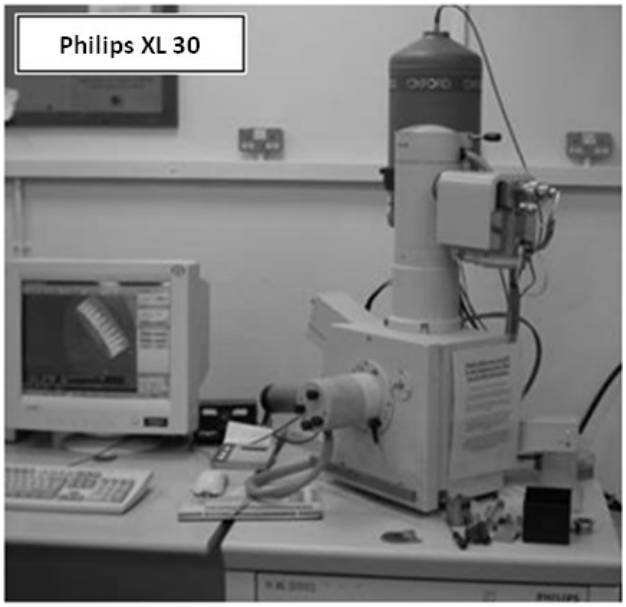

Figure 33 - The SEM used (Philips XL 30)

Cells must be snapped in two at the relevant position to take images of a cross-section. As such, it is a destructive technique. Samples were not polished, except when porosity analysis was the aim, to reduce preparation time and avoid the accidental introduction of scratches which could appear to be cracks.

Focused Ion Beam (FIB) SEM is a variant where a FIB is used to prepare a surface for SEM analysis. The FIB itself can also be used to image the surface, but in this work the ion beam was simply used to remove material, exposing a cross-section or internal layer for imaging (see Figure 34). A thin line of tungsten (visible in the bottom image of Figure 34) was first deposited on the surface to mark the edge of the trench and protect the desired section from the beam. The CFEI Quanta 3D FEG FIB-SEM was used for this work, with the help of Mrs. Theresa Morris.

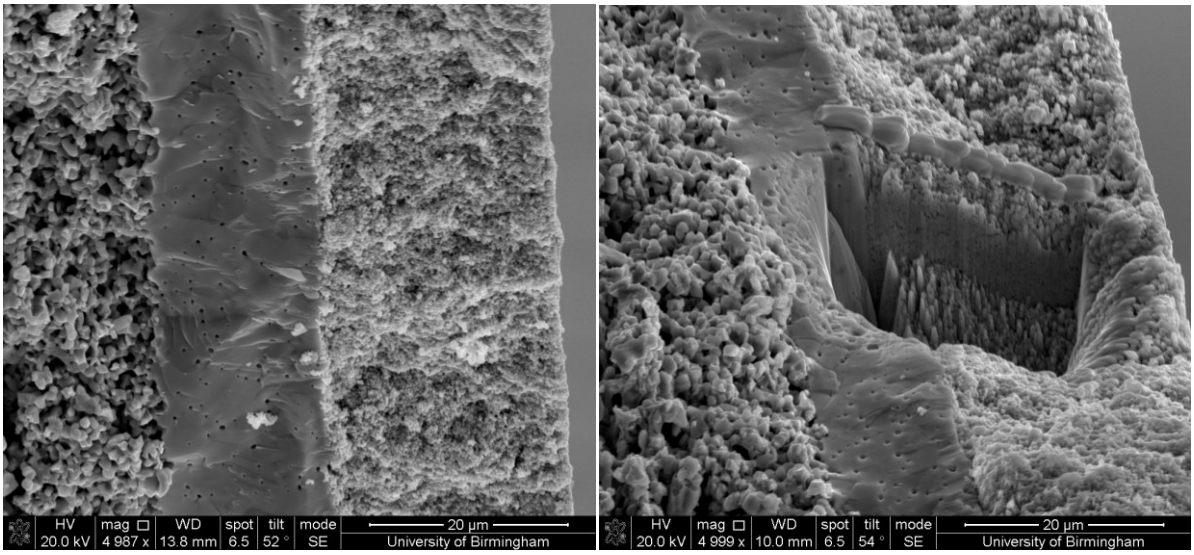

(a) (b)

Figure 34 - FIB-SEM sample preparation: (a) cell cross-section before use of FIB and (b) trench dug into surface using FIB to reveal a smooth plane inside the cathode

SEM is used throughout this work to examine the thicknesses and morphology of the electrode and electrolyte layers, to look for defects and also in conjunction with energy dispersive X-ray spectroscopy (see below) to provide elemental maps of tube cross-sections. FIB-SEM is used when looking at the cathode of the larger AMI-15.2 cells used in Chapter 5.

3.5.2 Energy Dispersive X-ray Spectroscopy

This technique, used in conjunction with Scanning Electron Microscope (SEM) analysis, provided a simple technique for confirming that the new cells purchased from AMI were as stated (Chapter 5), and that the widths of each matched the specified measurements. With careful calibration to set standards, more qualitative work can also be done; this was not necessary for the analysis carried out here, however.

A Philips XL-30 was used for this work.

3.5.3 Atomic Force Microscopy

Unlike SEM, which provides a purely 2D image, Atomic Force Microscopy (AFM) provides 3D imaging. In addition, no coating or sample preparation is needed. The main drawback as compared to SEM is that only a much smaller area can be scanned at once. The resolution is normally limited by the tip size (on the cantilever shown in Figure 35) – if features are smaller than the tip, odd artefacts may appear in images.

Dr James Bowen provided access to this technique, which was used in Chapter 5 to examine surface roughness of the AMI-15.2 µSOFCs used. A plot of the surface profile of the cathode of one of these tubes is shown in Figure 36.

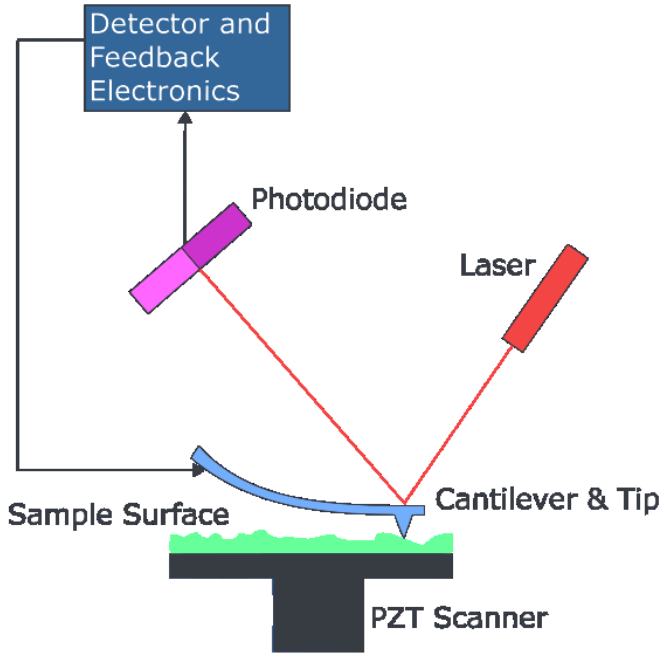

Figure 35 - Principles of AFM - schematic (image from Wikimedia Commons)

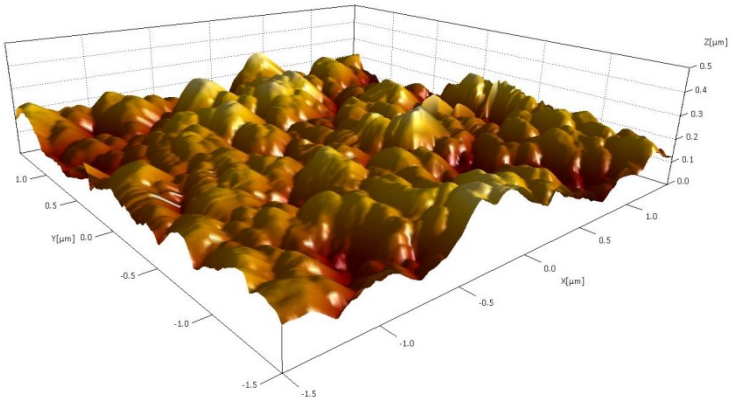

Figure 36 - Surface plot obtained by AFM - µSOFC supplied by AMI

3.5.4 Optical Interferometry

For cells with a fairly small diameter (< 5 mm), AFM imaging is not ideal due to the curvature, as sufficient area must be covered to be representative of the surface character and the individual particle sizes involved in the cathodes made in-house are 0.7-2.0 µm.

Optical interferometry is an alternative technique for examining surface topography. It uses the interference patterns of identical coherent beams of light to gauge the distance from the detector to a point on the sample; a schematic is shown in Figure 37. This technique is again used in Chapter 6.

Figure 37 - MicroXAM optical interferometer schematic [218]

3.5.5 X-ray photoelectron spectroscopy

X-ray photoelectron spectroscopy (XPS) measures the elemental composition and chemical state of the elements in the surface layer (1-10 nm) of a material quantitatively. A spectrum is obtained by measuring the number of electrons that escape from the surface, and their kinetic energies, when an X-ray beam is directed at the sample. XPS must be performed in a vacuum, but is non-destructive.

XPS detects all elements with an atomic number greater than or equal to three, so cannot detect hydrogen. Using X-rays of known wavelength, and so known energy, the electron binding energy of each emitted electron can be determined using the following equation (from the work of Rutherford):

$$E_b = E_X - (E_k + \varphi) \qquad \textit{...(Eq. 3.3)}$$

where E_b is the binding energy of the electron, E_X is the energy of the X-ray photons used, E_k is the kinetic energy of the electron (measured) and φ is the work function of the spectrometer (independent of the material).

This technique was used, with the help of Dr Anders Barlow of the National EPSRC XPS Users Service (NEXUS), to attempt to identify a compound formed from the silver wire during cell operation (Chapter 5).

Results Section I: Cell and Stack Performance

4. SINGLE CELL ANALYSIS

The overall aim of this project is to provide a power unit fuelled by hydrocarbon gases such as propane. Initial tests were performed using hydrogen to gauge the repeatability and reliability for a single cell and levels of variability between batches. Using pure hydrogen fuel eliminates the issue of carbon deposition for these initial experiments. Various fuel compositions were tested once a baseline had been established.

Two different methods of fuelling the cells were also investigated. These methods are the use of an injector tube or an injection block and cement, as described in Section 3.2. Alphabetically labelled cells (e.g. C and D) were brush-painted, and otherwise made according to the techniques described in Chapter 3 whereas numerically labelled cells (1 and 2) were made previously in the research group (by Dr Chinnan Dikwal [219]), with internal anode current collection using a pin and mesh. As well as a variety of Current-Voltage (IV) curves, the two standard test programmes given below were used repeatedly in these early tests, with one data point being collected per second. These tests were used as a baseline for comparison of further improvements, and to check for any hysteresis effects which could influence future test designs.

Programme 1: Voltage Control

1. 15 minute rest at OCV (during which time the cell is heated to temperature)
2. 5 minute IV curve (current controlled, increasing current over time)
3. 1 minute rest at OCV
4. 30 minute load to 0.5 V
5. 5 minute IV curve
6. 1 minute rest
7. 30 minute load to 0.5 V
8. 5 minute IV curve

Programme 2: Current Control

1. 10 minute rest at OCV
2. 5 minute IV curve (as before)
3. 30 minute load to 750 mA
4. 2 minute IV curve (increasing current)
5. 2 minute IV curve (decreasing current)
6. 30 minute load to 750 mA
7. 2 minute IV curve (increasing current)
8. 2 minute IV curve (decreasing current)

The total IV curve times can vary slightly depending on the safety limits set. The intervals between steps in current for the IV curve are around twenty seconds for the five minute

curves and around ten seconds for the two minute curves. As discussed later in this chapter, the dynamic adjustment time is less than half a second even for steps that cover the majority of the cell's range, so a five or ten second interval is more than sufficient. The limits are designed such that current is never driven through the cell by the Solartron, nor the voltage reversed. A safety margin is given; the setting being V≥0.2 V rather than V≥0.0 V and I≥0.01 A not I≥0.00 A.

4.1 Performance

Current and power densities (over the active cell area) are generally used to allow comparisons between different cells. Sample IV curves are shown in Figure 38 for two cells. Cells C and D were made according to the techniques described in Chapter 2 (and brush-painting, not dip-coating) and the data here were obtained at 750°C using cement and an injector block to feed 20 ml/minute of hydrogen fuel to the cell.

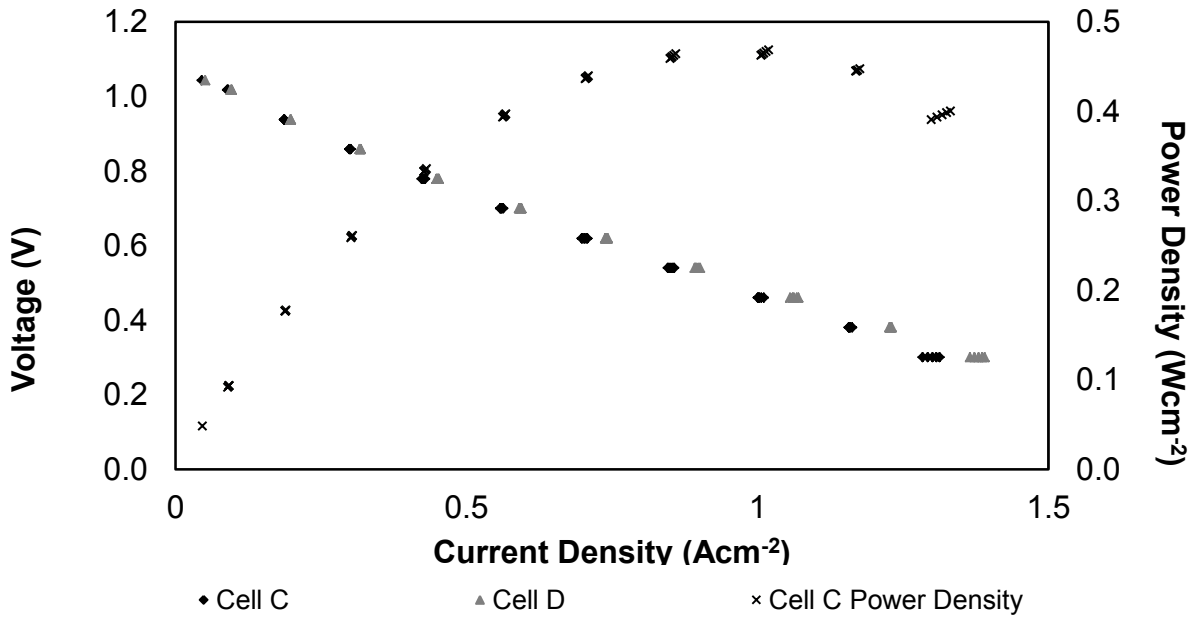

Figure 38 – Baseline single cell performance (voltage-controlled I-V curves) of single AMI-5.5 µSOFCs at 750°C with 20 ml/minute H_2

This peak power of just under 0.5 W/cm^2 and current density of 0.6 A/cm^2 at 0.7 V is typical for these cells[5], operated in these conditions. With 20 ml/minute of pure hydrogen, no mass limitation effects are seen.

4.2 Reproducibility

There are several aspects of reproducibility for single-cell results; these are listed below. Current-Voltage (IV) curves and power density curves are standard ways of demonstrating cell performance graphically, so were used for these comparisons.

I. *Hysteresis on reversal of direction of current change in IV curves*

Presence of hysteresis could indicate that the interval used for the current steps was too short, giving incomplete adjustment to the new level. Non-instantaneous re-equilibration of mass transport and temperature distribution on a change in demand could cause differences in measurement when the direction of the change was reversed.

II. *Performance change after half-hour periods of operation*

Improvements due to further catalyst reduction or activation or worsening due to fatigue are both possibilities. Longer-term testing is required for degradation studies (hundreds of hours), as no drop in performance should be seen on such a short timescale.

III. *Performance change after thermal cycling*

Cells are cooled to room temperature before being reheated for further testing if required; thermal cycling degradation (as explained in Chapter 2) would not be

[5] The geometric area of the cathode is used to calculate power density

expected in the slow cooling and heating conditions used in normal procedures, but this was checked experimentally. Harsher thermal cycling conditions are investigated later.

IV. Variability between batches with known differences in manufacture

Reassuringly, differences between current- and voltage-controlled IV curves for the same cell and test were very small and seem likely to be random noise (see Figure 39). As such, order of tests relative to first cell use and cycling are shown to be much more significant, and current versus voltage control should not be an issue.

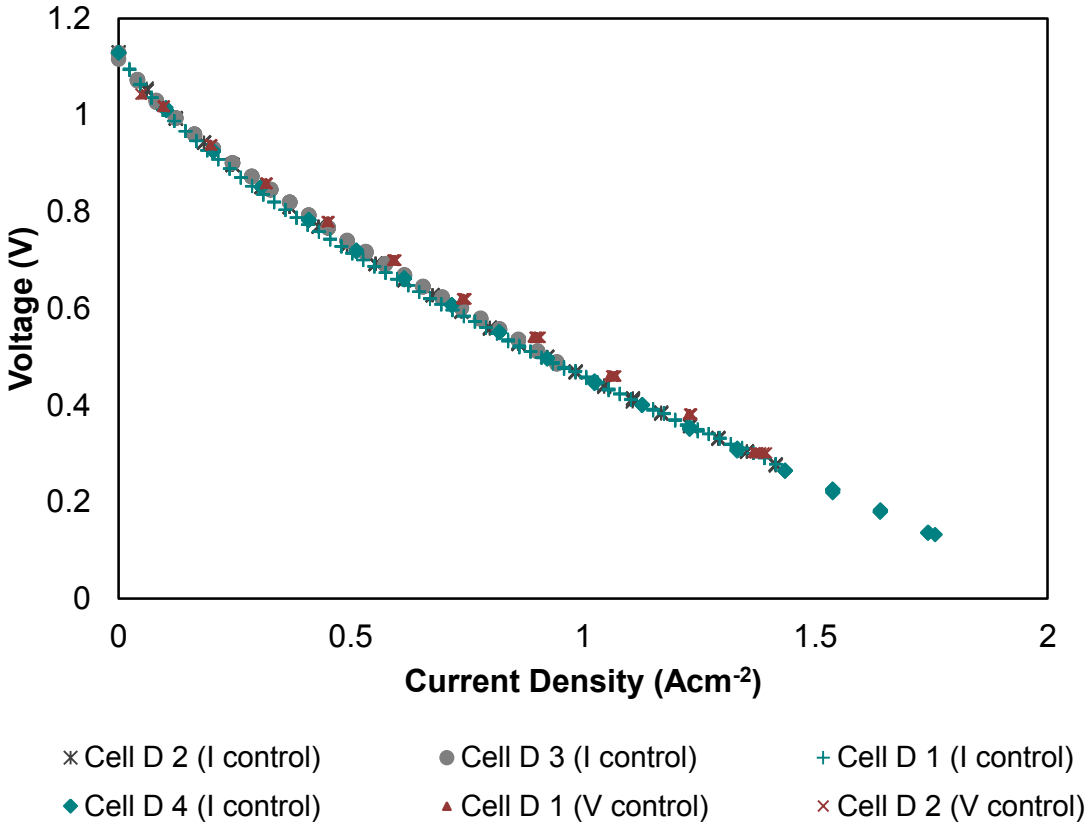

Figure 39 - Current- and voltage-controlled I-V curves for the same AMI-5.5 µSOFC, again tested at 750°C with 20 ml/minute H_2, confirming that results are the same whichever is controlled

I. Consecutive IV Curves:

Consecutive IV curves for a particular cell showed good agreement, with no evidence of hysteresis. Examples of pairs of consecutive curves are shown in Figure 40 and Figure 41. Voltage and current controlled tests were performed.

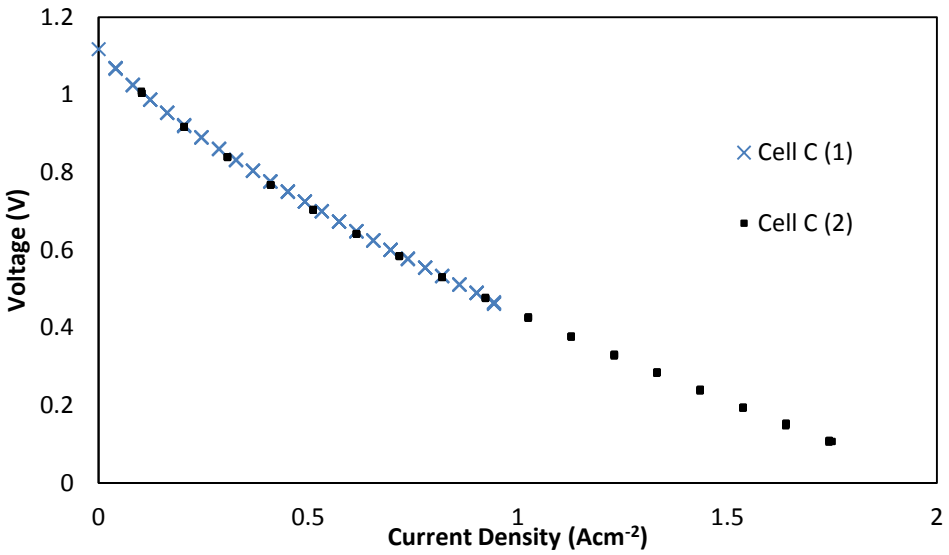

Figure 40 – No hysteresis found in current-controlled I-V curves (Cell C, AMI-5.5 µSOFC, 750°C with 20 ml/minute H_2)

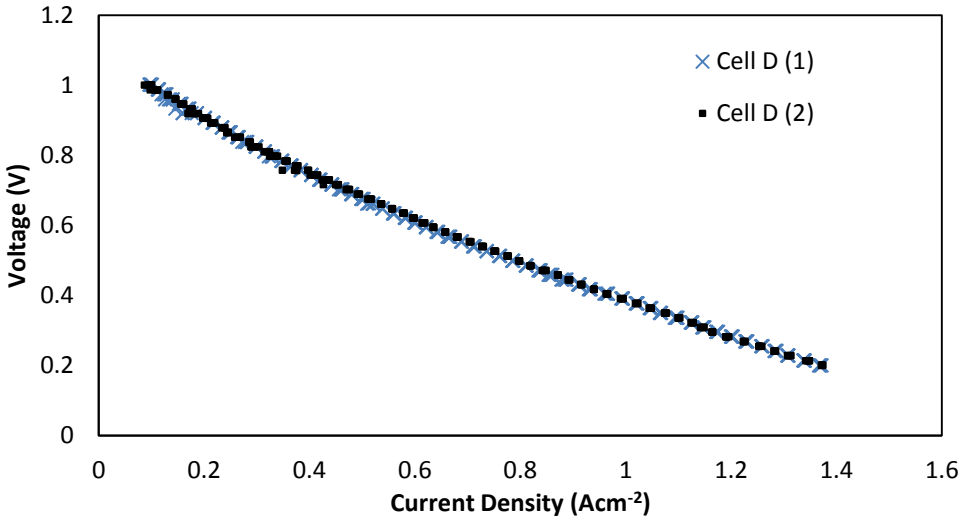

Figure 41 – No hysteresis found in voltage-controlled I-V curves (Cell D, AMI-5.5 µSOFC, 750°C with 20 ml/minute H_2)

If hysteresis had been observed, the step durations in the IV curves would have been increased in subsequent tests to allow equilibrium to be reached: this was not necessary.

II. Before and After Operation Periods

The results obtained are shown below in Figure 42. The first IV curve (Curve 1) was performed after heating the cell up in a hydrogen flow, with only a few minutes at temperature before the readings were taken. This is lower than the later two curves (Curves 2 and 3) which were recorded after one and two thirty minute periods in hydrogen at 0.5 V, respectively.

This suggests that the cell had not completely reduced during the pre-use reduction period (or had re-oxidised a little since due to backflow of oxygen into the tube), so that the cell performance improved after a longer time in the test set up. LSM activation could also be responsible for this improvement [220] (see Chapter 7).

The fact that an improvement was seen, instead of a worsening, shows that operation “wear and tear” has a negligible effect over timescales of approximately two hours at the shortest.

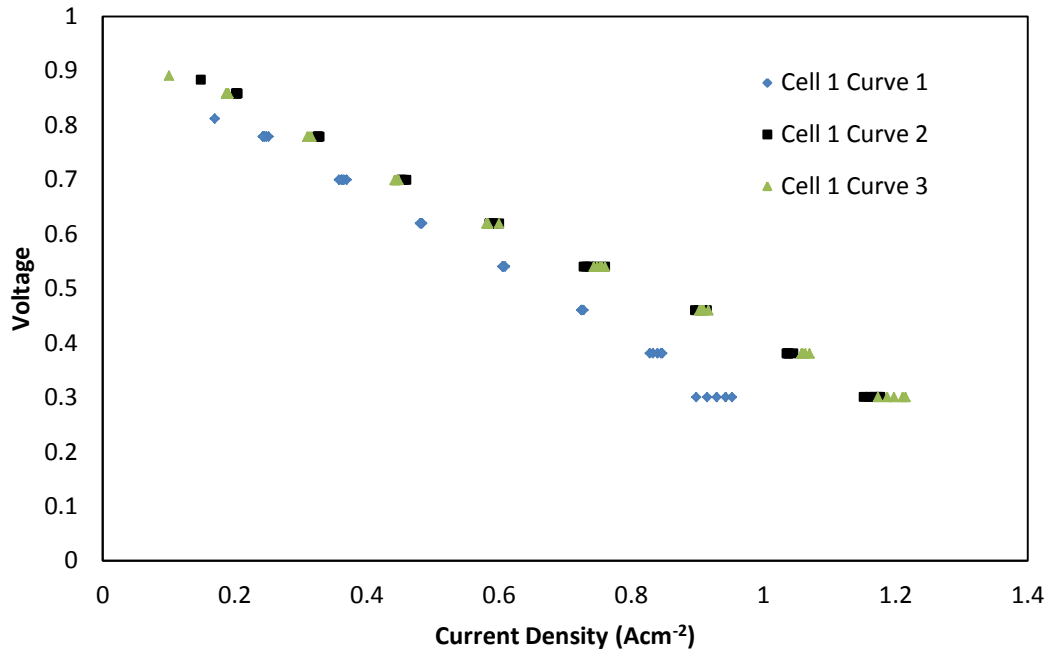

Figure 42 – I-V curves showing the effect of periods of constant voltage operation on performance (voltage-controlled, AMI-5.5 µSOFC at 750°C with 20 ml/minute H_2)

III. Before and After Cycling

Between days of testing, the cells were cooled back to room temperature, and then left overnight. As detailed in Chapter 2, cycling can have negative effects on cell performance due to a combination of oxidative and thermal effects. This was indeed observed, as shown in Figure 43.

At low current densities, the difference was not strongly apparent; the difference increased as current density increased, however. It is unsurprising that any weakening of the cell becomes more apparent when more is demanded from it. The same cell was then tested again after another cycle, and other cells tested in the same way, and the trends were the same.

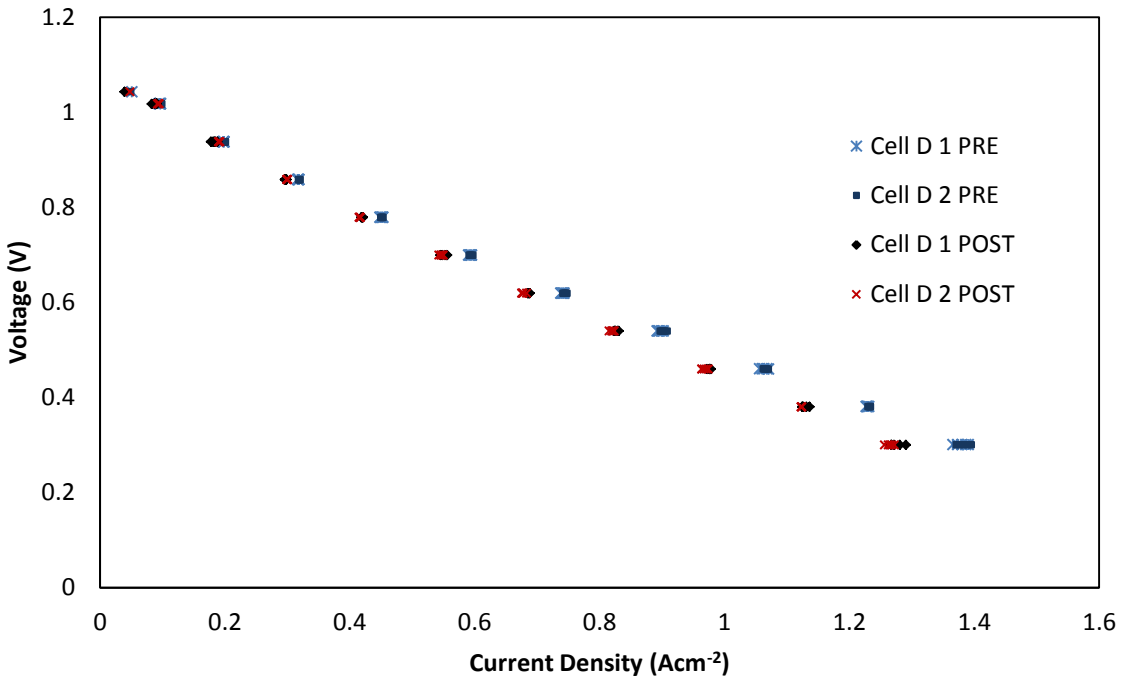

Figure 43 – Voltage controlled I-V curves of an AMI-5.5 µSOFC pre- and post-thermal cycling (750°C, 20 ml/minute H_2)

Open Circuit Voltages (OCVs) for each of the three runs (data averaged over step 6 of the constant voltage programme, excluding the first reading from each set) show that the incremental damage of a second cycle was much smaller than the initial damage with respect to the voltage at zero current.

Table 6 - OCVs on consecutive days for the same AMI-5.5 µSOFC – assessing the effect of thermal cycles

Cell D	OCV
First Run	1.130
Second Run - 1 cycle period	1.125
Third Run - 2 cycle periods	1.123

This highlights the fact that identical performance cannot be guaranteed from the same cell once it has been cycled. A fuller investigation of more aggressive thermal cycling is given in Section 4.3.

IV. Variability Between Batches

Whilst not identical, the cells within the first batch are very similar in terms of OCVs and IV curves, as illustrated in Section 4.2. The two cells prepared by a former group member, Dr Dikwal that were tested also showed very similar IV characteristics. There were noticeable differences between these two batches, however; the cells made according to the methods given in Chapter 3 gave distinctly better characteristics than the cells made by Dr Dikwal, following older methods (see Figure 44, details of the methods he used are given elsewhere [203]). These differences between batches were of larger magnitude than the pre- and post-cycling differences for one type.

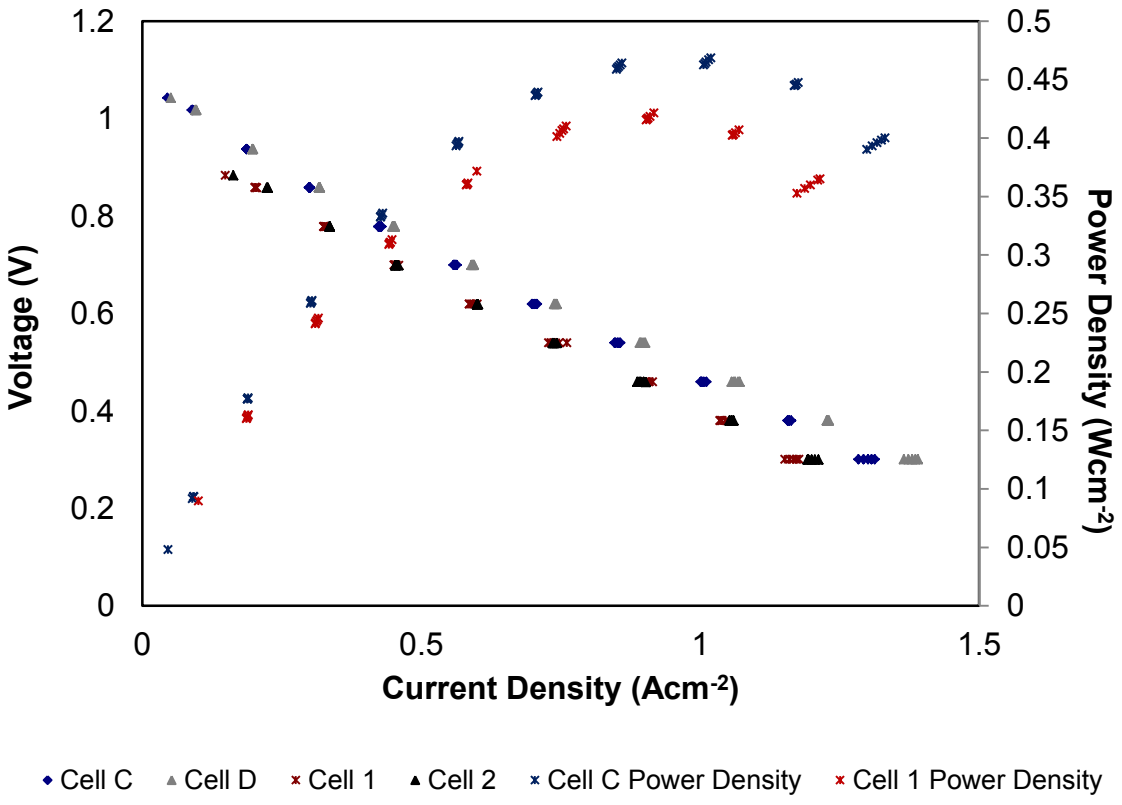

Figure 44 - Variation between batches of AMI-5.5 µSOFCs of differing interconnection designs tested under identical conditions (voltage-controlled I-V and power curves at 750°C with 20 ml/minute H_2)

4.3 More Aggressive Thermal Cycling

SOFCs are usually subjected to many thermal cycles over their lifetimes – thermal cycling tolerance is therefore crucial. Cells were therefore tested with more, steeper heating and cooling ramps to simulate accelerated aging and analyse performance drop.

Two cells, prepared identically, were tested over 56 thermal cycles between 750°C and 400°C, at 100°C per minute. IV curves were performed between each set of cycles, and the peak power recorded (see Figure 45). Other than one temperature-related anomaly, the repeatability was very good. Power degradation of 6.5% was seen for these cells over the full 56 rapid cycles. As most cells tested in this work are not cycled more than ten times, and are subject to much less steep thermal ramps, this is more than satisfactory for testing purposes.

Factors that affect cycling stability are discussed in Chapter 2, and experimental work on anode and cathode preparation techniques to improve cycling stability is reported in Chapter 7.

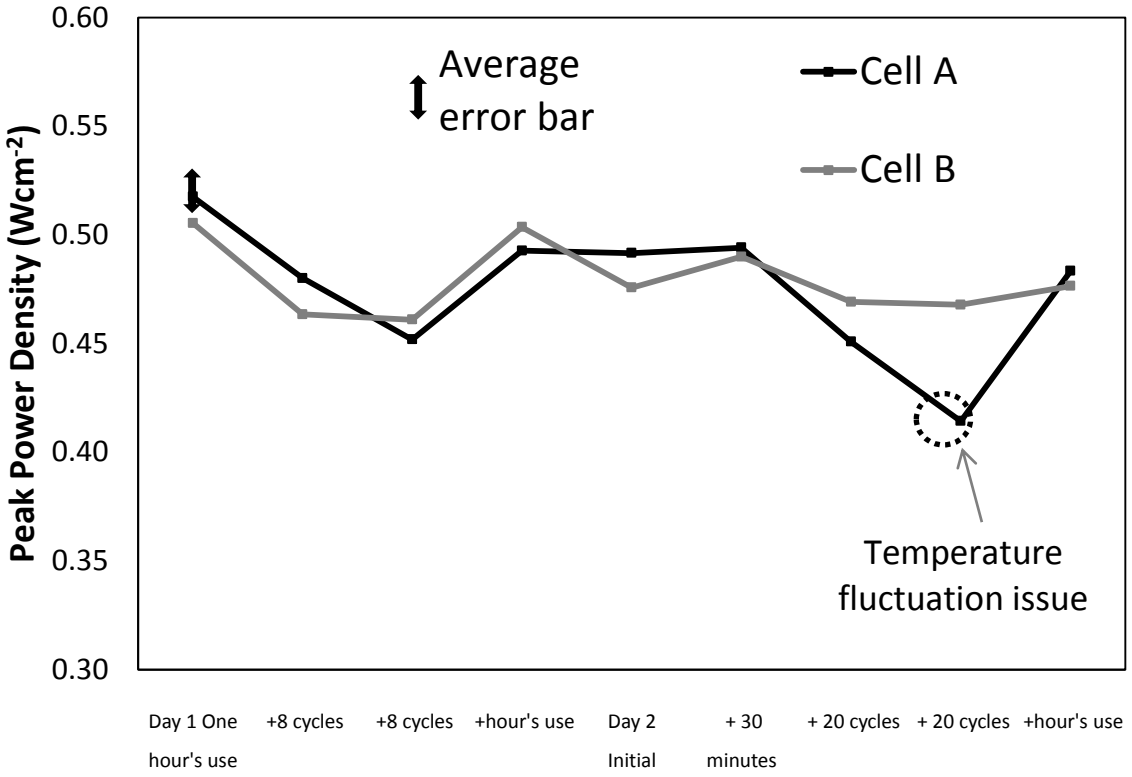

Figure 45 - Power drop on thermal cycling of AMI-5.5 µSOFCs (56 rapid cycles in total, 750°C with 20 ml/minute H_2)

4.4 Gas Mixtures

Having performed extensive testing with pure hydrogen as a fuel, the use of hydrocarbon fuels was then investigated. It is known that single tubes can give comparable performance on methane to that on hydrogen (Figure 46, courtesy of T. J. Lee [221]), although degradation due to carbon deposition poses a problem. The SUAV project goal is to use propane that has passed through a pre-reformer (to reduce average chain length and hence the risk of coking). The gas mixture will be likely to contain propane, methane, hydrogen, carbon dioxide, carbon monoxide, nitrogen, water vapour and perhaps some oxygen. The hydrocarbon testing should help to establish the acceptable range of gas mixture concentrations to maintain high performance.

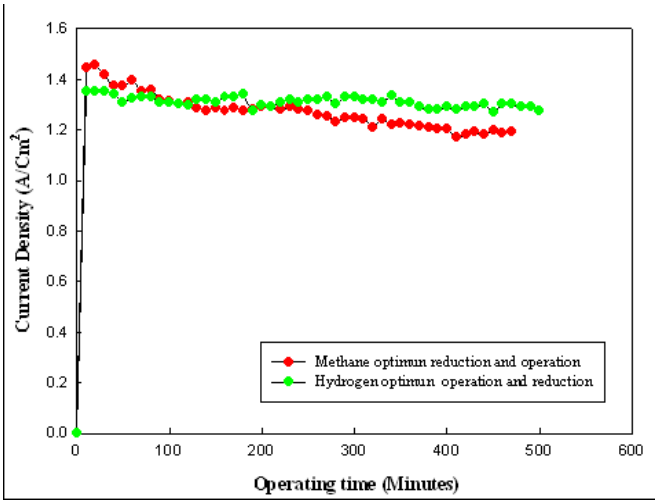

Figure 46 - Single AMI-5.5 µSOFC results showing that methane and hydrogen can give comparable performance. Source: UoB PhD Thesis [221]

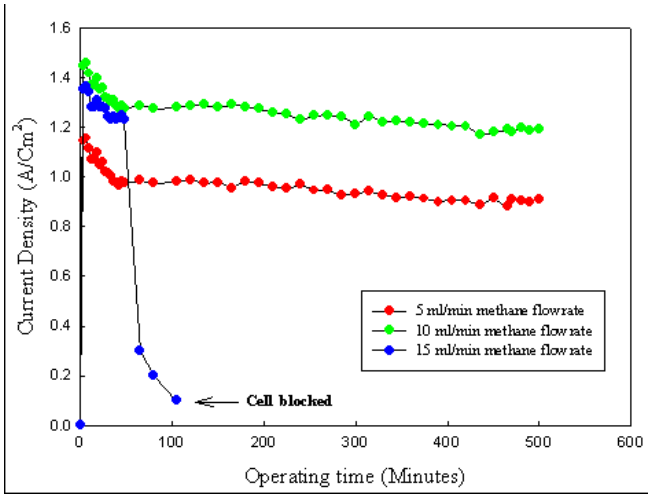

Figure 47 - Results showing AMI-5.5 µSOFC sensitivity to methane flow rates (with helium buffer gas). Total flow rate ~20ml/minute. Source: UoB PhD Thesis [221]

As shown in Figure 47, too much hydrocarbon gas leads to carbon deposition which can clog the cell. Lee's results [221] also showed that increasing fuel flow rate did not continuously increase performance, but rather reached a peak somewhere between 5 and 15 ml/min, with a 15 ml/min flow rate causing entire blocking of the cell after around an hour (Figure 47). Using helium as a buffer gas helps to keep the pressure higher when the flow rate of methane is low, but adding a buffer gas increases system complexity and is therefore unwanted for this project.

4.4.1 Cell Production

Previous experience in the group [115, 203] was used to optimise manufacturing techniques for the cells for use with hydrocarbons. The cells were therefore made using an in-house cathode ink recipe, and a reduction temperature of 650°C (previously found to be optimal over a range of operating temperatures [203]). The method of constant temperature reduction [115] was used. Higher breakage is expected when preparing cells for

hydrocarbon testing instead of testing on pure hydrogen, due to the lower reduction temperature. The breakage rate was still higher than expected, however; of the 50 cells made, six broke during this process. Poorer quality of the batch of AMI tubes is suspected, as surface defects were visible on some cells on arrival.

Dr Dhir found 4 ml/min of methane with 20 ml/min of helium to be best. Flow rates of fuel and buffer around these values were therefore tested. An operating temperature of 800°C has been found to be optimal with respect to carbon deposition [203], so this was used for all tests bar one.

4.4.2 Performance

Consecutive IV curves on hydrogen and methane for the same cell showed better performance on methane (Figure 48), confirming that these cells have been optimised for use with methane. This could be due to the deposition of a small amount of carbon helping to stabilise the anode structure obtained at the lower reduction temperature and improve conductivity [115]. These IV curves showed a more marked activation energy drop for methane than for hydrogen. This suggests that, although the overall performance is better with methane, the electrode kinetics are poorer. The rate-determining step is thought to be the dissociative adsorption of methane [222].

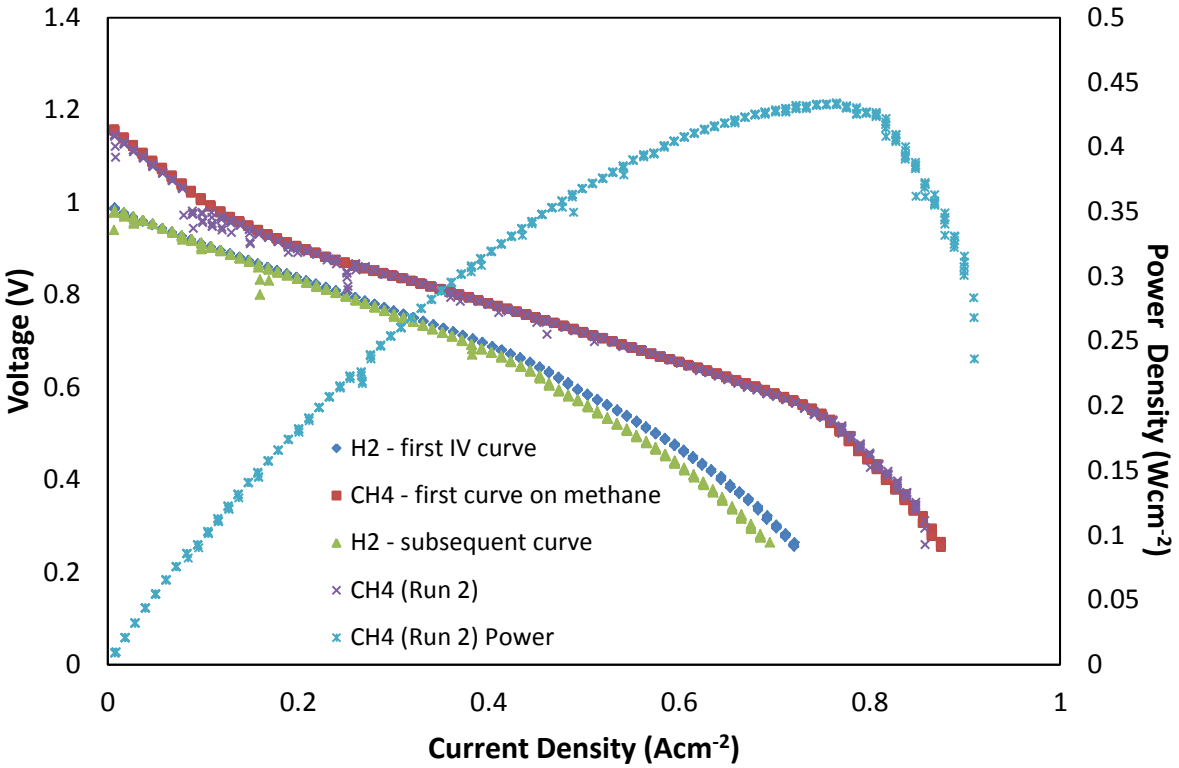

Figure 48 - IV curves for an AMI-5.5 µSOFC, optimised for hydrocarbon fuels by using a lower reduction temperature of 650°C, tested on hydrogen (20 ml/min.) and on methane (4 ml/min.) with helium (20 ml/min.), tested at 800°C.

4.4.3 Buffer Gas Flow Rates

The flow rate of helium was changed at constant temperature (800°C), demanded voltage (0.5 V) and methane flow rate (5 ml/minute). A higher total flow rate increases the pressure within the anode, which helps to remove the steam generated and improves performance [223]. As compared with the graphs shown in Figure 47, these tests were performed in the early section of operation where significant degradation is still expected. The steps in output were, nonetheless, very marked, when the helium flow rate was altered. A graph showing three such steps is given in Figure 49. An increase in helium flow rate increases the pressure in the system without changing the amount of fuel, although it does reduce the partial pressure of the fuel.

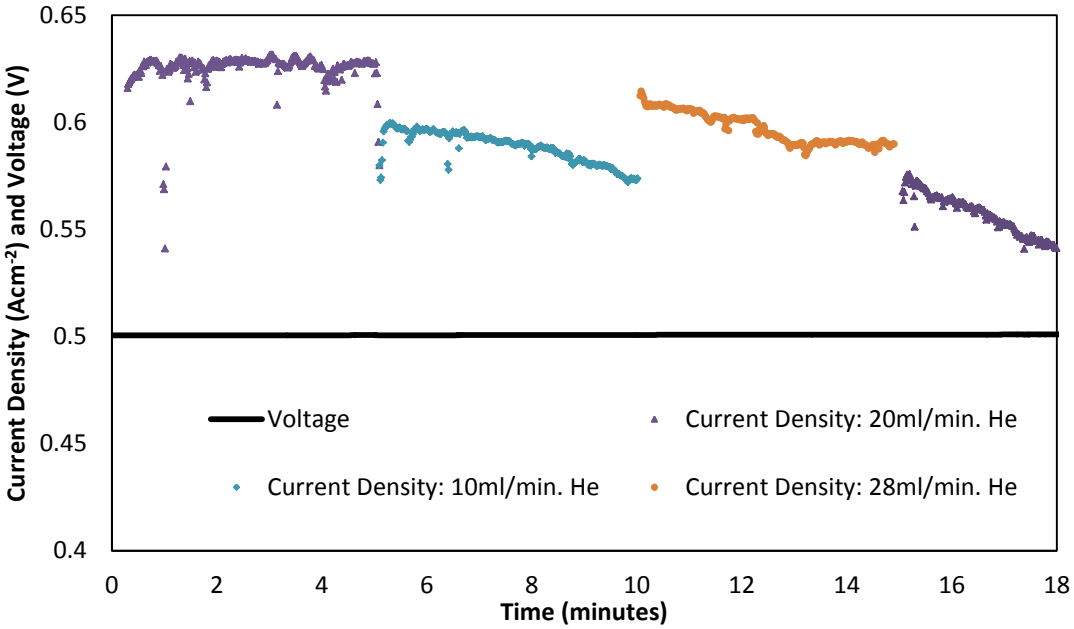

Figure 49 - Effect of helium flow rate on hydrocarbon-optimised (see Figure 48) AMI-5.5 µSOFC performance at 800°C with 5 ml/minute of methane; different colours used to highlight the different helium flow rates

4.4.4 Methane Flow Rates

With the helium flow rate held at 20 ml/min, different flow rates of methane were then investigated. Five different flow rates were tested for their effect on immediate power – long-term degradation effects were not studied here. Current density was clearly shown to increase when flow rate increased, at the same voltage, as shown in Figure 50.

Despite the steps upwards in flow rate increasing in magnitude, the steps upwards in current density became smaller as flow rate increased. This suggests convergence towards a limit beyond which further increases in flow rate have no effect.

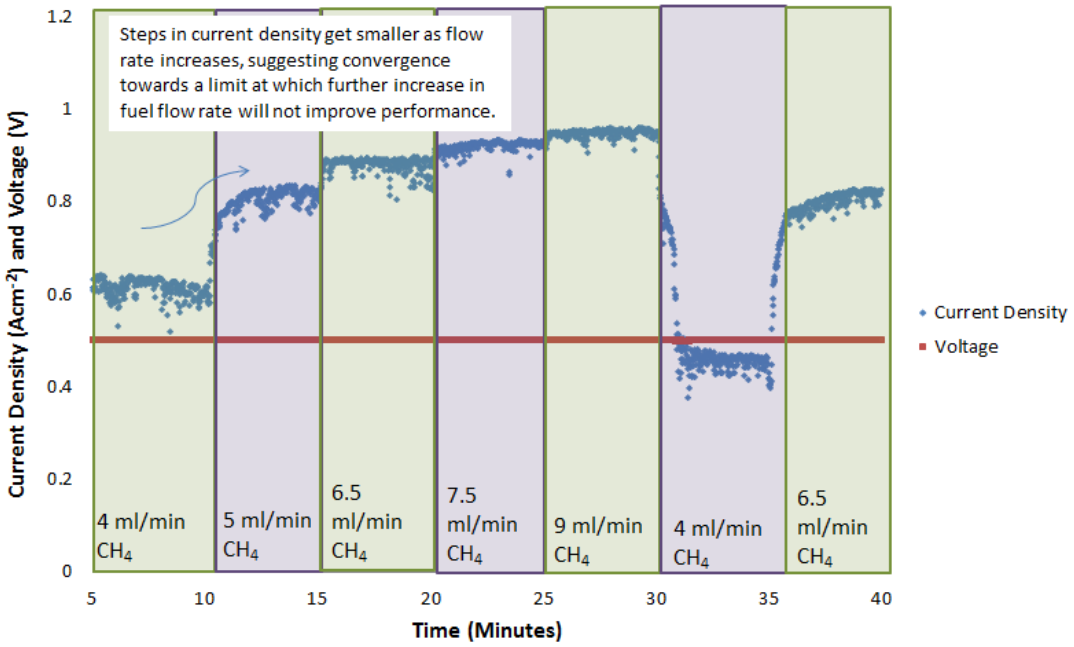

Figure 50 - Effect of methane flow rate on rate on hydrocarbon-optimised (see Figure 48) AMI-5.5 µSOFC performance at 800°C with 20 ml/min He

On returning to the original methane flow rate of 4 ml/minute, significant degradation in current density was observed as compared to the earlier period at that flow rate. This is likely to be due to carbon deposition. The fact that less degradation was seen at the following 6.5 ml/min period suggests that a brief period with a lower flow rate of methane may have helped to remove some carbon, allowing better performance afterwards. Experimentation showed that running these cells on hydrogen can help to restore performance when methane is then reintroduced, supporting this idea of anode "cleaning".

The following conclusions were reached, from experiment and the literature, and are considered in the SUAV system design:

- Total flow rate, and so pressure, is very important. Keeping this to around 20 ml/minute gives good performance (around 0.5 W/cm^2 at 36% fuel utilisation). Increasing the flow rate further by using a buffer gas gives marginal incremental gain,

but is not worth the extra storage capacity required (tested and discussed further in Chapter 5).

- A maximum of 10 ml/min carbon-containing fuel (50% by volume of anode gas in this regime) is sensible to avoid significant degradation due to carbon deposition [221].
- More testing with propane, carbon dioxide and water vapour is needed, and will be carried out by other SUAV team members.
- Recirculating the anode exhaust gas will increase utilisation and add more humidification to the gas stream.

4.5 Transient Performance

This section is heavily based on work previously published by the author, with some sections being extracts from papers written in the course of this work [6].

Solid oxide fuel cells are generally characterised by their steady state behaviour, but their load-following abilities are crucial for any "real world" applications. The response to changes in demanded current or voltage with time, without any change to gas flows or furnace temperature, was investigated. There is very little experimental data on this in the literature, but there are, however, various papers analysing transient performance from a theoretical and computational approach (Nehter's paper [224] being an example of such).

[6] **Relevant Publications:**
K.S. Howe and K. Kendall, Transient Performance of Micro-Tubular Solid Oxide Fuel Cells and Stacks. ECS Transactions, 2011. ***35****(1): p. 419-423.*
K.S. Howe and K. Kendall, Transient Performance of Micro-Tubular Solid Oxide Fuel Cells. Journal of Fuel Cell Science and Technology, 2011. ***8****(3): p. 034502.*

The following experiments were designed to investigate this transient performance, getting an idea of how long it takes an individual µSOFC to respond to a given change in current demand.

4.5.1 Theory and Rationale

It is known that three main time constants are observed for SOFC transients; these are:

1. Characteristic time of the electrochemical response (on the order of milliseconds)
2. Characteristic time of the mass transport response (on the order of seconds for planar cells, but found to be around an order of magnitude shorter for µSOFCs in this work)
3. Characteristic time of thermal re-equilibration (on the order of minutes or hours for planar cells, and around forty seconds for tubular cells [225])

A more thorough discussion of these is given in the paper of Bhattacharyya and Rengaswamy [226], with the conclusion that the thermal transport time constant is usually the longest. For the much smaller micro-tubular cells, the thermal transport can be rationally expected to re-adjust much more quickly. Thermal transport time constants of 35-40 seconds were found computationally by Hajimolana and Soroush [225] for a single tubular cell with a +5% change in external load, so those for a single µSOFC should be shorter.

Computational studies such as that of Achenbach [227] (on planar SOFCs) predict an "undershooting" of the voltage, where it drops to below the new, lower steady-state voltage before rising to it, on an increase in demanded current. The magnitude of this undershoot was found to be related to the size of the current density step, whereas the relaxation time was independent of that. Achenbach explains this by the fact the initial cell temperature

after the jump to a higher current density is still relatively low, and related to the first current density, "The higher amount of waste heat produced at ... [the higher, second current density] causes the cell temperature to increase which results in an increase in the cell voltage due to the decreasing internal cell resistance." The same principles should apply to μSOFCs, although the faster thermal equilibration may reduce the effect. The modelling work of Serincan et al. [228], based on μSOFCs, predicts dynamic response times of around 20 s, with heat transfer being the limiting factor (a shorter adjustment time than for Achenbach's cells (200 s), as would be expected given the smaller size).

By contrast, other research suggests that it is actually the mass transport effects that determine dynamic responses [225, 226, 229]. Although the settling time for mass transport adjustments is generally shorter, this has been seen to have a more marked effect on performance by some researchers [226, 229]. The voltage and current are seen to reach their new steady state values within a fraction of a second, before the new thermal equilibrium is reached, as shown in the modelling work of Hajimolana and Soroush [225] (Figure 51). Bhattacharyya et al. [229] found that incorporating Knudsen diffusion in their (isothermal) model gave a very good fit to the overshoot seen in the experimental data, with no consideration of thermal transients needed. This appears to be disagreement in the literature, with two possible mechanisms being given to explain the transient response. Both mechanisms are plausible, and they may occur concurrently – the type of cell used may be the differentiating factor, as Achenbach's work [227, 230] was on a planar SOFC stack, not μSOFCs. Given that the time periods for thermal readjustment in tubular cells are longer than those for the step changes in voltage, it seems unlikely that a temperature change

could be responsible for the short-lived effect seen for tubular cells [225, 229]. The voltage adjustment times of around 150 seconds seen by Achenbach [227] could fit with the timeframe of thermal equilibration. Figure 51 clearly shows that the thermal equilibration time constant is quite different from the time constant for voltage adjustment for the (smaller) tubular cells modelled [225], suggesting that the limiting factors for transient behaviour differ with SOFC type.

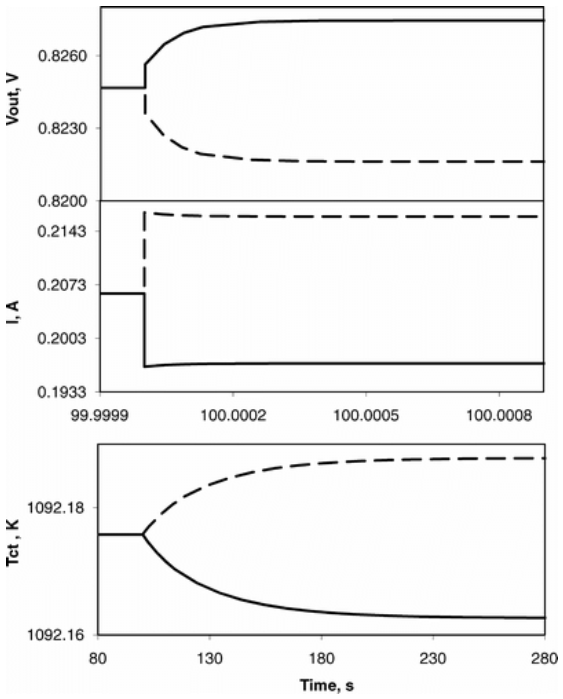

Figure 51 - SOFC response to step changes of ±5% in the external load resistance (solid line: R_{load} increased from 4 Ω to 4.2 Ω, dashed line: R_{load} decreased from 4 Ω to 3.8 Ω) [225]

4.5.2 Experimental Work

A second batch of µSOFCs was made in the same way as cells A-F for further testing. One of these was tested with current-controlled square pulses and the voltage response was examined. These tests again took place at 750°C with 20 ml/minute of hydrogen, with the same heat-up procedure as used previously. The experimental procedure was as follows:

1. Initial 30 minute rest period (10 minutes for the cell to reach temperature and 20 minutes to allow for any further reduction and ensure a steady reading of the OCV)
2. IV curve data taken (over five minutes, readings at 1 Hz, termination condition to cancel the step if the voltage dropped below 0.3 V, to protect the cell) to check cell performance for comparability with the rest of the batch
3. Brief rest at OCV (~five minutes)
4. Higher resolution IV curve data taken (10 Hz) to check for short-lived transient effects that could be missed at 1 Hz resolution
5. One minute cycle of current demand square pulses of ten second period (50 Hz data collection, step from 0.6 A to 0.1 A current demand)
6. One minute cycle of current demand square pulses of ten second period (50 Hz data collection, step from 0.9 A to 0.1 A current demand)
7. Higher resolution IV curve data taken (10 Hz)
8. Brief rest at OCV (~15 minutes)
9. One minute cycle of current demand square pulses of ten second period (100 Hz data collection, step from 0.9 A to 0.1 A current demand)
10. One minute cycle of current demand square pulses of ten second period (100 Hz data collection, step from 1.0 A to 0.01 A current demand)
11. Higher resolution IV curve data taken (10 Hz)
12. Brief rest at OCV (~10 minutes)
13. Final high-resolution IV curve sample taken (OCV down to 0.7 V over 65 seconds at 1000 Hz data collection)
14. Cell cooled in hydrogen with no demands

Different research groups control either current or voltage in the square-pulse steps, with very similar results. Current control was chosen in this work. This test profile is shown in Figure 52.

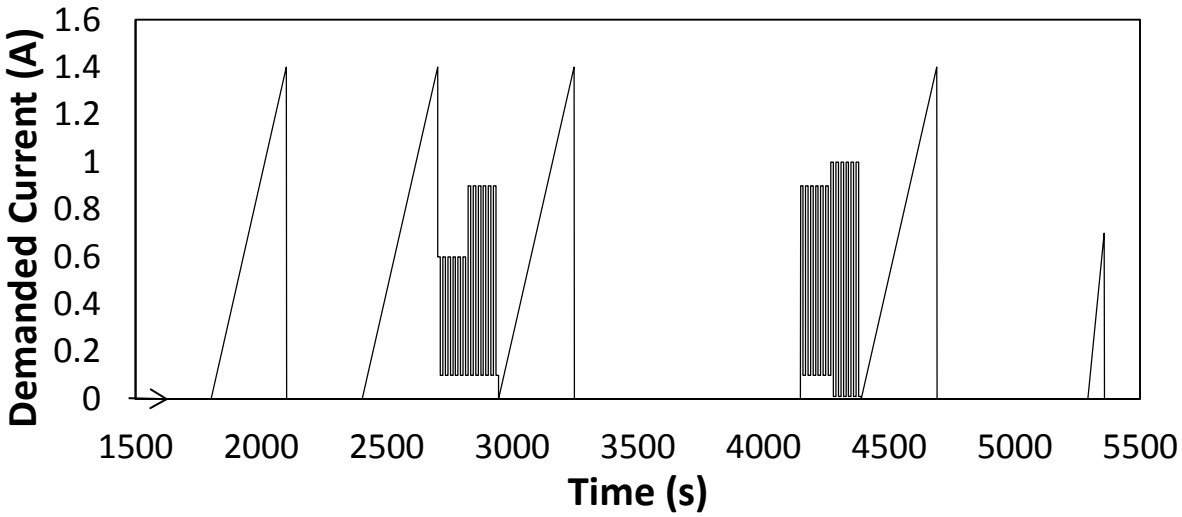

Figure 52 - Transient test profile used for AMI-5.5 µSOFCs – current-controlled

4.5.3 Results

The first and second sets of pulses (Steps 5 and 6) showed very promising load-following behaviour (quick adjustment and close load following), after some initial distortion, as shown in Figure 53 and Figure 54 below. The odd behaviour observed on the first pulse is not worrying as it was not repeated. Closer examination of steps here revealed the relaxation times of these two steps to be less than 0.5 s, and equal to within the bounds of experimental error. Highly annotated graphs for one step from each of Figure 53 and Figure 54 are shown below in Figure 55 and Figure 56. No evidence was observed for the overshooting phenomenon predicted by Achenbach [227] amongst others. The data sampling rate was increased to 100 Hz for the second two sets of pulses to check for the occurrence of this effect on a shorter timescale.

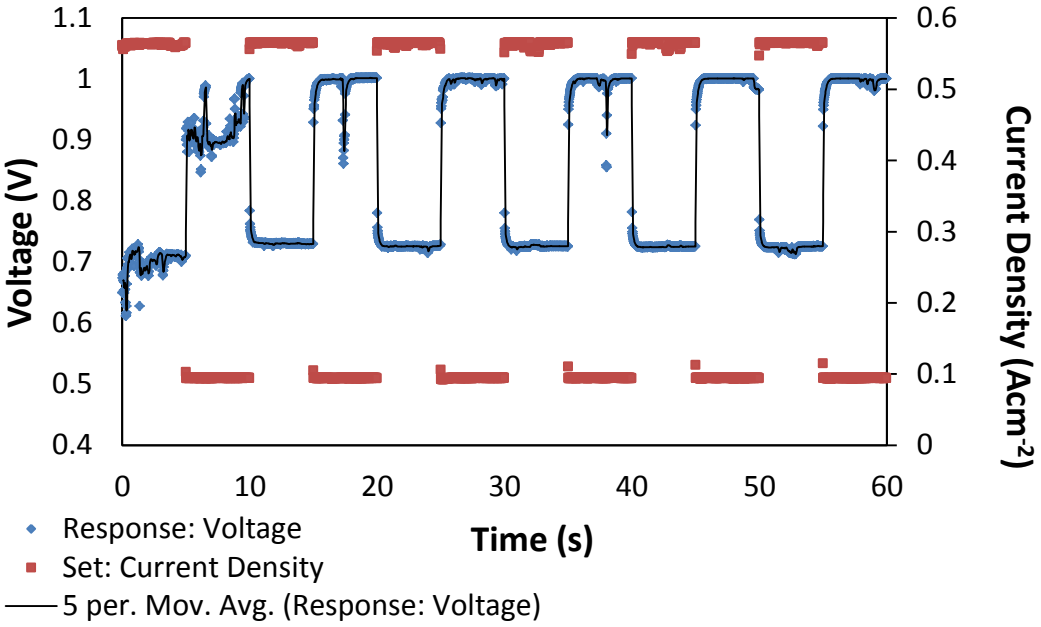

Figure 53 - Transient performance of an AMI-5.5 µSOFC with 0.5 A current-controlled square-pulse steps (750°C, 20 ml/minute H_2)

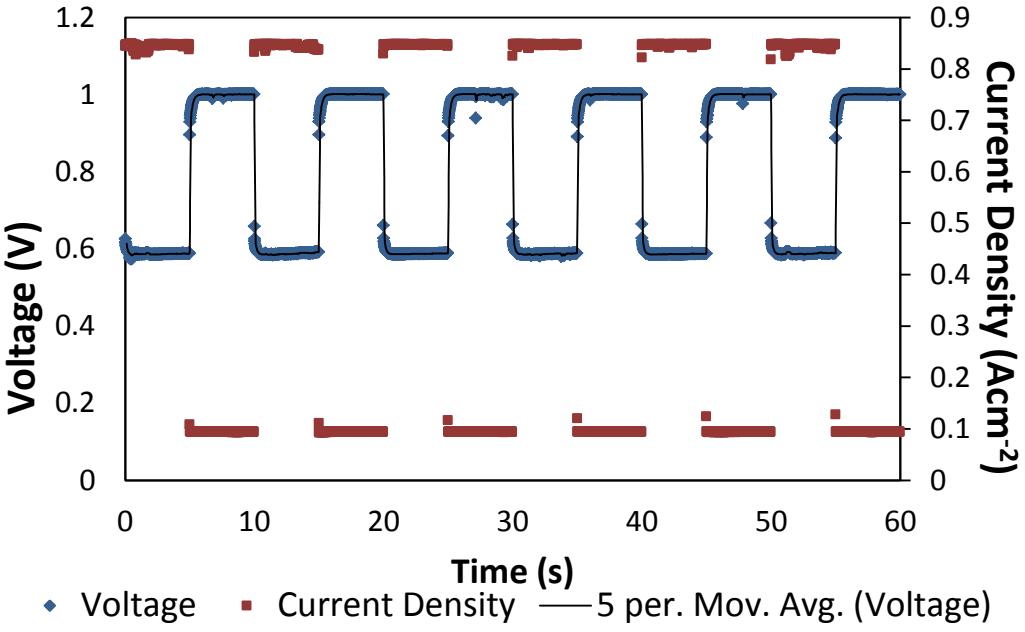

Figure 54 - Transient performance of an AMI-5.5 µSOFC with 0.74A current-controlled square-pulse steps (750°C, 20 ml/minute H_2)

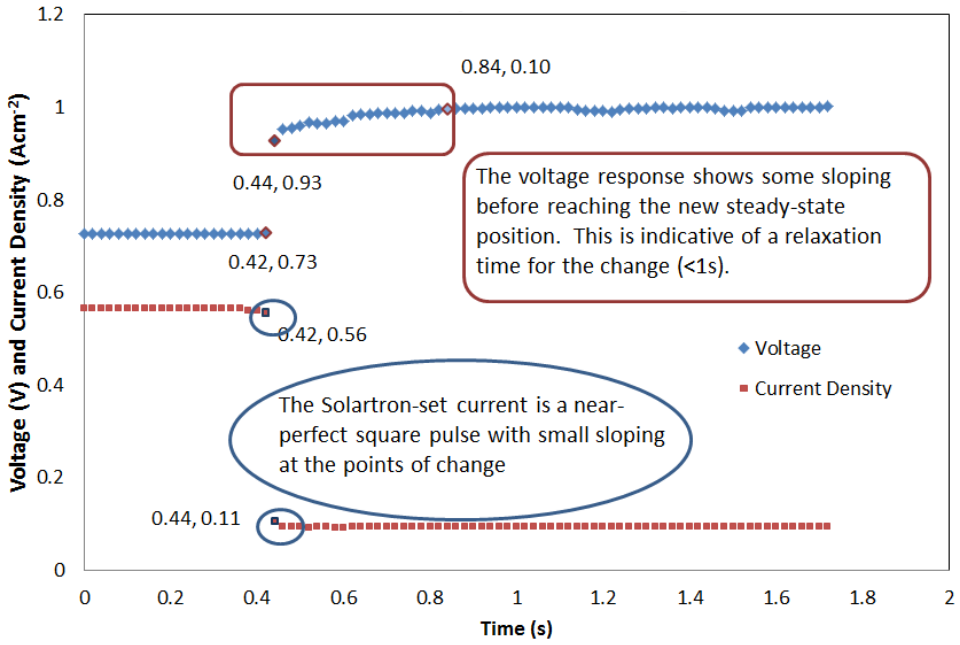

Figure 55 – Step-change results for an AMI-5.5 µSOFC undergoing a current-controlled 0.5 A step (750°C, 20 ml/min. H_2)

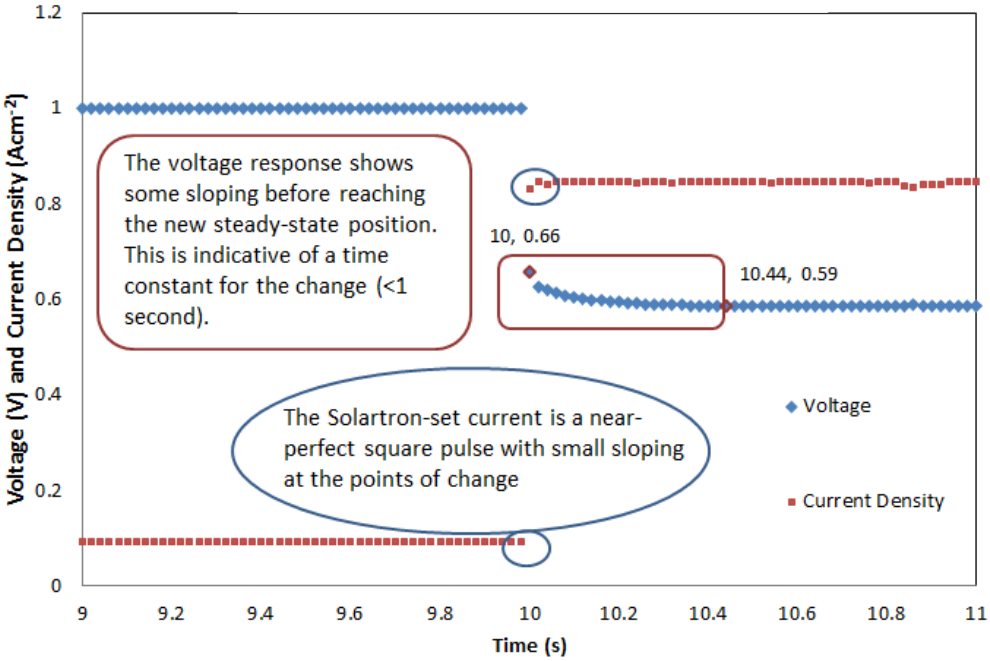

Figure 56 – Step-change results for an AMI-5.5 µSOFC undergoing a current-controlled 0.74 A step (750°C, 20 ml/min. H_2)

The third set of pulses (Step 9) was identical to the second set apart from the increased resolution; although the interim tests may have had a degrading effect on the cell, the similarities of IV curves suggest any such effects were minimal. These data showed more and larger "spikes" away from the steady state readings (Figure 57), but no clear evidence of overshooting voltage changes. The relaxation time remained less than half a second.

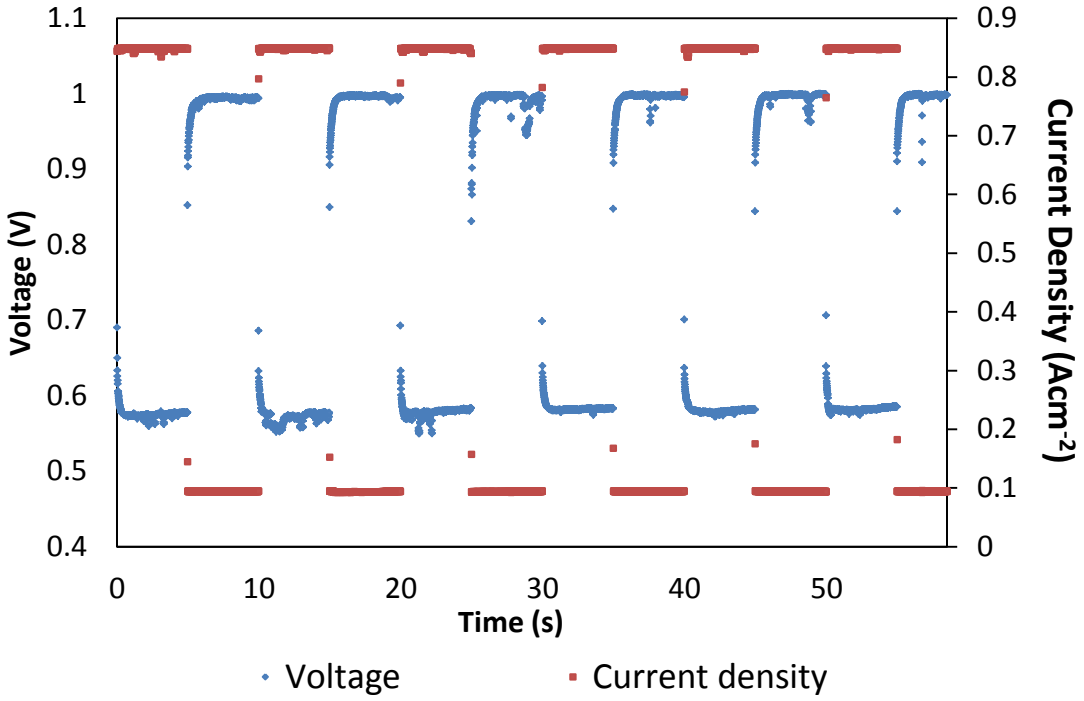

Figure 57 - Transient performance results for an AMI-5.5 µSOFC at higher resolution – 100 Hz data sampling of a 0.74 A step (750°C, 20 ml/minute H_2)

The largest magnitude pulses tried (Step 10) gave a very unsteady highest voltage (see Figure 58, and a close-up in Figure 59). This is probably more to do with the level of the highest voltage (very close to the OCV, and, as such, on the steepest section of the IV curve, where smaller current fluctuations have a larger impact on voltage) than with the magnitude of the step. The relatively steady lower voltage sections (at a much more demanding current density) give some confidence in this hypothesis.

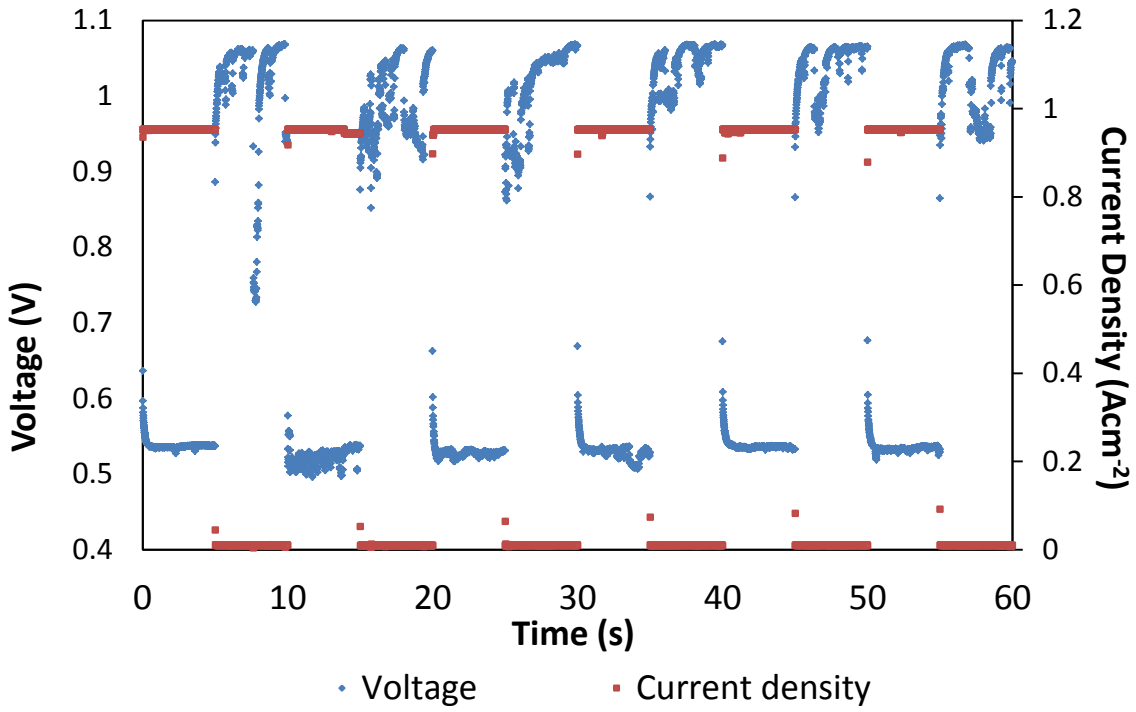

Figure 58 - Transient performance for an AMI-5.5 µSOFC undergoing steps of 0.99 A - very large magnitude relative to the cells range (100 Hz data sampling, 750°C, 20 ml/min. H_2)

Although no such readings could be taken from the higher voltage sections, a step to a lower voltage again took about 0.44 s to stabilise. This is in agreement with Achenbach's theoretical calculations [227] in that this relaxation time appears to be independent of step magnitude. Yet again, however, there was no clear evidence of any overshooting of the voltage when it dropped from the higher level to the lower level.

As the predicted voltage overshoot is thought to be due to the non-instantaneous mass transfer re-equilibration [229], it is not entirely surprising that this effect was not seen for the much smaller micro-tubular cells.

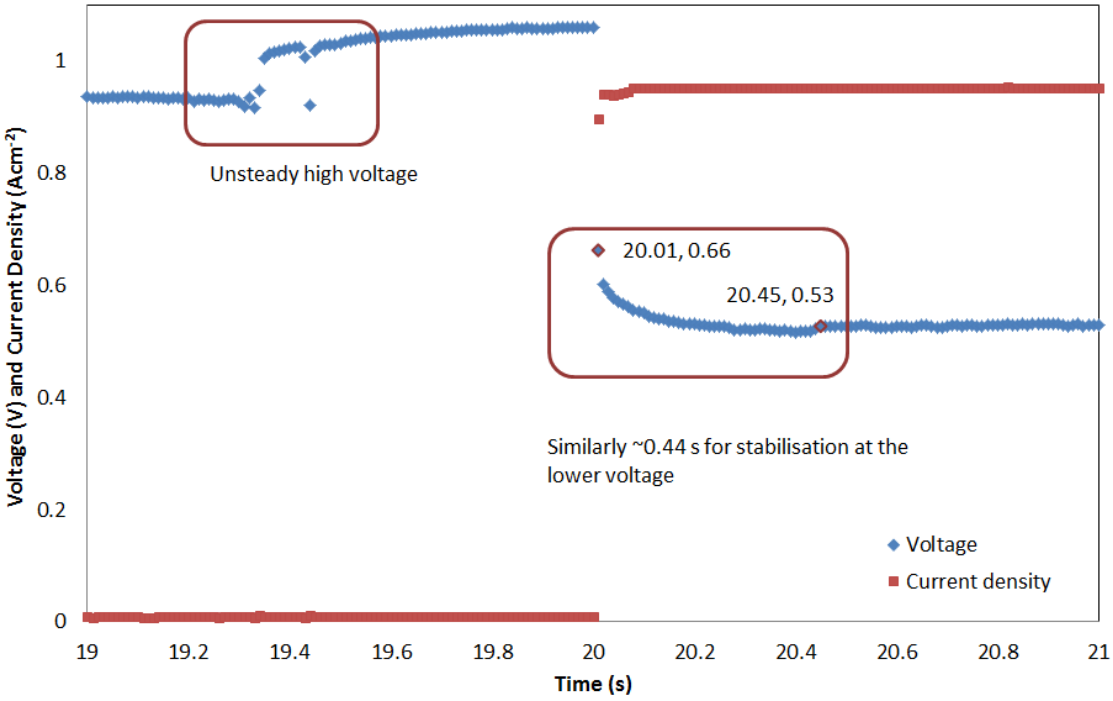

Figure 59 - A close-up showing the unsteady high voltage in 0.99 A current-controlled steps (AMI-5.5 µSOFC, 100 Hz data sampling, 750°C, 20 ml/minute H_2)

Even at resolutions of 0.001 s, admittedly for a significantly smaller step (Figure 60), no overshooting was observed, but rather a slight smooth curve down to the new voltage. The level of random noise in this system hides any effect if it is present. As such, it can be concluded that this overshooting effect is negligible for µSOFCs of this type. Porosity and tortuosity are also vital factors for mass transfer, so electrode thickness alone is not a sufficient guide – effects with a different cathode (identical anode and other cell dimensions) are described later in this section and discussed in Section 4.5.4.

The cell was then tested with sets of square pulses of the same magnitude (0.2 A) ranged over the breadth of the IV curve. The current-controlled profile used is shown in Figure 61 below. This run was repeated five times to check for consistency, and two sample runs are

shown in Figure 62. The most variation and deviation from straight line steps is seen at the highest voltage end of the spectrum. Although the step from the high-current end of the preceding IV curve to the low-current, high-voltage start of the pulses could explain the initial noise, the second step is also distorted, suggesting that the position on the cell's range also has a significant effect. Further work investigating reversal of the order of these steps would be interesting, but was not a priority for the SUAV project so was not pursued.

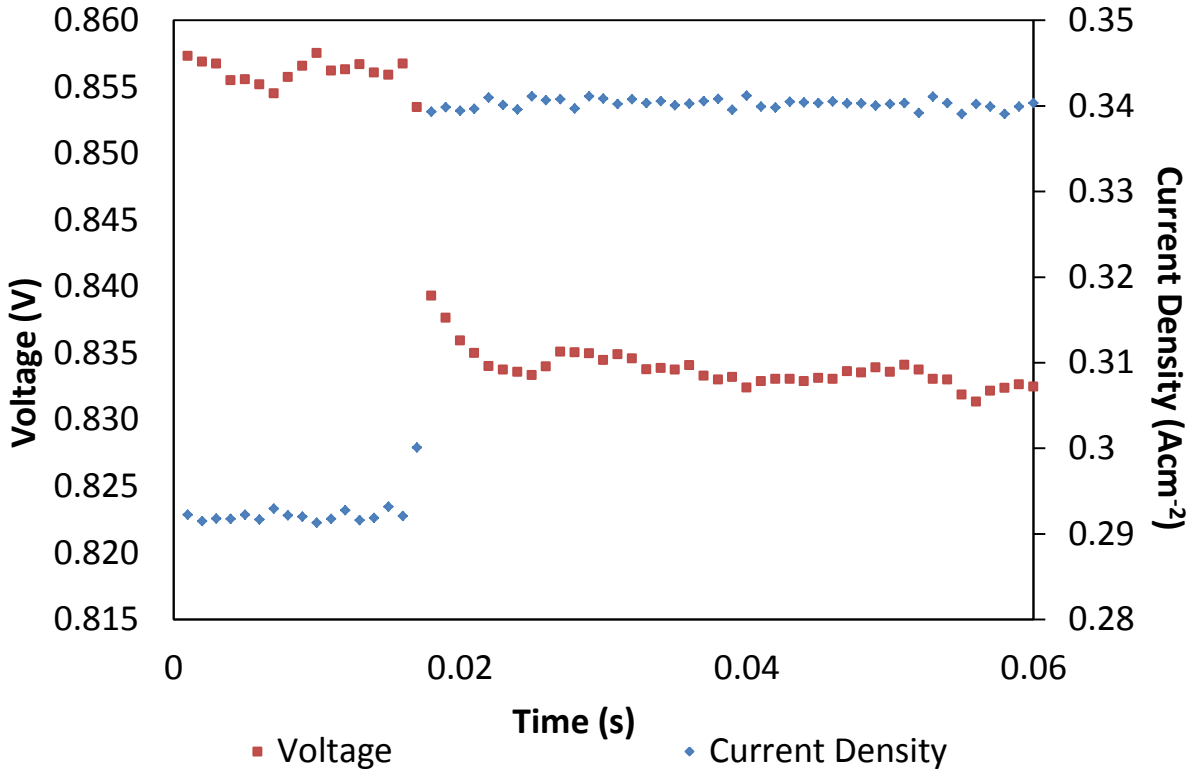

Figure 60 - Data checking for voltage overshoots in an I-V curve segment for an AMI-5.5 µSOFC (1000 Hz data sampling, 750°C, 20 ml/min. H_2)

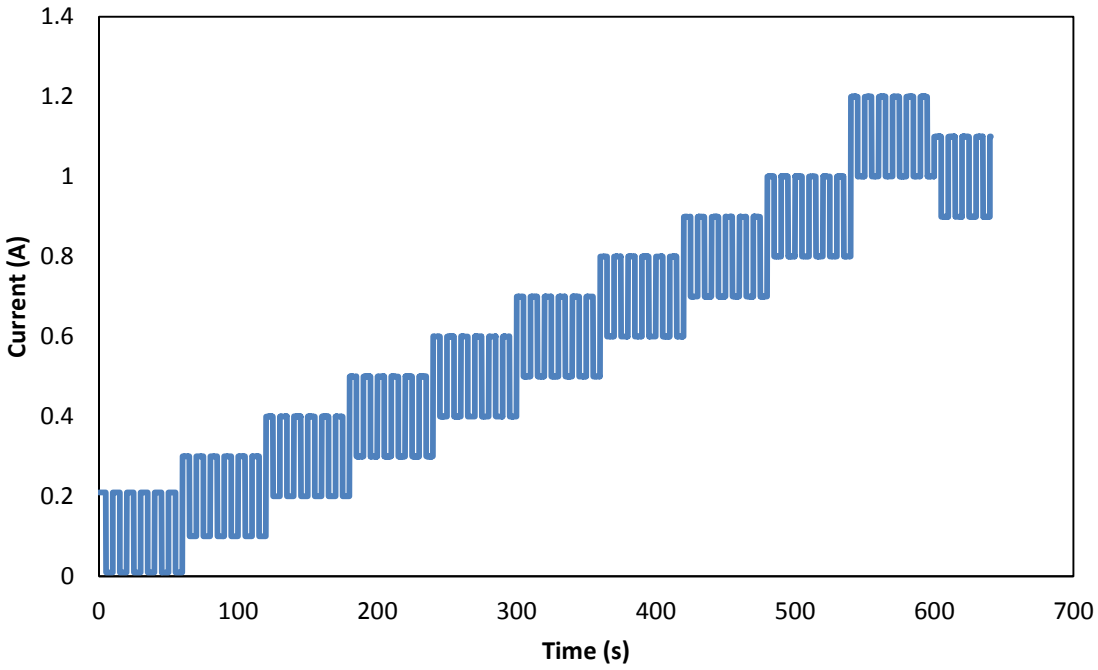

Figure 61 - The current-controlled profile used for transient tests of AMI-5.5 µSOFCs

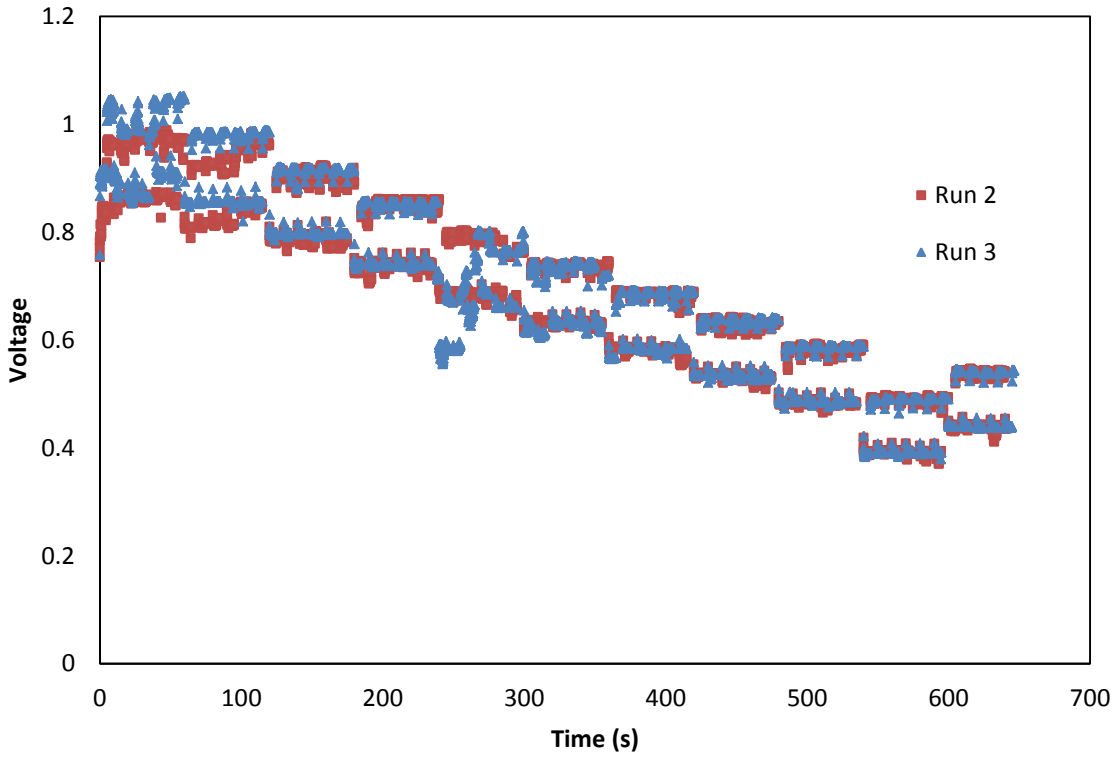

Figure 62 - Sample runs of step-changes in current across the voltage range (AMI-5.5 µSOFC, 750°C, 20 ml/min. H_2)

By contrast, transient performance of the dip-coated cells tested later (see Chapter 6) was much weaker, having a recovery time of 10-15 seconds and also showing the over-shooting behaviour predicted by Achenbach [227] amongst others. A different test profile was used for these cells as their performance was not strong enough to run the previously used programme. The same principle of current-controlled square pulses was used, however. A standard example of this is shown in Figure 63.

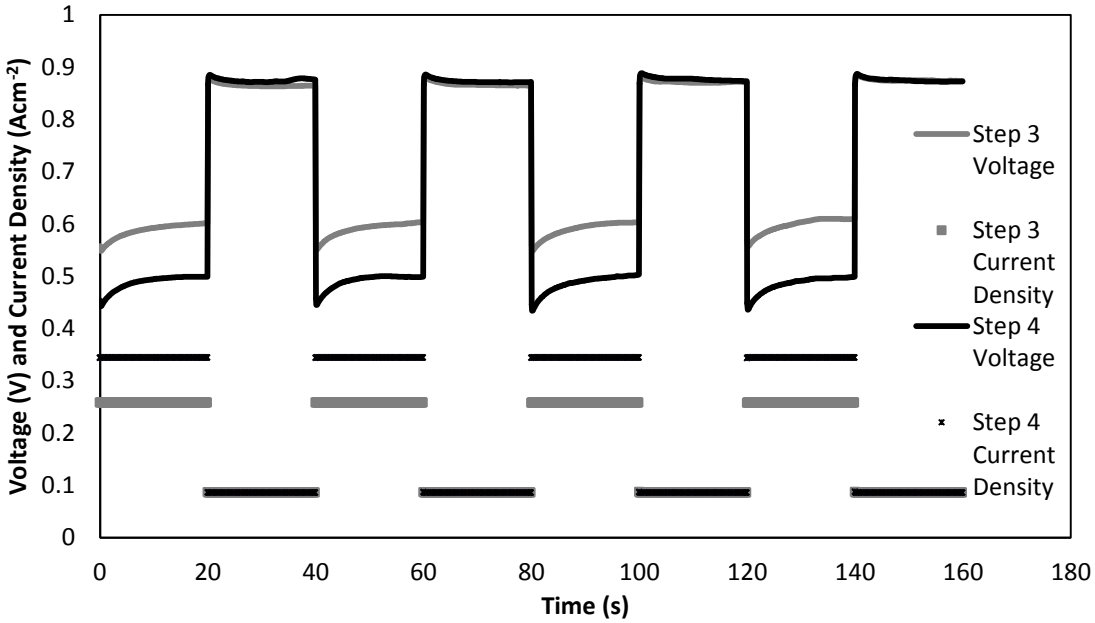

Figure 63 - Transient results for dip-coated AMI-5.5 µSOFCs; the current was controlled, hence showing almost perfect square pulses, the voltage shows under- and over-shooting (all at 750°C, 20 ml/min. H_2)

The size of the over-shoot is seen to increase with step size, as also shown by Bhattacharyya *et al.* [229], whereas the recovery time is unaffected. The increased overshoot on a step down in voltage as opposed to a step up also agrees with their modelling and experimental data. This suggests that the dip-coated cells take significantly longer to redistribute gases after a step change than the brush-painted cells did, possibly due to a difference in cathode structure (discussed below).

4.5.4 Discussion

Mass transfer in the porous electrodes is dominated by gas diffusion [217], so the diffusivity of the gas in the porous electrode and the electrode thickness should be related to the dynamic response time if this is a limiting factor, as hypothesised. The dip-coated cathodes, although thinner than the brush-painted cathodes (around 8 µm rather than 21 µm), were much less porous (see Figure 64), which may explain the slower readjustment time. Unfortunately accurate values of porosity, pore diameter and tortuosity of the cathodes are unavailable (both for my cells and in the rather limited literature), making a direct comparison of effective diffusion coefficients impossible.

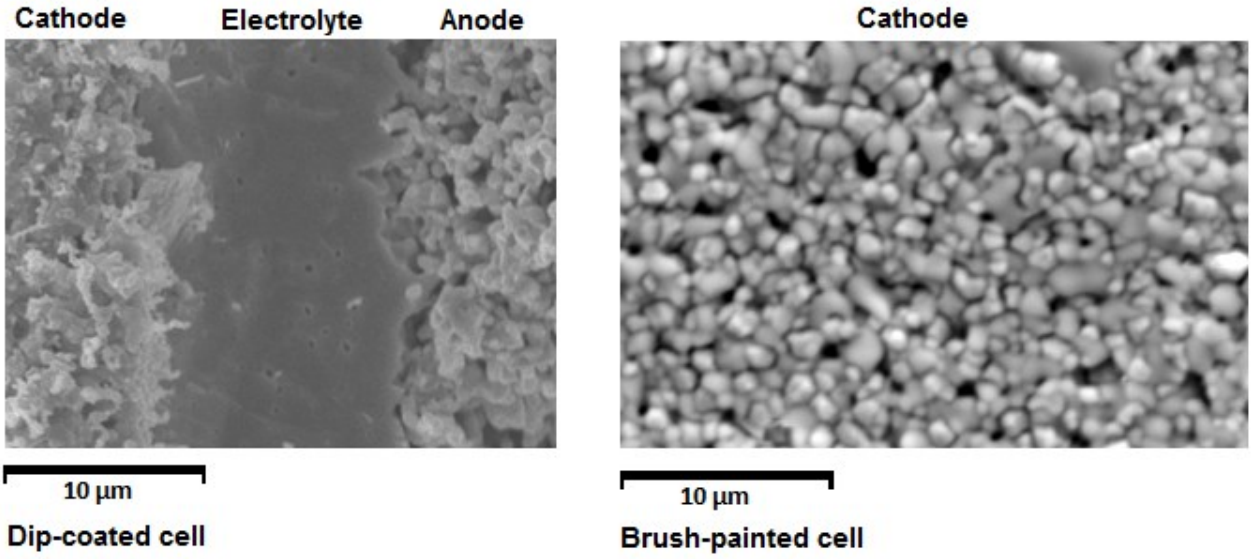

Figure 64 - SEM images of dip-coated and brush-painted AMI-5.5 µSOFCs made with the same ink recipe. The image of the brush-painted cell was kindly provided by Lina Troskialina

Previous work [229] suggests that Knudsen diffusion effects are behind the overshooting seen. Knudsen diffusion occurs when the mean free path of the molecules is comparable to the length scales of the system in which the molecules are moving; i.e. the pore diameters. Knudsen diffusivity is defined as shown in Equation 4.1.

$$D_k = 4850 d_{pore} \sqrt{\frac{T}{M}} \quad \text{....(Eq. 4.1)}$$

The constant factor in Equation 4.1 comes from the kinetic theory of gases [231], d_{pore} is average pore diameter (cm), *T* is temperature (Kelvin) and *M* is molecular weight (g/mole).

As the operating temperature, anode structure and reactant gases used were the same for both the brush-painted and dip-coated cells, there must be a difference in average pore diameter in the cathode if Knudsen diffusion is responsible for the overshooting seen only with the dip-coated cells. More specifically, for Knudsen diffusion to be significant, the average pore diameter in the dip-coated cells must be smaller than that for the brush-painted cells, and around the mean free path length for oxygen or lower (2.2 μm at 750°C, under atmospheric pressure).

As can be seen in Figure 64, the pores in both cathodes are in this small size range, and the dip-coated cathode does have smaller pores than the brush-painted cells. Effects of Knudsen diffusion would therefore be expected to be present for both types of cells, although more significant for the dip-coated cells. In the experiments performed, the overshooting was only seen for the dip-coated cells. If there is an overshooting effect on the brush-painted cells, it must either happen on a timescale too short for the data sampling rate used (1000 samples per second at the highest rate), or be of small enough magnitude that it is not visible within rounding errors of the apparatus used. The overshoot lasted around ten seconds for the dip-coated cells; a difference in time constant of five orders of

magnitude is too large to be explained by pore size effects, given that the pores in the brush-painted cells have diameters ≤2 µm, making sampling rate issues unlikely. An overshoot too small to be detected is possible, however; the approximate pore size in the brush-painted cells is not much below the mean free path length of the gas, so a very small effect is likely. More accurate apparatus (capable of accurately and repeatably detecting micro-Amp levels of perturbation), multiple repeats and more *in situ* thermocouples to check temperature uniformity would be required to pursue this.

Returning to thermal equilibration timescales, these will mainly depend on the thermal mass of the cells. Given that the basic cell materials used are the same in this work and in the literature used [226, 227, 229, 230], the heat capacities should be very similar, leaving the mass as the differentiating factor. To a first approximation, some proportionality between mass and adjustment time would be expected if heat transfer was the limiting factor in both cases.

Unfortunately experimental data in this area is very limited, but it can be seen (Table 7) that although the ratio of thermal mass to adjustment time is similar for the two models that list thermal effects as the main cause of the lag [227, 228] (no experimental verification given), there was nearly two orders of magnitude difference between that ratio and the ratio obtained experimentally. The similarity of the two values from the models, despite the huge difference in cell type, lends support to the approximation of proportionality between mass and response time.

Table 7 - Mass and power adjustment times following step changes for SOFCs – assessing transient performance

		Mass (g)	Approximate adjustment time (s)	Ratio (mass/time)
Cells tested here	Experimental	0.52	0.4	1.30
Bhattacharyya [229]	Experimental & Model	?[a]	0.6	≥1.7[a]
Achenbach [227, 230]	Model	16.5[b]	200	0.08
Serincan [228]	Model	0.15[c]	20	0.01
a: insufficient data to give a mass, but cell probably at least twice the size of the µSOFCs used in house, based on current and maximum reported areal current densities b: approximate value estimated from stated density and rough dimensions as a range of thicknesses (and therefore of masses) was modelled, although this was not the focus c: estimated from dimensions, porosities and rough densities				

4.5.5 Conclusions

Mass transport limitations are shown to be the most likely dominating factor in the transient response of the tested µSOFCs due to the timescales for adjustment observed, as the timescales for thermal re-equilibration are longer. The overshooting seen with the cells with much smaller pores in the cathode lends support to the statement by Bhattacharyya *et al.* [229] that Knudsen diffusion is responsible for the overshooting seen on rapid load changes, although more tests with a wider range of more accurately controlled pore sizes would be needed to prove this hypothesis. Overall, this transient response was much better than expected from previous work and general opinion. This is hypothesised to be due to the smaller sizes (both in terms of electrode thickness and gas channel dimensions) making mass transport transients much more short-lived. The short response time should facilitate load balancing in real-world situations, although the near-instantaneous response of a battery will still be needed to smooth the output.

5. INTERCONNECTIONS & STACKING

5.1 Manifold Design and Stack Testing

A gas manifold is used to supply fuel to the individual µSOFCs in a stack from one supply pipe. In µSOFC stacks, an even gas supply is needed to each cell, but it is impractical to have a valve for each. As such, manifolds must give even flows to several tubes from the same valve-controlled feed-pipe. Modelling of fluid flow in various injection manifold designs was therefore performed. COMSOL Multiphysics™ was chosen due to ease of use and past experience in the group. Rough calculations of Reynolds numbers using Sutherland's law to find the viscosity ([232] and Equation 5.1) confirmed that the system falls well within the laminar regime, so turbulence models were not needed. Experimental constants from the literature and conditions chosen are detailed in Table 8.

Table 8 - Parameters for gas manifold modelling

Material properties & boundary conditions	**Value/Property used**
Fluid - Hydrogen	
Density (assumes standard conditions)*	0.09 *kg/m3*
Dynamic Viscosity (assumes 750°C and Sutherland's formula)†	1.9×10^{-5} Pa.s
Initial Conditions	
Pressure	101325 Pa (1 atm.)
Fluid velocity	0.0 m/s
Boundary Conditions	
Inlet	Velocity (0.19 m/s‡, normal to inlet)
Outlets	Pressure, no viscous stress (101325 Pa)
Walls	Wall, no slip.
*Standard conditions density is higher than that at the operating temperature, therefore this gives an upper limit to the Reynolds number with respect to density † Factor of 2 smaller at RTP; Reynolds numbers remain firmly in the laminar regime ‡Speed used currently; can easily be adjusted	

$$\mu = \mu_{ref}\left(\frac{T}{T_{ref}}\right)^{3/2}\frac{T_{ref}+S}{T+S} \quad \text{....(Eq. 5.1)}$$

Where μ is the viscosity (Pa.s), T is temperature and S is the Sutherland temperature (both in Kelvin). The "*ref*" subscript indicates a reference temperature at which the viscosity is known.

A modular stack design is being considered in this project, so that individual modules can be removed and replaced if required should a cell fail, rather than requiring replacement of the whole stack. Various potential designs for the gas manifold for a small module, or sub-stack, are discussed below and the optimal design for the problem at hand considered.

5.1.1 Modelling

Three basic designs were tested; namely injection blocks, where several tubes are connected to one hollow block, "gentle" branches and staggered branches (see Figure 65). Plots were then made of the outlet velocity profiles for cross-sections of these designs; an even gas flow to all tubes is the target. The injection block design has the advantage that it allows the incorporation of outlet gas recycling more easily, as an anode off-gas feed-pipe can easily be connected to the hollow block, making it a mixing chamber.

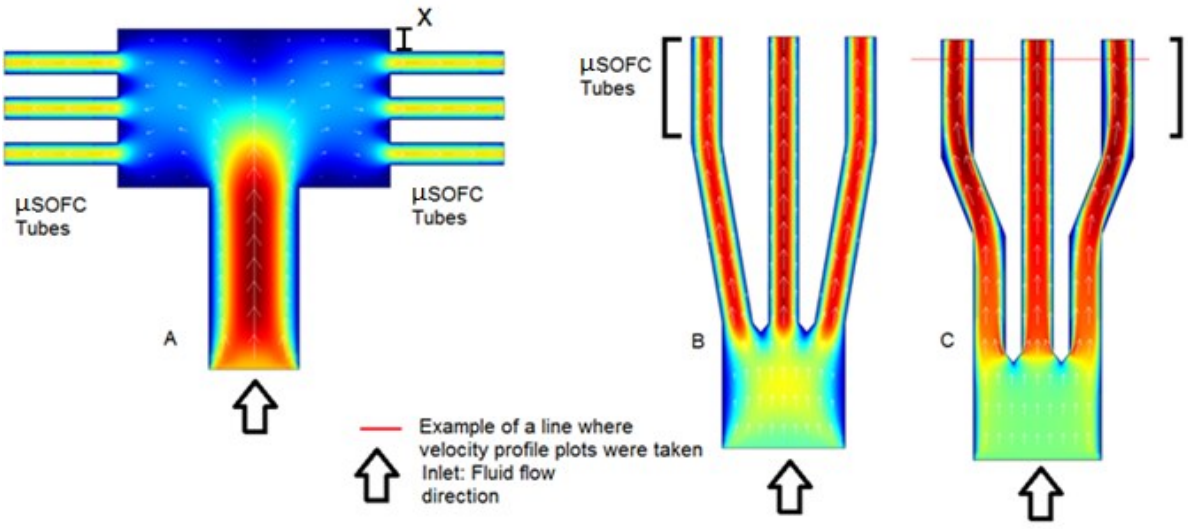

Figure 65 - Injection manifolds. (A) Injection block, (B) "gentle" branches, (C) staggered branches. The scales show flow velocity (redder being faster flow); the scale is different for A, although the same for B and C. Inlet flow rate can be adjusted to give the desired outlet flow based on these model calculations

Overall, it was found that gentle branches (B) gave a more uniform set of velocity profiles than staggered branches (C) (see Figure 66), and that having an injection block wider than the edges of the outer-most tubes (distance X in Figure 65 A>0) helped to reduce the range in velocity peaks (Figure 67). With branching designs, the central branch has a slightly higher peak velocity if no baffles or narrowed necks are used. This is a trade-off between ideal performance and complexity of design.

These results made it clear that an injection block based design would be more sensible than a splitting-pipe based design, as the flows in the tubes have been shown to be more even. A small module with an injection block was then built and tested.

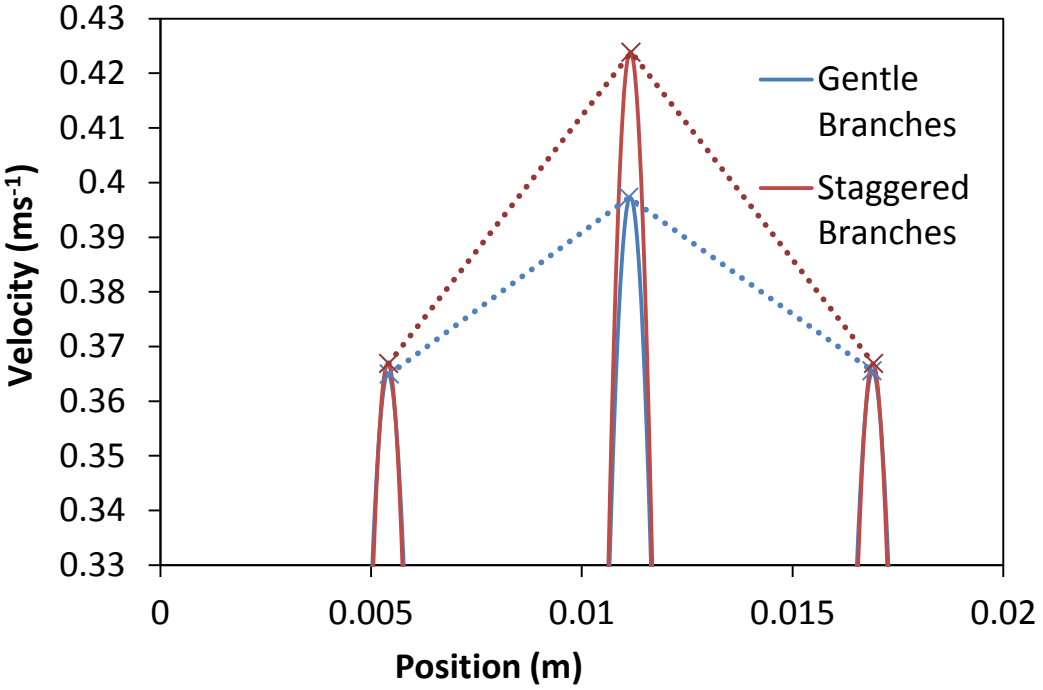

Figure 66 - Comparing branching manifolds: velocity profiles across the tubes

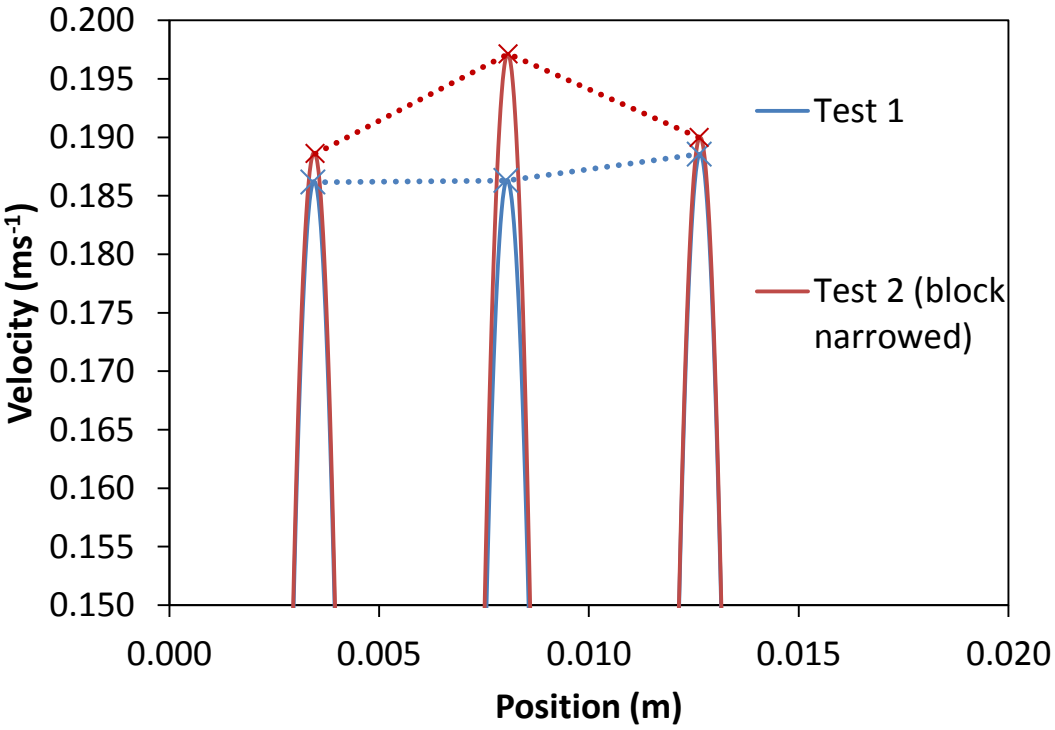

Figure 67 - Comparing injection block designs: velocity profiles across the tubes

5.1.2 Testing

This section is based on work previously published elsewhere by the author [7]. A six-cell module was designed and built using Thompson's design [72]; this is shown in Figure 68.

A Macor™ ceramic injection block was used to supply the hydrogen as this had been shown to give more even flows than a branched injection pipe by the modelling performed. This was tested in two configurations – all cells in series, and all cells in parallel. The cells were also tested individually to check for any cells with poorer performance which could have a negative impact on stack performance.

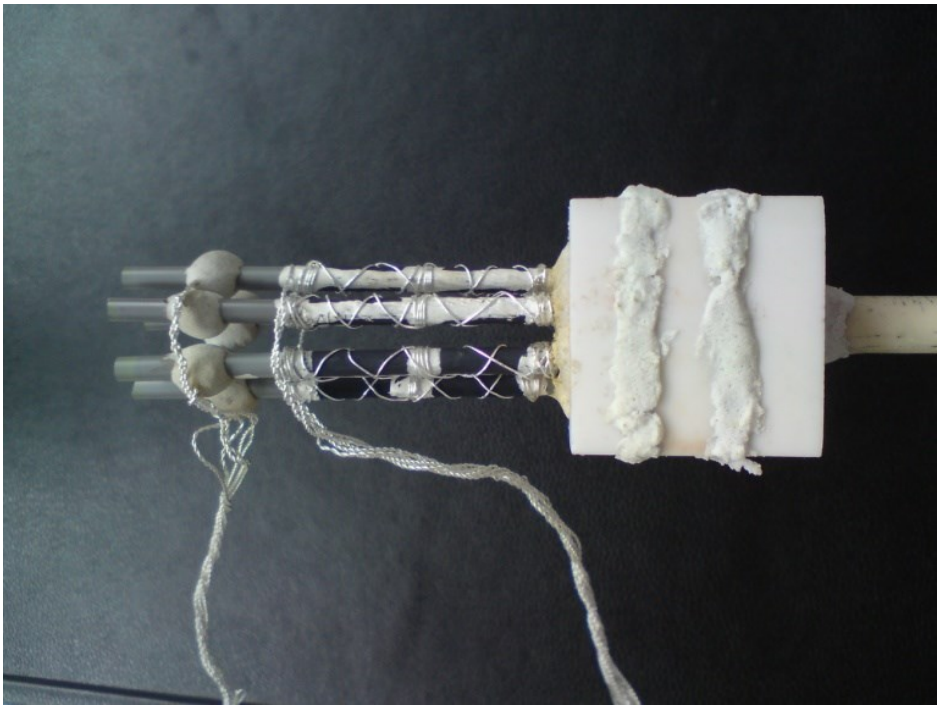

Figure 68 - A six-cell module - AMI-5.5 µSOFCs

[7] **Relevant Publications:**

Howe, K.S. and K. Kendall, *Transient Performance of Micro-Tubular Solid Oxide Fuel Cells and Stacks*. ECS Transactions, 2011. 35(1): p. 419-423)

Howe, K. S., Thompson, G. J., and Kendall, K., 2011, "*Micro-tubular solid oxide fuel cells and stacks*," Journal of Power Sources, 196(4), pp. 1677-1686.

Steady-State Performance

Cells in Series

At 750°C with 100 ml/minute of hydrogen, the peak power was 2.77 W (fuel utilisation of 34%). Mass flow limitation is observed above 0.15 A/cm^2 (Figure 69). Running with a higher throughput of hydrogen might remove this power reduction, but would also lower utilisation and hence efficiency. IV curves recorded before and after five hours of testing (IV curves, the transient testing discussed below and three hours of constant voltage operation at 3 V, i.e. around 0.5 V per cell) showed no noticeable degradation (Figure 70).

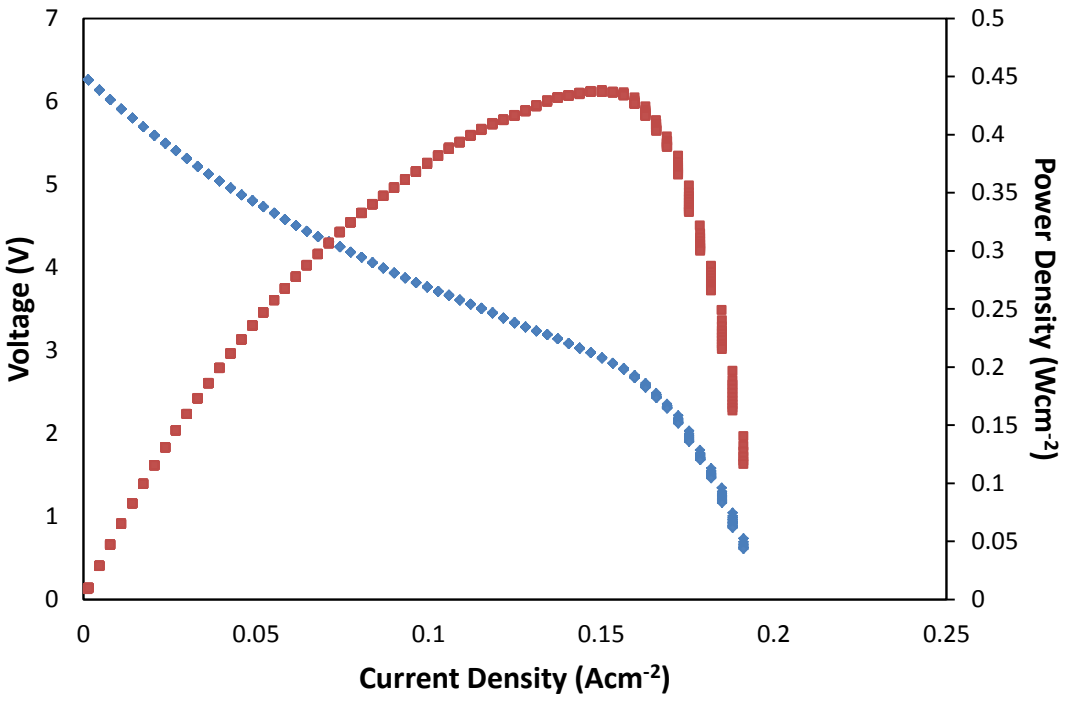

Figure 69 – I-V and power curves for six AMI-5.5 µSOFCs in series showing mass flow limitation (100 ml/minute H_2, 750°C)

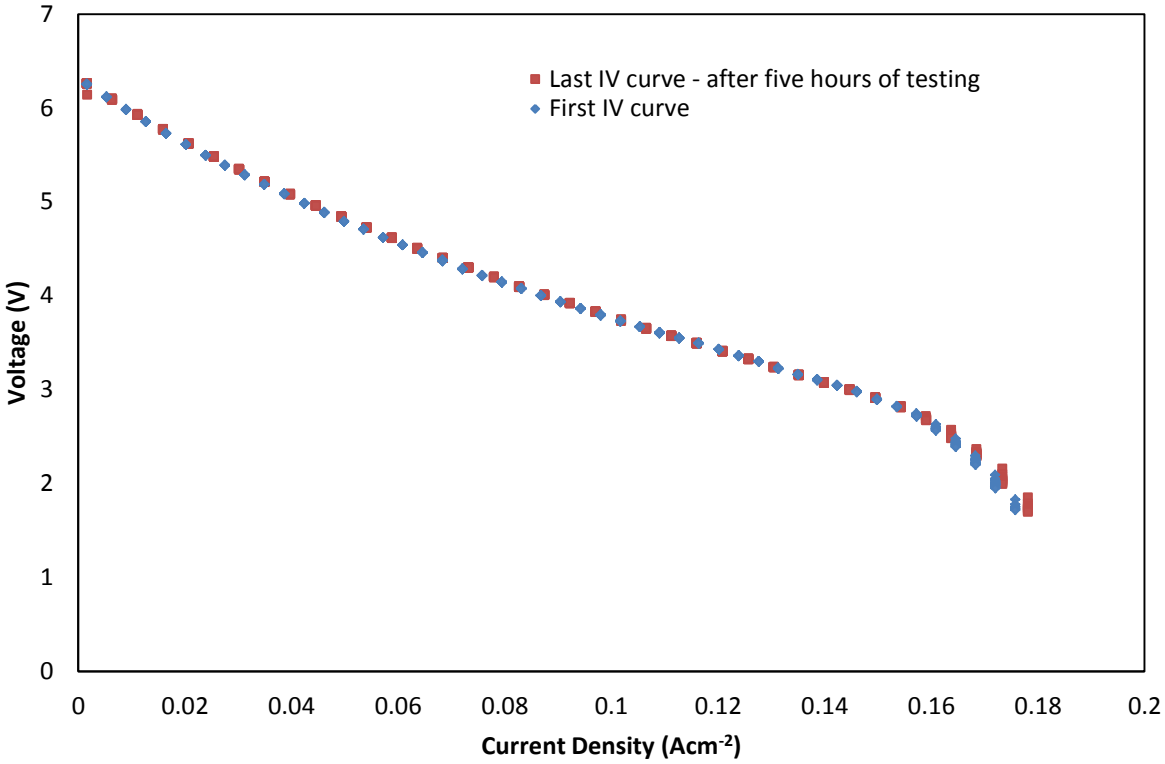

Figure 70 - I-V Curves for a stack of six AMI-5.5 µSOFCs in series before and after testing (100 ml/minute H_2, 750°C)

Cells in Parallel

Under the same test conditions (750°C with 100 ml/minute of hydrogen), the peak power was 2.04 W (fuel utilisation of 23%). This peak power is lower than expected, probably because the Solartron used cannot take currents higher than 4 A. An IV curve for a single cell from the same batch is shown alongside that for the module in

Figure 71; this suggests that the peak power may indeed be higher than this value, if the Solartron allowed higher currents. The current cut-off meant that the mass-flow limited section was never reached.

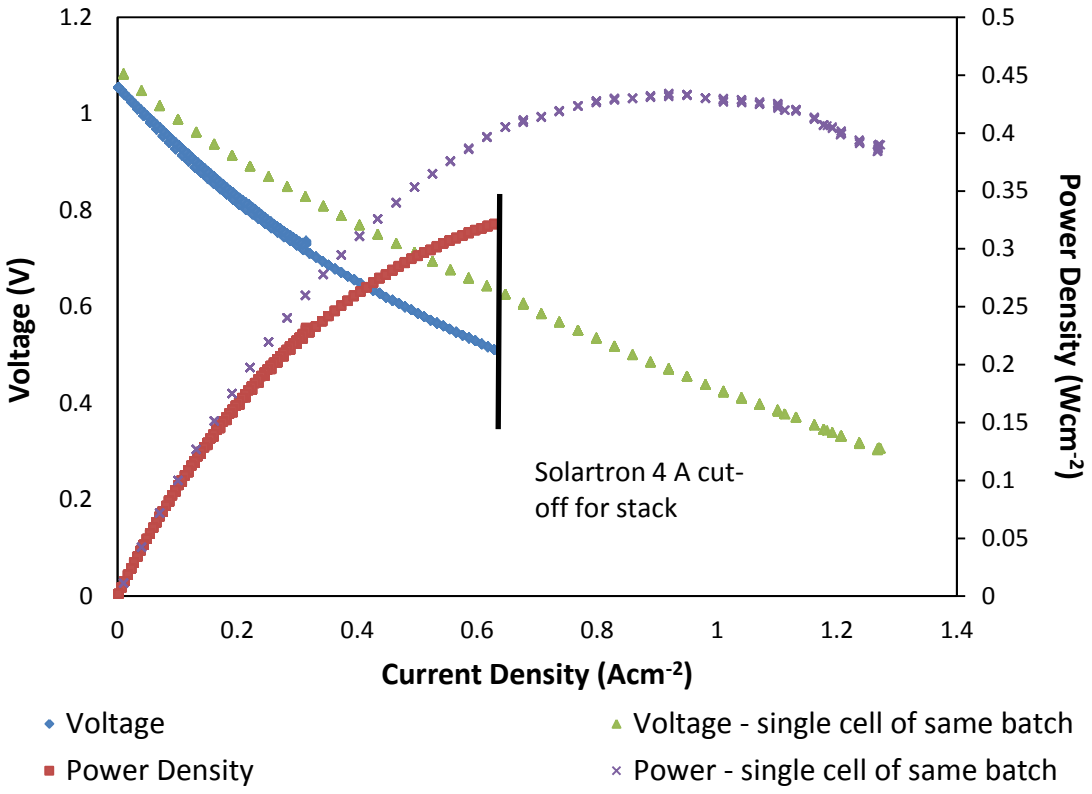

Figure 71 - IV and power curves for six AMI-5.5 µSOFCs in parallel (100 ml/minute H_2, 750°C)

Transient Performance

As for the single cell transient work performed (see Chapter 4), the module made of hand-painted µSOFCs was shown to have very strong dynamic performance:

- No over- or under-shooting of the voltage was seen, even when the steps in current were very large (70% of the maximum range).
- The readjustment time was 0.5 s for a single cell, but slightly higher at 0.6-0.8 s for the six-cell module.

There was no noticeable difference in transient behaviour between the two configurations; Figure 72 and Figure 73 show representative plots.

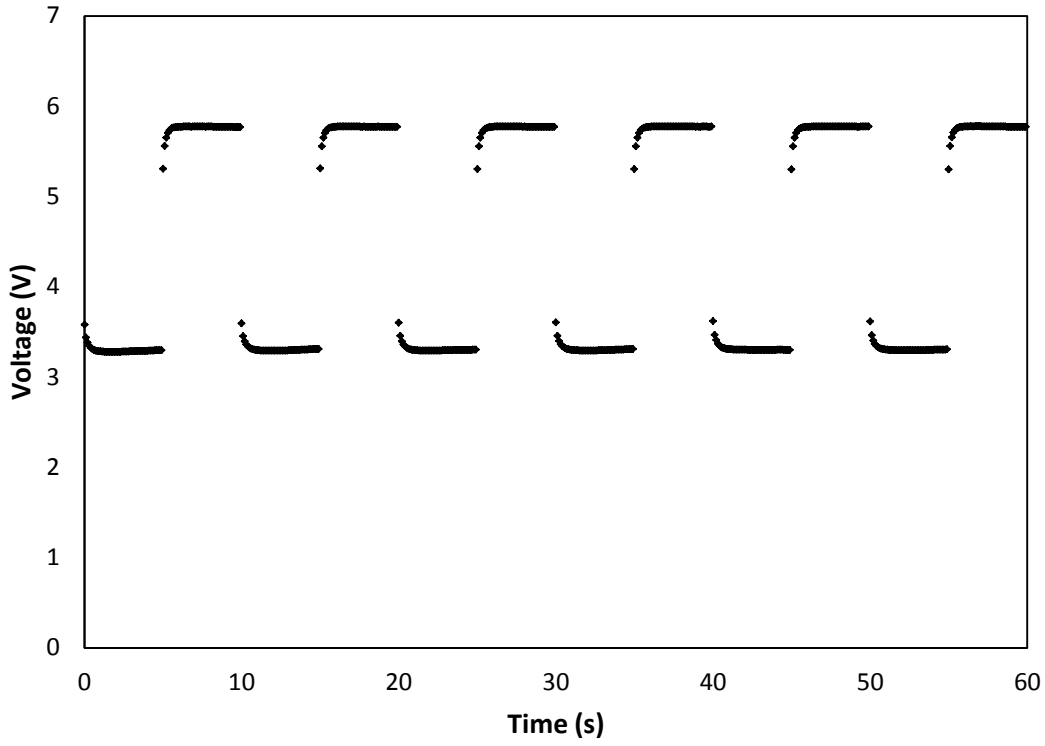

Figure 72 - 0.7 A magnitude steps for the series stack of six AMI-5.5 µSOFCs (100 ml/minute H_2, 750°C)

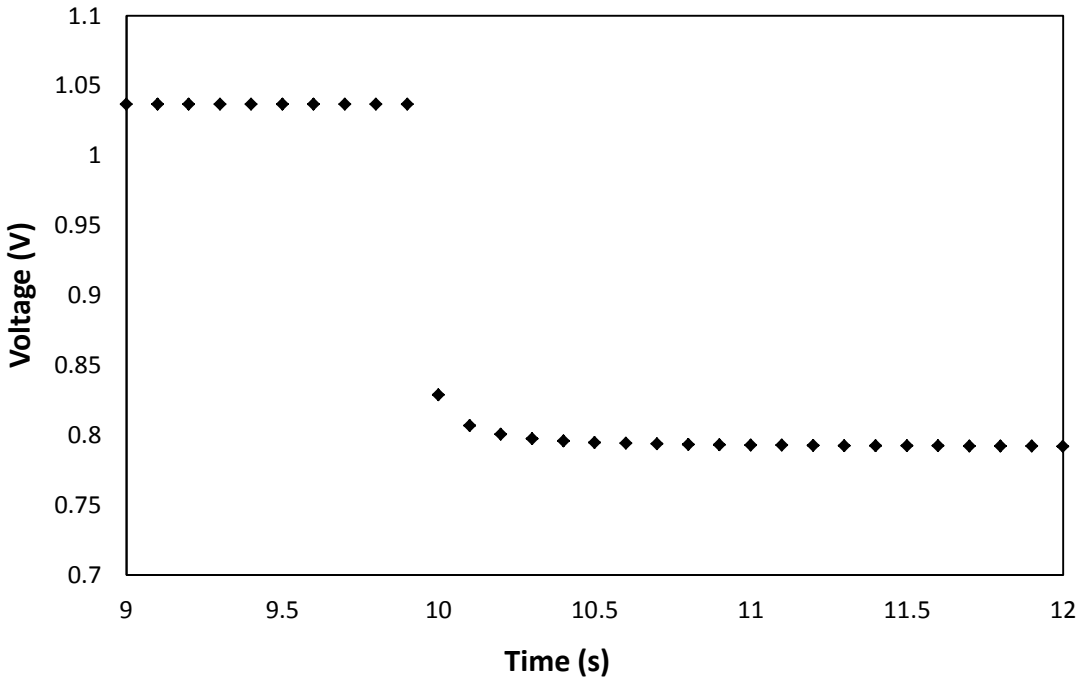

Figure 73 - 1.5 A magnitude step for the parallel stack of six AMI-5.5 µSOFCs (100 ml/minute H_2, 750°C)

5.1.3 Discussion

A six-cell module showed promising results, with performance only being slightly below that expected for the total output of six single cells. The dynamic adjustment time was also not much longer than that for single cells (0.6-0.8 s instead of 0.5 s).

The main issue for this stack design is the difficulty of making the interconnections. Although power density scales with the inverse of cell diameter, making wider cells less attractive, it was decided to move to larger diameter cells due to the interconnections being problematic. Fewer, larger cells will be needed for the same power, reducing the complexity of the interconnections and manifolding significantly. The same principles of mass flow and manifold design can be applied to the larger cells as the geometries are similar.

5.2 Interconnection Design

A brief review of the literature on cell connections is given, in the context of the new (larger) micro-tubular cells purchased. These new cells, type AMI-15.2 (see Chapter 3) come already reduced and with cathodes applied, but without interconnections.

5.2.1 The New Cells – AMI-15.2

At 15.2 cm in length and 6.6 mm in diameter (see Figure 74), the new tubes are significantly larger than those used previously. The anode and electrolyte are very similar (NiO-YSZ anode, with a thin YSZ electrolyte covering the full length), but the cathode is different. The

black layer is an LSCF cathode, which should have higher performance at lower temperatures than an LSM cathode (see Section 2.2 Materials Used). The durability, and so life-time, of LSCF is thought to be inferior to that of LSM [103], but Ultra-AMI state at least 20 flights before failure[8], which is sufficient for the project at hand.

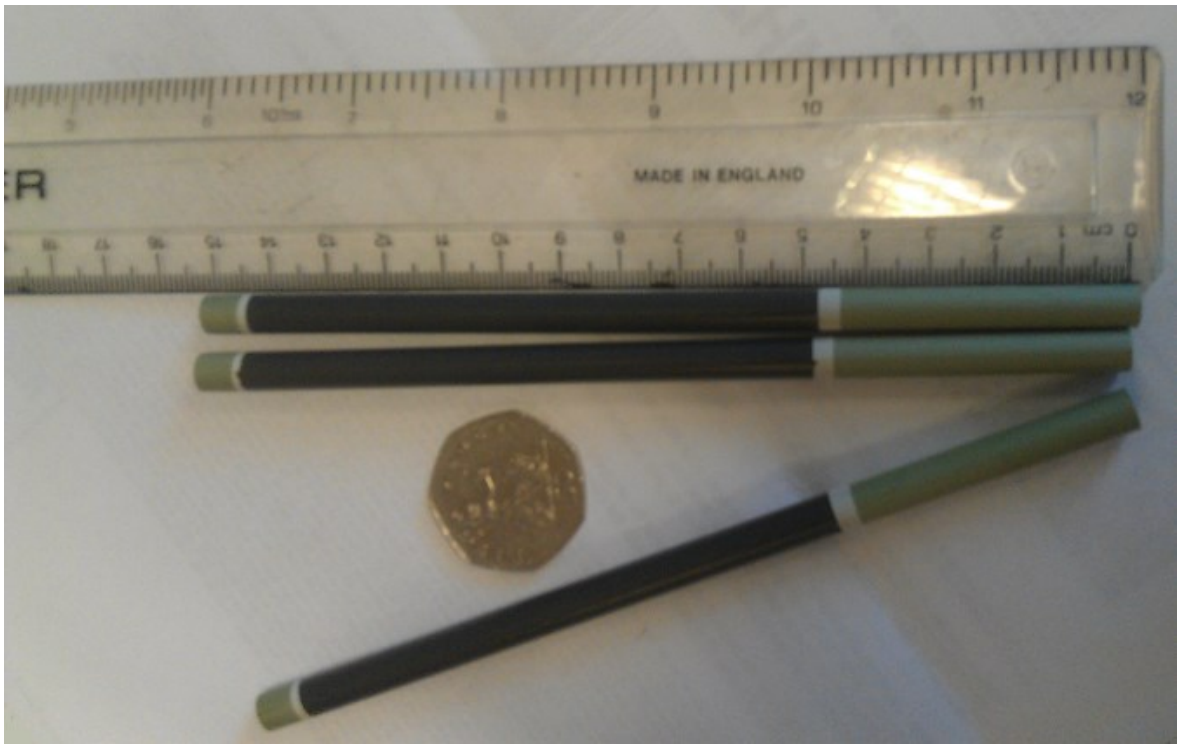

Figure 74 - New, larger Ultra-AMI µSOFCs - AMI-15.2 µSOFCs (un-reduced)

As LSCF and YSZ can react to form unwanted phases such as $SrZrO_3$ [233] when in contact at 700°C or above, a barrier layer is needed. The white layer (samaria-doped ceria, SDC) is this barrier layer (see Figure 75). These different layers were imaged and measured using SEM and EDS imaging (see Figure 76).

[8] Ultra-AMI have not publically stated the cause of failure; this may not be due to the cathode

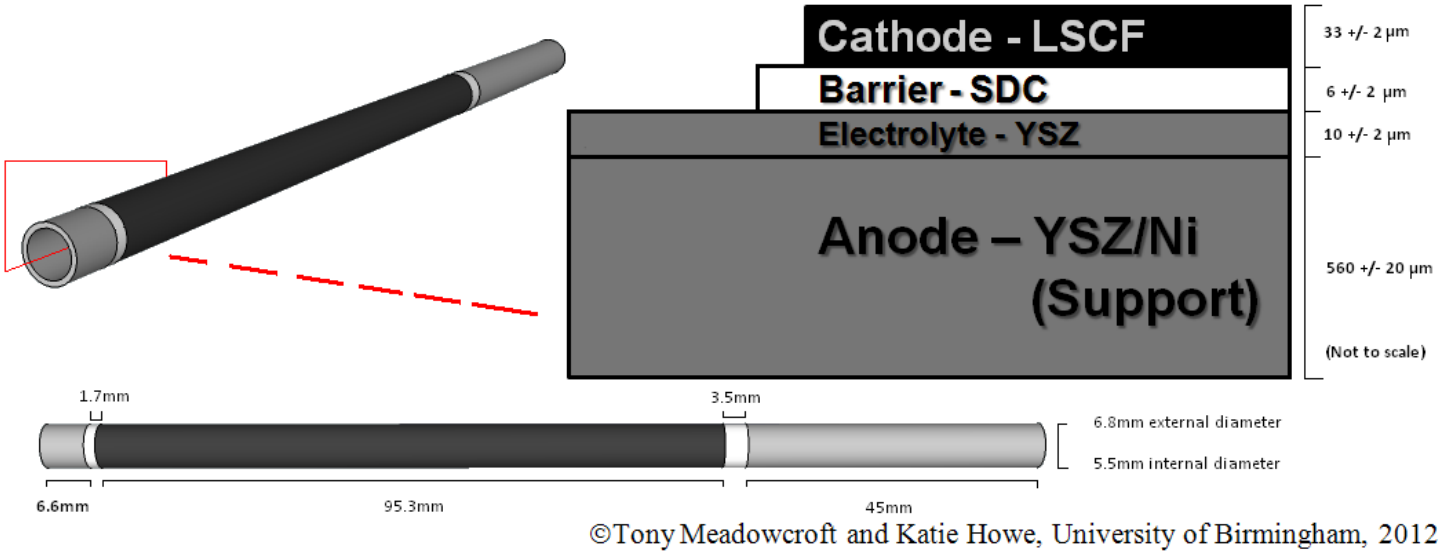

Figure 75 - Ultra Electronics-AMI tube schematic (AMI 15.5 µSOFC)

The cathode and barrier layer are almost indistinguishable in the SEM image (A), but are clearly visible when elemental analysis is used to map the same area.

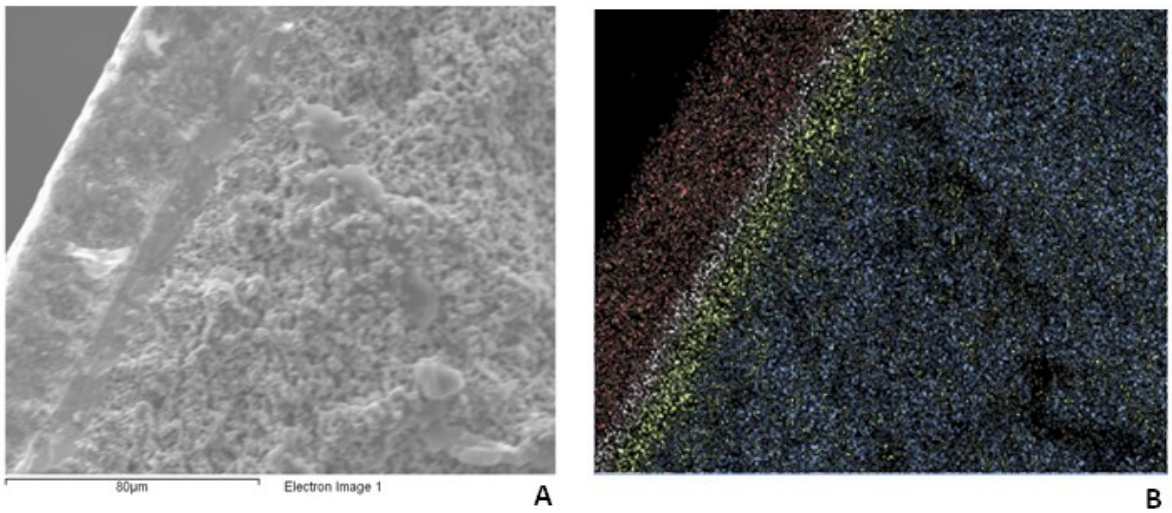

Figure 76 - SEM (A) and EDS (B) images of AMI-15.2 µSOFC cross-section. (La in red, Ni in blue, Ce in white, YSZ in green)

FIB-SEM analysis of the cathode was also undertaken as the initial SEM image (Figure 76 A) suggested that the porosity is lower than that of the in-house cathodes made previously. A trench was etched in the cathode with the ion beam, and then polished. The images taken

were then binarised and coloured, as shown in Figure 77. The number of blue pixels (representing voids) was then taken as a percentage of the total number of pixels in the area to calculate the porosity. A value of 18.8±2.7% porosity was found, which is indeed lower than was expected.

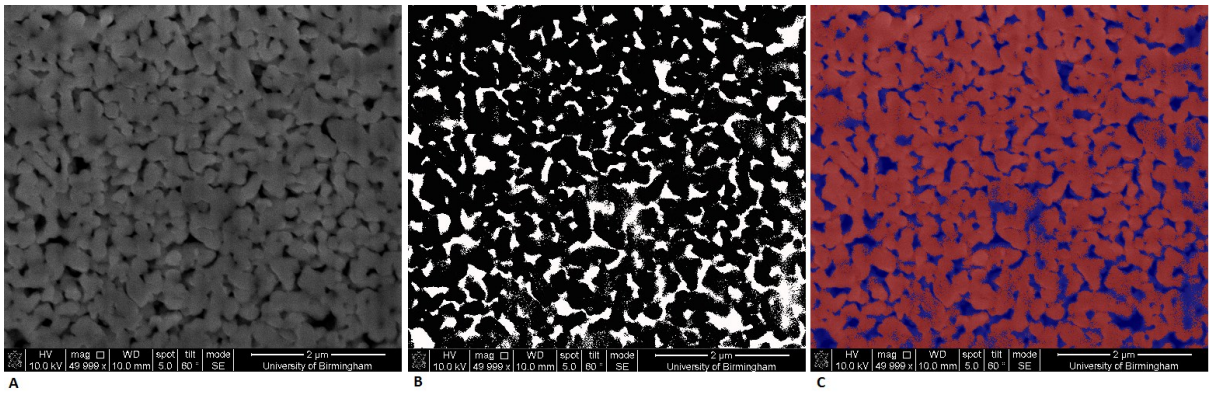

Figure 77 - FIB SEM images of AMI-15.2 µSOFC cathode (a) initial SEM image following FIB etching, (b) binarised image with material in black and pores in white, (c) colourised image, with the pores in blue - image processing courtesy of James Courtney

5.2.2 Designing Interconnections

As the new cells are larger and longer, more connection points and/or better conductivities along the anode and cathode will be needed to keep the resistance low. A new interconnection design is therefore necessary. Designing an interconnection that can more easily be used in stacks would also be very beneficial.

Modelling work [234] has shown that, if just one connection is taken from each electrode, it is better to have these at the same end to minimise resistance, especially as cell length increases. This confirms earlier in-house work. Having one connection at each end of each electrode is shown to significantly improve performance. Theoretically having more

connections would reduce resistive pathway length further, although making contacts to the anode in the middle of the tube is non-trivial.

Several very different interconnection designs are known. The in-house technique [203], using an external coil of wire for the cathode and etching away a small section of the electrolyte to take the anode connection from the outside, is simple and effective and has been used elsewhere. Small variations on this are used, for example [57], with some groups still attaching the anode connection wires internally, which has been shown to increase the risk of contact failures [203]. Internal wire coils and mesh and pin arrangements have both been tried [203] but tend to slip on thermal cycling, leading to loss of contact. Although taking the anode connection from a single, external, point increases the resistive pathway, the reliability is greatly improved as compared to these internal coils or meshes [203]. Other designs from the literature are discussed below.

Sammes *et al.* [196] use a metal plate with two extended cylinders; one fits around the outside of the tube, making contact with the cathode, and the other slips inside, making contact with the anode. This allows for simple connection of cells in series forming planar layers (see Figure 78). Obviously the cells must be joined to this interconnector to prevent slipping on heating and cooling or vibration. In this work, brazing was used. Silver was chosen due to its thermal expansion being compatible with that of both the cell and the interconnection material and its melting temperature and conductivity being sufficiently high. The brazing procedure had to be conducted carefully under a controlled atmosphere

to prevent damage. This fabrication method therefore requires a larger number of carefully controlled stages than the in-house technique, and gives longer current collection paths for the cathode especially, but removes the problem of having many thin silver wires and provides an intuitive basis for a stack.

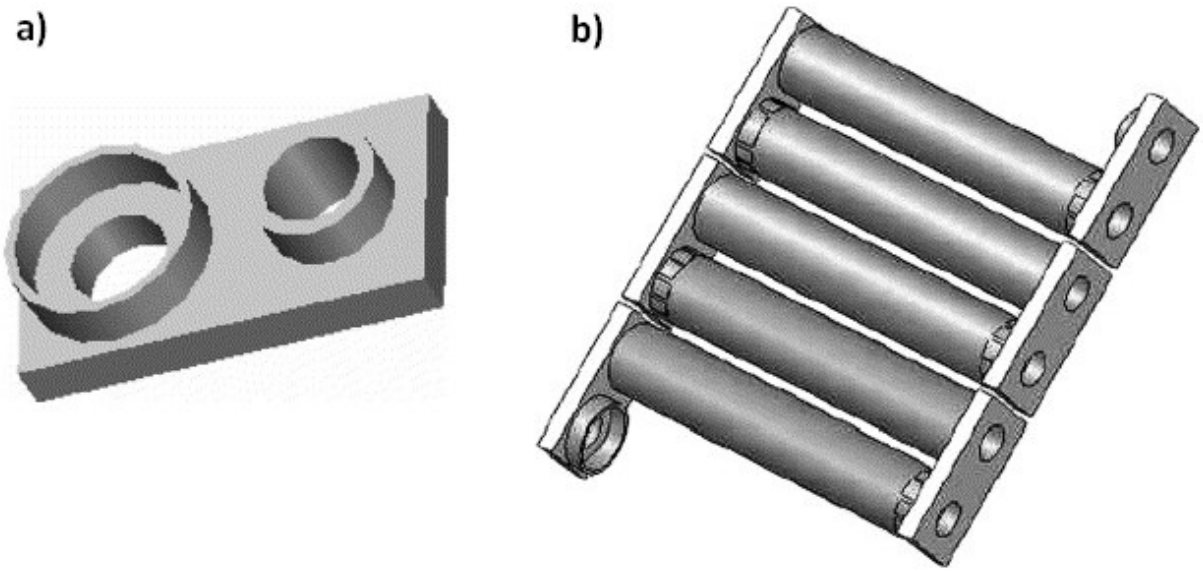

Figure 78 - Interconnection design: Sammes *et al.* [196] a) current collector and b) five µSOFCs arranged in series using this interconnection style

The honeycomb stack design shown earlier in Figure 15 [178] (interconnection design shown in Figure 79) loses the advantages of rapid heating and cooling of the µSOFCs due to losing the tubular shape. Conductive silver paste was used for both anode and cathode connections (around the outside surface of the honeycomb block for the cathode).

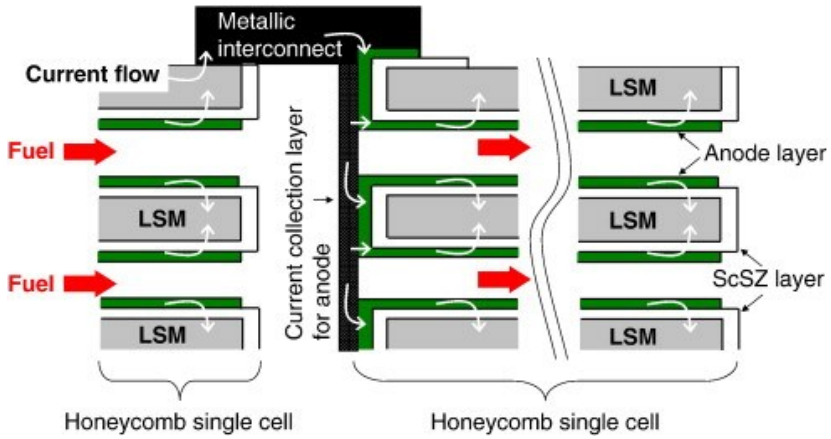

Figure 79 - Interconnection design: Yamaguchi et al. [178]

Conductive ceramic-based paste such as LSCF mixed with silver can also be used for the interconnections [179]; an example of this is pictured in Figure 80. This reduces problems of thermal cracking due to more similar expansion coefficients, but the conductivity is lower than for a pure metal. Conductive pastes have the advantage that, being easily made porous, more of the surface can be covered without losing significant amounts of active area.

With the longer cells, conductivity along the anode or cathode length is a much greater issue, and the use of woven or knitted wire meshes to increase conductivity has been patented [235]. Gür *et al.* [236] used woven silver and copper meshes on the cathode and anode, respectively, to ensure good conductivity, with wires connected to the meshes. Conducting spines [234] along both the anode and cathode have also been suggested to increase conductivity along the electrode. Combinations and variations of these techniques were tested with the longer tubes.

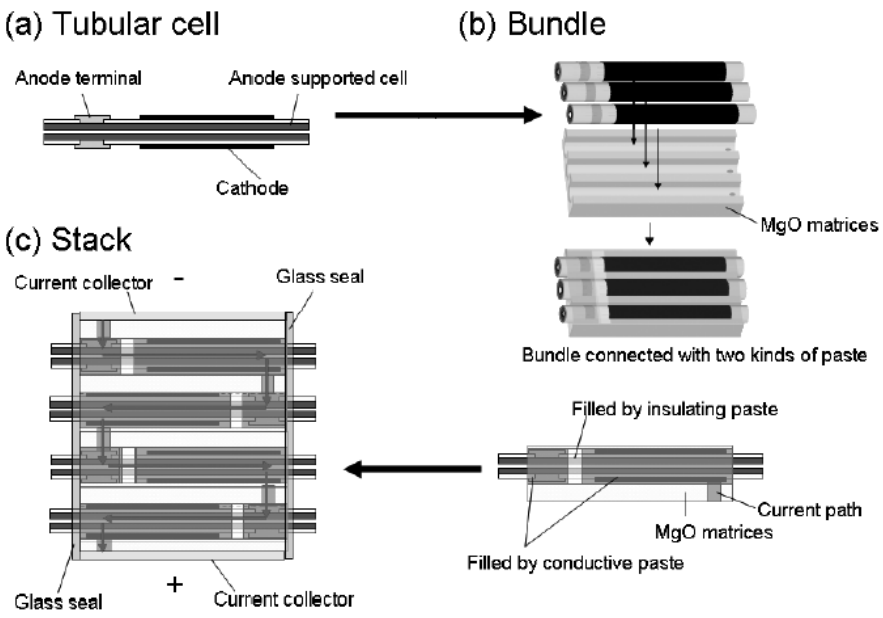

Figure 80 - Interconnection design: Funahashi et al. [179]

5.2.3 Testing

The new cells purchased from AMI are provided with the anode, electrolyte, barrier layer and cathode in place – all that has to be added are the interconnections. It was initially hoped that using the same interconnection style as the old cells would give a reasonable baseline performance, so a cell was prepared identically to the original µSOFCs (see Figure 18, earlier). This gave only slightly more total power than the small cell (0.8 W rather than 0.5 W), despite the significant increase in size. A larger number of interconnections was an expected requirement, as the longer cells mean that current paths along the anode and cathode are longer (e.g. 9.5 cm cathode length as opposed to the 3.5 cm length of the AMI-5.5 µSOFCs), and so resistance higher, for the same number, but this 0.8 W peak power was

much lower than the 7-8 W expected from manufacturer data in the same operating conditions [64].

Electrochemical Impedance Spectroscopy (EIS) was performed on a cell prepared with two anode connections (one at each end, hence halving the path-length), seven cathode connections and a coating of porous silver ink covering the cathode to reduce the lateral resistivity (all of these variables are discussed and investigated later in this chapter). The equivalent circuit model discussed in Section 3.4.2 Electrochemical Impedance Spectroscopy was used. Initial tests at various temperatures (Figure 81) confirmed that the series resistance (given by the distance between the origin and the point at which the plot first crosses the x-axis) is higher at lower temperatures – decreasing from around 0.31 Ω at a furnace temperature of 400°C to 0.11 Ω at 650°C. The majority of this resistance is due to the electrolyte, so a reduction of resistance at higher operating temperatures is expected as YSZ conducts oxide ions better at these temperatures.

It can be seen from the decrease in length on the x-axis between the initial and final curve intersections that the resistance in the electrode RC-pair(s) also decreases with increasing temperature. The increase in the frequency of the point at the peak of the arc with increasing temperature shows that the capacitance also reduces. From this plot it can also be seen that either the anode and cathode arcs overlap, giving one large curve, or one of the two is outside the frequency range tested, so not visible.

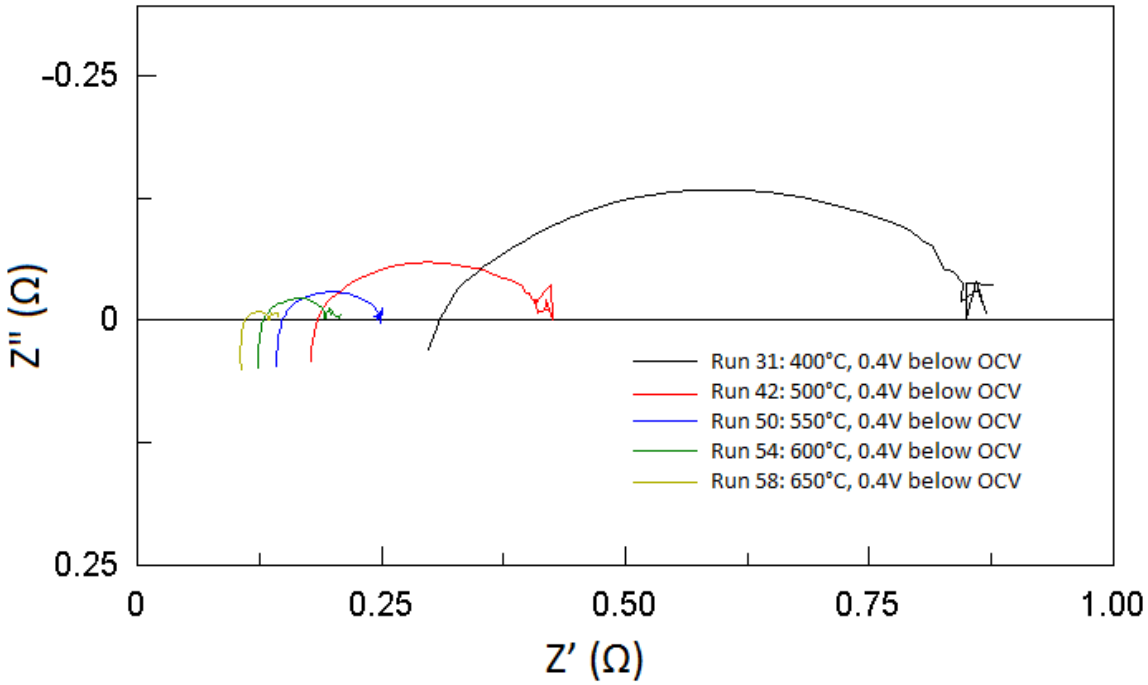

Figure 81 - Nyquist plots for the same AMI-15.2 µSOFC at various temperatures (60 ml/min. H_2)

Several constant voltage levels were then tested at the operating temperature (650°C furnace set point) and the plots are shown in Figure 82. As expected, the series resistance does not change. This plot confirms that the second electrode arc is present, but is near the low frequency limit of the test-range, so is not shown as clearly. The resistance and capacitance increase at higher voltages (lower currents), which could be due to activation barriers. The work of McIntosh *et al.* [148] found the anode semi-circle to be the one at lower frequencies; tests with different anode fuel gases or gas flow rates should confirm which is which.

Figure 83 shows the results of trying different hydrogen flow rates at the same voltage level (0.4 V below OCV). The anode would be expected to show better performance (i.e. lower

resistance and capacitance) at higher flow rates. The data therefore suggest that the lower frequency arc (on the right hand side of Figure 83) is indeed from the anode.

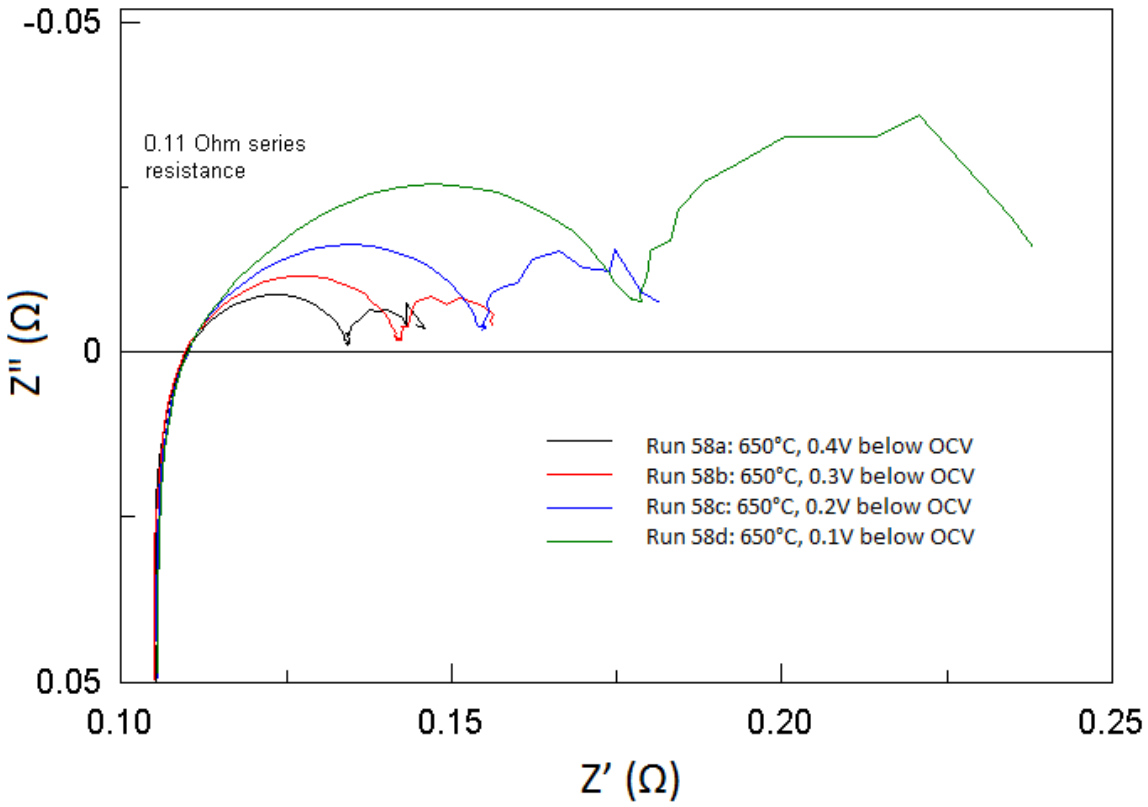

Figure 82 - Impedance plots for the same AMI-15.2 µSOFC at different voltage levels (650°C, 60 ml/min. H_2)

The cathode arc was expected to be unaffected, but the arc changed in the opposite way (higher R and C at higher anode fuel flow rates; the cathode is not actively supplied with air, simply left open to the furnace atmosphere), albeit giving a lower percentage change in either. This shows that the anode and cathode processes have not been entirely decoupled – potentially due to the higher current at the given potential with the higher fuel flow rate making more demands on oxygen mass transport at the cathode. This confirms that, as expected, the "real" equivalent circuit will be much more complex than the simple model used.

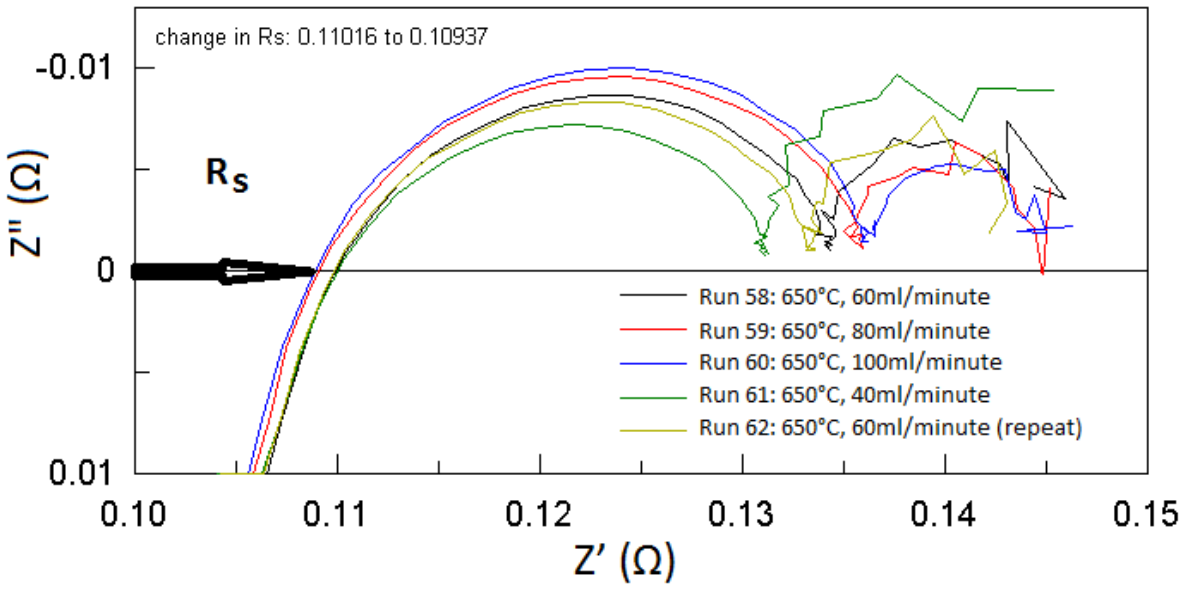

Figure 83 - Impedance plots for the same AMI-15.2 µSOFC at different hydrogen flow rates (650°C, 0.4 V below OCV)

Having identified which plot feature corresponds to which physical component, model fitting was then attempted using ZView software. As can be seen in Figure 84, the arcs are flattened semicircles so the model fit (in green) does not give a good match to the data (in red).

Constant Phase Elements (CPEs) are often used to give a better match to data in cases like this, to model "imperfect" capacitance or resistance. Replacing the capacitor in the RC pair with a CPE gives a depressed semicircle. Various phenomena have been invoked to explain this result and justify use of the CPE, depending on the nature of the system being modelled. Explanations normally centre on a property of the system being inhomogeneous or there being a distribution of values for a particular physical property of the system.

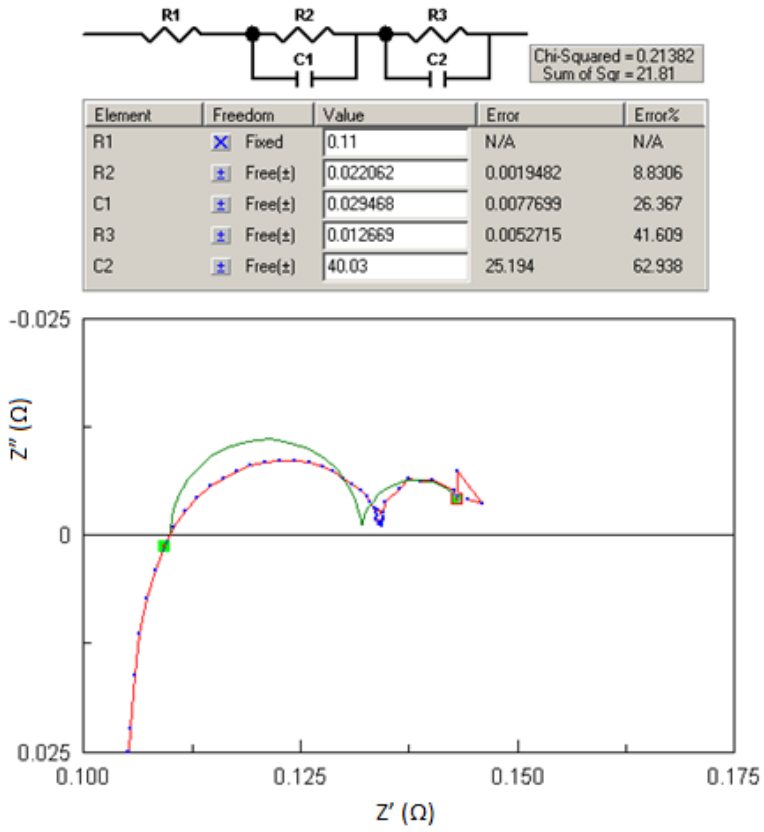

Figure 84 – EIS model fitting (AMI-15.2 µSOFC, 0.4 V below OCV, 650°C, 60 ml/minute H_2)

This is certainly justifiable in a fuel cell system where grain sizes, available crystallographic faces, pore sizes and temperatures, amongst other aspects, all vary throughout the matrix and have an effect on many key parameters. Unlike the simple resistance and capacitance values, three separate values need to be defined for each CPE used. The risk of this is that close fits can be obtained at the cost of physical meaning. Figure 85 gives an example of how the anode arc obtained could be fitted using a CPE. A great deal of work would be needed to ascribe and test any physical meaning to the values found from the fitting algorithm.

Leonide [216, 237] used CPEs and focused on the distribution function of relaxation times of the various processes involved in fuel cell operation. A very close fit to the data was achieved and various loss mechanisms firmly identified, but doing similar for these cells would require a larger time commitment than this PhD schedule allows. As such, EIS was left at this point.

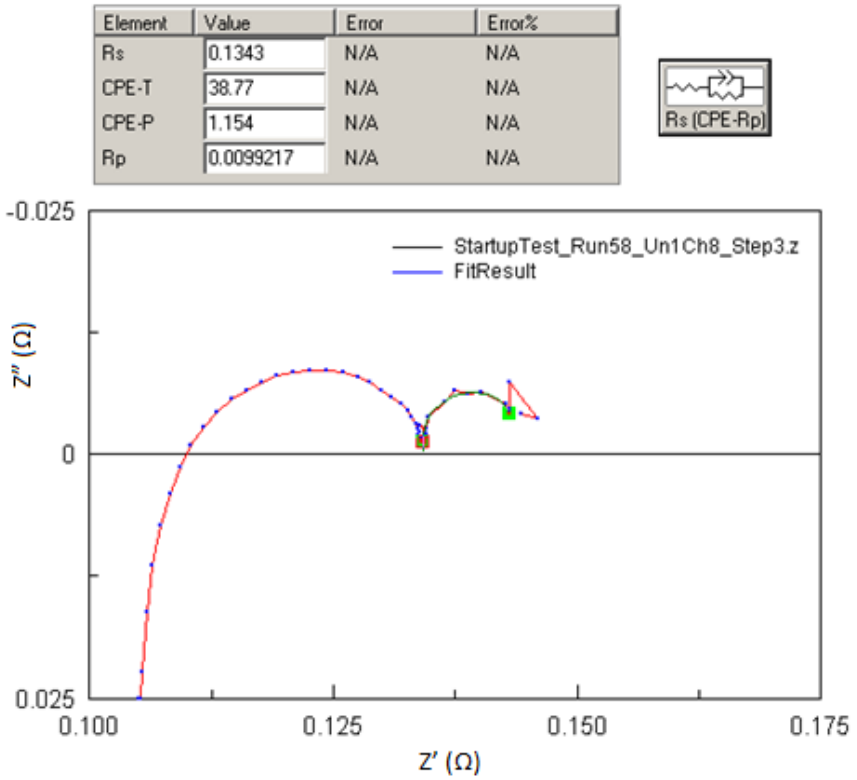

Figure 85 - CPE fitting to the anode arc – the model was fitted to the section highlighted in green only in this case (data collected at 0.4 V below OCV, 650°C, 60 ml/minute H_2, AMI-15.2 µSOFC)

Degradation

Aside from the low power, two further issues were seen, both related to degradation. Over a two-hour constant voltage test period, operating on hydrogen, the current could be seen to drop. No significant degradation should occur over such a short time period, especially in the conditions used (pure hydrogen fuel and constant temperature). The open outlet end of

the tube was seen to have gone green (see Figure 86), indicating the oxidation of nickel in the anode to nickel oxide.

Figure 86 shows the damage observed – the silver wire formerly covered by the (cracked) cement has clearly reacted, as it has become white and brittle. This suggests that the cement was not preventing oxygen getting to the wire surface, so presumably was not stopping hydrogen escaping either. The silver wire on the outside of the cathode has not been damaged. This suggests that the temperature at the end of the tube was much higher, probably due to hydrogen and oxygen mixing and burning.

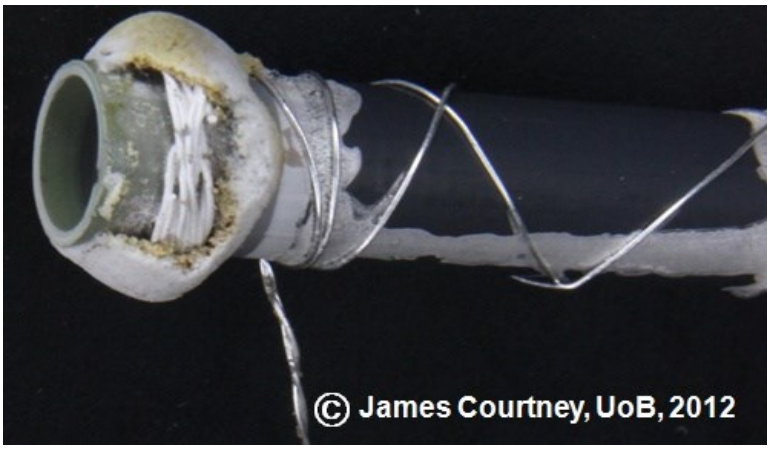

Figure 86 - AMI-15.2 µSOFC without baffle or outlet manifold damaged by oxidation

Two points were identified that led to the degradation shown in Figure 86:

1. Burn-off of hydrogen and nickel oxidation at the outlet: manifolding or baffling the outlet would help to reduce oxygen backflow, thus avoiding oxidation of the nickel. This would also reduce hydrogen burn-off, so keeping the temperatures below those at which the silver wire would oxidise.
2. The ceramic sealant used (Fortafix high-temperature tolerant cement) is not sufficiently gas tight with the higher flow rate and larger exposed area. Alternative

sealants were therefore investigated, and a new glassy sealant acquired (Schott Glass sealant G018-311 paste).

Once the outlet was manifolded, a significant increase in optimum set furnace temperature was found (up to 750°C from 650°C), confirming that significant burn-off had been occurring. Thermocouples placed close to unmanifolded cells confirmed that the temperature near the cell inlet (far end from the burn-off) was around 725°C when the furnace set point was only 650°C.

It was hypothesised that the white material formed was a silver oxide, but silver oxide is not normally white. This compound was therefore investigated to check for any other unexpected reactions, for example with the cement, which could be causing this problem. Options for analysis techniques were limited due to the very small amount available, the high silver content and the lack of water solubility. XPS was selected, and a survey spectrum is shown in Figure 87; the elements present were identified as being silver, oxygen, carbon and sodium (trace). No carbon or sodium would be expected within the material, but as this technique only looks at a thin surface layer, this is due to dust on the surface of the compound. The oxygen could be part of this impurity, or could be bonded to the silver.

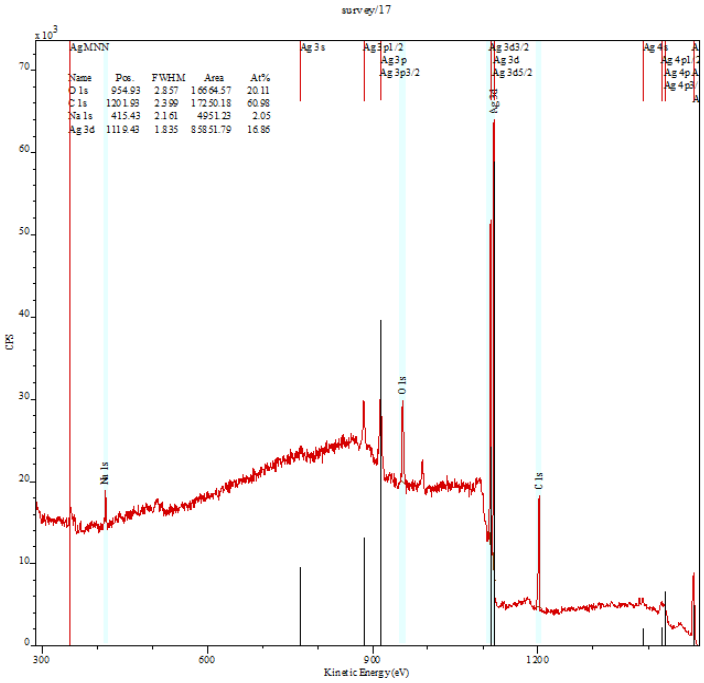

Figure 87 - XPS survey spectrum of silver compound formed on damaged AMI-15.2 µSOFC wires

Looking at the Auger electron peak for silver (Figure 88) revealed a split, suggesting that some metallic silver is present in elemental form, and some has reacted. A higher resolution scan in that energy range was then performed with the intention of identifying which bonds to silver are present. The energy of each peak in this splitting is within the range that can be found for elemental silver, silver oxides and silver nitrates. The fact that it is split confirms that some of the silver has reacted, and the survey spectrum does not suggest that a significant amount of nitrogen is present, leaving silver oxide as the main possibility.

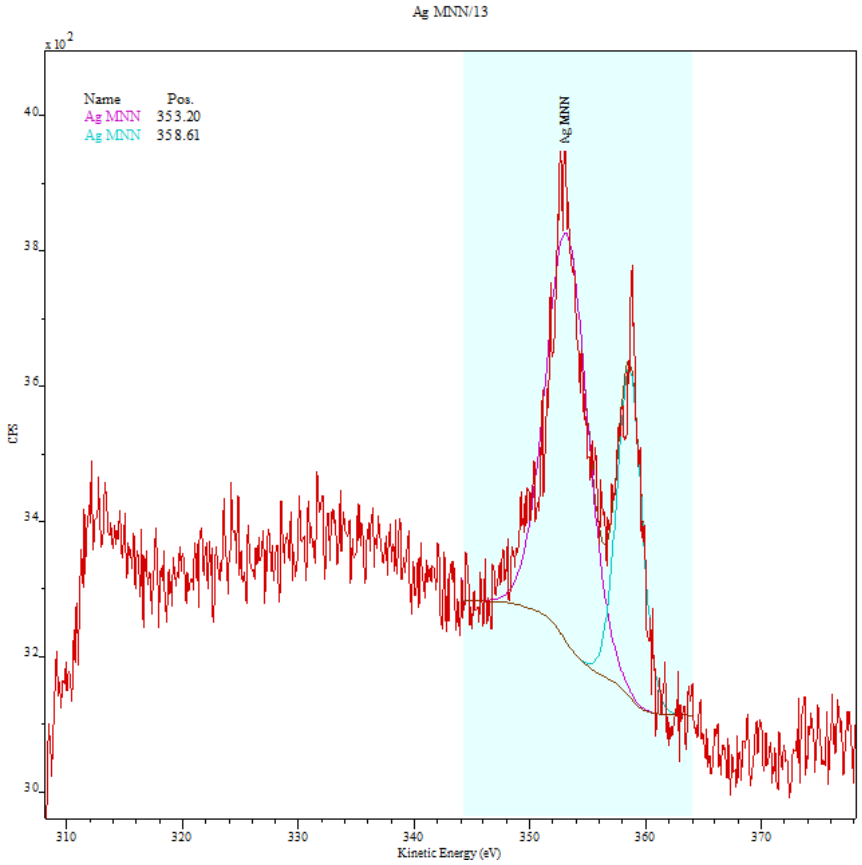

Figure 88 - Auger electron peak for Ag from the section of damaged wire tested

The white substance being a mixture of silver and silver oxide sounds reasonable, but still does not explain the white colour. SEM images of the substance (Figure 89) suggest a solution. The structure of the silver has changed dramatically, with many small, spikey crystallites covering the surface. The change in structure on this small scale may well change the reflectivity of the surface significantly, so leading to a much more white appearance than normal. The formation of these crystallites also explains the significantly more brittle and friable nature of this material as compared to the annealed silver wire from which it formed.

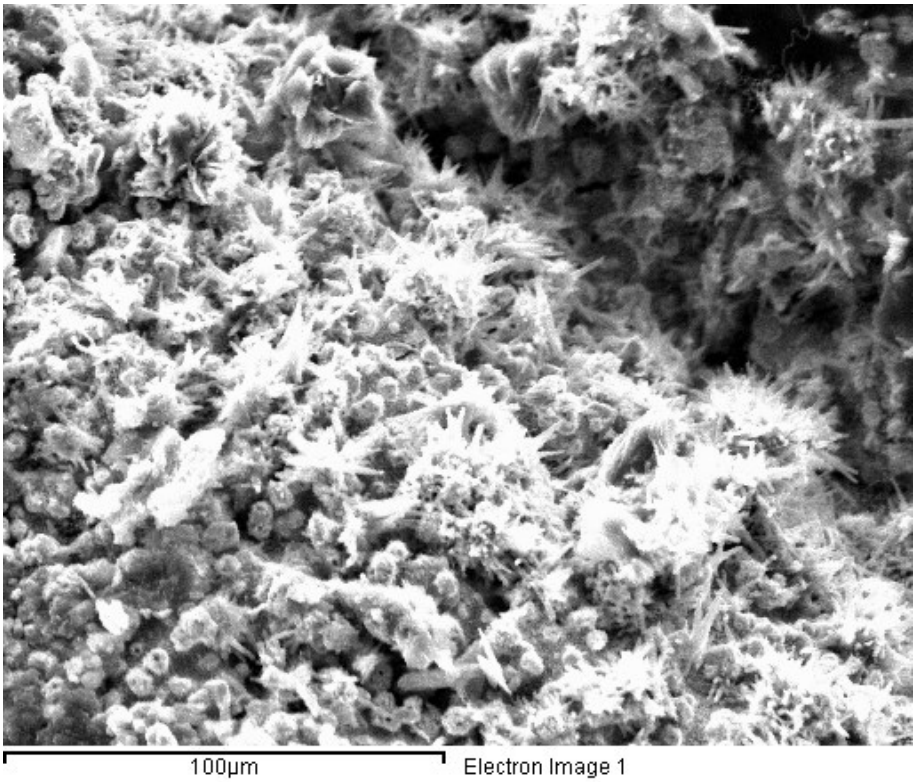

Figure 89 - SEM image of damaged silver wire

The white compound was seen again with a manifolded cell for which the seal had failed. A whitened section of wire was formed in the hydrogen flame area which was not in contact with the cement, confirming that a cement reaction was not responsible. This confirms that silver oxide, significant structural change of pure silver, or a combination of the two, is responsible for this phenomenon.

Numbers of Interconnections

The number of anode connections was limited to two (one each at the inlet and outlet) due to the impracticality of attaching wires inside the tube. (Other work performed in-house[9] trialled drilled holes and silver rod contacts to the anode at various points along the tube,

[9] By Tony Meadowcroft, under the supervision of Kevin Kendall and Waldek Bujalski

but the breakage and failure rate was found to be too high for this to be practical.) Having two connections gave noticeable improvement (Figure 90). Nickel mesh and thin layers of silver ink (Dupont ink 5029) were used to try to increase the contact at different points, but no significant improvement was seen. It is not surprising that the anode resistance is not a limiting factor, as the resistance per unit length is almost an order of magnitude less than that of the cathode (0.04 Ω/cm for the anode, as compared to 0.30 Ω/cm for the cathode) [10]. Literature values for LSCF conductivity [238] allowed a resistance per unit length of 0.6 Ω/cm to be calculated, although thermal treatment history is known to have a significant effect [239]. Values for Ni-YSZ anodes [240] give a resistance per unit length of around 0.1 Ω/cm (strongly dependent on volume percentage of nickel). These values are similar to those found experimentally, and confirm the conclusion that cathode resistance is significantly higher.

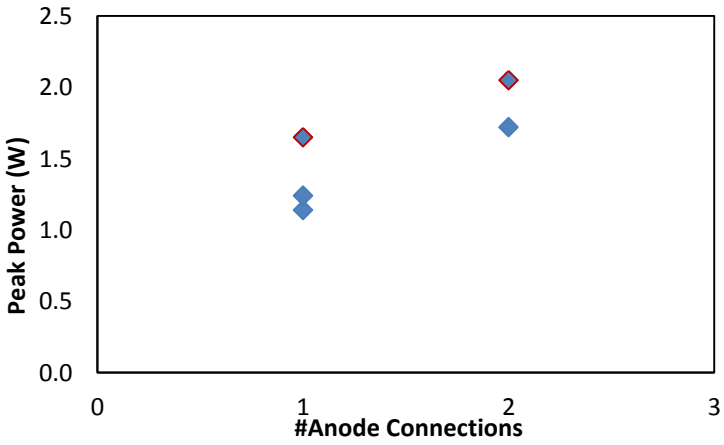

Figure 90 – Peak power at 650°C with 60 ml/minute H_2 for AMI-15.2 µSOFCs with varying numbers of anode connections (red-lined points show cells with four cathode connections, points without borders have just one)

The number of cathode connections (design shown in Figure 91) can be increased much more easily – results are shown in Figure 92. A definite increase was seen when moving

[10] Multimeter and Solartron IV-sweep measurements (true 4-point measurements only performed for the cathode due to difficulty of making reliable anode connections).

from one to four cathode connections. This is unsurprising as more connections mean shorter resistive current pathways. Beyond that, the power started to decrease again. This is probably due to active area limitation as an extra portion of the cathode surface is blocked by the silver ink and wire for each additional connection.

More generally, this result can be analysed in terms of the resistive pathways along the cathode. As shown in Figure 91, each connection point consists of two 2 mm wide bands of silver ink, connected by a silver ink stripe X mm long. There were between one and eight of these along each cell tested.

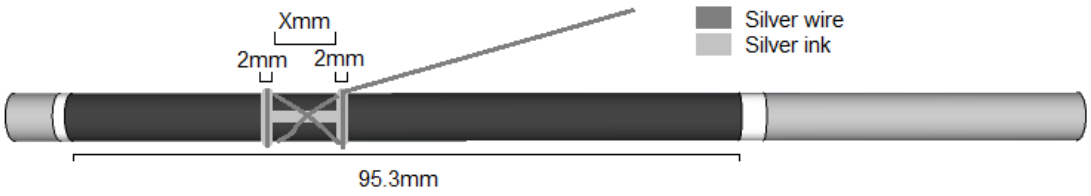

Figure 91 - Schematic of AMI-15.2 µSOFC interconnection design

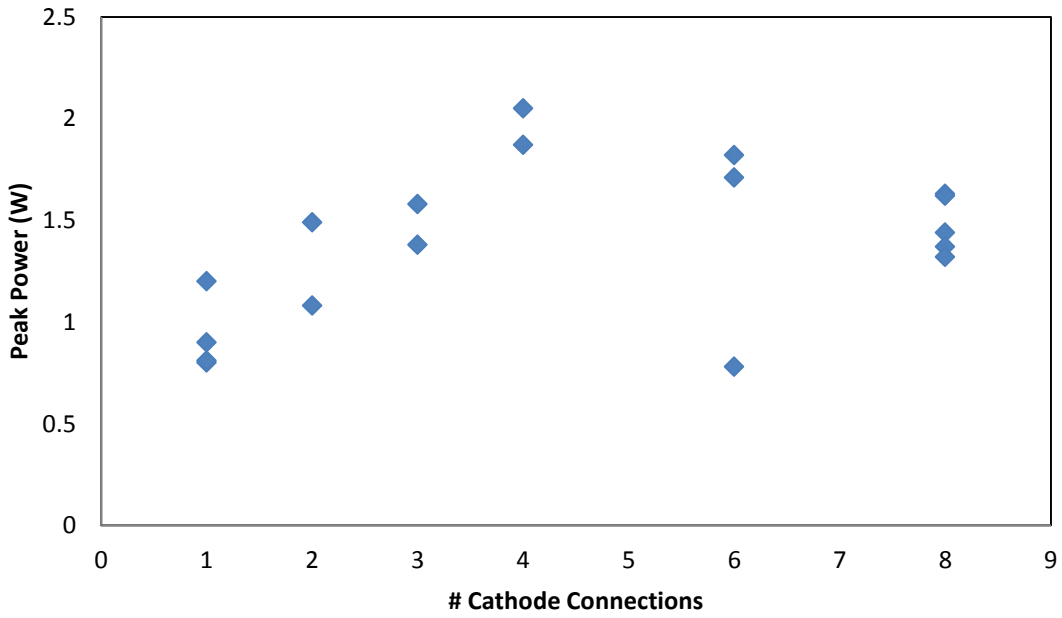

Figure 92 – Peak powers of AMI-15.2 µSOFCs tested at 650°C with 60 ml/minute H_2 with varying numbers of cathode connections (spread is due to changes in other variables e.g. # anode connections)

The value of X determines the maximum distance the current could be expected to travel through the cathode to reach the connecting wire. The presence of the silver stripe should help to reduce the resistance.

A four-point test was conducted, eliminating the effects of contact resistance, to measure the resistance of a 5 cm length of cathode at operating temperature. As the cathode consists of bi-layered SDC/LSCF, it is unsurprising that the voltage-current characteristics seen (Figure 93) do not show the perfect straight line expected for a simple Ohmic resistance (and as seen for the anode) – non-linearities in interfacial current transfer have an effect. Nonetheless, the section of the graph at smaller currents is fairly linear, allowing a resistance of 1.49 Ω to be measured from the gradient. This translates into a resistivity of 2.5×10^{-5} Ω.m, which is in line with values cited elsewhere [241, 242].

Returning to the connection spacing, this gives a resistance of 0.3 Ω for every cm the current must travel through the cathode. The optimal number of cathode connections was found to be four, giving a path length of just under 2 cm per connection once the widths of the Ag bands are accounted for. This gives a recommended upper limit of 0.6 Ω on current path resistance for μSOFC connections. By contrast, the anode resistance was only 0.04 Ω/cm, giving a maximum total resistance of 0.38 Ω along the total active cell length.

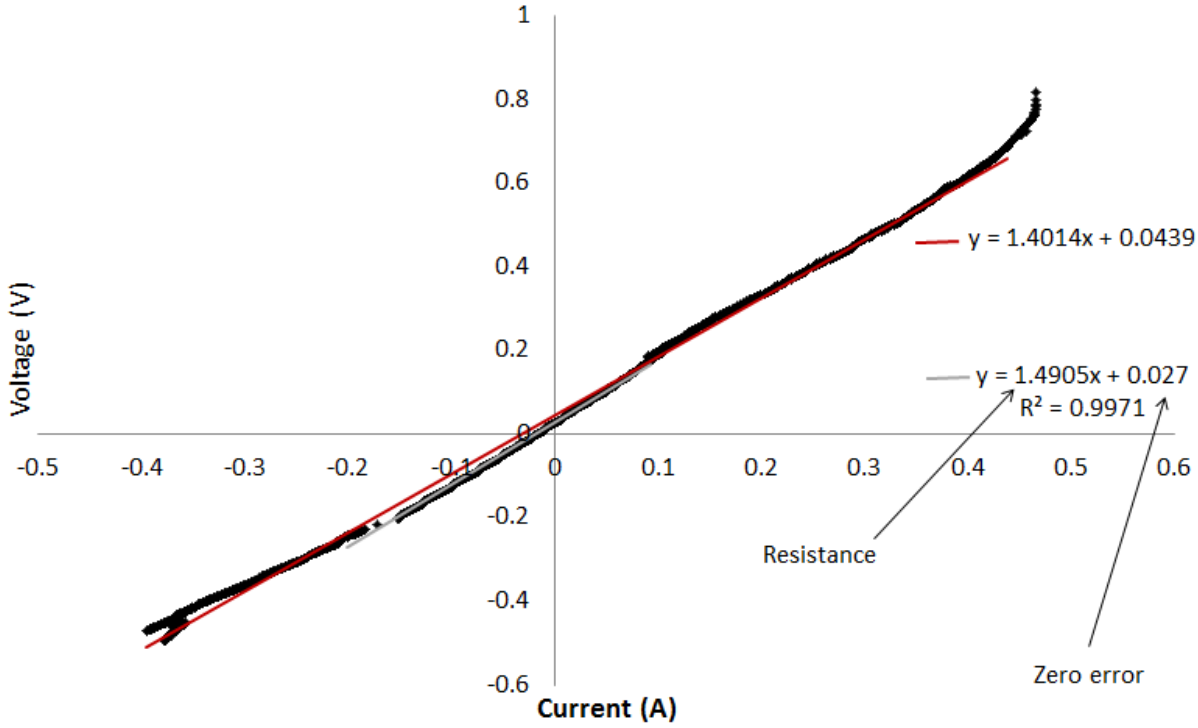

Figure 93 - Four-point test to measure cathode resistivity of AMI-15.2 µSOFCs under operating conditions (5 cm of cathode tested at 750°C with a flow of 60 ml/min. H_2 to prevent anode damage)

Once the cathode resistance had been measured, a mathematical model was devised in Excel to examine the trade-off between active area loss and reduced connection resistance. To avoid the risk of adding in enough variables that the model could be fitted to any dataset, a simplistic approach was chosen based on the following assumptions:

1. Silver ink and wire conductivities taken to be effectively infinite, compared to the high resistance of the cathode
2. Silver ink fully blocks gas flow to the cathode area beneath it, rendering these areas inactive
3. Current generation across all non-covered cathode area is uniform
4. Current only flows into the wire when the wire is in contact with silver ink (the area of wire directly in contact with the cathode is very small - see Figure 91 – with the

area in physical contact being even smaller than the geometrically covered area due to the circular cross-section of the wire)

5. All sources of power loss unrelated to cathode conductivity (anode losses, mass transport etc.) are treated as negligible

Each connection consists of two silver bands around the circumference and a connecting longitudinal stripe. The following approximations were used:

1. The width of the silver bands around the circumference, b, is 2 mm (see Figure 91)
2. The width of the silver stripe along the cell length is 2 mm
3. (X+2*b) is the total cathode length divided by the number of connections, given that X is the length of each active section

In reality, hand-painting will cause variations of ±0.5 mm in these painted areas, and a ~1 mm gap was left between the painted sections in initial tests. This makes the average current path length calculated (discussed below) marginally higher than the actual value.

The approximate average path length travelled by the current through the cathode was calculated as a function of the number of cathode connections, N. Picture unwinding the section of cathode delineated by the silver bands shown in Figure 91: the silver stripe forms both the top and bottom edges of the rectangle of length X, shown in Figure 94. The height of this rectangle, h, is the circumference of the tube minus the 2 mm covered by the silver stripe. This rectangle was then split this into three sections, as shown: a middle section, and one by each band.

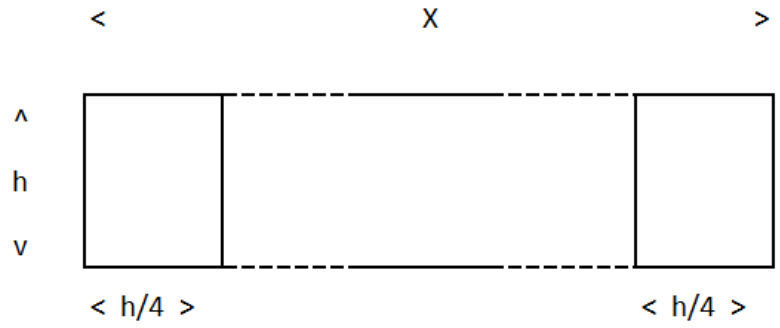

Figure 94 - Schematic of active cathode area section

In the middle section, the shortest current path to the silver ink is always to the silver stripe, giving a maximum path length of h/2, so an average path length of h/4. All minimum path lengths are below this average in the end sections (maximum: h/4, average <h/8). This could be further sub-divided, but this would add more complexity than such a simplistic model warrants. An upper bound on the average path length is then found by Equation 5.2:

$$L = IF(\left(X > \frac{h}{2}\right), ((\frac{X-h/2}{X}) * (h/4) + (\frac{h/2}{X}) * (h/8)), \frac{L}{4}) \quad \textit{...(Eq. 5.2)}$$

Where $X = \frac{Total\ Cathode\ Length}{N} - 2b$

At 0.5 V (around the peak power point), the current generation per unit area is expected to be between 0.5 and 1 A/cm^2. As a precise value is not known, this was the one "variable" in the model. The total current generated was then calculated and the resistive losses (using Ohm's Law) subtracted from the total. A plot of the model for the effect of number of connections on power is shown in Figure 95. The shape of the trend agrees well, and the position of the peak, at around five connections (varies slightly with current density), also coincides with the peak seen in the data collected. One outlier (circled in black in Figure 95) reveals a limitation with the model – with only one connection, the resistive losses calculated are higher than the total power generated, so giving a negative result. Physically, current would tail off with heat dissipation, making only the areas closer to the silver active.

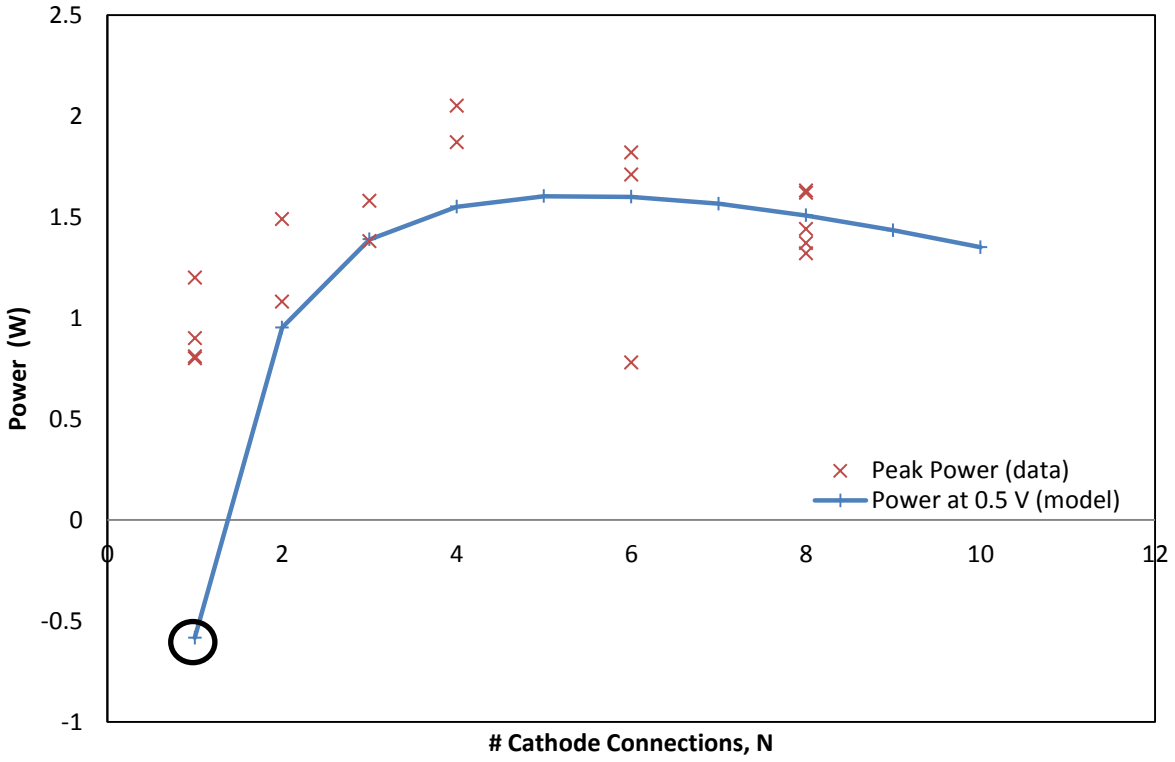

Figure 95 – Comparing experiments and models for the trade-off between resistive pathway length and active area using a current generation value of 0.5 A/cm^2 (experimental data for AMI-15.2 µSOFCs recorded at 750°C with 60 ml/min. H_2)

This model confirms that the two competing factors hypothesised to be responsible for this trend could indeed give the trend found, and could be used as a tool for calculating the optimal number of connections given different band and stripe widths. Other techniques are available, however, hopefully avoiding this trade-off.

A silver wire mesh was then tested in an attempt to have more contact points without the loss of active area (see Figure 96 – small spots of silver ink were used to increase contact). Due to the cost of commercial silver meshes, this mesh was crocheted from available silver wire to test the principle. Although the peak powers were comparable to those obtained previously, they were not better. This is probably due to the lack of contact between the

mesh and the cell, as it is not trivial to maintain tension over the temperature range required.

Figure 96 - AMI-15.2 µSOFC with silver mesh cathode connection

The silver ink used with the AMI-15.2 µSOFCs described above is Dupont's 5029 silver ink, which is designed for screen printing and has a "high print thickness in a single print". This means that the porosity is low, so gas access to the cathode area under the ink will be blocked. Switching to a more porous ink should allow the covered cathode to become at least partly active. In addition, a thinner ink is more likely to penetrate the cathode surface, thus improving contact and so current collection.

SPI conductive silver paint (#5002AB) has been used successfully in this way by Ultra-AMI, so was chosen for further study. No data were gathered to explicitly confirm the claimed increase in porosity, but a cell completely coated with this ink was still able to function (Figure 97). By contrast, a cell coated with ink 5029 did not give notable power.

Figure 97 – Silver ink-coated AMI-15.2 µSOFC with a silver wire coil around the cathode

A limit on current transfer at temperature due to the diameter of the silver wire had been considered previously, but trials with 0.35 mm diameter wire, instead of the usual 0.25 mm, showed no improvement. Once the silver coating was added, increasing the diameter of the collecting wire was shown to give improvements, as the lateral conductivity limitation was reduced. Wire resistance increases with both current (due to Joule heating) and temperature, so although the "standard" double strand of 0.25 mm diameter wire can take the expected currents of ~10 A from a well-performing cell at room temperature, it fails at operating temperatures. With a current of 8 A, two-strand twisted 0.25 mm diameter silver wire melted through at a furnace temperature of 750°C, and the 0.35 mm diameter equivalent failed at 850°C. 1 mm diameter wire (single strand) was therefore chosen as this can cope with the expected current demand at temperature. The contact resistance is slightly higher as the wire is less flexible so does not conform as well to the tube surface. This is soon made up for by the slower increase in resistivity with increasing current, however. For the 0.35 mm diameter wire, resistivity increased by nearly 50% when the current was increased from ~0 A to 7 A at 750°C; the increase was only 16% for 1 mm diameter wire. These values are slightly lower than those expected from literature values of the temperature coefficient of resistivity as the ends of the wires are at a lower temperature than the section within the furnace. Higher accuracy was unnecessary for this work.

5.2.4 Coil and Spine Connections

As the cathode has by far the higher resistance, a coil of wire the length of the cathode was tested. To directly test the effect of a silver coating in addition to a full-length coil, four cells were prepared as shown in Figure 98; cells 1 and 2 are prepared identically and cells 3 and 4

were prepared in the same way, but with the addition of a coating of porous Ag ink underneath the cathode coil. After testing, cells 1 and 3 were then adjusted, replacing the double-strand of 0.35 mm diameter wire to the anode with 1 mm diameter wire. The 0.35 mm cathode coil was temporarily removed, then replaced over a "spine" of 1 mm wire, which was then used as the cathode connection. This was to test the change in wire diameter; a coil with such a large number of turns of the thicker wire would be impossible, but the current carried by each turn of the 0.35 mm wire should be low with the spine in place, so the limits of that wire should not be reached. The cells tested are summarised in Table 9. A slip-on outlet manifold was used for all tests to minimise burn-off whilst still allowing the cells to be removed and interconnections changed as required, unlike a manifold cemented in place.

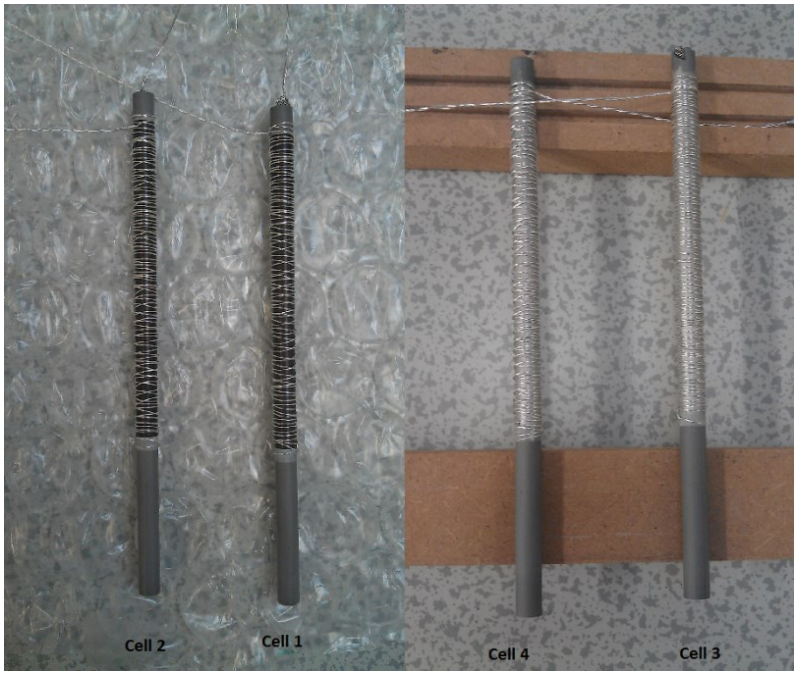

Figure 98 - AMI-15.2 µSOFCs prepared with coil cathode connections, with and without silver ink coatings

As expected, adding the silver coating and moving to thicker connection wires both had a positive effect on performance.

Table 9 - Summary of AMI-15.2 µSOFCs tested and interconnection adjustments made

Cell Name	Interconnection Style
Cell 1 Cell 2	0.35 mm diameter Ag wire coil; no Ag ink coat
Cell 3 Cell 4	0.35 mm diameter Ag wire coil; Ag ink coat under wire coil
Cell 1 with spine	Cell 1 with 1 mm diameter Ag wire “spine” under coil
Cell 3 with spine	Cell 3 with 1 mm diameter Ag wire “spine” under coil

The lateral conductivity of the cathode should be better with the dense coil as compared to the previous versions with only a few turns of wire along the length; the silver coating should improve wire contact as well as increasing surface conductivity between the wire turns. Figure 99 shows that this was the case, although the variation between supposedly-identical cells was greater than expected given the small variation between the smaller cells (AMI-5.5 µSOFCs) when prepared in the same manner.

The change in wire diameter had a larger effect than the addition of the silver coating, as shown in Figure 100. The peak power was 3 W, and mass limitation actually had a noticeable effect for the first time at higher currents. With this improvement, a flow rate of 100 ml/minute became the new standard, replacing the 60 ml/minute used previously.

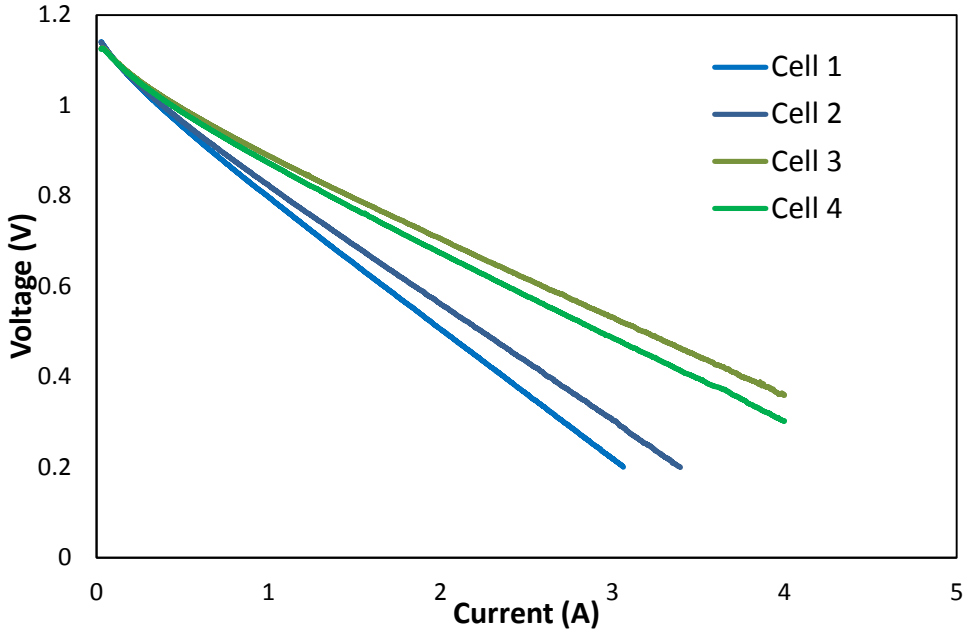

Figure 99 - AMI-15.2 µSOFC performance at 750°C with 60 ml/minute H_2, with (3,4) and without (1,2) an Ag coat (porous ink) under the wire coil (no Ag wire spine)

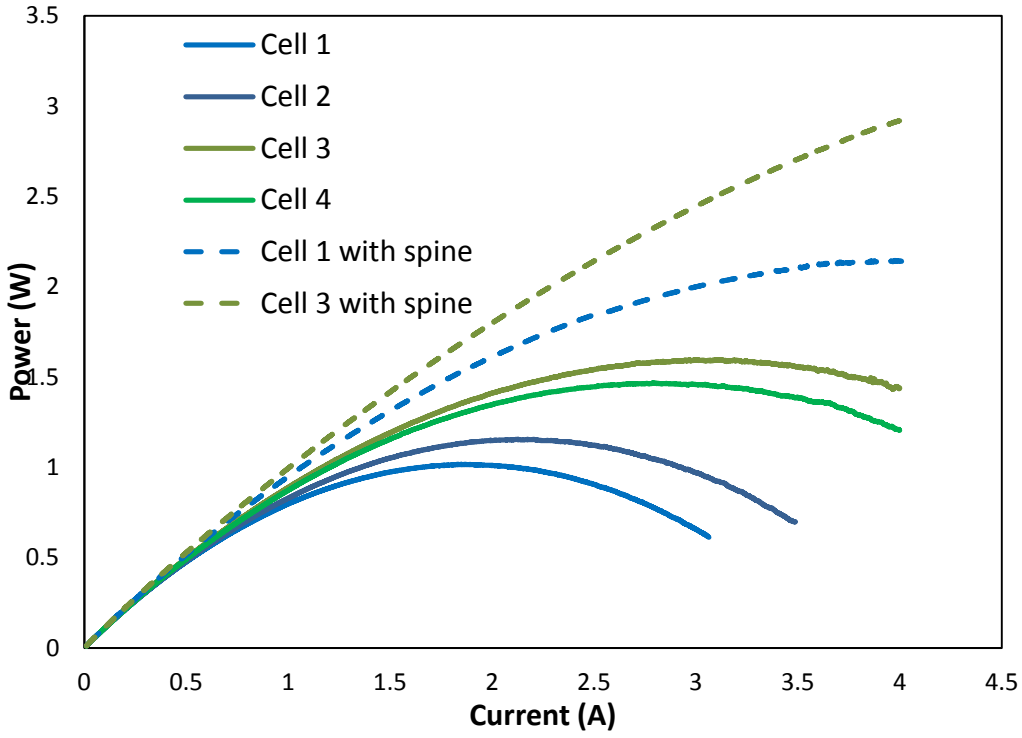

Figure 100 - AMI-15.2 µSOFC performance at 750°C with 60 ml/minute H_2 with and without silver wire spines

All of the above tests were performed with a single connection to each electrode. Previous tests, supported by the literature [234], show that having multiple connections can improve

the performance. Cell 3 was therefore modified to have an anode connection at both the inlet and the outlet and the "spine" split into two half-cell lengths, each with an off-take wire, as shown in Figure 101. This was tested with 100 ml/min. of dry hydrogen, giving a peak power of 4.1 W.

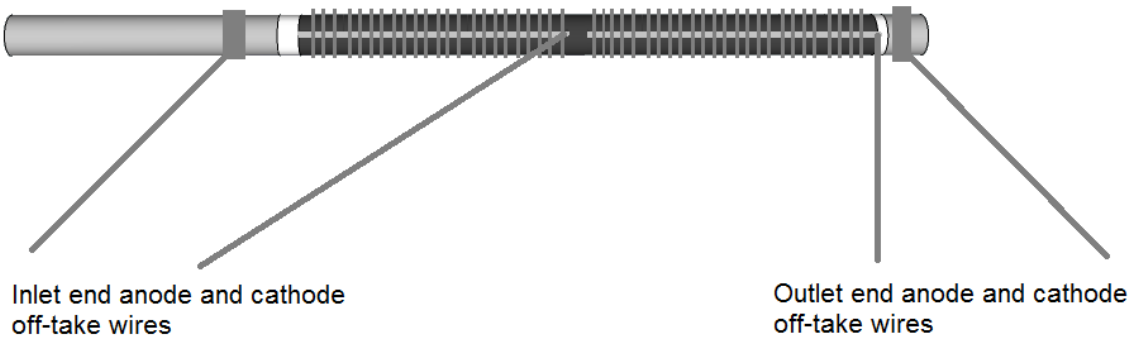

Figure 101 - Schematic of two-section coil and spine interconnection design for an AMI-15.2 µSOFC

The change of gradient of the Ohmic region of the IV curves confirmed that the Ohmic resistance was significantly reduced when a second connection was introduced. The rate of decrease of voltage with current dropped by around 50% upon use of two connections per electrode.

5.2.5 Discussion and Further Work

The work performed gave a 300% increase in power output from the cells as compared to using the interconnection regime previously used in-house. Combinations of techniques drawn from different parts of the literature were used, and a crocheted mesh was also tested. The upper limit on cathode current path resistance to avoid this limiting cell performance was found to be 0.6 Ω for the materials tested.

Data from the tube suppliers [64], AMI, shows a peak power of just under 8 W per tube [11]. An extension of the work above, carried out by Tony Meadowcroft, has increased this from 4.1 to 5.4 W per tube (in-house work).

Various options, beyond the scope of this work, remain to be tested. These could hopefully increase the power still further:

- Softer, porous conducting ceramic layer on top of the cathode and over the mesh or wire connection to improve lateral conductivity and connection contact
    - This would be a cheaper replacement for the silver ink coating
- Adding the in-house cathode to cathode-free cells supplied by AMI
- Thicker layers of a more porous silver conducting ink, possibly using a pore-former

[11] At "high temperatures: 600-800°C" with "direct hydrocarbon fuels"; no precise operating conditions stated, although fuel utilisation is marked as being above 70%.

Results Section II: Electrode Optimisation

6. CATHODE INKS AND FABRICATION

In this chapter, optimisation of the cathode fabrication process is reported. This work was performed on the smaller AMI-5.5 µSOFCs as the newer cells (AMI-15.2) were purchased with cathodes already applied. Dip-coating was tested as a faster and more repeatable technique for applying the ink (Section 6.1). It was found that surface-drying of the acetone-based ink in the dipping pot was an issue over the timescales of the dipping process, leading to the development of a water-based cathode ink (Section 6.2). The use of dispersants that are pH neutral was then investigated to avoid the issues with buffering additives found in some water-based inks and slurries reported in the literature.

6.1 Technique Change: Brush-painting to Dip-coating

The parts of this section concerning dynamic performance of cells have been published previously by the author [12], although the dip-coating optimisation process reported here has not been published elsewhere.

[12] **Relevant Publication:**
K.S. Howe and K. Kendall, Transient Performance of Micro-Tubular Solid Oxide Fuel Cells. Journal of Fuel Cell Science and Technology, 2011. ***8****(3): p. 034502.*

The previously-used technique of brush-painting the cells has several disadvantages as listed below:

- Unrepeatability – From cell-to-cell, but more significantly between people with different techniques, different paint brushes or different hand steadiness. (50 µm variation in cathode thickness often being observed between cells prepared "identically", an example is given in Figure 102)
- Limited Precision – layer thickness depends strongly on the volume of ink on the brush and the time for which that ink has been outside the airtight container (drying time). Cathode length is determined by eye against a ruler, so precisions of less than 1 mm are not possible.
- High Labour Requirement – each cell has to be painted sequentially; no economies of scale are possible.

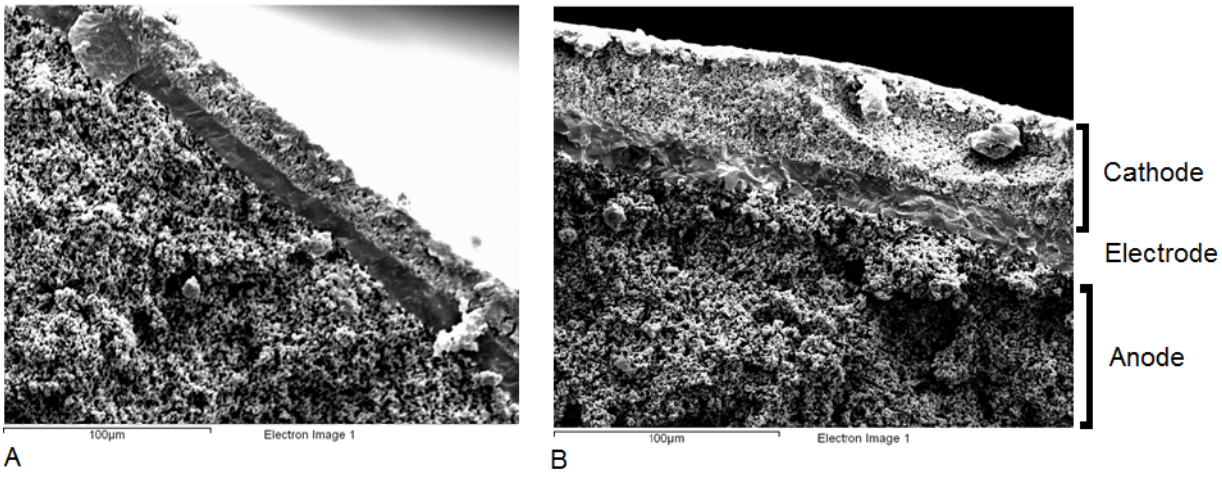

Figure 102 - SEM images showing two cathodes of brush-painted AMI-5.5 µSOFCs prepared identically, showing cathode thickness variation between (A) ~25 µm and (B) ~65 µm

With an automated dip-coater, a standard programme can be recorded and run by all users, ensuring repeatability between individual cells and users. The layer thickness should also be more consistent, so long as the rheology of the ink remains unchanged,

as the dipping speed is constant. Having thread seal tape at the bottom of the tube avoids the problem of a drip forming at the bottom of the dipped substrate, as well as ensuring no cathode ink comes into contact with the interior anode layer. The length should again be more accurate as distances moved can be set precisely and the raising of the ink level as the tube enters the fluid can be calculated (or measured) and accounted for as necessary. This can also be made into a batch process, with many cells being dipped simultaneously. It was also hoped that this technique would allow for thinner layers, to enhance performance either by allowing better gradient matching from the YSZ electrolyte to the high percentage LSM outer cathode current-collection layer or simply by reducing resistance due to a reduced current path length.

On the other hand, it was thought possible that the brush-painting technique would actually provide a greater cathode surface area due to the inherent slight unevenness of the layer due to the brush bristles. A larger surface area facilitates the cathode reactions, so a more perfectly tubular layer could theoretically lead to reduced performance.

6.1.1 Initial Dip-coating Trials

A dip-coating ink recipe published by Acumentrics in a 2005 technical progress report [243] was used initially. As with the in-house recipe, this consists of two ink layers, with differing LSM concentrations.

This forms a bi-layer cathode, with the layer in contact with the electrolyte (C1) being a mixture of the cathode and electrolyte materials (LSM and YSZ) to maximise the triple phase boundary (TPB) area, and so the number of reaction sites available. This is the electrochemically active layer – also referred to as the cathode functional layer. The second layer (C2) contains no YSZ, so is not electrochemically active due to the lack of oxide ion conduction. This layer acts as the current collection layer.

The relevant extract from this report is shown in Figure 103 . The milling time of the second layer ink was extended to 30 minutes due to the lack of adhesion and floating powder seen in the first run. A small batch of cells was then produced and tested[13] both for current-voltage characteristics and with Scanning Electron Microscopy (SEM) to examine the coated layer.

Extract from an Acumentrics Technical Report

C1 and C2 slurries were first formulated from the (80/20) LSM cathode material and YSZ (-1μ). The formulations for the C1 and C2 slurries are shown in Table 3.

Table 3: Experimental LSM Slurry Formulation

	Material Percentages by Weight			
Cathode Slurry	**LSM**	**YSZ**	**Terpineol**	**Iso-Propanol**
C1 Slurry	16%	16%	13%	58%
C2 Slurry	40%	NA	13%	47%

The YSZ fraction for the C1 slurry was milled in iso-propanol for 24 hours before the terpineol and LSM powder were added. The final formulation was then milled for an additional 15 minutes. The C2 slurry was milled for 15 minutes with the addition of all the materials. The slurries were then tested for particle size distribution and viscosity before applying them to cells.

Figure 103 - Acumentrics cathode ink recipe [243]

[13] Second year students (K.F. Lee, Sean Howley, Matthew Lavelle, Mohammad Syahrul and Wing Kung) performed some of this experimental work, under the instruction and supervision of the author.

All current-voltage tests for dip-coated cells were performed at 750°C with 20 ml/minute of hydrogen. The first cell tested showed an Open Circuit Voltage of 1.1 V, in close agreement with the theoretical value. The IV-curve produced showed the cell to perform poorly compared to the in-house brush-painted cells (Figure 104), but gave reassuring proof-of-concept.

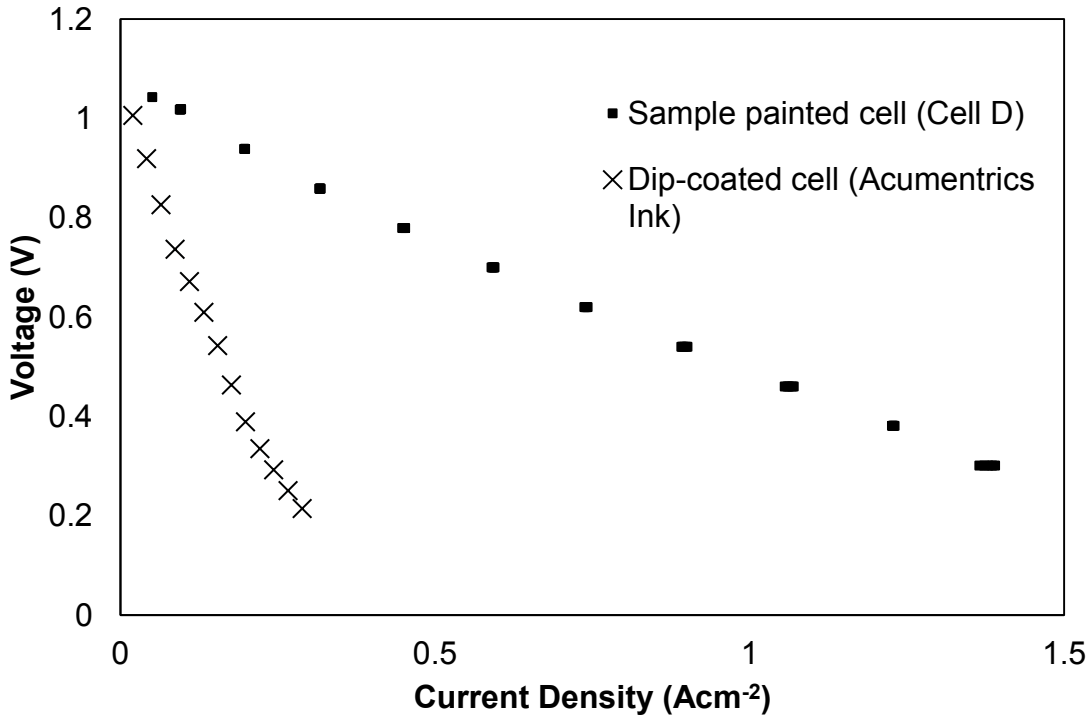

Figure 104 – Comparing a dip-coated AMI-5.5 µSOFC to a brush-painted cell: first dip-coating trial

Other cells in this batch were unable to provide significant currents; SEM imaging of the remaining pair revealed a likely cause of this unreliability. By eye, the grey colour of the cathode layer was visibly different from the black of the hand-painted cells, suggesting a much thinner layer (given equivalent percentages of YSZ in the outer layer). The SEM images confirmed this, revealing the cathode layer to be very thin, which is desirable, but also uneven. In areas, the cathode layer had delaminated entirely, leaving the electrolyte exposed. This suggested that the adhesion of the

Acumentrics ink to AMI tubes is insufficient. Figure 105 shows representative SEM images of two of these cells. On both cells, there were areas of entirely exposed electrolyte, and areas with a thin cathode layer. The painted cathode layer is generally around 20 µm thick, whereas the dip-coated layer was found to be approximately a tenth of that. This reduced thickness is an advantage for creating thin and even layers if the adhesion can be improved. The lateral resistance of the cathode is increased significantly for a thinner cathode, however, so a high-performing current collection layer would be needed.

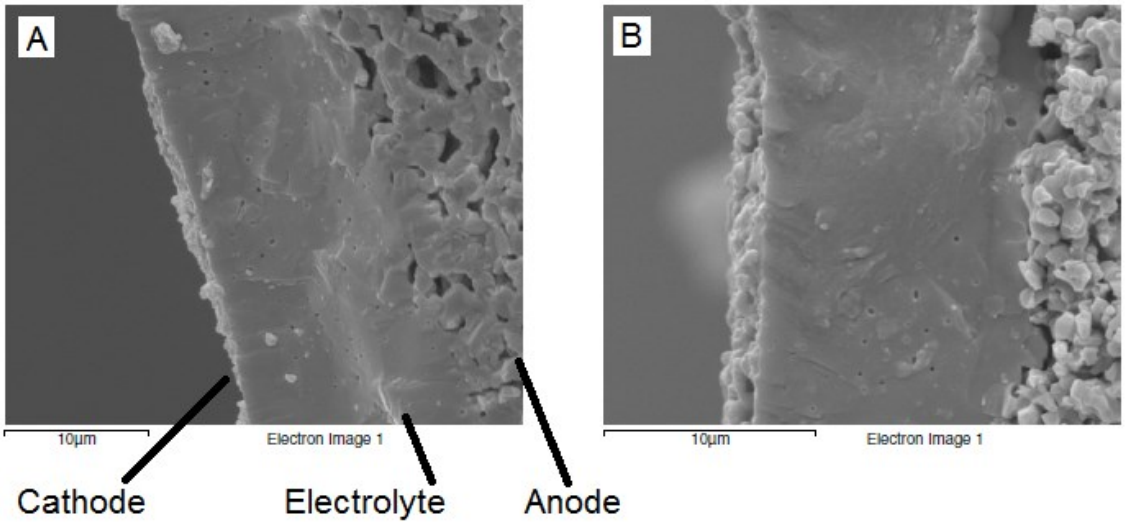

Figure 105 - SEM images of dip-coated AMI-5.5 µSOFCs, showing thin and uneven cathode layers in both un-reduced (A) and reduced (B) samples

6.1.2 Process Optimisation

Inserting a third cathode ink layer with a higher percentage of YSZ between the tube and the "C1 slurry" (see Figure 103) might eliminate this problem of delamination. Alternatively, delamination of the in-house ink recipe has never been an issue, so adapting that to work with the dip-coater was another possible solution.

As the in-house recipe was more familiar, the next set of experiments was performed using that recipe; one change was made – the quantity of acetone was increased to 16 g and 14 g in inks 1 and 2, respectively, to improve the consistency for dip-coating. The method of sealing the tube (thread-seal tape) and ink recipe (see Section 2) were fixed, so the dipping speed and number of layers became the test variables. A brief tabulation of considered variables is given in Table 10.

Table 10 - Dip-coating trial variables

Potential Variables:	**Suggestions:**	**Decision:**
1. Type of ink	House recipe tried and tested Limited success with Acumentrics ink recipe Design of new ink would be a large project in itself	In-house recipe used
2. Number of inks	House recipe currently requires two; more could be added in to get a better catalyst gradient Acumentrics ink also required two - extremely thin layer obtained suggests more would be feasible	Two layers used
3. Number of layers	At present, one of each is used. This could be increased to boost thickness/reduce chance of gaps.	Selected variable
4. Dip speed	Suzuki [78]: The anode tubes were dipped in the slurry and coated at the pulling rate of 1.5 mm/s (90 mm/min) Takeuchi [244]: 0.8 mm/s = 48 mm/minute (aqueous slurry) Initial Tests: 20-40 mm/minute (Acumentrics inks, very thin layer)	Selected variable
5. Dwell time	Too long allows liquid surface to dry (acetone solvent) Unlikely to have much of an effect on adhesion (non-porous substrate)	Kept constant at e.g. 2 s
All other parameters of cell manufacture held constant (see Chapter 3). Regrettably, a new silver ink with suspected poorer properties had to be used as it was impossible to acquire more of the previous make. This new ink was used consistently in these tests.		

Two consecutive batches of fourteen cells were made with the same ink; the combinations of speeds and layers tested are shown below (Table 11). The cell names consist of three letters, with the first letter (A to F) denoting the dipping speed, the second letter denoting the number of layers of Ink 1 used (s=single (1), r=repeat (2) or t=triple (3)), and the third denoting the number of layers of ink 2. The second batch extended the variable range to follow the trend of improving performance seen in the first batch.

Table 11 - Experimental matrix test plan for dip-coating

Experiment Matrix		**Dipping Speed (mm/min)** *(Cells shown in bold were in Batch 1, the remainder constituted Batch 2)*					
Number of layers of...		A	B	C	D	E	F
Ink 1	**Ink 2**	20	50	80	100	120	140
1	1	**Ass**	**Bss**	**Css**	**Dss**		
2	1	**Ars**			**Drs**		
1	2	**Asr**	**Bsr**	**Csr**	**Dsr**	Esr	Fsr
2	2	**Arr**	**Brr**	**Crr**	**Drr**	Err	Frr
1	3			Cst	Dst	Est	Fst
2	3				Drt	Ert	Frt
Naming: [DipSpeed][**s**ingle/**r**epeat/**t**riple layer for Ink 1][**s**ingle/**r**epeat/ **t**riple layer for Ink 2]							

6.1.3 Comparing Technique Variations

As shown in Figure 106, the results for all of the dip-coated cells in Batch 1 were poorer than those obtained previously for hand-painted cells, although all bar two gave higher powers than the cell made with the Acumentrics ink recipe. The one "Sample painted cell (Cell D)" outperforms all the others by a clear margin. The scatter

of results was used to inform further experiments, however. Figure 107 shows some selected IV curves that demonstrate the trend of faster dipping speeds and more layers giving better performance. Dipping speeds were therefore increased for Batch 2, and a third layer was added in some cases.

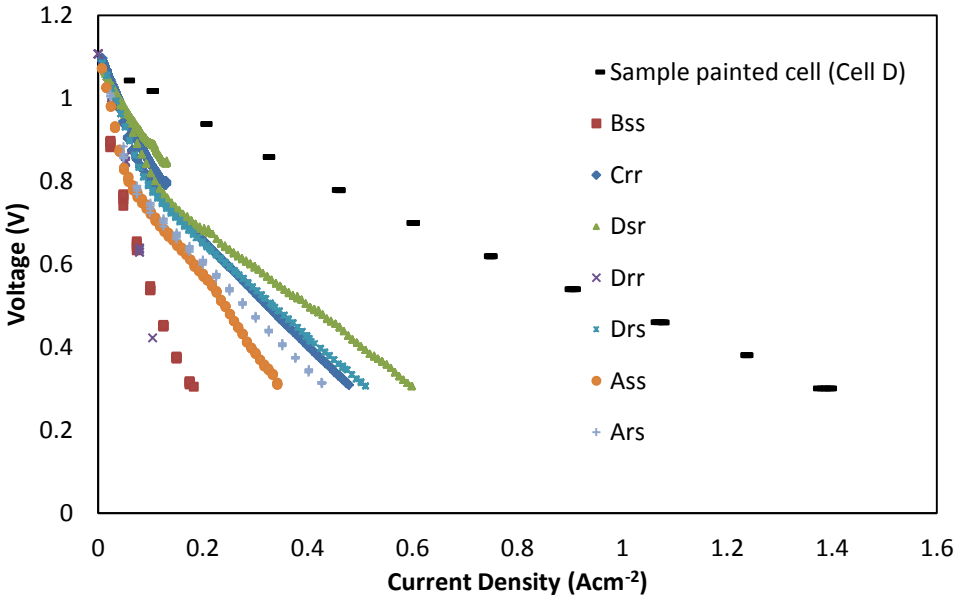

Figure 106 – I-V curves at 750°C with 20 ml/min. H_2 to compare various dip coated AMI-5.5 µSOFCs to a standard brush-painted cell (nomenclature explained in Table 11 - Experimental matrix test plan)

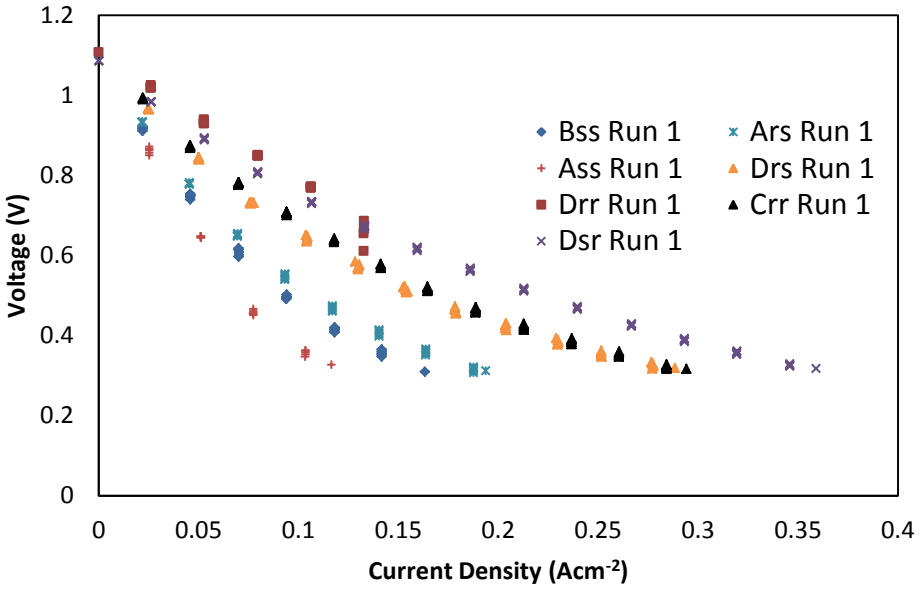

Figure 107 - Comparing dipping speeds and layer combinations in Batch 1 (AMI-5.5 µSOFCs, 750°C, 20 ml/min. H_2)

A definite peak in performance around a certain combination of methods was seen when Batch 2 was tested, as shown in Figure 108. Having two layers of each ink was found to be optimal. Repeating the first layer helps to ensure good adhesion as well as giving increased thickness which should ensure sufficient available TPB for reactions. Repeating the second layer, which acts as current collector, increases the conductivity due to the increased thickness. Adding a third layer of ink 2 caused a drop in performance, potentially due to mass transport effects with the thicker layer limiting gas transport to the cathode functional layer. The peak in the 0.6-0.8 A/cm^2 range is higher around Drr than around Fsr.

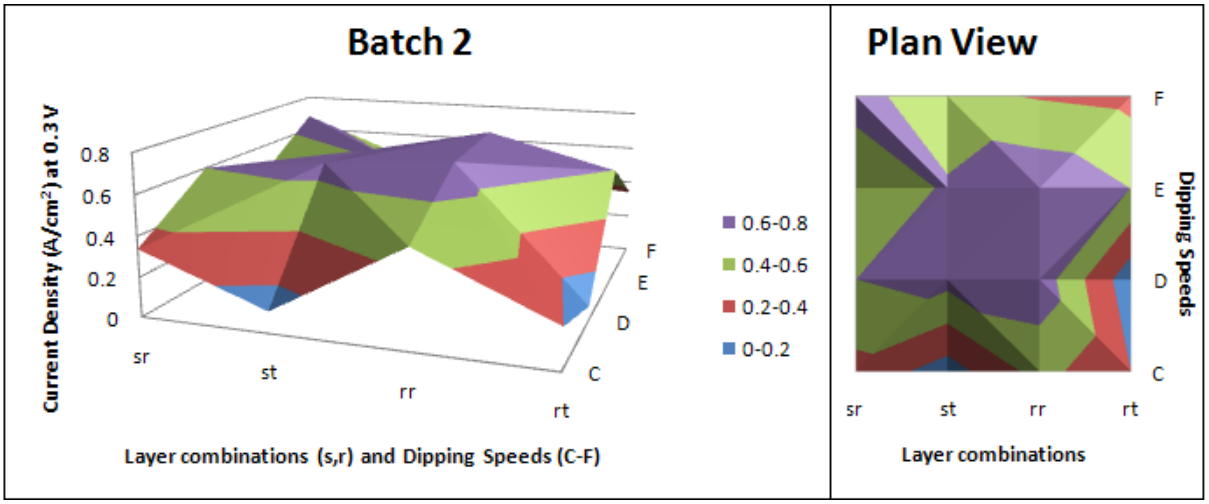

Figure 108 - Comparing dipping speeds and layer combinations in Batch 2 – currents recorded at 750°C with 20 ml/min. H_2 (AMI-5.5 µSOFCs)

The use of the new silver ink (DuPont 5025) for these cells may have hindered their performance, as shown in Figure 109, below. Further investigation into the performance of different silver inks has been performed, and the results are detailed in Table 12. Ink 5029 was found to be the closest competitor for the no longer available Johnson Matthey (JM) ink, and so became the new standard.

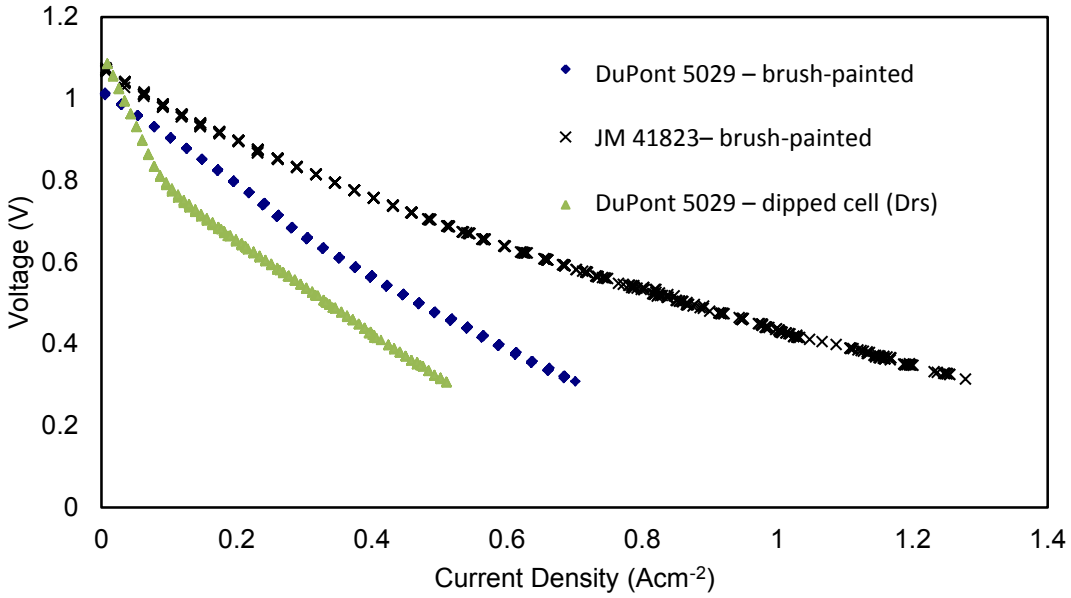

Figure 109 – I-V curves demonstrating the effect of a change in silver ink (750°C and 20 ml/min. H_2, AMI-5.5 µSOFCs)

Table 12 - Comparison of silver ink conductivities

Company	Product Code	Curing Conditions	Cell Ohmic Resistivity (as % of ink 5025 cell resistivity)
Johnson Matthey	41823	N/A (dried overnight at room temperature and pressure)	70±5%
DuPont	LF131	5 minutes drying at 180°C, 850°C peak held for 10 minutes	115±5%
DuPont	5025	5-6 minutes at 120°C	100%
DuPont	5029	5-6 minutes at 120°C	75±5%

6.1.4 Discussion and Conclusions

To summarise the results above:

- Faster dipping speeds give better electrical performance up to a point (120 mm/min.).

- A double layer of each ink gives better performance than a single layer of each, but adding a third layer does not continue this trend.
- A repeated layer of ink 2 (single layer of ink 1) gives better performance than vice versa.
    - Suggests that adhesion is not the only issue
    - Confirms theory that a thicker, so lower resistance, current collection layer is needed for these thin cathodes

It is noteworthy that the IV curves obtained for dip-coated cells drop much more rapidly from OCV than those for brush-painted cells. The slope of this section is due to activation energies; this suggests that either the amount of catalyst or electrode area should be raised or the temperature increased [25]. For the current project, raising the temperature would not be ideal due to the low required skin temperature of the UAV (50°C). Needing more surface area of the cathode and more catalyst suggested that the dip-coated layers are thinner and possibly less porous - this was indeed found to be the case, as shown in Figure 110. Thinner layers will facilitate the fabrication of multi-layer cathodes, but when just two different inks are used, the reduced thickness increases lateral resistance. The low porosity means that adding more layers to reduce the resistance causes mass transport issues, so the optimum number of layers found here is a trade-off between these competing demands.

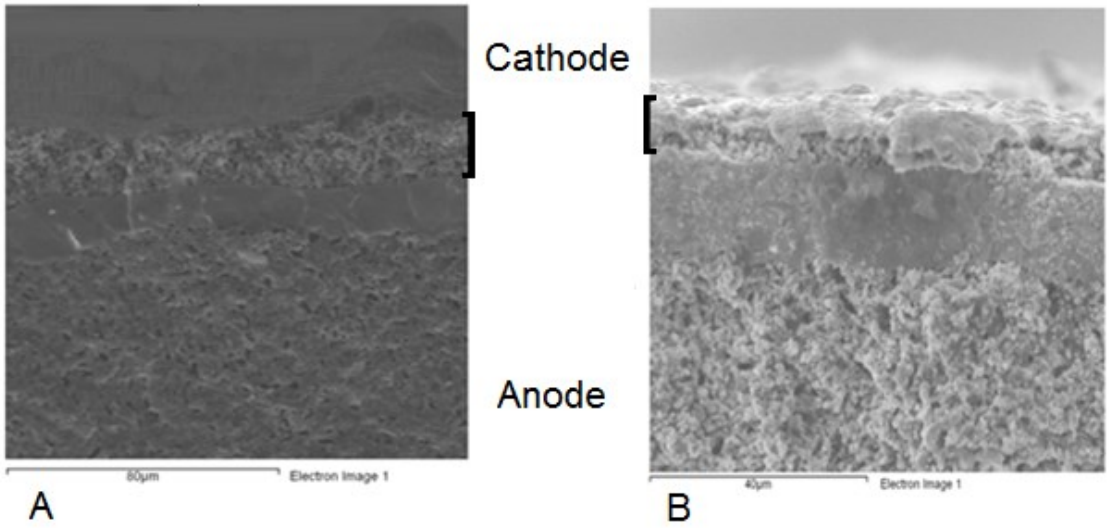

Figure 110 - SEM images of painted (A: cathode thickness 21±6 µm) and dip-coated (B: cathode thickness 7±1 µm) AMI-5.5 µSOFCs. Note that the cathode of cell B looks significantly smoother in texture, especially on the outer surface, suggesting reduced porosity (N.B. two different scales)

In the Ohmic section of the IV curve, the gradient for the dip-coated cells is still higher than that for the brush-painted cells, indicating a higher area specific resistance (ASR), but the difference in gradient is not as great. This increased ASR is expected due to the conductive layer of LSM being thinner.

Increasing dipping speed did improve performance up to a limiting speed of around 120 mm/minute, although a further increase caused performance to drop once more for cells with more layers (Figure 111). Withdrawal speed is known to have a significant effect on layer thickness when polymeric binders, surfactants or dispersants are used (as here) due to normal stresses on the surface layer [245], with thicker layers normally obtained at higher dipping speeds. This was confirmed by measurements taken from SEM images, showing that the cathode thickness for Drr (7±1 µm) was greater than that for Brr (5.4±1 µm) and Arr (5.3±0.5 µm).

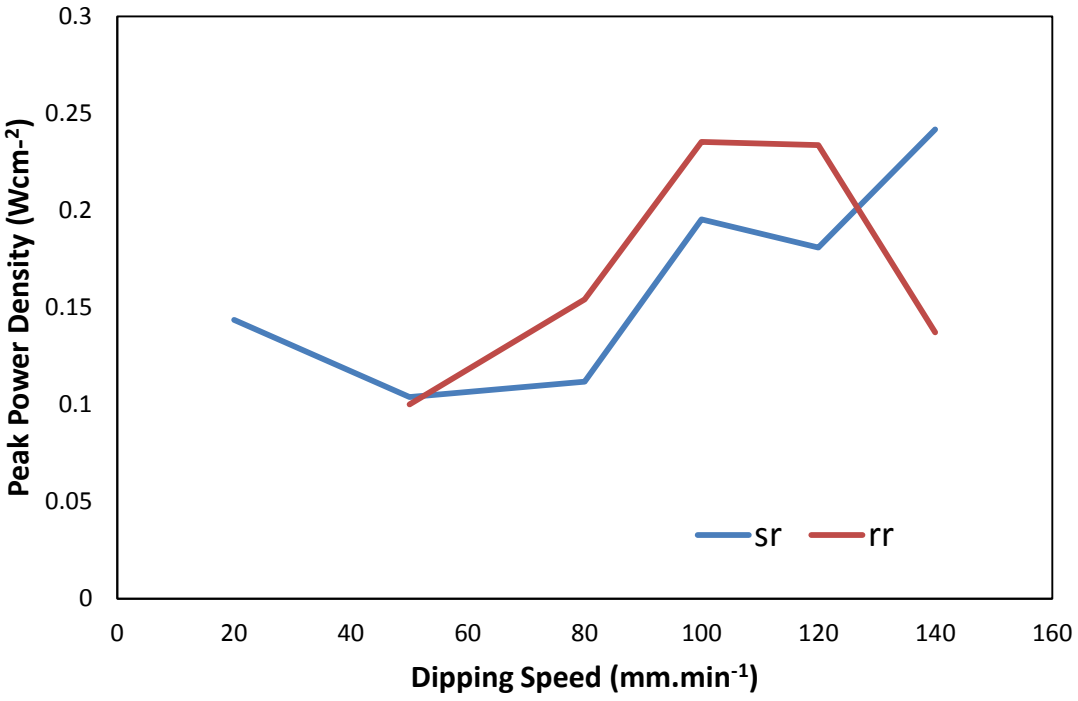

Figure 111 - AMI-5.5 µSOFC peak powers at 750°C with 20 ml/min H_2 with a double layer of each ink (rr) and with a single layer of the first ink and a double layer of the second (sr)

The number of layers also gave a very marked effect. More layers were shown to be good up to a point, but having five layers gave a reduction in performance.

Both of these trends can be explained by the same physical reasoning: very thin cathodes with these materials have insufficient reaction sites and conductivity to allow strong fuel cell performance, so increasing the cathode thickness (either with more layers or a faster pulling speed) improves performance as the resistance drops. Due to the low porosity of the cathode structure, however, a trade-off between conductivity increasing and mass transport limitation is reached, and performance falls again for too great a cathode thickness.

The volatile nature of the acetone ink makes it unsuitable for dip-coating as it quickly loses solvent to evaporation whilst in the dipping pot, altering the consistency. Layer thickness would therefore vary over time as the ink dried. Development of a water-based ink was therefore investigated to improve ease and scalability of production.

6.2 Development of a Water-Based Cathode Ink

This chapter is heavily based on work previously published, and is also the subject of a patent application [14].

At present, a variety of organic solvents is used for cathode inks, including acetone (as for the in-house recipe [145]), iso-propanol [243] and a mixture of methyl ethyl ketone and ethanol [78] or of terpineol and ethyl cellulose [246], but development of water-based inks has not proved widely successful. A water-based cathode ink offers several advantages:

- Reduced volatility, allowing longer-term storage and times for which containers can be open to the atmosphere without the surface drying.
- Fewer safety concerns or restrictions in terms of handling

[14] **Relevant Publications:**

K.S. Howe and E.R. Clark, A Novel Water-Based Cathode Ink Formulation for Solid Oxide Fuel Cells – UK Patent Application Number: 1107672.6

K.S. Howe, E.R. Clark, and K. Kendall. A Novel Water-Based Cathode Ink Formulation. in Zing Hydrogen and Fuel Cells Conference. 2011. Xcaret, Mexico.

K. S. Howe, E. R. Clark, J. Bowen, and K. Kendall, A Novel Water-Based Cathode Ink Formulation, *International Journal of Hydrogen Energy,* 38 (2013), 1731-36.

- Improved environmental credentials – as for the printing industry [247], it is reasonable to assume that fuel cell producers may in future be asked to improve their "green" credentials.

Only one paper mentioning a water-based cathode ink recipe [248] was found in the literature, although that of Luebbe *et al*. [249] details the preparation of an aqueous ceria slurry for an interlayer. In Luebbe's work, polyvinyl alcohol (PVA) was used as the binder, and polyacrylic acid (PAA) of molecular weight 2000 a.m.u. was used as the dispersant. Due to the similarity of the systems, PVA was chosen to be the binder for this research. Other polymeric binders, such as Heraeus V006, have also been shown to be effective in similar systems [250], but were not tested here.

The expense of PAA, and the fact that addition of a base is required to increase the pH in order to optimise chain properties and reduce unwanted side-reactions, make this a less appealing choice. Darvan C is another possible binder [251], but its active agent is again PAA, meaning that pH balancing must still be performed, even if by the supplier, not the SOFC manufacturer. The dispersant used in the work of Yashiro *et al*. [248] (carboxylic acid ammonium salt copolymer, A-6114, Toa Gosei Co. Ltd), likewise requires a basic solution to raise the pH. Raichur *et al*. [252] found Dolapix CE 64 to be an excellent dispersant for zirconia suspensions, but it is based on carbonic acid, so gives the same issues. Zhang *et al*. [9] used Triton X-114 (Octylphenol Ethoxylate) as a dispersant, and found it to be effective in producing well-stabilised zirconia solutions,

but again, it is mildly acidic. A non-acidic binder is preferable to avoid the complexity of pH adjustments.

Polylvinylpyrrolidone (PVP) is a neutral, water soluble oxygen-donor polymer which has been employed as a dispersant and anti-agglomerant in the synthesis of colloidal metal nanoparticles involving a range of metals [253-255]. PVP is known to undergo clean, thermally-activated breakdown to volatile by-products [256]. The neutral nature of PVP, coupled with its facile decay properties, makes it an attractive target for research as an inexpensive dispersant for inks for SOFC systems involving minimal additives.

The resultant novel cathode ink formulation is the subject of UK Patent Application Number 1107672.6 [257].

6.2.1 Ink Formulations

A batch of micro-tubular Solid Oxide Fuel Cells (µSOFCs) was prepared using in-house techniques[15]. For the PVP dispersant, polymer chain-length and amount added were observed to have system-specific effects on the size distribution of particles formed [253-255], so various chain lengths and amounts were tested. The in-house recipe

[15] Cells prepared by undergraduate students Olatunji Oduola, Mauricio Santos, Graham Lloyd, and Thomas Wood at the University of Birmingham under K.S. Howe's supervision.

(given in Chapter 3) was compared to various new cathode ink combinations (detailed in Table 13).

These are again bi-layer cathodes, so each is composed of two separate inks. The first, containing some Yttria-Stabilised Zirconia (YSZ), improves adhesion to the YSZ electrolyte as well as providing a large triple phase boundary area for reactions. This composite layer improves the ionic conductivity so that oxide ions can reach the LSM; it is the cathode functional layer. The second contains purely Lanthanum Strontium Manganite (LSM), which acts as the current collection layer. The inks were milled for 24 hours using milling beads of diameter 10 mm, then applied by brush-painting and left to dry.

Table 13 - Water-based cathode ink formulations

Component	**Cathode ink 1**		**Cathode ink 2**		**Cathode ink 1**		**Cathode ink 2**	
	PVP of molecular weight 10,000 (PVP10k)				**PVP of molecular weight 40,000 (PVP40k)**			
LSM (Merck 0.82/0.18)			10.00	g			10.00	g
LSM (SSC 0.5/0.5)	3.25	g			3.25	g		
TOSOH (TZ8Y)	3.25	g			3.25	g		
PVA (binder - 12% of powder weight)	0.78	g	1.20	g	0.78, 0.90, 1.00	g	1.20, 1.30, 1.40	g
Water	8.00	ml	7.00	ml	8.00	ml	7.00	ml
PVP (dispersant - 3.7% of powder weight)	0.24	g	0.37	g	0.24	g	0.37	g
#Milling beads used	7		8		7		8	
Ink 2 was also made with 0.37 g of PVP of average molecular weight 29,000 a.m.u. , with 0.74 g of PVP 10k, and with no PVP at all, for particle size comparisons. All other inks here used PVP with an average molecular weight of 40,000 a.m.u..								

The painted cells were then etched, silver-painted and silver wire-wrapped to provide current interconnections, as detailed elsewhere [203] and described in Chapter 3. A

simple test rig was used for cell testing, consisting of a furnace, temperature controlling apparatus and a Solartron™ analytical 1400 Cell Test System connected to a computer where purpose-built programmes were run using Cell Test™ (v 5.2.0) software. The cells were tested at 750°C with a flow rate of 20 ml/minute of hydrogen. After electrical testing, surface topography analyses were performed on the cells using a MicroXAM2 interferometer[16] (Omniscan, UK) operating a white light source at a magnification of 100X. Roughnesses and voidage analyses were performed using Scanning Probe Image Processor software (Image Metrology, Denmark). Areas of 86 µm by 64 µm were examined, which covered sufficient area to be representative of the surface character, given the individual particle sizes involved (0.7-2 µm). Three such areas were analysed per ink type.

Ink 2 samples were also examined using optical microscopy[17] to obtain approximate particle/agglomerate size distributions.

6.2.2 Results: Comparing Inks

Current-Voltage (IV) and power curves were plotted, as shown in Figure 112. Current density is calculated to allow the comparison of cells of differing areas – the active cathode area is used, excluding interconnections. Figure 112 shows that the water-based ink using PVP of average molecular weight 40,000 a.m.u. ("PVP 40k") gave similar, but marginally improved, results as compared to the "in-house" recipe. When

[16] Interferometry performed by Dr James Bowen
[17] Some of the microscopy work performed by undergraduate students Conor Macklin and Chung Chan Tham at the University of Birmingham under K.S. Howe's supervision.

the PVP was replaced with that with a lower average molecular weight of 10,000 a.m.u. ("PVP 10k"), the performance was poorer. This is hypothesised to be due to the difference in ceramic particle sizes, as discussed later in this section. Simply replacing the acetone with water in the in-house recipe also showed good performance – only slightly weaker than the acetone-based version – but does not give the advantage of simplicity due to the extra additives used.

The repeatability of these results was checked by running repeats on separate cells made in the same ways, with the same inks. Cells were also tested immediately after reaching temperature, and after a few hours of operation. Very good agreement was seen for all inks, and a sample of data for the best, water-based, ink is shown in Figure 113.

An improvement in performance was seen when comparing the initial IV curves to those taken two hours later. This suggests that some "pre-treatment" is useful – potentially the anode was not entirely reduced so the operating time at temperature can improve its structure.

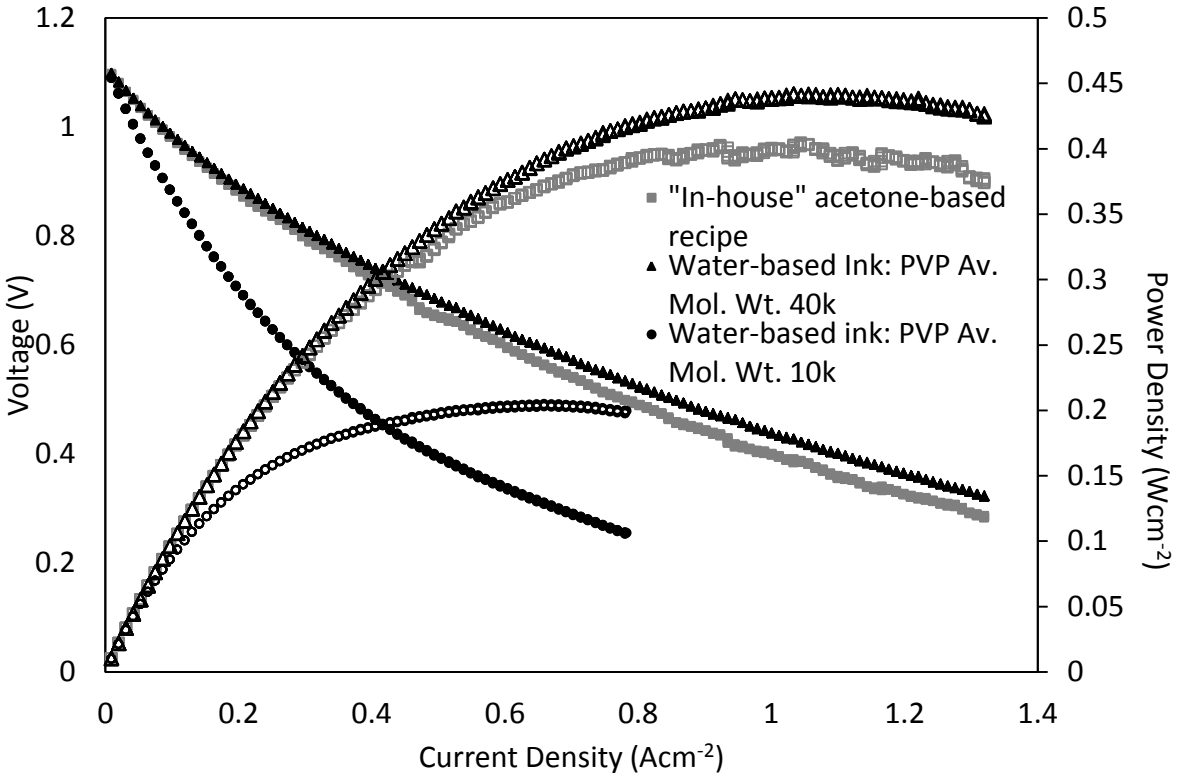

Figure 112 - Comparing I-V curves for AMI-5.5 µSOFCs with the different cathode inks (750°C, 20 ml/min. H_2)

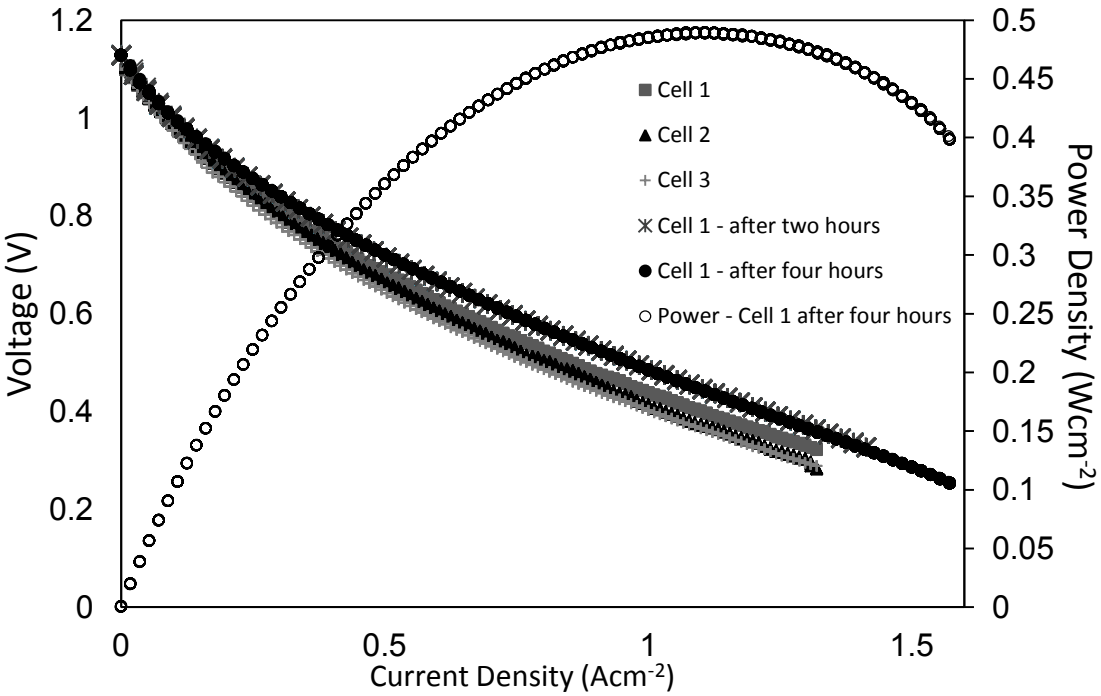

Figure 113 – I-V curves for AMI-5.5 µSOFCs demonstrating the repeatability of results with the new ink using PVP of molecular weight 40,000 (750°C, 20 ml/min. H_2)

Adjusting the amount of PVA used within the range tested had no noticeable effect on cell performance. Only a very small amount of delamination was seen, with a slight trend towards more delamination at higher PVA concentrations (Figure 114). These small delaminated areas were not deducted from the area used in current density calculations.

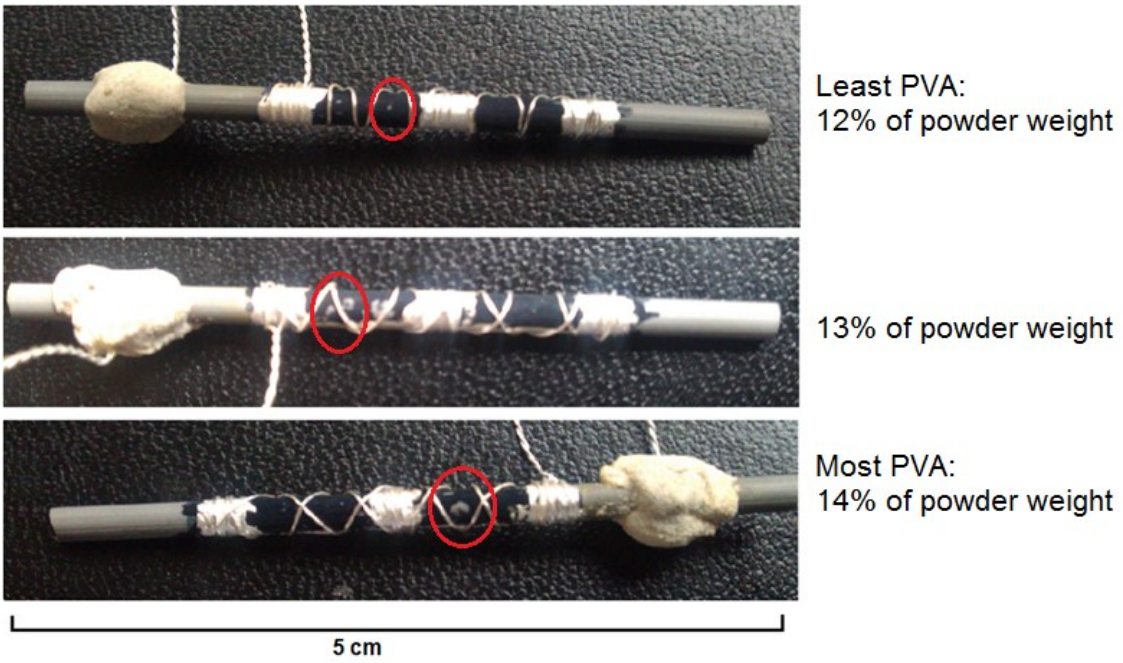

Figure 114 – AMI-5.5 µSOFCs with varying PVA concentrations showing slight delamination (examples circled in red) of cathode layer

Agglomeration of the ceramic powders used for the cathode ink can affect the surface area available for cathodic reactions and the porosity and tortuosity of the cathode, and hence electrical performance. The choice of dispersant controls this agglomeration for a specific powder. The effect of PVP has been seen to be very system-dependent; Wheatley *et al*. [253] observed positive correlation between PVP

chain length and particle size for their system of polymer-coated copper nanoparticles. By contrast, Miyake *et al*. [255] found that PVP chain length had no significant effect on platinum particle size, although the ratio of PVP to metal did - a smaller average particle size was observed when a larger quantity of PVP was used.

For the cathode ink under test, both PVP chain length and weight percentage of PVP were found to influence size distributions (Figure 115). A higher chain length shifted the distribution towards smaller particles, as did increasing the wt. % of PVP used. As molecular weight increased from 10,000 to 40,000 a.m.u., the average particle size decreased by nearly 40%. Doubling the mass of PVP used gave a more significant effect than quadrupling the chain length: an average size decrease of nearly 50% was observed, and the standard deviation was reduced, with only 5% of particles being above 4μm across. The larger weight percentage of dispersant present would increase the cost, however. A control ink sample, with no PVP, was also prepared, confirming that PVP has a real and beneficial effect. The average particle size in the absence of PVP was 4.3 μm; more than double that seen for inks using PVP 40k or the doubled mass of PVP 10k. Particle sizes were measured using an optical microscope, at x100 magnification, and graticule, with a minimum of 100 measurements taken per ink. Each sample was equally diluted with distilled water to facilitate the microscopy.

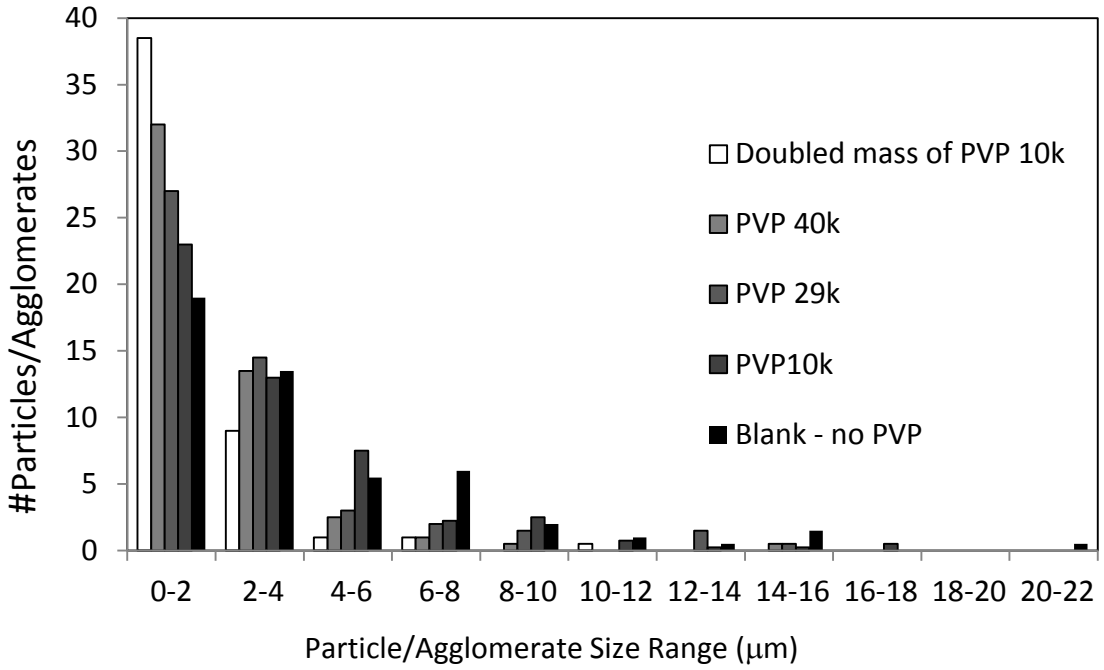

Figure 115 - Particle size distributions for cathode ink 2 with differing kinds and amounts of PVP; numbers scaled to per fifty particles over 100-200 measurements per ink

The void analyses performed suggest that the porosities of the cathodes made with the PVP 10k and PVP 40k inks are the same within errors, with a void percentage of 17.9±3.4% for the PVP 10k ink and 16.9±4.6% for the PVP 40k ink[18]. Roughness characteristics of the surfaces were very different, however. The average roughness, S_a, was found to be 1.17±0.02 μm for the PVP 10k ink and only 0.59±0.05 μm for the PVP 40k ink. The peak-to-valley roughness, S_y, was also significantly higher for the PVP 10k ink. Peak-to-valley measurements for the PVP 10k ink were up to one third of the total cathode thickness (~30 μm). This increased roughness may impede current flow from the cathode current collection layer to the metal interconnection, as contact area

[18] This analysis is only quasi-three dimensional, as pores not visible from the surface are not counted. A systematic underestimation of the porosity is therefore likely, explaining the lower than expected values, but the trends should be accurate. These values should not be compared to true porosity values obtained by other techniques.

would be reduced, as well as potentially leading to problematic thermal and potential gradients, which would be expected to give the lower electrical performance of the cells made with PVP 10k ink.

Cathodes made with the original "in-house" ink had similar surface roughness to those made with the PVP 40k ink, whilst having slightly lower porosities (void percentage of 14.8±3%), to which may be attributed their similar but slightly weaker performance.

PVP has been shown to have very different effects on particle sizes in different systems. This extreme specificity of behaviour is justified by the fact that PVP binds differently to different surfaces and crystal faces. Xia *et al*. [258] have shown that the size and shape of silver particles can be strongly affected by the molecular weight and concentration of the PVP, due to the differing surface free energies of the Ag(111) and Ag(100) facets when PVP is adsorbed. It seems probable that a similar effect is occurring with the LSM and YSZ particles used.

In light of these promising results, the scope was expanded to examine additional pH-neutral surfactants. Options include Triton X-100, which has previously been used alongside PVA with some success in pressed-pellet cathode preparation by Barnett and Tsai [259] and polyethylene glycol, used by Kim *et al*. [260] and Nishimoto *et al*. [261].

6.3 Dispersant Optimisation for the Water-Based Cathode Ink

Further optimisation work was then undertaken, focusing on the dispersant: Poly(N-VinylPyrrolidone) - PVP [19]. The effects of chain length and weight percentage of PVP have been investigated, and Poly (ethylene glycol) – PEG - was tested for comparison. PEG was found to give good performance at lower weight percentages, but had a negative impact on ink rheology at higher concentrations. Optimisation of the ink formulation increased the peak power from 0.48 to 0.64 W/cm^2 under identical test conditions (the power at 0.7 V increased from 0.33 to 0.46 W/cm^2). Trends were analysed in both peak power and power at 0.7 V, confirming that, as expected in excess fuel test conditions, the choice of comparison point does not have a significant effect on the results.

PVP is not the only possible dispersant to meet the requirements discussed in Section 6.2. PEG also has a fairly neutral pK_b and is soluble in both water and various organic solvents [262]. It has been used as binder and dispersant [263-267] in fuel cell fabrication, in both aqueous and organic solutions. In aqueous solutions, it has a large exclusion volume [262], which could make it ideal for reducing particle agglomeration if the ceramic powder particles are coated in PEG chains. However, in high concentrations, other polymers can be excluded to the extent that a biphasic system forms. This could have a negative effect on the ink miscibility as poly(vinyl alcohol) is used as binder in the formulation under test.

[19] 4th year students Z. H. Song and T.H. Kueh performed some of the experimental work, under the supervision of the author

In this study, PVP and PEG were tested and compared as dispersants to optimise the previously-developed cathode ink recipe.

6.3.1 Experimental

µSOFCs were prepared using the in-house techniques discussed previously [203]. Eleven different cathode types were used, as detailed in Table 14 and Table 15.

Ink Formulations

The ink formulation used is the same as that discussed in Section 6.2, with the optimal loading of PVA chosen and the dispersant type and loading being the test variables. This formulation is summarised again in Table 14 for clarity. The type and quantity of dispersant was varied with all other components unchanged. Quantities of binder and dispersant used were calculated as weight percentages of the ceramic powder weight used.

Table 14 – Cathode ink formulations – the basic recipe

Component	Cathode Layer 1	Cathode Layer 2
LSM (Merck 0.82/0.18)		10.00 g
LSM (SSC 0.5/0.5)	3.25 g	
YSZ (TOSOH TZ8Y)	3.25 g	
Binder: PVA (12% of powder weight)	0.78 g	1.20 g
Solvent: distilled water	8.00 ml	7.00 ml
Dispersant: PVP or PEG	*(various)*	*(various)*
#milling beads used	7	8

The variations made to the ink formulation are listed in Table 15. For each cell made, the same weight percentage of dispersant was used in cathode layer 1 as in cathode layer 2. For PVP, the quantity used was calculated as a total weight percentage of all

ceramic powders. The range of values chosen was around those tested and found successful in previous work [268]. For PEG, the quantity used was calculated as a weight percentage of the YSZ powder plus a different weight percentage of the LSM powder, based on ratios used by McCoppin *et al.* [269] in their fabrication of LSM and YSZ inks.

Ink Analysis

Particle size distributions were analysed by optical microscopy, with 50 randomly-selected particles measured per ink, and High Performance Particle Sizing (HPPS). HPPS allows a greater number of particles to be measured more quickly and can be used to examine trends between inks, but is quantitatively less accurate. The effect of dispersant type and concentration on the size distribution was examined.

Table 15 – Cathode ink formulation variations

Ink	Dispersant	Molecular Weight (a.m.u)	Weight Percentage
PVP - 1	PVP	40000	3.70[a]
PVP - 2	PVP	10000	3.70
PVP - 3	PVP	40000	7.40
PVP - 4	PVP	40000	1.85
PVP - 5	PVP	40000	5.55
PVP - 6	PVP	40000	11.10
Blank	N/A	N/A	0
PEG - 1	PEG	8000	LSM: 16.00, YSZ: 3.00
PEG - 2	PEG	8000	LSM: 8.00, YSZ: 1.50
PEG - 3	PEG	8000	LSM: 6.40, YSZ: 1.20
PEG - 4	PEG	8000	LSM: 3.20, YSZ: 0.60
[a]This ink showed good agreement with previous work using the identical formulation (Section 6.2 and [268])			

Cell Testing

As before, the cells were tested at 750°C with a flow rate of 20 ml/minute of hydrogen at 1.5 bar. Each cell was heated to temperature and then tested over a three hour period consisting of an IV curve, two hours of operation at 0.5 V then a final IV curve.

Peak power densities and power densities at 0.7 V were taken from the IV curves and compared to judge cell performance with the different inks. Three cells were prepared and tested for each ink variant to ensure reliability of the results.

6.3.2 Results and Discussion

Comparing Chain Lengths of PVP

Two different molecular weights of PVP (10,000 a.m.u and 40,000 a.m.u.) were tested to investigate the effect of chain length on ink performance. Although there was some variation between the three repeats for each ink, as shown by the error bars in Figure 116, PVP-1 gave significantly stronger performance than PVP-2, confirming previous results that ink performance improves with PVP chain length [268]. Increasing the molecular weight from 10,000 to 40,000 a.m.u. gave a 39% increase in power at 0.7 V for the same weight percentage of dispersant used.

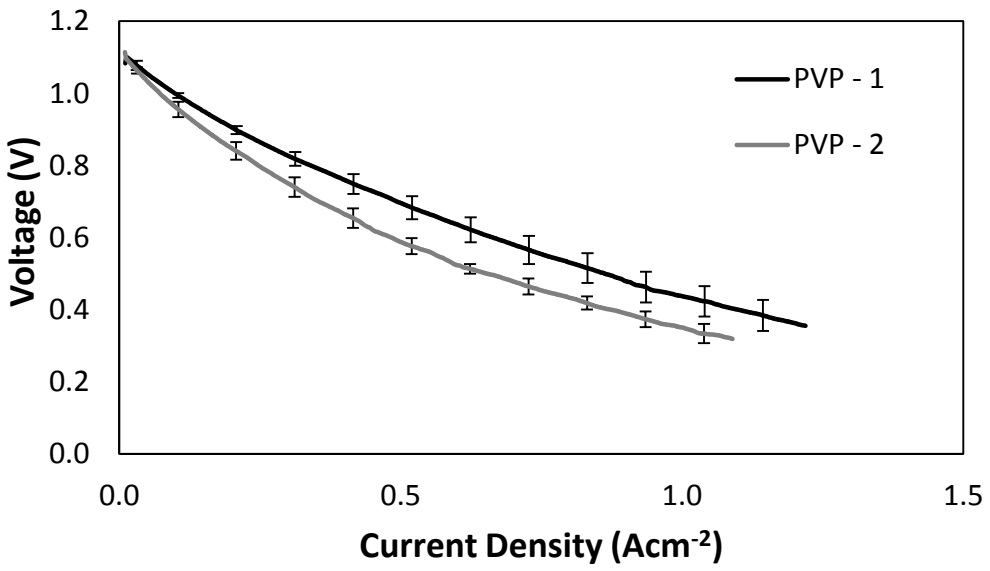

Figure 116 – I-V curves for AMI-5.5 µSOFCs at 750°C with 20 ml/min H_2 to compare the performance of cathode inks made with PVP of molecular weight 40,000 a.m.u (PVP-1) and 10,000 a.m.u. (PVP-2)

Studying particle size distribution by optical microscopy firstly confirmed that the dispersant does have a significant effect on particle size distributions: presence of PVP narrowed the size distribution and reduced the average particle size by nearly 20% (Figure 117). The average size was seen to decrease further when PVP of molecular weight 40,000 a.m.u. was used instead of that with a molecular weight of 10,000 a.m.u.. These results were confirmed by HPPS.

The higher molecular weight arises from a longer, linear PVP molecular chain. It is hypothesised that the longer polymer can coat the particles more effectively, so reducing aggregation and thereby giving smaller average particle sizes. Reduced agglomeration should provide a larger surface area for reactions, hence allowing a higher power density to be generated.

Due to its stronger performance, the efficacy of PVP of molecular weight 40,000 a.m.u. was then investigated further by adjusting the loadings used.

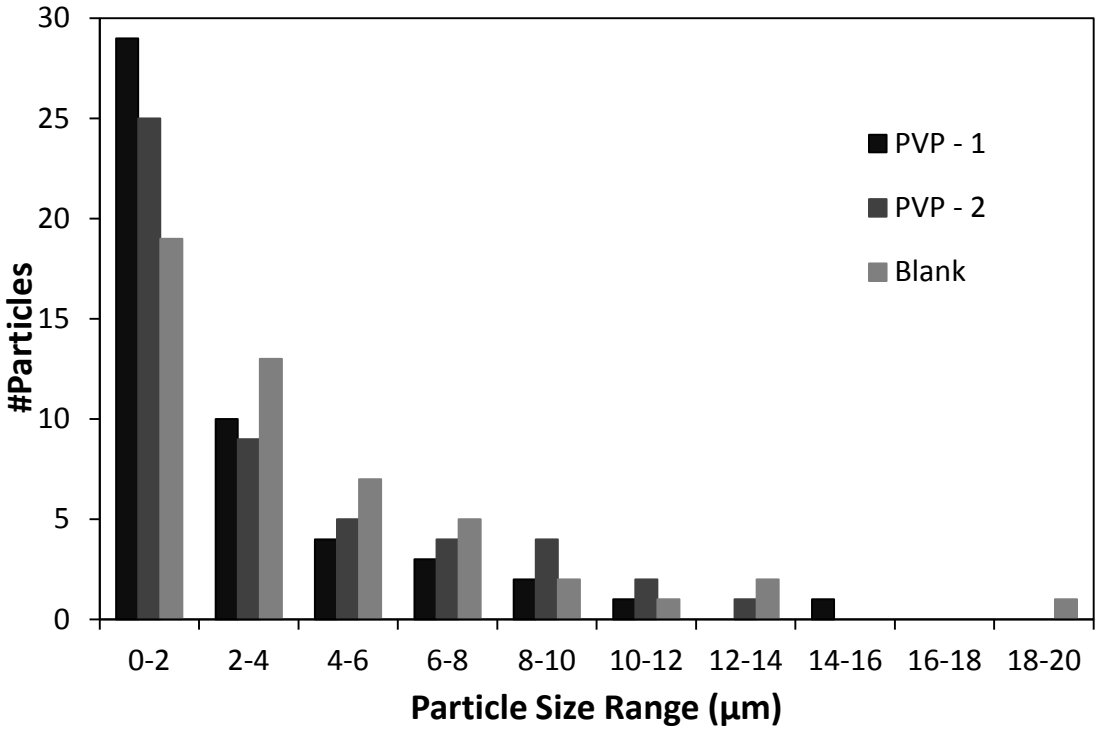

Figure 117 - Particle size distributions in cathode inks made with no dispersant, with PVP of molecular weight 40,000 a.m.u (PVP-1), and PVP 10,000 a.m.u. (PVP-2).

Comparing Weight Percentages of PVP

Including the blank (0 wt.% PVP), six different loadings of the dispersant were tested. The relationship between PVP loading and power at 0.7 V was not simple, as shown in Figure 118. This figure also illustrates the similarity between comparisons of peak power and of power at 0.7 V, confirming that either comparison point is valid.

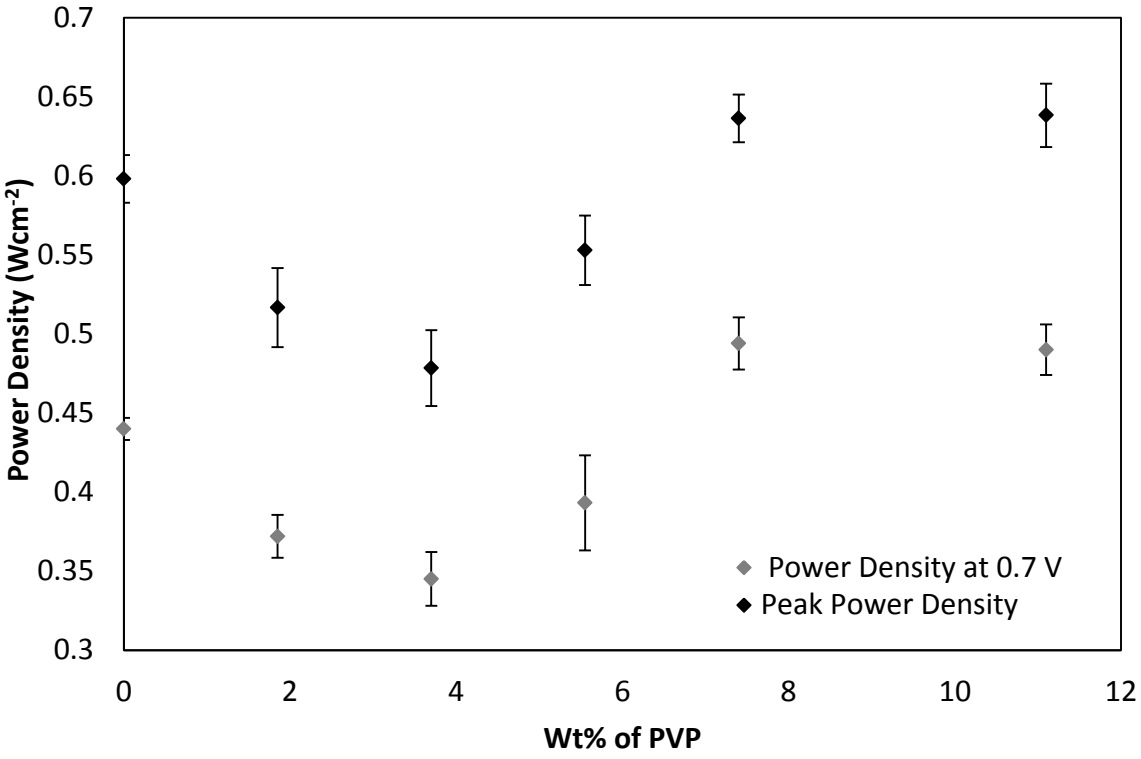

Figure 118 - Average power densities at 0.7 V and peak power densities obtained from AMI-5.5 µSOFCs made with various loadings of PVP with a molecular weight of 40,000 a.m.u. as dispersant (at 750°C with 20 ml/min. H_2)

Unexpectedly, at low loadings, the power obtained decreases as the weight percentage increases, however this changes after the weight percentage reaches 3.7 wt.%. The average power then increases with a further increase in wt.% before levelling off from 7.4 wt.%. The average particle size does decrease with increasing PVP loading, so this cannot be purely a particle size effect.

To explain this behaviour, it is hypothesised that when a small amount of PVP is present, the polymer tends to break up agglomerates but give little dispersion of the smaller particles, thus lowering the peak power. Although the particles are smaller, they may be more closely packed in the final cathode structure, so reducing the porosity and internal surface area after sintering. Further increase in the amount of

dispersant provides sufficient polymer to coat most of the ceramic particles and excess polymer present between the coated particles should help to avoid close packing and agglomeration on sintering and create a more porous, open structure. This increases the surface area available after sintering, which enables the fuel cell to achieve a higher peak power and better performance. Beyond this point, all the ink particles are well dispersed, with no remaining agglomerates, so increasing the amount of dispersant does not bring further improvement to the peak power.

To test this hypothesis, surface analysis of the cathode layers obtained from the different inks was performed using AFM[20]. The data were unfortunately inconclusive, with no clear trends in either voidage or roughness characteristics. Further testing with a larger sample size would be needed to prove or disprove this hypothesis.

The Effect of PEG

Cells prepared with 3.2 wt.% of PEG gave a power density of 0.40 W/cm^2 at 0.7 V which is slightly higher than that obtained with PVP in previous research [268], but lower than that obtained with the optimised weight percentage discussed above. This promising result suggests that PEG has strong potential as a cathode ink dispersant.

The performance of PEG was investigated by changing the proportion used in the cathode ink recipe. The original quantity of PEG used was doubled (6.4 wt.%) but this lowered the power density obtained to 0.29 W/cm^2. This unexpectedly low power may

[20] Courtesy of Dr James Bowen

be due to rheology and polymer exclusion issues associated with higher concentrations of PEG in water having a deleterious effect on cathode structure [262].

The cathode inks prepared with 6.4 wt.% PEG or less (PEG-3 and PEG-4) show similar physical properties to those prepared with PVP. However, at higher concentrations of PEG, the cathode ink began to show immiscible behaviour and some aggregates were noticeable while applying ink onto the fuel cell. When the ink was left over time, two layers of liquid formed showing significant separation of the ink ingredients. PEG-1 and PEG- 2 did not give satisfactory fuel cell performance.

Trials of PEG with reduced molecular weights, and of additional dilution with water, may yield more suitable ink behaviour. Preliminary testing of additional dilution was promising, but this line of research was not taken further. Removing PVA is also an interesting option, as PEG can act as binder and the absence of PVA may avoid phase separation of the ink.

6.3.3 Conclusions and Further Work

Dispersant optimisation for use in a water-based cathode ink for SOFCs has been performed. The dispersants tested were PVP and PEG, with a range of weight percentages and molecular weights tested.

Over the range of variables tested, PVP was found to be a more suitable dispersant in this system due to solubility effects associated with aqueous PEG causing problems in the ink rheology. The power density at 0.7 V (at 750°C with 20 ml/minute of hydrogen) obtained was significantly increased - from 0.33 to 0.46 W/cm^2 - by optimising the loading of PVP with a molecular weight of 40,000 a.m.u. A summary of the improvements made - from the original acetone-based recipe to initial testing of water-based inks and then dispersant optimisation – is shown in Figure 119.

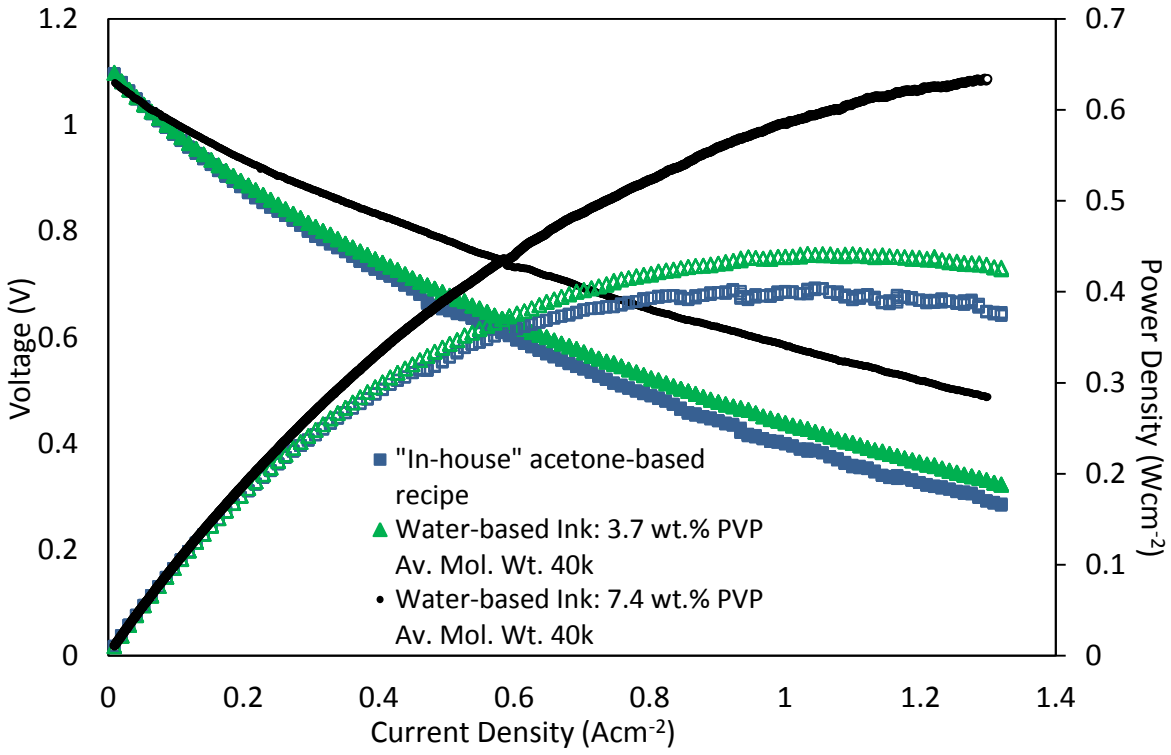

Figure 119 – I-V and power curves to demonstrate overall progress in AMI-5.5 µSOFC performance with ink development (750°C with 20 ml/min H_2)

The relationship of the loading of PVP in the ink to fuel cell performance was found to be more complex than initially thought, and further work will hopefully elucidate the dispersion mechanism in this system.

Overall, a novel, water-based ink formulation for use in solid oxide fuel cells has been successfully demonstrated, giving a peak power density of 0.64 W/cm^2. In addition to the improvement of ink safety and environmental credentials by avoiding the use of organic solvents and acidic and basic additives, a slight increase in performance was seen as compared to the in-house ink. Peak power densities given in the literature under similar conditions [72] suggest that the in-house ink performance falls well within the expected range.

A strongly performing, simple, more user-friendly and "green" ink has been developed, and has potential appeal for all SOFC researchers and manufacturers. Being water-based, this ink is less volatile than the previous acetone-based ink used in-house, so should be more suitable for dip-coating. Further work would be needed to test and optimise the dip-coating parameters for this ink.

7. ELECTRODE INFILTRATION

This chapter reports work performed in collaboration with Dr A. R. Hanifi from the University of Alberta, and has been the subject of two publications [21]. The infiltration was performed by A. R. Hanifi, and the infiltrated cells were prepared and tested, and the results analysed, by the author.

Electrode production by infiltration for micro-tubular solid oxide fuel cells (µSOFCs) has been investigated previously with the aim of improving their RedOx and thermal cycling resistance [270] due to improved thermal expansion coefficient matching of the electrolyte-electrode . The microstructure of the porous YSZ substrate used as a scaffold for infiltration was shown to have a strong influence on effective infiltration which resulted in improvement of cell power [271]. This technique has been investigated by various groups, for example [270-272], with remaining scope for optimisation [273]. It was first developed to allow separation of the YSZ calcination temperature from the sintering temperature of the other components [273], but other advantages emerged, such as improved conductivity at lower percentage compositions of the conductive oxide [274]. This is explained by a thin surface coating of LSM allowing good connectivity, whereas, for a random composite, the electrically

[21] **Relevant Publications:**
Howe, K. S., Hanifi, A. R., Kendall, K., Etsell, T. H., and Sarkar, P., "New Methods of Electrode Preparation for Micro-Tubular Solid Oxide Fuel Cells", 2012, 10th European Solid Oxide Fuel Cell Forum, Fuel Cell Forum, Lucerne.

Howe, K. S., Hanifi, A. R., Kendall, K., Etsell, T. H., and Sarkar, P., "Performance of Microtubular SOFCs with Infiltrated Electrodes under Thermal Cycling", International Journal of Hydrogen Energy, 38 (2013), 1058-67.

conductive phase (i.e. LSM) must be at least 30% of the composite by volume to allow that phase to ‘‘percolate’’ the random structure [275].

In this work, tubes consisting of a co-extruded dense YSZ electrolyte and porous NiO-YSZ anode were modified with different cathodes, and with anode infiltration to investigate the effects on both power and thermal cycling tolerance.

Several variables were investigated, namely the type of cathode (produced by infiltration of LSM into a porous YSZ matrix or by hand-painting of an LSM-YSZ ink), the type of pore former used in the cathode and the infiltration of the anode (no infiltration, or with infiltration steps using a co-precipitated nickel-samaria-doped ceria (Ni-SDC) solution, or SDC solution). The overall aim of this work is to produce higher performing cells, as compared to those made by current in-house techniques, monitoring cell stability upon thermal cycling. As the Ni-YSZ anode of these cells is vulnerable to RedOx cycling (see Chapter 2), only thermal cycling was tested here.

There are three key hypotheses to be addressed:

1. The infiltrated cathode should give better performance than the painted cathode due to the higher surface area and catalytic activity of nano-sized LSM particles
2. Infiltration of the anode should increase the available active surface area, and conductivity, thus improving performance

3. The limiting factor for thermal cycling tolerance is expected to be the cycling degradation of the Ni-YSZ anode; infiltration of SDC into the anode may help to reduce sintering of fine nickel particles, thereby reducing degradation

In addition, the choice of pore former for the TPL (graphite or PMMA) was investigated, and data gathered on thermal cycling capabilities.

High electrode porosity is crucial to facilitate gas flow to the triple phase boundary (see Chapter 2), where reactions occur, but conductivity and mechanical strength would be compromised if the porosity were too high. According to Jin *et al.* [111], anode porosity should be no greater than 55% to avoid a detrimental increase in resistivity. Pore size was also identified as significant, with large pores reducing mechanical strength. Suzuki *et al.* [93] found that "a highly porous microstructure" with very small constituent particles (<100 nm for the Ni particles in the anode) optimised the cells' electrochemical performance. For the anode, adding a dopant such as ceria [88] has been seen to improve performance on thermal and RedOx cycling. It has been shown that the infiltration of SDC into Ni/YSZ composite anodes inhibits Ni grain growth [276] and improves the electrochemical performance of the anode since the doped ceria is a mixed ionic and electronic conductor and is catalytically active for the oxidation of hydrogen and reduction of oxygen [277, 278]. In addition, infiltration of ceria-based catalysts improves the sulphur tolerance of Ni/YSZ anodes greatly [279, 280]. Control of YSZ particle size and porosity [92, 93] also helps to improve the stability under RedOx conditions.

Various different materials have been tested for their suitability as pore formers, for example flour and graphite (which can then be burned off) and magnesium oxide (removed using an acidic solution) [87, 111, 164, 165]. Although flour offers a low-cost option, it showed more significant shrinkage on sintering, leading to the formation of overly large pores [111]. Graphite and PMMA were tested as cathode pore formers in this work.

Research [273, 274, 281, 282] suggests that infiltration can greatly enhance the ionic and/or the electronic conduction pathway and the catalytic activity, as compared to a mixed matrix. For example Sholklapper *et al.* [272] found that infiltration of LSM into their cathode decreased the cell's total Ohmic resistance (found by EIS) by around 90%. The polarisation resistance also decreased from 110 Ωcm^2 to 2.9 Ωcm^2 on infiltration, indicating the huge increase in electrochemically active surface area provided by the infiltrated nanoparticulate LSM. Figure 120 shows SEM images of the cells used in that work.

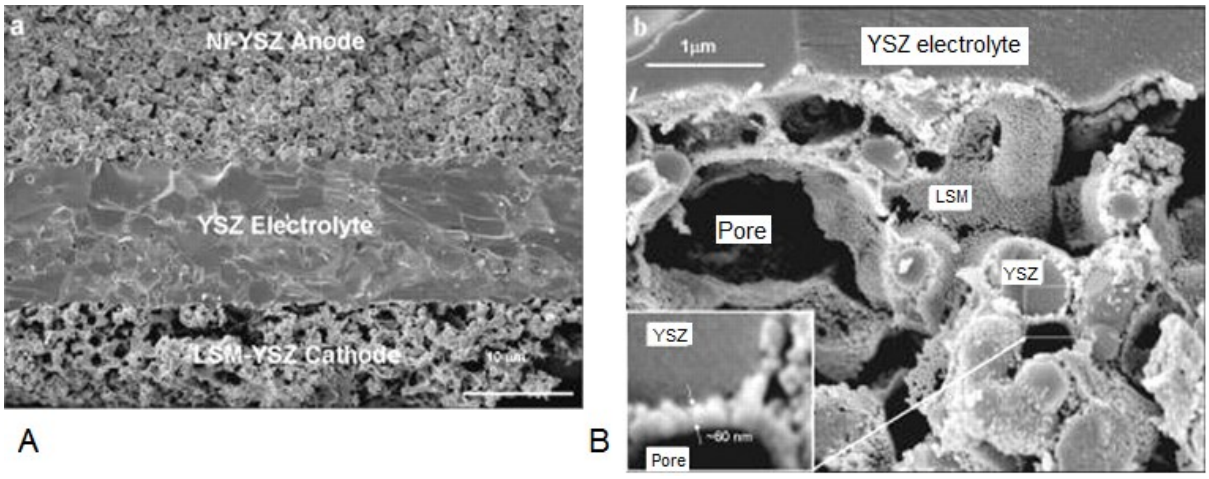

Figure 120 – SEM images of mixed composite (A) and infiltrated (B) YSZ-LSM fuel cells [272]

7.1 Experiments

Due to lack of time and AMI ceasing production of the AMI-5.5 µSOFCs used, it was unfortunately only possible to test a total of ten cells. Preparation routes for each of these cells were selected, as shown in Table 14, to cover the desired variables whilst minimising the number of experiments required. There is only one pair of direct repeats, but the other tests can be grouped in different ways to give repeat tests of a given variable.

7.1.1 Cell Fabrication

Cells 1-8 were prepared by infiltration at the University of Alberta and tested alongside two cells (Cells A and B) made purely to current in-house techniques at the University of Birmingham (details of preparation methods available elsewhere [21, 22] and in Chapter 3), using the same co-extruded YSZ-NiO anode, YSZ electrolyte tubes. Cells A and B have bi-layer (LSM-YSZ, LSM), hand-painted cathodes, with no infiltration.

The infiltration processes described below (performed by A. R. Hanifi for cells 1-8) allows addition of electro-active materials throughout a porous matrix. His method is reported here for reference:

To coat a thin porous layer (TPL) for cathode infiltration, YSZ (calcined at 1500°C, milled for 72 hours in water and dried) was mixed with 20 vol.% graphite (Sigma Aldrich US 325 mesh) or PMMA (CA 6, product of Microbeads Company, Norway), dispersant (Menhaden fish oil), azeotropic solvent (toluene/ethanol) and binder (polyvinyl butyral). The components were

mixed at 300 rpm for one hour in a planetary mill prior to coating. The mixture was applied to the electrolyte surface by dip coating. The tube was heated in air at 300°C and then at 700°C for one hour at each temperature to burn off the organic components, PMMA and graphite, then sintered at 1350°C for three hours.

Table 16 - Prepared infiltrated AMI-5.5 µSOFCs

	TPL* pore-former	Thickness of Cathode (µm)	Weight % of LSM in the Cathode	Anode Infiltration	Cathode Infiltration
Cells with infiltrated cathodes					
Cell 1	Graphite	10-15	32	None	LSM x2
Cell 2	Graphite	10-15	30	SDC x2 (2.5wt.%)	LSM x2
Cell 3	Graphite	10-15	35	Ni-SDC x4 (3.5wt.%)	LSM x2
Cell 4	PMMA	10-15	33	None	LSM x2
Cell 5	PMMA	10-15	33	SDC x2 (1.6wt.%)	LSM x2
Cell 6	PMMA	10-15	26	Ni-SDC x4 (3.8wt.%)	LSM x2
Cells with thicker infiltrated cathodes					
Cell 7	Graphite	30-40	28	None	LSM x2
Cell 8	PMMA	20	33	None	LSM x2
Cells with hand-painted cathodes					
Cell A	N/A	100[†]	70	None	None
Cell B	N/A	10-15	70	None	None

*TPL: Thin Porous Layer (basis for infiltrated cathode)
[†] Much thicker than intended – brush-painting does not give fine control; however, little difference is observed due to the increased thickness as a) it is sufficiently porous to facilitate gas transport and b) sufficient LSM is present within the usual thickness

The SDC infiltration of the Ni-YSZ support was carried out using a mixture of $Sm(NO_3)_3.6H_2O$ (Alfa Aesar) and $Ce(NO_3)_3.6H_2O$ (Alfa Aesar), a small amount of a polymeric dispersant Triton X-45 (Union Carbide Chemicals and Plastics Co. Inc.) and water, to give $Sm_{0.2}Ce_{0.8}O_{1.9}$ after decomposition. For Ni-SDC infiltration, $Ni(NO_3)_2.6H_2O$ was mixed with SDC nitrate salts. The mixture was heat treated at 100°C to give a high viscosity concentrated solution. The

increased viscosity solution was then infiltrated into the porous Ni-YSZ support using a vacuum chamber. The tube was heat treated at 350°C for 15 minutes to convert the nitrate salt to oxide compounds. The infiltration procedure was repeated twice to deposit SDC or Ni-SDC particles into the anode matrix. The cathode was also prepared by precursor infiltration. The solution used for infiltration of the cathode, LSM ($La_{0.80}Sr_{0.20}MnO_3$), was prepared by mixing appropriate amounts of $La(NO_3)_3 \cdot 6H_2O$ (Alfa Aesar), $Mn(NO_3)_2 \cdot XH_2O$ (X ~ 5, Sigma Aldrich), $Sr(NO_3)_2$ (Sigma Aldrich), a small amount of Triton X-45 (Union Carbide Chemicals and Plastics Co. Inc.), and the minimum amount of water to dissolve all components when heated at 96°C to give a highly viscous, concentrated solution. This solution was then impregnated into the porous support as for the anode. The impregnated tube was dried in an oven at 150°C prior to heat treatment at 350°C. The total addition of LSM on infiltration was 30 wt.% of the TPL.

The cells were then transferred back to the University of Birmingham for continued preparation and subsequent testing.

After sintering, the cells were reduced in pure hydrogen and etched to create an external anode connection. Silver ink and wires were used to create the interconnections. Each cell has an active cathode area of ~1 cm^2.

Cells 1-8 have approximate cathode porosities (calculated from pore:ceramic ratios in the SEM images) of 55%, which is higher than that of Cells A and B (~30%). The prepared cells were all tested under the standard conditions of 750°C with 20 ml/minute of dry hydrogen.

Harsh thermal cycles were performed between 750°C and 400°C, at 100°C/minute, with current-voltage (IV) curves taken before and after sets of cycles. Furnace insulation hinders rapid cooling below this temperature. The test schedule below was run over two days.

Day 1 test schedule:

1. 30°C/minute heat-up with measurement of open circuit voltage (OCV)
2. IV curves
3. One hour constant operation at 0.5V
4. IV curves
5. Eight thermal cycles (100°C/minute) with two minute pauses at each extreme (OCV recorded)
6. IV curves
7. Eight thermal cycles (100°C/minute) with two minute pauses at each extreme (OCV recorded)
8. IV curves
9. One hour constant operation at 0.5V
10. IV curves
11. Natural cooling with measurement of OCV

The Day 2 test schedule was the same, but with steps 5 and 8 each replaced with twenty thermal cycles with one minute pauses at each extreme.

7.2 Results

The results below are arranged according to the three hypotheses listed earlier and the comparison of pore-former type.

Given the small sample sizes, the Kolmogorov-Smirnov Test (K-S Test) was used to compare datasets to check the statistical significance of the results. The two-sample K-S Test is a nonparametric test for assessing whether or not two datasets differ significantly by examining the difference between cumulative distributions. The null hypothesis is that the two datasets are samples from the same distribution – if the probability value, P, calculated is "small", the probability of the null hypothesis being true is small. Therefore a small P value confirms that there is a statistically significant difference between the two datasets.

As a reference point, the dataset of peak powers for Cell A (i.e. each cell's dataset being ten peak powers – one drawn from each of the even-numbered steps in the test profile described above) was compared to the dataset for Cell B. As these two cells were prepared identically, it would be hoped that the null hypothesis of their datasets coming from one distribution is not rejected. The maximum difference between the cumulative distributions, D, was found to be 0.3, corresponding to a P value of 0.675. As significance cut-off level of P=0.05 or P=0.01 is usually used to reject the null hypothesis, this P value is high, so the null hypothesis is not rejected. This test indicates that there would be a 67.5% probability of obtaining a D value at least as large as that found by chance assuming that both datasets were drawn from the same distribution.

7.2.1 Infiltrated Cathode – Improved Power?

The current-voltage (IV) curves recorded for each cell were compared before any thermal cycling. An improvement in performance is often seen over initial operation as this period allows any remaining unreduced nickel oxide in the anode to be reduced to nickel. IV curves from Step 4 are, therefore, used in preference to those from Step 2. Cells 1 and 4 were compared to Cells A and B, as these pairs of cells should only differ in the cathode structure; the IV curves are given in Figure 121.

As previously mentioned, direct repeats were generally not performed due to cost and time limitations, but Cells A and B give almost identical IV curves, as would be expected for two cells prepared by the same method. The unintended large difference in cathode thickness has not given a significant effect. Cells 1 and 4 were noticeably more resistive than A and B, in direct opposition to what was expected. The cathodes prepared as a porous YSZ matrix with infiltrated fine LSM particles were expected to give higher catalytic activity than the standard in-house cathode, due to the higher surface area, and better connectivity of conductive phases, hence significantly better cell power. This may only be valid when the total amount of LSM present is similar, however. The poorer performance was hypothesised to be due to the lower total amount of LSM in the infiltrated cathodes (approx. 30 wt.%, as compared to 70 wt.% in the painted cathodes). The electronic conductivity depends on weight percentage rather than total weight, to guarantee percolation, and this should be more than sufficient as 30% is the minimum acceptable for a random composite, and infiltration reduces this threshold, as mentioned earlier [274].

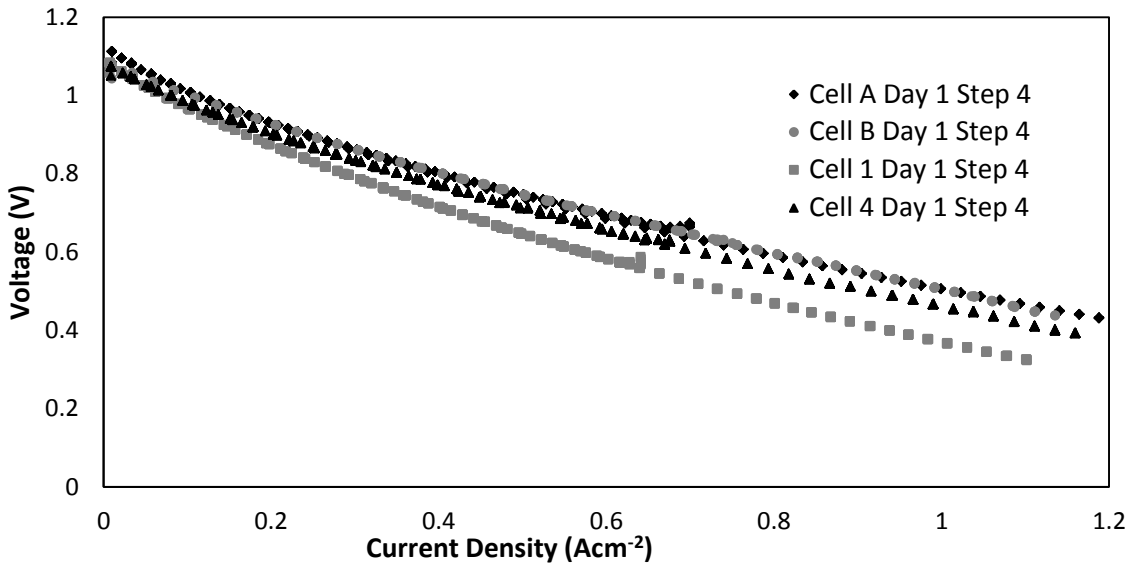

Figure 121 - Comparing I-V curves at 750°C with 20 ml/min H_2 for painted AMI-5.5 µSOFCs (A,B) to those for AMI-5.5 µSOFCs with infiltrated cathodes (1: graphite pore-former, 4: PMMA pore-former)

In the painted cathodes (Cells A and B), the higher amount of LSM provides more surface area, which overcomes the loss in surface area per unit weight of the larger particle sizes. To test this hypothesis, Cells 7 and 8 were made by infiltration, with thicker cathodes so the mass of LSM, not the loading, changed. The electrical conductivity should therefore theoretically be unaffected. These performed much better than Cells 1 and 4, giving marginally higher performance than the painted cells (Figure 122). The slopes of the IV curves for Cells 7 and 8 are slightly shallower than those for Cells 1 and 4. This indicates a slight decrease in the area-specific resistance (ASR). This is unsurprising, as although the conductivity is the same, given the same loading of the conductive species, the width is increased. Cells 7 and 8 show comparable performance to Cells A and B despite having less LSM in the cathode (total, as well as per unit weight). This supports the hypothesis that the infiltrated cathodes would give higher performance than painted cathodes, for the same amount of LSM, as an increase in power has been observed with more LSM present.

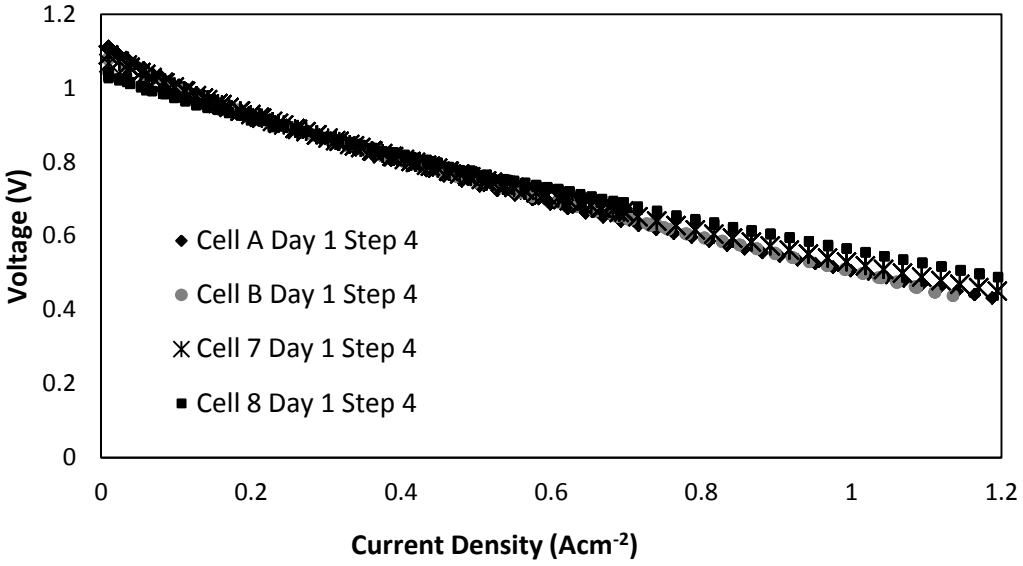

Figure 122 - Comparing I-V curves at 750°C with 20 ml/min H_2 for painted AMI-5.5 µSOFCs (A,B) to those for AMI-5.5 µSOFCs with thicker infiltrated cathodes (7: graphite pore-former, 8: PMMA pore-former)

Returning to cells A, B, 1 and 4; the cells with painted cathodes also show better performance after cycling. This is unsurprising as their initial power was higher, but the lower percentage degradation for the "traditional" cells (Figure 123) was unexpected.

The higher than expected thermal cycling degradation in the infiltrated cells may be due to the lower wt.% of LSM causing more significant connectivity, and thus conductivity, issues when some sinters or cracks than when excess is present, as is the case for the painted cells. Due to experimental issues data beyond Day 2 Step 6 were unfortunately unreliable for Cell 4, and so were discounted.

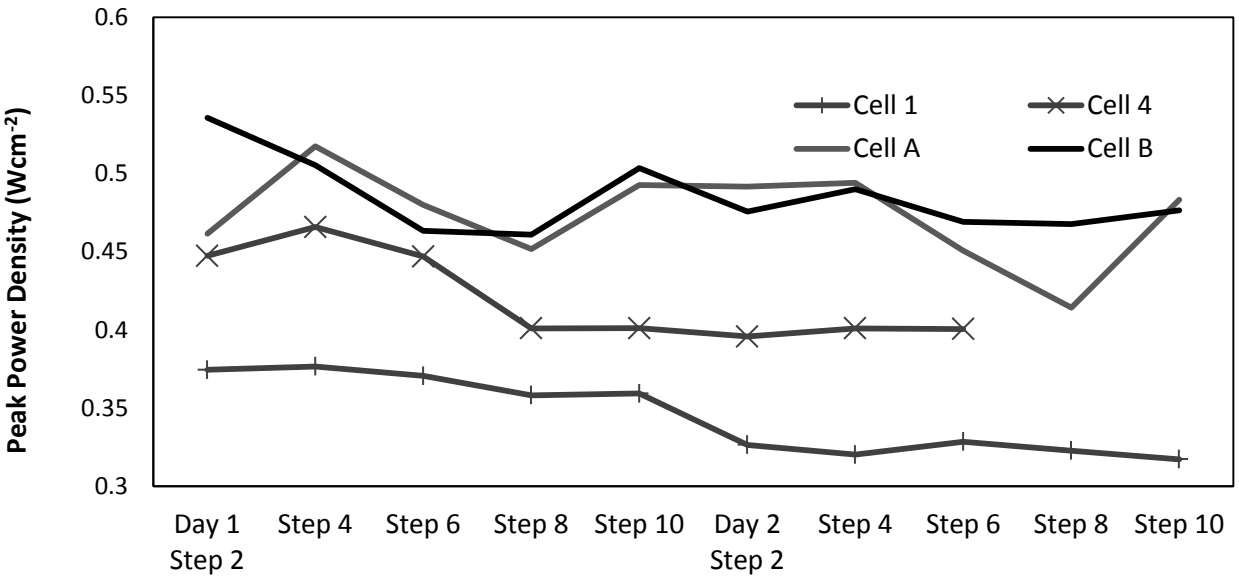

Figure 123 – Peak powers measured at 750°C with 20 ml/min H_2 before and after sets of cycles to gauge thermal cycling degradation of infiltrated (1,4) and painted (A,B) cathode AMI-5.5 µSOFCs

Statistical analysis of the data gave P values of 0.000 for the data of either Cells 1 and 4 or Cells 7 and 8 being similar to that for A and B (D =0.9 and D=0.65, respectively). Statistical significance of the difference between Cells 1 and 4 and Cells 7 and 8 was also confirmed (D=0.9, P=0.000). Obtaining these trends by chance can therefore be ruled out at the P=0.01 significance level.

7.2.2 Infiltrated Anode – Improved Power?

Cells 1 to 6 were then compared to investigate the effect of anode doping with the same (infiltrated) cathode. Infiltration of SDC should improve the anode mixed ionic and electronic conductivity and so improve the cell performance. Infiltration of nano-sized Ni particles should provide a higher surface area and catalytic activity for hydrogen oxidation.

Cells 1 and 4 (no doping of the standard Ni-YSZ anode) gave noticeably lower performance than any of the other four, as shown in Figure 124. In addition to the general improvement observed with doping, the SDC doped cells showed slightly higher performance than those doped with Ni-SDC.

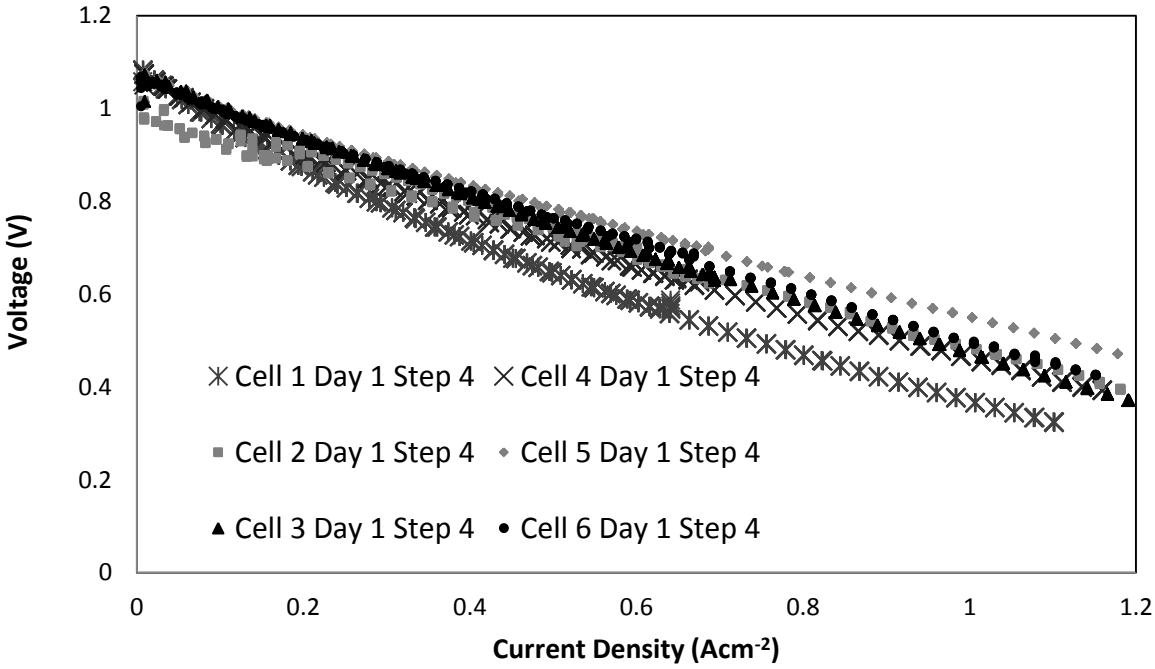

Figure 124 – I-V curves at 750°C with 20 ml/min H_2 to compare AMI-5.5 µSOFCs with the conventional anode (1,4), to those doped with SDC (2,5), and with Ni-SDC (3,6) before thermal cycling

These differences are more significant after cycling - Table 2 shows the changes in average peak power. The average degradation in peak power after 36 cycles (Day 2 Step 5) was 10% for the doped cells, and 13% for the undoped cells. SDC covers the Ni surface and prevents Ni sintering to some extent, explaining why SDC infiltration helps to reduce degradation. The addition of nano-sized Ni particles in the combined Ni-SDC infiltrate may partially counteract this beneficial effect, however, as the nanoparticles are more mobile than the Ni present in the cermet. This explains why the degradation seen was less for SDC-doped anodes than for Ni-SDC-doped anodes. Although there is visible overlap between results,

this strongly suggests that the doping has increased cell power and cell cycling tolerance. This study showed only a small effect on the cell power and degradation rate from SDC and Ni-SDC infiltration, possibly due to the low concentration of the infiltrate (2.5 wt.% for SDC and 3.5 wt.% for Ni-SDC).

Table 17 - Average powers from AMI-5.5 µSOFCs with thermal cycling

	Average Peak Power Before Cycling (W)	Average Peak Power After 16 Cycles (W)	Total Power Drop (W)
Undoped Anode (1,4)	0.42	0.38	0.04
SDC-Doped Anode (2,5)	0.52	0.50	0.02
Ni/SDC-Doped Anode (3,6)	0.49	0.46	0.03

Comparing the datasets statistically confirmed differences between the undoped and doped anodes at the P=0.01 level (P=0.000 when comparing Cells 1 and 4 to Cells 2 and 5, and to Cells 3 and 6). The P-value when comparing the SDC-doped cells (2,5) to the Ni-SDC-doped cells (3,6) was slightly higher (P=0.003), but still below the 0.01 significance level. This again helps to give confidence in the results, as the chance of obtaining this trend by chance would be below 1%.

7.2.3 Choice of Pore Former

Figure 125 shows IV curves taken from Day 1 tests for the cells made with a graphite pore former (Cells 1-3, shown in black) and those made with a PMMA pore former (Cells 4-6, shown in grey). Although the IV curves do overlap, the general trend shows the cells made using PMMA to have stronger performance (thermal cycling did not change this trend). Cell 5 (one of the cells made with PMMA) was the best performing cell overall.

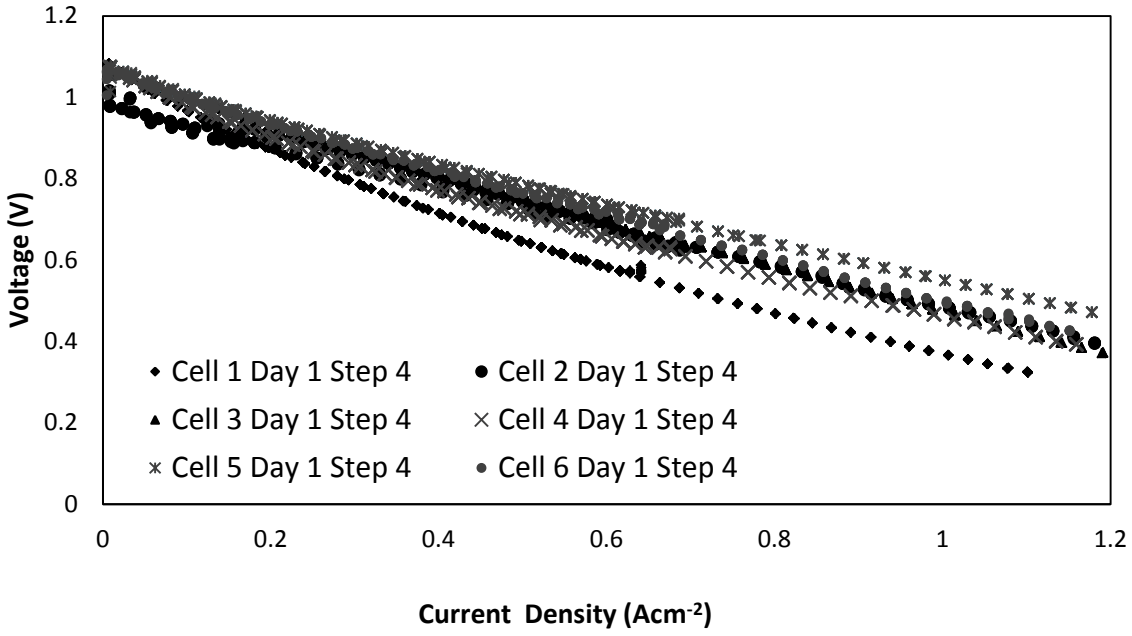

Figure 125 – I-V curves at 750°C with 20 ml/min H_2 to compare AMI-5.5 µSOFCs with graphite (Cells 1-3) and PMMA (Cells 4-6) pore formers

Extracting the resistances from the slopes of the IV curves shows this difference between the two pore-formers more clearly (Table 18). As would be expected from the slightly steeper IV curves, the average resistance of the cells using graphite as pore-former was higher than that for the cells using PMMA.

Table 18 - Resistances of AMI-5.5 µSOFCs tested (from Step 4 IV data)

Cell	Pore-former	Resistance (Ω)
Cell 1	Graphite	0.62
Cell 2	Graphite	0.50
Cell 3	Graphite	0.59
Average	*Graphite*	*0.57*
Cell 4	PMMA	0.54
Cell 5	PMMA	0.48
Cell 6	PMMA	0.54
Average	*PMMA*	*0.52*

Within the infiltrated cells, the pore former will cause significant differences in structure; graphite has previously been shown to give a more flaky, lamellar structure [283], which is

not surprising given the differences in pore-former morphology (see Figure 126). This lamellar structure may result in longer current path lengths, so explaining the higher resistance.

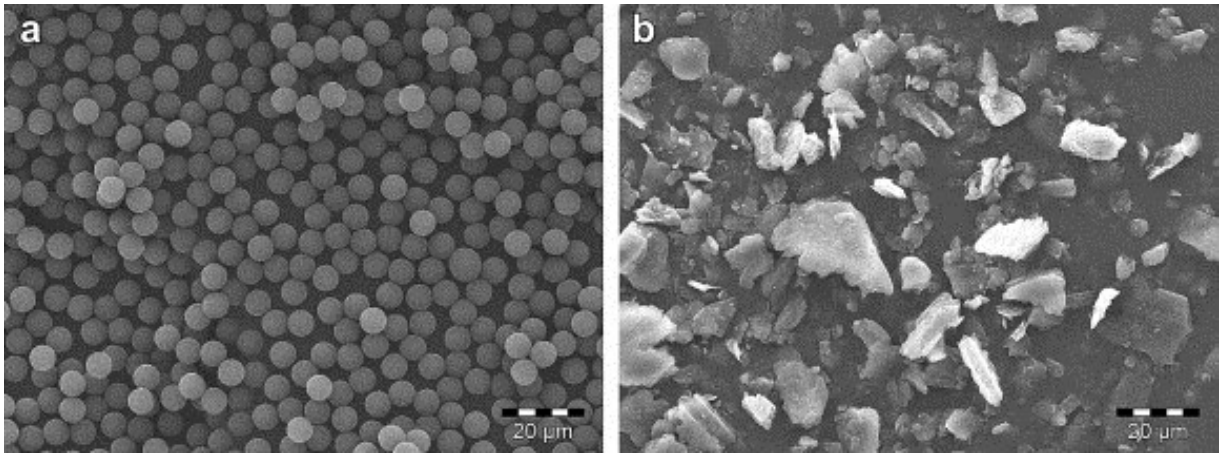

Figure 126 - SEM images of pore-formers, A: PMMA and B: graphite (images provided by A.R. Hanifi)

The average peak power density was 0.51 W/cm^2 for the cells using PMMA and only 0.45 W/cm^2 for the cells using graphite. As expected from the overlaps seen in Figure 125, the statistical significance of these results was not as strong – K-S testing gave a D value of 0.38 and a corresponding P value of 0.024. However the null hypothesis can still be rejected at the P=0.05 significance level, although not at the more stringent P=0.01 level.

In addition to power variations, the OCV at 400°C was notably higher for the PMMA cells than for the graphite cells (Table 19– data from Day 1 Step 5 cycling tests). As the OCVs were all very similar at 750°C, as expected theoretically, the reduction in temperature must be causing the differentiation, which was distinct and repeatable between cycles.

Table 19 - Open Circuit Voltage changes of AMI-5.5 µSOFCs with temperature

Cell tested	TPL pore former	OCV at 750°C (V)	OCV at 400°C (V)
Tube 1	Graphite	1.10	0.70
Tube 2*	Graphite	0.99	0.50
Tube 3	Graphite	1.09	0.85
Tube 4	PMMA	1.09	0.90
Tube 5	PMMA	1.09	0.98
Tube 6	PMMA	1.08	0.90
Tube A	N/A	1.09	1.05
Tube B	N/A	1.10	1.05
*Unusually low OCV; potentially a very small crack			

Thermodynamically, OCV is expected to decrease with increasing temperature, according to Equation 7.1:

$$E = E_0 + \frac{(T-T_0)\Delta\bar{s}}{zF} \quad \text{....(Eq. 7.1)}$$

Where E is the OCV at the relevant temperature (T, on the Kelvin scale), E_0 is the known value for the OCV under standard conditions, calculated from the Nernst equation, T_0 is standard temperature (298.15 Kelvin), F is the Faraday constant, z is the number of electrons transferred in the fuel cell reaction (2 for hydrogen fuel) and $\Delta\bar{s}$ is the entropy change in kJ/mole.

Figure 127 shows calculated and actual values of the cell OCV. Agreement is reasonable at higher temperatures, but the lines diverge at lower temperatures. This indicates that the data recorded do not represent true thermodynamic equilibrium values at lower temperatures: kinetic or other effects have moved the system away from equilibrium.

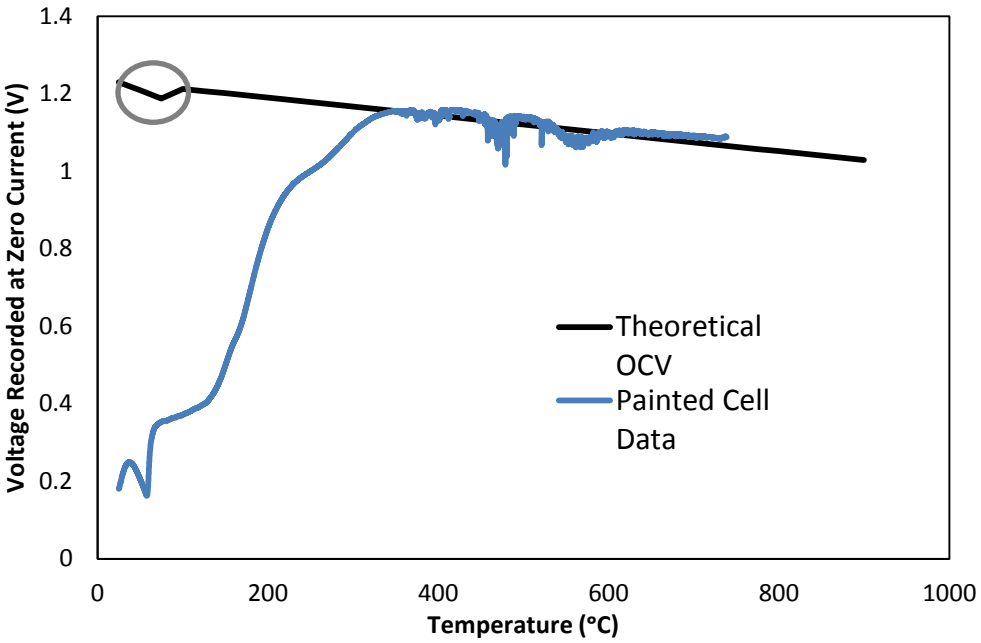

Figure 127 - Theoretical and actual OCV data with temperature. The circled kink in theoretical data is due to the change in phase of the water produced (liquid to gas). The low-temperature kink seen in data was not repeatable, but "noisy" data are often found around this temperature, probably due to the $H_2O_{(l)}$ to $H_2O_{(g)}$ phase change. (data for an AMI-5.5 µSOFC used)

This suggests an electron transfer kinetics effect; at zero net current, there is still activity at the electrodes, but the forward and reverse reactions occur at the same rate, cancelling each other out. The rate of these reactions is given by the exchange current density, i_0, which is affected by microstructure and operating conditions. The higher the exchange current density, the smaller the activation voltage drop, and so the higher the recorded voltage. In Ni-YSZ/YSZ/YSZ-LSM SOFCs, the activation overpotential (difference between the equilibrium and actual potential) at the Ni-YSZ electrode (the anode) is usually negligible so the activation polarisation can be almost entirely attributed to the cathode [284]. The cathodic exchange current density is known to be strongly affected by temperature [285]. The Butler-Volmer equation (Equation 7.2) gives the relationship between current density, i, and activation overpotential, η:

$$i = i_0 \left(e^{\frac{\alpha n F \eta}{RT}} - e^{\frac{-(1-\alpha) n F \eta}{RT}} \right) \quad \text{....(Eq. 7.2)}$$

Where α is the transfer coefficient (a measure of the fraction of the overpotential that affects the current density), *n* is the number of electrons transferred by the corresponding electrode reaction, *F* is the Faraday constant, *R* is the gas constant, and *T* is temperature (Kelvin). In the limit of low current density, overpotential is generally small, allowing the Butler-Volmer equation to be approximated by Equation 7.3, using the approximation of $e^x \rightarrow 1+x$ for small x:

$$\eta = i \frac{RT}{i_0 nF} = iR_{ct} \quad \text{...(Eq. 7.3)}$$

Where R_{ct} is the charge transfer resistance, which depends on operating conditions, microstructure and materials and is inversely proportional to the exchange current density. As i_0 increases more rapidly than *T* with increasing temperature [285], R_{ct} decreases, so decreasing the overpotential and allowing the recorded OCV to approach the equilibrium value. This therefore explains the rise in OCV with temperature.

Other factors affecting R_{ct} must be considered to explain why the drop in recorded OCV with temperature was different for the different cells. As operating conditions (partial pressures of fuel and oxidant, temperature etc.) and materials (LSM and YSZ) were the same, microstructure must be the differentiating factor. As the loadings, application methods and particle sizes of LSM are the same for cathodes made by both pore-formers, the area of triple phase boundary available would be expected to be the same. Studies [284, 286] have shown that unfavourable electrode characteristics, such as high resistances in composite electrodes, can depress the electrode kinetics. The electronic resistivity in such composite

cathodes is often seen as negligible compared to the resistance to ion transport [286], but if the conductive LSM layer is very thin compared to the YSZ (as is the case with the infiltrated cells), and the current paths are unusually tortuous (as for the cells using graphite as pore-former), and then electronic conductance could become a limiting factor.

The higher resistance of the cathodes made with graphite as pore-former, potentially due to longer current path-lengths, is responsible for the drop in power as compared to the cells prepared using PMMA. This increased resistance may also explain the lower OCV at 400°C.

7.2.4 Thermal Cycling Degradation

There are two main aspects of thermal cycling degradation. Firstly, cracks can form in the electrolyte leading to a change in partial pressure of oxygen, oxygen cross-over and potentially oxidative damage of the anode. This leads to drops in the open circuit voltage (OCV). Secondly, degradation can be due to the loss of conductivity in the electrodes due to a reduced connection between conductive particles, often limited by the connectivity of Ni particles in the anode. This may not affect the OCV, but does decrease the peak power attainable. To monitor cell stability following thermal cycling, measuring the cell power is, therefore, a better tool than measuring OCV alone. Using both metrics helps to identify the cause of power degradation in the cells; either electrolyte cracking or electrode microstructure change. Figure 128 shows peak power densities for each cell at different points during testing. There is a general downwards trend, showing that all cells are

adversely affected by this harsh thermal cycling. Slight improvement is often seen between Steps 2 and 4, as mentioned earlier, due to reduction of any remaining NiO over the hour's constant operation and also activation of the LSM cathode [220, 287]. A small increase was also usually seen between Steps 8 and 10. Step 8 was recorded immediately after a period of cycling at OCV, with no current passing. This can again be explained by LSM activation [220]: in operation, oxygen is being used and oxygen vacancies form in the LSM, so enhancing oxygen diffusion, which activates the oxygen reduction reaction. By contrast, at OCV, oxygen is not being used, so oxygen vacancies are filled and the cathode is deactivated. The cell therefore performs better after a period in which current is drawn than after a significant length of time at OCV.

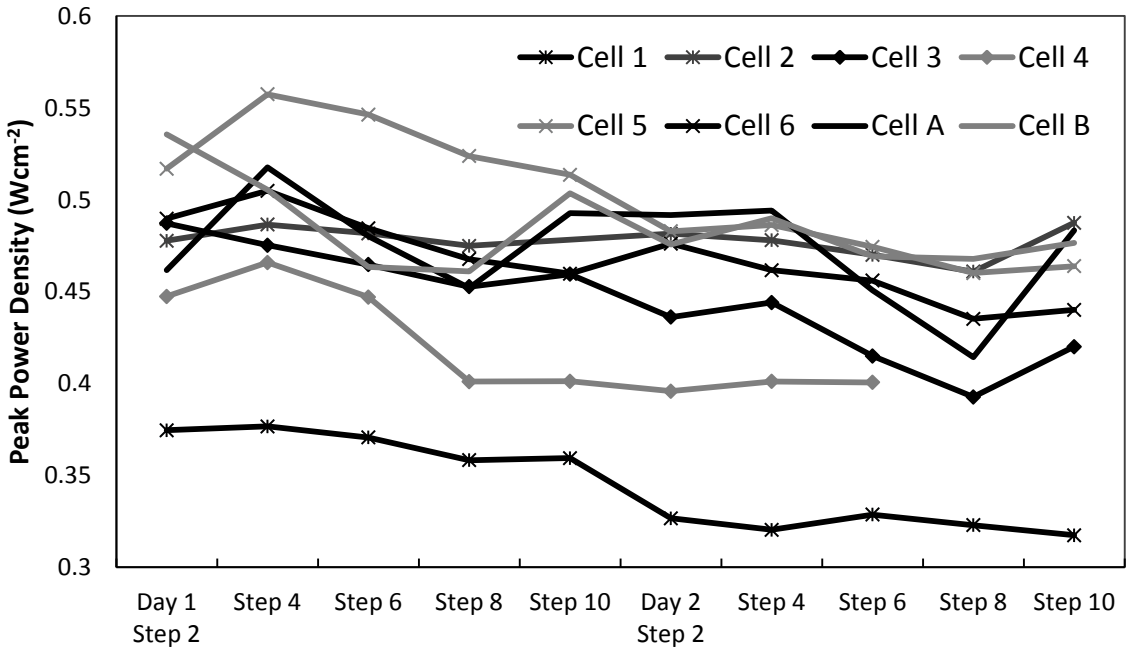

Figure 128 – Peak powers of AMI-5.5 µSOFCs at 750°C with 20 ml/min H_2 before and after sets of cycles to measure thermal cycling degradation

OCVs before and after each cycling step were examined. Very little change in OCV was observed at the end of testing; the difference was <5% of the pre-cycling value for all cells,

with only cells 4 (damaged in testing) and 2 showing changes above 2%. As the degradation in peak power was around 10% on average, this suggests that the majority of thermal cycling degradation was due to electrode changes rather than electrolyte cracking.

7.3 Discussion and Conclusions

This work supports the hypothesis that infiltrated cathodes give slightly higher performance than painted cathodes, for a comparable mass of LSM, due to the higher surface area and thus catalytic activity. It was found that the total mass of LSM present was more significant than expected, probably due to the increase in surface area per unit mass not quite compensating for the decrease in mass; this could be increased with more infiltration steps, but significantly increasing the loading of infiltrated LSM risks blocking the pores in the YSZ substrate and potentially also gas access to the YSZ surface. Increasing the cathode thickness was therefore chosen to increase the mass, keeping the loading constant. As expected from other work [274], conductivity was sufficiently high to give equivalent performance at a weight percentage of LSM much smaller than that used in a randomly structured composite, once the cathode thickness and hence total LSM mass was increased.

More surprisingly, the thermal cycling resistance of the infiltrated cathode was poorer than that of the painted cathodes. This is hypothesised to be due to any micro-cracks formed having a stronger effect on connectivity in the infiltrated structure, where the LSM is a coating on the YSZ, than in the random structure where there are multiple different percolation routes. The change in structure, with the LSM forming a thin layer on the surface in the infiltrated cathode, rather than being mixed in with the YSZ, could potentially be weaker in thermal cycling as the surface layer could delaminate more easily than larger

grains in a porous matrix would crack. Cathode preparation by infiltration improves the cell structure's thermal cycling properties as the electrolyte and cathode support have perfect expansion coefficient matching – these results suggest that delamination of the LSM surface layer is occurring. The fact that the drop in power on cycling was much greater than the drop in OCV on cycling (which was generally negligible) confirms that electrolyte cracking is not responsible for the degradation, lending support to the idea that cathode delamination may be. Unfortunately too few cells were available in this study to permit (destructive) SEM analysis both before and after testing to check for delamination.

Anode infiltration was shown to have a significant, positive effect on cell performance. It is known that SDC has a positive effect on Ni-YSZ anodes as it improves the mixed ionic and electronic conductivity of the anode [288] and reduces Ni mobility. The Ni-SDC doping was less beneficial than the pure SDC doping; although the extra nickel would increase the catalytically active surface, the nickel mobility would also be increased by the presence of the added nano-particles, potentially leading to more, unwanted sintering.

Using PMMA as the pore former gave slightly better performance than using graphite, both in terms of higher peak powers and higher OCVs at 400°C. This is hypothesised to be due to resistance issues within the cathode layer, as discussed in Section 2.3.

Thermal cycling at 100°C/minute caused power degradation of 0.2% per cycle, on average across all the cells. This was shown to be mainly due to electrode changes, rather than electrolyte cracking, as the open circuit voltages did not decrease significantly. This shows

that power monitoring during cycling is more important than OCV changes, for both painted and infiltrated cells.

In summary, anode infiltration was shown to have a particularly advantageous effect on performance, raising the peak power by around 20% and reducing the degradation in peak power seen after aggressive cycling by almost 50%. Cell power can be improved by LSM infiltration into a porous YSZ layer when thickness of the YSZ layer is optimised and there is sufficient LSM (an 8% increase in power was seen as compared to cells prepared with a brush-painted cathode). When Poly(methyl methacrylate) (PMMA) was used as the pore former in the porous YSZ matrix, average peak power obtained increased by 14% as compared to that for cells with graphite as the pore former. For studying the effect of thermal cycling on cell stability, monitoring the power variation is found to be a more reliable tool than OCV measurements. Due to availability, cost and time limitations on the number of experimental repeats (see Section 7.1), the significance of these results was checked and confirmed statistically, as discussed in Section 7.2.

8. OVERVIEW AND CONCLUSIONS

Experimental testing and characterisation have improved cell performance, both in terms of electrode improvements and new interconnection designs, and steps have been taken towards reducing manufacturing costs and environmental impact. Some of these developments have also contributed to the European SUAV project (FCH JU Grant Agreement Number 278626 [56]), which is still underway.

8.1 Summary of Conclusions & Novelty

8.1.1 Transient Behaviour

The focus of fuel cell research is on steady-state behaviour, but dynamic response to load changes is vital in real-world applications, as highlighted by power demand analysis undertaken during the placement with SurveyCopter. The transient response of fuel cells to load changes has often been overlooked, so experiments were performed to analyse this and the results published [289]. No transient undershooting of the current was seen when the voltage stepped up, unlike previously reported in the literature [227]. This is hypothesised to be due to improved mass transport thanks to the smaller size and improved porosity/pore interconnectivity of the µSOFC tubes used. Full adjustment was seen for a single tube within half a second, even when the voltage step covered a large proportion of the cell's total range.

The dynamic response of single cells was found to be much better than expected based on the literature. This finding suggests that more dynamic systems, where the fuel cell load and

battery load are both varied as appropriate may be useful (rather than the fuel cell load being held completely constant, as is more usually expected).

8.1.2 Stacking

A stack of six cells was built based on previous in-house work and simplistic manifold modelling using COMSOL Multiphysics. This was tested in both series and parallel configurations, and gave a power drop of less than 10% as compared to six times the power expected from a single cell made in the same manner. Dynamic performance characterisation was also performed for the stack; the response time was not much longer than that for a single cell, at less than 0.7 seconds. Even less in the way of experimental analysis of dynamic response is available for stacks than for single cells in the literature, so publication of this work [46] made a significant contribution.

This has positive implications for the electrical interface and control system between the stack and UAV (or other platform). Only a very brief (~0.7 s) spike in power from the battery would be required to smooth the power output on a change in demand from the fuel cell. In many systems, a time lapse smaller than a second would not be significant, and may be dwarfed by lag times of other components. A simpler control system can therefore be used.

8.1.3 Interconnections

At least 500 of the small µSOFCs initially used would have been needed to reach the 250 W stack requirement of the SUAV project. Making interconnections would therefore have been

very difficult. Acquiring the larger cells from AMI meant that only around 60 cells are needed, but the increased length per cell provided new challenges as the electronic conductivities of the anode and cathode became critical. Adaptation of various techniques used previously and discussed in the literature increased powers per tube to around 300% of the initial values obtained, making these cells a feasible option for the SUAV project stack requirements. A silver ink that gave a layer sufficiently porous to allow a full coating of the cathode without significantly impeding mass transport was identified. This provides good contact to a silver wire "spine" running the length of the cell, as well as lateral cathode conduction, in the optimal configuration tested in the course of this work.

It was decided that the advantages of using fewer tubes, in terms of manifolding and interconnections, outweighed the disadvantages of lower volumetric power density as compared to smaller tubes (AMI-5.5 µSOFCs). The improvements made in interconnection design have helped to improve the volumetric power density of the larger AMI-15.2 µSOFCs.

8.1.4 Cathode Ink

A cheaper and more environmentally friendly cathode ink that should also aid future large-scale production of SOFCs has been developed and characterised. This water-based ink has several advantages over the organic solvent based inks normally used, including reduced cost, improved environmental credentials and increased ease of handling and storage. In addition to the advantages of being water-based, the maximum power density obtained

increased by 20% with the fully-optimised new ink. A patent is pending on this work [257], and aspects of this research have also been published in a peer-reviewed journal [268].

8.1.5 Electrode Infiltration

Cells prepared with infiltrated anodes and with cathodes formed by infiltrating LSM into a YSZ matrix were tested and compared to in-house cells prepared by the normal technique. The analysis was performed in collaboration with Dr Amir Hanifi of the University of Alberta, to test the hypothesis that the infiltrated cathode would provide a higher power density and improved thermal cycling tolerance. For a comparable weight percentage of LSM, the infiltration technique was shown to give higher power densities, but the thermal cycling tolerance was actually weaker. This is hypothesised to be due to the thinner LSM layer flaking off more easily and any micro-cracks having more significant negative effects on connectivity and conductivity in the more open structure.

Doping the anode with SDC or Ni-SDC improved the power density; the Ni-SDC doping was less beneficial than the doping with SDC, but this could simply be due to the lower percentage of SDC applied in the former case. Further experimentation would be needed to ascertain the effect of the nickel; it would be expected to increase the catalytically active surface area, but the nickel mobility would be increased by the addition of these nanoparticles, which could lead to deleterious sintering. This work was published in a peer-reviewed journal [290].

8.2 Recommendations for Further Work

To attain the original aim of the project, namely building a stack of µSOFCs to power a small UAV, two further major developments are needed:

1. **Increase the power density per tube**

   The volume and weight restrictions placed on the power unit are very strict. Although the power output from a single tube was increased significantly by the developments discussed in this thesis, at least an extra Watt per tube would be needed to enable us to meet the power requirement within these restrictions.

2. **Develop a sufficiently compact and light-weight stack design**

   The cells need to be close enough together to obtain the required power density whilst still allowing air to flow between them. Manifolding and insulation also has to be included in the size and weight limits.

Potential routes for increasing the power density include replacement of the porous silver layer with a softer, potentially unsintered, layer of LSM to improve contact and conductivity and testing the newly-developed water-based cathode ink and the investigated doping methods on the anode and electrolyte half-cells recently purchased from AMI. Interconnection design is a recurring issue in µSOFC research; good interconnection design reduces losses, so also increasing the power obtained per cell.

Stack designs have been compared and considered; options for the final design are very much dependent on the total number of cells required, and hence on exactly how much power is obtainable per cell. Interconnection design is an integral part of the stack design, so these two aspects are very closely linked. Use of a conductive ceramic matrix is popular in the literature, but this is too heavy for the intended application, and impedes air flow too much (a more powerful blower would be required, thereby increasing the required power). Optimising cell spacing and wire positioning is therefore likely to be the way forward.

This work is in the scope of the SUAV project and is being taken forward by other European project team members.

APPENDICES AND REFERENCES

Funding Acknowledgements

With thanks to RCUK and EADS Innovation Works for their sponsorship of Miss K.S. Howe.

Some sections of this research received funding from the European Union's Seventh Framework Programme (FP7/2007-2013) for the Fuel Cells and Hydrogen Joint Undertaking under grant agreement n° 278629 - SUAV.

Appendix I: Fuel Cell UAVs

UAV Name	UAV Type	Produced by	Fuel Cell Supplier	Year	Fuel Cell Type	Fuel Storage	Max. Power (W)	Weight (kg)	Wing-span (m)	Flight Duration (hr)	Refer-ences	Comments
Hornet	Fixed-wing	AeroVironment/ Lynntech	Lynntech	2003	PEMFC	H_2 Hydride		0.17	0.381	0.08	[291]	Several flights of around five minutes each managed - water management problems. No battery
Helios	*Fixed-wing*	*NASA- Dryden Flight Research Centre/ AeroVironment*		*2003*	*PEMFC*	*Gaseous H_2*	*10,000 to 25,000*		*75.29*	*15*	*[292-294]*	*Solar Power/Fuel cell hybrid, destroyed in a crash in 2003*
Hy-Fly	Fixed-wing	FH-Wiesbaden	Heliocentris	2005	PEMFC	Gaseous H_2	65	1.75	2	0.025	[295, 296]	
Spider Lion	Fixed-wing	Naval Research Laboratory	Protonex	2005	PEMFC	Gaseous H_2	115	3.1	2.2	3.3	[297], [298]	
Global Observer	Fixed-wing	AeroVironment		2005	PEMFC	Liquid H_2			15.24	1	[299], [300]	Little available information, Odyssey prototype
	Fixed-wing	Adaptive Materials Inc.	AMI	2006	SOFC	Propane	60	1.94		4.3	[301]	
	Fixed-wing	Georgia Institute of Technology	BCS Technology Inc. (much modified)	2006	PEMFC	Gaseous H_2	550	16.4	6.58	0.03	[302-304]	"needs no batteries or booster for take-off"
	Fixed-wing	Cal State LA MFDCLab	Horizon	2006	PEMFC	Gaseous H_2	513	12.9	5.49	0.03	[305]	Led into the Pterosaur project

UAV Name	UAV Type	Produced by	Fuel Cell Supplier	Year	Fuel Cell Type	Fuel Storage	Max. Power (W)	Weight (kg)	Wing-span (m)	Flight Duration (hr)	Refer-ences	Comments
Pterosaur	Fixed-wing	California and Oklahoma State Universities	Horizon	2007	PEMFC	Gaseous H_2	150	5	4	3.67	[306-308]	78 miles used ~25% of fuel. 60 W battery in addition
HyFish	Fixed-wing	German Air and Space Centre/Horizon	Horizon	2007	PEMFC	Gaseous H_2	1300	6.1	1	0.25	[309, 310]	Different style, complex manoeuvres are the aim rather than endurance. Speeds up to 200 km/hr
	Fixed-wing	KAIST	in-house	2007	PEMFC	H_2 Hydride		2	1.2	10	[294], [311]	Unconfirmed as to whether flight time is predicted or demonstrated
Endurance	Fixed-wing	University of Michigan/AMI	AMI	2008	SOFC	Propane		5.3	2.44	10.25	[312]	Fuel remaining for ~5 hours' flight; curtailed due to darkness
Puma AE	Fixed-wing	AeroVironment	AMI	2008	SOFC	Propane				7	[296], [313]	
Puma AE	Fixed-wing	AeroVironment	Protonex	2008	PEMFC	H_2 Hydride		6.5	2.59	9	[314, 315]	Payload included in weight. 7 hour flight in 2007.
EO-360 UAV	Fixed-wing	EnergyOr	EnergyOr	2009	PEMFC					5 (approx.)	[36], [316]	"Planned" eight-hour flight. Flights in Canada and Israel claimed in 2007-2008, but no details available
Kenyalang-1	Fixed-wing	Universiti Teknologi MARA (UiTM)	Horizon	2009	PEMFC	Gaseous H_2	500	15	5	0.02	[317]	

UAV Name	UAV Type	Produced by	Fuel Cell Supplier	Year	Fuel Cell Type	Fuel Storage	Max. Power (W)	Weight (kg)	Wing-span (m)	Flight Duration (hr)	Refer-ences	Comments
Boomerang	Fixed-wing	Bluebird Aero Systems/Horizon	Horizon	2009	PEMFC	H_2 Hydride	500	9.5	2.75	9	[296], [318, 319]	Up to 1.3 kg payload
NAVAIR Mako UAV	*Fixed-wing*	*Office of Naval Research/ Penn State University/ Kuchera Engineering*	*Jadoo Power Systems*	*2009*	*PEMFC*	*H_2 Hydride*	*63*	*50*	*3.94*	*N/A*	*[320, 321]*	*Fuel cell system powers payload only; internal combustion engine used for propulsion*
Ion Tiger	Fixed-wing	Naval Research Laboratory	Protonex	2009	PEMFC	Gaseous H_2	550	16.1	2.5	26.02	[297], [298], [322]	Record in Nov, Oct. Flight of 23 hours and 17 minutes. $80,000 per UAV [323]
stealth XFC UAV	"Fixed"-wing (folding)	Naval Research Laboratory	Protonex	2010	PEMFC	Gaseous H_2	550	12.3	3	6	[298]	Folded wing to launch from a submerged submarine torpedo tube, 90g payload
EAV-1 (RemoEye 006)	Fixed-wing	KARI	Horizon	2010	PEMFC	H2 Hydride	600*	6	2.7	5	[30]	6kg is the maximum take-off weight, fuel left after landing.
Skylark	Fixed-wing	Elbit Systems	Horizon	2010	PEMFC	H_2 Hydride$^+$	600*	5.5	2.4		[324]	"expected to double the current endurance (around 3 hours)"
Birdeye 650LE	Fixed-wing	Israel Aerospace Industries	Horizon	2010	PEMFC	H2 Hydride		11		6	[325, 326]	Weight includes 1.2 kg payload
CIAM-80 mini-UAV	Fixed-wing	P.I. Baranov Central Institute of Aviation Motors, Russia	Horizon	2010	PEMFC	Gaseous H_2					[327]	Little information available. Flight of “several minutes”
Grey-Faced Buzzard	Fixed-wing	National Cheng Kung University	in-house	2010			1000	22	3.4	0.25	[328]	Payload of up to 8 kg on top of the 22 kg. Speeds up to 100 km/hr. 2500 W power including battery

UAV Name	UAV Type	Produced by	Fuel Cell Supplier	Year	Fuel Cell Type	Fuel Storage	Max. Power (W)	Weight (kg)	Wing-span (m)	Flight Duration (hr)	Refer-ences	Comments
AKBABA	Fixed-wing	TOBB University of Economics and Technology, Turkey		2010	PEMFC			15	5.05	3	[329, 330]	Little information available; flight time unverified
Stalker Extreme Endurance (XE)	Fixed-wing	Lockheed Martin	AMI	2011	SOFC	Propane		6.3	3.04	8	[331]	Weight includes surveillance payload. DARPA-sponsored
FAUCON H2/Robosaur	Fixed-wing	EnergyOr/ Robota LLC	EnergyOr	2011	PEMFC			7.7	3	10.07	[332], [333]	UAV built around power system. Can carry 1.8kg payload in addition.
	Fixed-wing	KAIST/ Chosun University	Horizon	2011	PEMFC	Hydride (aqueous)	100	2.5	2.12	2	[334, 335]	Maximum battery power of 300 W. Weight minimised.
Windex	Fixed-wing	Defence Research & Development Canada (DRDC)/EnergyOr	EnergyOr	2011	PEMFC						[336]	
Thunderbird (LN60F)	Fixed-wing	Shenyang Aerospace University, AVIC Group		2012		Gaseous H2		257	10.5	4	[337]	
Ion Tiger	Fixed-wing	Naval Research Laboratory	Protonex	2013	PEMFC	Liquid H_2	550		2.5	48	[338, 339]	Same vehicle as for the 2009 flight, but with cryogenic fuel storage

UAV Name	UAV Type	Produced by	Fuel Cell Supplier	Year	Fuel Cell Type	Fuel Storage	Max. Power (W)	Weight (kg)	Wing-span (m)	Flight Duration (hr)	Refer-ences	Comments
	Fixed-wing	Radiant Coral Digital Technologies (RCDT)	EnergyOr	2013	PEMFC						[340]	Appears to be a repeated test of the FAUCON H2 - little information available
muFly	Heli-copter	EU consortium project	Technical University of Berlin	2008	PEMFC		10	0.35		0.25	[341, 342]	Small bird sized
	Heli-copter	United Technologies Corporation	UTC research centre	2009	PEMFC	Gaseous H_2	1750*	10	2	0.33	[341]	2.3 kg payload possible in addition.

N.B. Two references [294, 296] included significant tabulation of fuel cell UAVs – these have been incorporated here, with various errors/differences removed :
Ref.[296] included two manned vehicles (not wanted here), one reference was incorrect and others out-dated. Also, his definition of "endurance" does not mean maximum single flight duration (as is given here), but rather total time flown. Ref. [294] included two internal combustion engine UAVs (Boeing's Phantom Eye [343] and the HALE Global Observer [344] – the Odyssey prototype of the latter was made to use fuel cells, although little information is available and that project seems to have been discarded in favour of internal combustion engines), and one that has never been made (BlueBird's "Thunderbird" [345]), as far as public information shows.

Key

*Maximum power stated is for fuel cell-battery hybrid system, as that for the fuel cell itself was not specified

[+]Fuel storage method uncertain. Horizon documentation suggests it uses their standard system (hydride), but [Ref. [294]] claims gaseous hydrogen (unsubstantiated)

Italic Text: There is another significant contributor to the propulsive power or the fuel cell does not give propulsive power, see comments

Appendix II: Calculations of Fuel Utilisations

The formula used is Equation 2.4 given earlier: $\boldsymbol{U_f = \frac{I}{nFv}}$

Precise details of the methods used are given below. Numbers in bold are taken directly from the papers**.**

T. Suzuki et al. [93]

Electrolyte area = **0.3 cm^2**

Linear fuel velocity of **0.8 m/s**

The cell was **1.9 mm** in diameter… a cross-section of 0.028 cm^2

Fuel flow is therefore 0.028x80 cm^3/s =2.268 ml/s

=1.01x10^{-4} moles/s

Current densities at each temperature, and the calculated total cell currents:

550^{o}C - 1.25 Acm^{-2}……0.375 A

600^{o}C – 2.2 Acm^{-2}……..0.66 A

(Current densities read off the graphs in Figure 3 A and B)

For Hydrogen, n=2.

Combining these results using (i) gives:

550^{o}C ……U_f=1.9%

600^{o}C ……..U_f=3.4%

N. Sammes et al. [109]

The effective cell area was **0.13 cm^2**

Current densities at each temperature, and the calculated total cell currents:

550^{o}C - 2.4 Acm^{-2}……0.312 A

570^{o}C – 3.0 Acm^{-2}……..0.39 A

(Current densities read off the graph in Figure 11 of this paper)

Hydrogen flow rate: **5 ml/minute**

Assuming this is an ideal gas at room temperature, and ignoring the humidification as no details are given, this gives 3.72x10^{-6} moles/second.

For Hydrogen, n=2.

Combining these results using (i) gives:

550^{o}C …….U_f=43%

570^{o}C …….U_f=54%

T. Suzuki et al. [78]

0.13 cm^2 effective cell area

Current densities at each temperature, and the calculated total cell currents:

550^{o}C - 3.1 Acm^{-2}……0.403 A

500^{o}C - 1.8 Acm^{-2}……..0.234 A

450^{o}C - 0.8 Acm^{-2}……0.104 A

Hydrogen flow rate: **5 ml/minute**

Assuming this is an ideal gas at room temperature, and ignoring the humidification as no details are given, this gives 3.72x10^{-6} moles/second.

For Hydrogen, n=2.

Combining these results using (i) gives:

550^{o}C ……U_f=56%

500^{o}C ……..U_f=33%

450^{o}C ……U_f=14%

C. Jin et al. [111]

0.31 cm^{2} effective cathode area

Current density **1.2 Acm^{-2}**……..0.372 A

75 ml/minute fuel flow rate, **3%** water by volume at **25^{o}C**

97% of volume is therefore Hydrogen (72.75 ml/min)

This gives: 5.41x10^{-5} moles/second.

For Hydrogen, n=2.

Combining these results using (i) gives: U_f= 3.6%

T.J Lee and K. Kendall [114] - Insufficient data given in paper

A. Dhir and K. Kendall [115]

1.6 cm^{2} active cathode area

0.85 Acm^{-2} maximum current density…1.36 A

3 ml min^{-1} methane, so 2.23x10^{-6} moles/second.

For methane, 8≥n≥4

Used n=8 here to give a minimum utilization,

Combining these results using (i) gives: U_f= 79%

K.V. Galloway and N. Sammes [116] - Fuel Utilisation read off graph given in Figure 8 of [33]

Appendix III: Material Characterisation Techniques – Operating Principles

This appendix gives further details of the underlying science behind the characterisation techniques listed in Section 3.5.

Scanning Electron Microscopy

Scanning Electron Microscopes (SEMs) are microscopes that use a beam of electrons instead of a beam of light to produce an image of a sample. The same principles of focussing beams and magnifying an image are used.

SEMs have numerous advantages over light microscopes; these include:

i) A larger depth of field, meaning that more of the sample can be in focus at any one time.

ii) Higher magnification – the picture can be made bigger for ease of examination

iii) Higher resolution – small features very close together can be examined. Without high resolution, a highly magnified picture would lack detail.

iv) Elemental analysis is possible – described later.

One restriction on SEM samples is that they must be conductive; as such, the tubes must be carbon- or gold-coated before analysis. Additionally, SEMs are designed to look at a solid, reasonably flat, surface, and are not suitable for liquid or gas analysis, nor for 3D imaging of internal cavities or similar. Care must also be taken to avoid any contamination of the SEM vacuum chamber, as contaminants can cause artefacts in imaging [346].

Focused Ion Beam (FIB) SEM is a variant where a FIB is used to prepare a surface for SEM analysis. Once a sufficiently large and smooth area has been exposed by etching the sample with the FIB, SEM imaging can be performed as usual. The FIB itself can also be used to image the surface. The FIB and SEM columns are at different angles to the sample, providing two different views of the same area.

Energy Dispersive X-ray Spectroscopy

A focused, high-energy beam of charged particles can be used to stimulate the release of X-rays from a sample. Electrons are the usual choice, although other charged particles, such as positrons, could be used in the same way. The beam electrons interact with electrons in the surface atoms. In these electron beam-atomic electron interactions, electrons in the material can move between different "shells", releasing energy in the form of X-rays. The energies of these X-rays can be used to identify the elements present. The number of X-rays emitted from a sample, and the energy of each, can be recorded by an energy-dispersive spectrometer.

The capabilities of this technique are due to the unique atomic structure of each element; enabling X-rays characteristic of a certain element to be identified to that element. When an incident electron excites an atomic electron from one energy level to a higher one, an "electron hole" is created in the initial energy level. An atomic electron in a higher energy level can "fall" down the potential well to fill this hole, releasing an amount of energy equal to the energy difference between the two levels. This energy is released in the form of an X-ray.

Atomic Force Microscopy

Atomic Force Microscopy (AFM) is a very high resolution form of scanning probe microscopy, with fraction of a nanometre resolution. Piezoelectric elements allow very precise control of a fine mechanical tip on a cantilever. Light from a laser reflected from a point on the top of the cantilever is used to form the image. Forces measured by the AFM can include mechanical contact force, Van der Waals forces, chemical bonding and electrostatic forces.

Appendix IV: Modules Undertaken

Modules Taken / Module Title	Status	Credits	Academic year
Measurement Techniques	Attended. Coursework finished and submitted – 72%	10	2009/10
Marketing and TQM	Attended. Coursework finished and submitted – 90%	10	2009/10
The Energy System	Attended. Coursework finished and submitted – 75%	10	2009/10
Materials for Sustainable Environmental Technologies	Attended. Coursework finished and submitted – 73%	10	2009/10
Business Methods, Economics and Strategy	Attended. Coursework finished and submitted – 74%	10	2009/10
Effective Project Management	Attended. Coursework finished and submitted – 82%	10	2009/10
Materials for Hydrogen and Fuel Cell Technology	Attended. Exam taken– 86%	10	2009/10
Mathematical modelling of time-dependent processes	Attended – not taken for credit	0	2009/10
Process Engineering Fundamentals	Attended – not taken for credit	0	2010/11
Electrochemistry and Electrochemical Engineering	Attended – coursework finished and submitted – 74%	10	2010/11
Teamwork and Presentation Skills	Coniston programme and presentation skills course	5+5	2011/12
Public Awareness	Attended – coursework finished	10	2011/12

	and submitted – 70%		
From the Bench to the Bank	Attended – coursework finished and submitted – 61%	20	2011/12
Postgraduate Certificate of Academic Practice – Associate Module	Attended – coursework finished and submitted – 62%	20	2012/13

Other courses attended: postgraduate teaching, reference managing software, health and safety, Intellectual Property, COMSOL Multiphysics and CFX, French Level 6 (Distinction), summer course in French (Advanced), French Level 7 (Distinction), summer course in French (Higher Advanced) and French Level 8 (Distinction).

Appendix V: Conferences and Other Work

- Supervision of two Masters students per year – project setting and advice, laboratory demonstrations and help with final reports.
- Supervision of around five second year students per year - project setting and advice, laboratory demonstrations and help with poster and final report.
- Supervision of one summer student - project setting and advice, laboratory demonstration and help with final report.
- Review paper written and submitted to the 2010 Fuel Cell Forum – Conference attended and poster presented; paper in conference proceedings [347].
- Review paper expanded and adapted to include Gareth Thompson's experimental results on stacks [168] – joint paper accepted by the Journal of Power Sources [72]
- Abstract submitted to the IMA Conference on Fluid Problems in Process Engineering – poster presentation in September 2010.

- Attended various conferences and networking events at the university, NEC and QEII conference centre.
- Paper detailing experimental results on transient performance of cells published in the Journal of Fuel Cell Science and Technology.
- Extended paper including stacks presented at the 219th meeting of the Electrochemical Society in Montreal, May 2011.
- Patent application submitted for a water-based cathode ink
- Invited Talk: "L'Utilisation des Piles à Combustibles dans le Domaine des UAV" at Cassidian, Elancourt (November 2011)
- Paper on the water-based ink presented at the Zing Hydrogen and Fuel Cells Conference in December 2011
- Said paper then submitted to the International Journal of Hydrogen Energy (accepted)
- Poster on the above presented at the NEC Smart Hydrogen and Fuel Cell Power Conference, 8th International Conference, Exhibition and Partnering Event in Birmingham, March 2012
- Draft manuscript reviewed for the Journal of Applied Electrochemistry (April 2012)
- Invited Talk: "mSOFC Systems for Unmanned Aerial Vehicles" at the High and Low Temperature Fuel Cell Systems workshop in Bruges, Belgium (May 2012)
- Presentation at the EADS PhD Showcase – won "Best Presentation" Award
- Collaborative paper with A.R. Hanifi accepted for a poster presentation at the 10th European SOFC Forum in Lucerne, June 2012, and subsequently published

Mini-Projects

Part of the aim of the DTC programme is to give students experience of working with companies or in other ways outside the standard university environment. At least three mini-projects must be completed to demonstrate these capabilities.

Projects chosen:

1. Industrial: Raising public awareness of climate change

In October 2010, Tony McNally (of Climate Change Solutions) was contacted to ask what could be done to help in his work to increase public understanding of climate change. Three posters were prepared discussing hydrogen, how fuel cells work, and how fuel cells can be used for use in a display. Two meetings took place in Coventry to discuss details, but unfortunately the council reversed permission to use the location we were supposed to have for the event. In addition, a document promoting "Hydrogen and Fuel Cells in the Mainstream" was proof-read for Climate Change Solutions.

2. Outreach: Talk to school students (first of many outreach projects)

A presentation was prepared for a group of school students (in collaboration with T. Pike) discussing the role of fuel cells and the important challenges to be faced. This was presented to a group of around 25 on March 31st 2010. The children were then given a tour of the laboratory in groups - they seemed especially impressed with the fuel cell powered scooter! An individual laboratory tour and explanation of the ideas behind fuel cells was also given to a deaf boy due to be applying to university soon. This was achieved through a

combination of diagrams, him lip-reading and his mother doing some translation into sign language.

3. Interdisciplinary: Laser diagnostic technique

The work of Dr. M. Lengden and Dr. W. Johnstone from the Department of Electrical and Electronic Engineering at the University of Strathclyde was discovered at the 2010 Fuel Cell Forum. They are developing two novel approaches to tunable diode laser spectroscopy which could be very useful for in situ gas composition and temperature measurements for fuel cells. Dr. Lengden was given a tour of our laboratory facilities on August 10th 2010 and further collaboration is planned.

4. Industrial: DuPont silver ink testing

Samples of two conductive silver inks were obtained from DuPont and a technique for using them in μSOFC interconnections, in place of the old Johnson Matthey ink, was developed. These two inks were then compared against each other and the old ink. Methods and results were shared with my contact at DuPont (Dr. K. Adams) who came for a laboratory tour on August 4th 2010 to gain a better understanding of the techniques and systems used. After further discussion, a third ink sample was provided, which emerged as the strongest competitor for the now unavailable Johnson Matthey ink. A full report on the experiments undertaken and conclusions made was sent to DuPont and circulated within their Research and Development group.

5. International: Research abroad

SurveyCopter is the French company providing the UAV platform for the SUAV project. This placement involved two months working in France with SurveyCopter to introduce the company to hydrogen fuel cells, and how they can be used with Unmanned Aerial Vehicles.

Alongside these mini-projects, the main project is being undertaken in collaboration with EADS Innovation Works, who are providing personal sponsorship as well as a financial contribution to the university. There have been several meetings, both at the university and on EADS premises, with quarterly reports on progress being given.

References

1. Stern, N., *The Economics of Climate Change: The Stern Review*, in *The Stern Review*2007, HM Treasury: London.
2. Solomon, S., D. Qin, M. Manning, Z. Chen, M. Marquis, K.B. Averyt, M. Tignor and and H.L.M. (eds.). *Climate Change 2007: The Physical Science Basis*, in *Contribution of Working Group I to the Fourth Assessment Report of the Intergovernmental Panel on Climate Change*2007.
3. Wigley, T.M.L. and S.C.B. Raper, *Natural Variability of the Climate System and Detection of the Greenhouse Effect.* Nature, 1990. **344**(6264): p. 324-327.
4. Manabe, S. and R.J. Stouffer, *Multiple-Century Response of a Coupled Ocean-Atmosphere Model to an Increase of Atmospheric Carbon Dioxide.* Journal of Climate, 1994. **7**(1): p. 5-23.
5. Santer, B.D., et al., *Ocean Variability and its Influence on the Detectability of Greenhouse Warming Signals.* Journal of Geophysical Research-Oceans, 1995. **100**(C6): p. 10693-10725.
6. BP, *BP Statistical Review of World Energy*, 2009, BP Statistical Review of World Energy.
7. P. Sankey, S. Micheloto, and D.T. Clark, *The Peak Oil Market: Price dynamics at the end of the oil age*, in *FITT Research*2009, Deutsche Bank.
8. P. Hughes, S. Crombie, and I. Kershaw, *Ricardo study suggests global oil demand may peak before 2020*, 2011, Ricardo.
9. http://www.roads2hy.com/. *Roads2HyCom*. 2009 [cited 2013 24/06/2013]; Available from: http://www.roads2hy.com/.
10. IEA. *International Energy Agency FAQs: Renewable Energy*. Renewable Energy 2012 [cited 2013 April 23rd]; Available from: http://www.iea.org/aboutus/faqs/renewableenergy/.
11. http://www.worldcoal.org/resources/coal-statistics/. Statistics 2010.
12. Mulder, G., J. Hetland, and G. Lenaers. *Towards a sustainable hydrogen economy: Hydrogen pathways and infrastructure*. in *2nd European Hydrogen Energy Conference*. 2005. Zaragoza, SPAIN: Pergamon-Elsevier Science Ltd.
13. Thomas, C.E., *Fuel cell and battery electric vehicles compared.* International Journal of Hydrogen Energy, 2009. **34**(15): p. 6005-6020.
14. Andújar, J. and F. Segura, *Fuel cells: History and updating. A walk along two centuries.* Renewable and sustainable energy reviews, 2009. **13**(9): p. 2309-2322.
15. Kendall, K. and S.C. Singhal, *High-Temperature Solid Oxide Fuel Cells: Fundamentals, Design and Applications* 2003: Elsevier Ltd.
16. Lee, J.Y., et al., *Life cycle cost analysis to examine the economical feasibility of hydrogen as an alternative fuel.* International Journal of Hydrogen Energy, 2009. **34**(10): p. 4243-4255.
17. Kelly, N.A., T.L. Gibson, and D.B. Ouwerkerk, *A solar-powered, high-efficiency hydrogen fueling system using high-pressure electrolysis of water: Design and initial results.* International Journal of Hydrogen Energy, 2008. **33**(11): p. 2747-2764.
18. Birnbaum, K.U., R. Steinberger-Wilkens, and P. Zapp, *Solid Oxide Fuel Cells, Sustainability Aspects*, in *Fuel Cells*, K.-D. Kreuer, Editor 2013, Springer New York. p. 731-790.
19. Hansen, J. and N. Christiansen, *Solid Oxide Fuel Cells, Marketing Issues*, in *Fuel Cells*, K.-D. Kreuer, Editor 2013, Springer New York. p. 687-730.
20. Stambouli, A.B. and E. Traversa, *Solid oxide fuel cells (SOFCs): a review of an environmentally clean and efficient source of energy.* Renewable and sustainable energy reviews, 2002. **6**(5): p. 433-455.
21. Parliament, *Cleaner Coal*, P.O.o.S.a. Technology, Editor 2005.
22. Williams, M.C. *Status and market applications for the solid oxide fuel cell in the US - A new direction*. in *7th International Symposium on Solid Oxide Fuel Cells*. 2001. Tsukuba, Japan: Electrochemical Society Inc.

23. Jensen, S.H., P.H. Larsen, and M. Mogensen, *Hydrogen and synthetic fuel production from renewable energy sources.* International Journal of Hydrogen Energy, 2007. **32**(15): p. 3253-3257.
24. Carrasco, J.M., et al., *Power-Electronic Systems for the Grid Integration of Renewable Energy Sources: A Survey.* Industrial Electronics, IEEE Transactions on, 2006. **53**(4): p. 1002-1016.
25. Larminie, J. and A. Dicks, *Fuel Cell Systems Explained - Second Edition, pp. 5-7*2003: Wiley.
26. BloomEnergy. *New Fuel Cell Technology Generates Electricity on UCSB Campus*. Press Release 2012 [cited 2012 November 6th]; Available from: http://www.bloomenergy.com/newsroom/press-release-09-19-12/.
27. EFOY. *EFOY fuel cells for holiday homes*. 2009; Available from: http://www.efoy.com/en/mobile-homes-benefits.html.
28. Gangi, J. *Fuel Cell-Powered Forklifts: Raising the Bar*. Fuel Cells 2000 2008 [cited 2012 November 6th]; Available from: http://www.iuvmag.com/articles/2008_05-05.html#.UJkYqMUxqHU.
29. Mahadevan, K., et al., *Identification and Characterization of Near-Term Direct Hydrogen Proton Exchange Membrance Fuel Cell Markets*, 2007, Battelle: U.S. Department of Energy.
30. Horizon. *"Horizon's Fuel Cell Triples Flight Duration Capability of South Korean Close-Range UAV", Press Release*. 2010; Available from: http://www.hes.sg/files/AEROPAKkari.pdf.
31. Cox, T.H., et al., *A Report Overview of the Civil UAV Capability Assessment*, 2004, NASA.
32. Djololian, C. and T. Veitshans, *Etude Energie électrique embarquée « Drones Aériens »*, in *Direction de la Valorisation - Bureau d'Etude Markting*2011, Liten - CEA.
33. SIONpower. *"QinetiQ and SION Zephyr flight press release", June 2011*. 2011; 2011:[Available from: http://sionpower.com/pdf/articles/QinetiQ%20and%20SION%20Zephyr%20Flight%2011-21-06%20News%20Relea.pdf.
34. EnergyOr, *Fuel Cell UAV Propulsion Systems for Extended Flight Endurance: EPOD-310 Product Brochure*, 2010.
35. EnergyOr, *Fuel Cell UAV Propulsion Systems for Extennded Flight Endurance: EPOD-210 Product Brochure*, 2010.
36. EnergyOr. *EnergyOr Technologies Inc. - Media*. 2011 October 12th, 2011]; Available from: http://www.energyor.com/energyor/media/.
37. Protonex. *UAV-C250 Advanced UAV Propulsion Power Source, 2011*. 2011; Available from: http://www.protonex.com/downloads/products/Protonex_UAV_Spec_Sheet.pdf.
38. Ultra-AMI. *Portable Power - Amie50 Spec. Sheet*. 2011; Available from: http://www.ultra-ami.com/dynwbcntent/wp-content/uploads/Amie50SpecSheet.pdf.
39. Horizon. *AEROPAK Hydrogen Fuel Cell System, Product information*. Product information 2011; Available from: http://www.hes.sg/files/AEROPAK.pdf.
40. Horizon. *Products - AEROPAK Fuel Cell Propulsion System for Unmanned Aerial Vehicles, 2011*. 2011 [cited 2011; Available from: http://www.hes.sg/products.html.
41. Horizon, *AEROPAK - Technical Data Sheet*, 2010.
42. Wongchanapai, S., et al., *Performance evaluation of a direct-biogas solid oxide fuel cell-micro gas turbine (SOFC-MGT) hybrid combined heat and power (CHP) system.* Journal of Power Sources, 2013. **223**(0): p. 9-17.
43. Carnpanari, S., G. Manzolini, and F.G. de la Iglesia, *Energy analysis of electric vehicles using batteries or fuel cells through well-to-wheel driving cycle simulations.* Journal of Power Sources, 2009. **186**(2): p. 464-477.
44. Yalcinoz, T. and M.S. Alam, *Improved dynamic performance of hybrid PEM fuel cells and ultracapacitors for portable applications.* International Journal of Hydrogen Energy, 2008. **33**(7): p. 1932-1940.

45. Ahmed, S., D.J. Chmielewski, and Ieee. *Load Characteristics and Control of a Hybrid Fuel Cell/Battery Vehicle*. in *American Control Conference 2009*. 2009. St Louis, MO: Ieee.
46. Howe, K.S. and K. Kendall, *Transient Performance of Micro-Tubular Solid Oxide Fuel Cells and Stacks.* ECS Transactions, 2011. **35**(1): p. 419-423.
47. Mueller, F., et al., *Dynamic simulation of an integrated solid oxide fuel cell system including current-based fuel flow control.* Journal of Fuel Cell Science and Technology, 2006. **3**(2): p. 144-154.
48. Fagley, J., J. Conley, and D. Masten. *PEM fuel cell research direction for automotive application*. in *3rd International Conference on Fuel Cell Science, Engineering and Technology*. 2005. Ypsilanti, MI: Amer Soc Mechanical Engineers.
49. ITMPower. *Hydrogen Purity Certification*. 2010 23/11/2012]; Available from: http://www.itm-power.com/news-item/hydrogen-purity-certification/.
50. Atkinson, A., S.J. Skinner, and J.A. Kilner, *Solid Oxide Fuel Cells*, in *Fuel Cells*, K.-D. Kreuer, Editor 2013, Springer New York. p. 657-685.
51. Singhal, S.C., *Solid Oxide Fuel Cells: Past, Present and Future*, in *Solid Oxide Fuels Cells: Facts and Figures*, J.T.S. Irvine and P. Connor, Editors. 2013, Springer London. p. 1-23.
52. Zhang, J., et al., *High temperature PEM fuel cells.* Journal of Power Sources, 2006. **160**(2): p. 872-891.
53. http://www1.eere.energy.gov/hydrogenandfuelcells/fuelcells/fc_types.html. Fuel Cell Technologies Program 2010.
54. Finnerty, C., et al., *Geometric Effects on Tubular Solid Oxide Fuel Cells.* ECS Transactions, 2007. **7**(1): p. 589-596.
55. Bujalski, W., C.A. Dikwal, and K. Kendall, *Cycling of three solid oxide fuel cell types.* Journal of Power Sources, 2007. **171**(1): p. 96-100.
56. SUAV. *SUAV Project Website*. 2012 [cited 2013 April 24th]; Available from: http://www.suav-project.eu/.
57. Sammes, N.M., et al., *The properties and performance of micro-tubular (less than 2.0 mm OD) anode suported solid oxide fuel cell (SOFC).* International Journal of Hydrogen Energy, 2011. **36**(2): p. 1882-1889.
58. D. H. Archer, L. Elikan, and R.L. Zahradnik, *Hydrocarbon Fuel Cell Technologies*, ed. B. S. Baker1965: Academic Press, New York.
59. Pal, U.B. and S.C. Singhal, *Electrochemical Vapor-Deposition Of Yttria-Stabilized Zirconia Films.* Journal of the Electrochemical Society, 1990. **137**(9): p. 2937-2941.
60. Isenberg, A.O., *Energy-conversion via Solid Oxide Electrolyte Electrochemical-Cells At High-Temperatures.* Solid State Ionics, 1981. **3-4**(AUG): p. 431-437.
61. George, R.A., *Status of tubular SOFC field unit demonstrations.* Journal of Power Sources, 2000. **86**(1–2): p. 134-139.
62. Kendall, K. *Proceedings of the International Forum on Fine Ceramics*. in *International Forum on Fine Ceramics*. 1992. Japan Fine Ceramics Center, Nagoya.
63. Kendall, K., *Progress in Microtubular Solid Oxide Fuel Cells.* International Journal of Applied Ceramic Technology, 2010. **7**(1): p. 1-9.
64. Crumm, A. *ROAMIO P250i - Key Applications of Fuel Cell Back Up Power Supporting Critical Communications Infrastructure*. in *Fuel Cell Seminar*. 2012. Uncasville, CT.
65. Prica, M., T. Alston, and K. Kendall, *Mechanical and thermal properties of a 200 tube SOFC reactor*, in *Proceedings of the Fifth International Symposium on Solid Oxide Fuel Cells*, U. Stimming, et al., Editors. 1997, Electrochemical Society Inc: Pennington. p. 619-625.
66. Alston, T., et al., *A 1000-cell SOFC reactor for domestic cogeneration.* Journal of Power Sources, 1998. **71**(1-2): p. 271-274.
67. Kendall, K. and M. Prica. in *1st European SOFC Forum*. 1994. Luzern, Switzerland.

68. Tan, X.Y., et al., *Preparation of electrolyte membranes for micro tubular solid oxide fuel cells.* Science in China Series B-Chemistry, 2008. **51**(9): p. 808-812.
69. Luebbe, H., et al. *Cathode-supported micro-tubular SOFCs based on Nd1.95NiO4+delta: Fabrication and characterisation of dip-coated electrolyte layers*. in *11th Electroceramics Conference 2008*. 2008. Manchester, England: Elsevier Science Bv.
70. Liu, Y., et al., *Fabrication and characterization of micro-tubular cathode-supported SOFC for intermediate temperature operation.* Journal of Power Sources, 2007. **174**(1): p. 95-102.
71. Huang, K. and S.C. Singhal, *Cathode-supported tubular solid oxide fuel cell technology: A critical review.* Journal of Power Sources, 2013. **237**(0): p. 84-97.
72. Howe, K.S., G.J. Thompson, and K. Kendall, *Micro-tubular solid oxide fuel cells and stacks.* Journal of Power Sources, 2011. **196**(4): p. 1677-1686.
73. Liang, Z., *Coextrusion of multilayer tubes*, in *PhD (Chapter 8)*1999, University of Birmingham.
74. Jacobson, A.J., *Materials for Solid Oxide Fuel Cells.* Chemistry of Materials, 2010. **22**(3): p. 660-674.
75. Wachsman, E., et al., *Stable high conductivity ceria/bismuth oxide bilayered electrolytes.* Journal of the Electrochemical Society, 1997. **144**(1): p. 233-236.
76. Mori, T. and J. Drennan, *Influence of microstructure on oxide ionic conductivity in doped CeO2 electrolytes.* Journal of electroceramics, 2006. **17**(2-4): p. 749-757.
77. Sahibzada, M., et al. *Evaluation of PEN structures incorporating supported thick film Ce0.9Gd0.1O1.95 electrolytes*. in *5th International Symposium on Solid Oxide Fuel Cells (SOFC-V)*. 1997. Aachen, Germany: Electrochemical Society Inc.
78. Suzuki, T., et al., *Design and fabrication of lightweight, submillimeter tubular solid oxide fuel cells.* Electrochemical and Solid State Letters, 2007. **10**(8): p. A177-A179.
79. Liu, J. and W. Weppner, *Electronic conductivity measurement of gadolinia doped ceria by DC-partial-polarization.* Ionics, 1999. **5**(1-2): p. 115-121.
80. Yamaguchi, T., et al., *Evaluation of micro LSM-supported GDC/ScSZ bilayer electrolyte with LSM-GDC activation layer for intermediate temperature-SOFCs.* Journal of the Electrochemical Society, 2008. **155**(4): p. B423-B426.
81. Ahn, J.S., et al., *High-performance bilayered electrolyte intermediate temperature solid oxide fuel cells.* Electrochemistry Communications, 2009. **11**(7): p. 1504-1507.
82. Hibino, T., et al., *A low-operating-temperature solid oxide fuel cell in hydrocarbon-air mixtures.* Science, 2000. **288**(5473): p. 2031-2033.
83. Tuller, H. and A. Nowick, *Doped ceria as a solid oxide electrolyte.* Journal of the Electrochemical Society, 1975. **122**(2): p. 255-259.
84. Feng, M., et al., *Fuel cells with doped lanthanum gallate electrolyte.* Journal of Power Sources, 1996. **63**(1): p. 47-51.
85. Ishihara, T., H. Matsuda, and Y. Takita, *Doped LaGaO3 Perovskite-Type Oxide as a New Oxide Ionic Conductor.* Journal of the American Chemical Society, 1994. **116**(9): p. 3801-3803.
86. Du, Y.H. and N.M. Sammes, *Fabrication and properties of anode-supported tubular solid oxide fuel cells.* Journal of Power Sources, 2004. **136**(1): p. 66-71.
87. Haslam, J.J., et al. *Effects of the use of pore formers on performance of an anode supported solid oxide fuel cell*. in *102nd Annual Meeting of the American-Ceramic-Society*. 2000. St Louis, Mo: Blackwell Publishing Inc.
88. Larminie, J. and A. Dicks, *Fuel Cell Systems Explained - Second Edition, pp. 210-212*2003: Wiley.
89. Kurokawa, H., et al., *Ceria nanocoating for sulfur tolerant Ni-based anodes of solid oxide fuel cells.* Electrochemical and Solid-State Letters, 2007. **10**(9): p. B135-B138.
90. Kim, G., J.M. Vohs, and R.J. Gorte, *Enhanced reducibility of ceria-YSZ composites in solid oxide electrodes.* Journal of Materials Chemistry, 2008. **18**(20): p. 2386-2390.

91. Elangovan, S. and A.C. Khandkar, *SOFC anode for enhanced performance stability and method for manufacturing same, Patent Number: US 6099985 A*, 1997, Gas Technology Institute.
92. Pihlatie, M., T. Ramos, and A. Kaiser, *Testing and improving the redox stability of Ni-based solid oxide fuel cells.* Journal of Power Sources, 2009. **193**(1): p. 322-330.
93. Suzuki, T., et al., *Impact of Anode Microstructure on Solid Oxide Fuel Cells.* Science, 2009. **325**(5942): p. 852-855.
94. Tomida, K., et al., *Structural Modification of Segmented-in-series Tubular SOFCs Using Performance Simulation and the Effect of (Sm, Ce)O-2 Cathode Interlayer on the Generation Characteristics under Pressurization.* Electrochemistry, 2009. **77**(10): p. 865-875.
95. Zhang, S.Q., et al., *Fabrication of cathode supported solid oxide fuel cell by multi-layer tape casting and co-firing method.* International Journal of Hydrogen Energy, 2009. **34**(18): p. 7789-7794.
96. Belardi, R.M., et al., *The importance of the functional layer in SOFC half cathodic cell.* Materia-Rio De Janeiro, 2008. **13**(3): p. 522-532.
97. Mai, A., et al., *Ferrite-based perovskites as cathode materials for anode-supported solid oxide fuel cells Part I. Variation of composition.* Solid State Ionics, 2005. **176**(15-16): p. 1341-1350.
98. Mai, A., et al., *Time-dependent performance of mixed-conducting SOFC cathodes.* Solid State Ionics, 2006. **177**(19–25): p. 1965-1968.
99. Haanappel, V.A.C., et al., *Optimisation of processing and microstructural parameters of LSM cathodes to improve the electrochemical performance of anode-supported SOFCs.* Journal of Power Sources, 2005. **141**(2): p. 216-226.
100. Hansen, K.K., M. Sogaard, and M. Mogensen, *Gd0.6Sr0.4Fe0.8Co0.2O3-delta: A novel type of SOFC cathode.* Electrochemical and Solid State Letters, 2007. **10**(8): p. B119-B121.
101. Han, P. and et_al. *Novel oxide fuel cells operating at 600-800 degrees C*. in *EPRI/GRI Fuel Cell Workshop on Fuel Cell Technology R&D*. 1993. New Orleans, LA.
102. Sun, C.W., R. Hui, and J. Roller, *Cathode materials for solid oxide fuel cells: a review.* Journal of Solid State Electrochemistry, 2010. **14**(7): p. 1125-1144.
103. Tietz, F., et al., *Performance of LSCF cathodes in cell tests.* Journal of Power Sources, 2006. **156**(1): p. 20-22.
104. Blum, L., et al., *Solid Oxide Fuel Cell Development at Forschungszentrum Juelich.* Fuel Cells, 2007. **7**(3): p. 204-210.
105. Santarelli, M., et al., *Experimental investigations of the microscopic features and polarization limiting factors of planar SOFCs with LSM and LSCF cathodes.* Journal of Power Sources, 2008. **177**(1): p. 111-122.
106. Kilner, J.A., R.A. De Souza, and I.C. Fullarton, *Surface exchange of oxygen in mixed conducting perovskite oxides.* Solid State Ionics, 1996. **86–88, Part 2**(0): p. 703-709.
107. Ullmann, H., et al., *Correlation between thermal expansion and oxide ion transport in mixed conducting perovskite-type oxides for SOFC cathodes.* Solid State Ionics, 2000. **138**(1–2): p. 79-90.
108. Doshi, R., et al., *Development of Solid-Oxide Fuel Cells That Operate at 500° C.* Journal of the Electrochemical Society, 1999. **146**(4): p. 1273-1278.
109. Sammes, N., et al. *The Properties and Performance Of Micro-Tubular (Less Than 1 mm OD) Anode Supported Solid Oxide Fuel Cells*. in *32nd International Conference on Advanced Ceramics and Composites*. 2008. Daytona Beach, FL: Amer Ceramic Soc.
110. Suzuki, T., et al., *One-step sintering process of gadolinia-doped ceria interlayer–scandia-stabilized zirconia electrolyte for anode supported microtubular solid oxide fuel cells.* Journal of Power Sources, 2012. **199**(0): p. 170-173.
111. Jin, C., et al., *Electrochemical properties analysis of tubular NiO-YSZ anode-supported SOFCs fabricated by the phase-inversion method.* Journal of Membrane Science, 2009. **341**(1-2): p. 233-237.

112. Yang, C., C. Jin, and F. Chen, *Micro-tubular solid oxide fuel cells fabricated by phase-inversion method.* Electrochemistry Communications, 2010. **12**(5): p. 657-660.
113. Droushiotis, N., et al., *Effects of lanthanum strontium cobalt ferrite (LSCF) cathode properties on hollow fibre micro-tubular SOFC performances.* Journal of Applied Electrochemistry, 2012. **42**(7): p. 517-526.
114. Lee, T.J. and K. Kendall. *Characterisation of electrical performance of anode supported micro-tubular solid oxide fuel cell with methane fuel*. in *10th Grove Fuel Cell Symposium*. 2007. London, England: Elsevier Science Bv.
115. Dhir, A. and K. Kendall. *Microtubular SOFC anode optimisation for direct use on methane*. in *10th Grove Fuel Cell Symposium*. 2007. London, England: Elsevier Science Bv.
116. Galloway, K.V. and N.M. Sammes, *Performance Degradation of Microtubular SOFCs Operating in the Intermediate-Temperature Range.* Journal of the Electrochemical Society, 2009. **156**(4): p. B526-B531.
117. Akhtar, N., et al., *Mixed-reactant, micro-tubular solid oxide fuel cells: An experimental study.* Journal of Power Sources, 2009. **193**(1): p. 39-48.
118. UltraElectronics-AMI. *Ultra Electronics AMI - Fuel Cell Manufacturer*. Home Page - http://www.ultra-ami.com/ 2012; Available from: http://www.ultra-ami.com/.
119. eZelleron. *eZelleron - Power to go*. Home page - http://www.ezelleron.eu/en/ 2012; Available from: http://www.ezelleron.eu/en/.
120. KoMiCo. *KoMiCo leads the way to the future of advanced materials parts*. Home page - http://www.komico.com/en/ 2012; Available from: http://www.komico.com/en/.
121. CoorsTek. *CoorsTek Technical Ceramics: CeramicCell*. Home page - http://www.coorstek.com/markets/energy_equipment/fuel_cells.php 2012; Available from: http://www.coorstek.com/markets/energy_equipment/fuel_cells.php.
122. KoMiCo, *Micro Tubular Technical Information Sheet*, 2012, Provided on request.
123. Hawkes, A. and M. Leach, *Solid oxide fuel cell systems for residential micro-combined heat and power in the UK: Key economic drivers.* Journal of Power Sources, 2005. **149**(0): p. 72-83.
124. Calise, F., G. Restucccia, and N. Sammes, *Experimental analysis of performance degradation of micro-tubular solid oxide fuel cells fed by different fuel mixtures.* Journal of Power Sources, 2011. **196**(1): p. 301-312.
125. Singh, P. and N.Q. Minh, *Solid Oxide Fuel Cells: Technology Status.* International Journal of Applied Ceramic Technology, 2004. **1**(1): p. 5-15.
126. Minh, N.Q., *Ceramic Fuel Cells.* Journal of the American Ceramic Society, 1993. **76**(3): p. 563-588.
127. Clague, R., et al., *Stress analysis of solid oxide fuel cell anode microstructure reconstructed from focused ion beam tomography.* Journal of Power Sources, 2011. **196**(21): p. 9018-9021.
128. Park, S., J.M. Vohs, and R.J. Gorte, *Direct oxidation of hydrocarbons in a solid-oxide fuel cell.* Nature, 2000. **404**(6775): p. 265-267.
129. Lin, Y., et al., *Direct operation of solid oxide fuel cells with methane fuel.* Solid State Ionics, 2005. **176**(23-24): p. 1827-1835.
130. Millichamp, J., et al., *A study of carbon deposition on solid oxide fuel cell anodes using electrochemical impedance spectroscopy in combination with a high temperature crystal microbalance.* Journal of Power Sources, 2013. **235**(0): p. 14-19.
131. Koh, J.-H., et al., *Carbon deposition and cell performance of Ni-YSZ anode support SOFC with methane fuel.* Solid State Ionics, 2002. **149**(3–4): p. 157-166.
132. Laosiripojana, N. and S. Assabumrungrat, *Catalytic steam reforming of ethanol over high surface area CeO2: The role of CeO2 as an internal pre-reforming catalyst.* Applied Catalysis B-Environmental, 2006. **66**(1-2): p. 29-39.
133. Chen, F.Z., et al., *Pre-reforming of propane for low-temperature SOFCs.* Solid State Ionics, 2004. **166**(3-4): p. 269-273.

134. Finnerty, C., et al., *SOFC system with integrated catalytic fuel processing.* Journal of Power Sources, 2000. **86**(1-2): p. 459-463.
135. Zheng, J., J.J. Strohm, and C. Song, *Steam reforming of liquid hydrocarbon fuels for micro-fuel cells. Pre-reforming of model jet fuels over supported metal catalysts.* Fuel Processing Technology, 2008. **89**(4): p. 440-448.
136. Bessler, W.G. *Hydrocarbon direct oxidation or internal reforming? A critical discussion from an elementary kinetic viewpoint*. in *8th European Solid Oxide Fuel Cell Forum,* . 2008. Lucerne, Switzerland: Fuel Cell Forum.
137. Gorte, R.J. and J.M. Vohs, *Novel SOFC anodes for the direct electrochemical oxidation of hydrocarbons.* Journal of Catalysis, 2003. **216**(1–2): p. 477-486.
138. Zhu, W., et al., *Ceria coated Ni as anodes for direct utilization of methane in low-temperature solid oxide fuel cells.* Journal of Power Sources, 2006. **160**(2): p. 897-902.
139. Zhang, L.S., et al., *Samaria-doped Ceria Modified Ni/YSZ Anode for Direct Methane Fuel in Tubular Solid Oxide Fuel Cells by Impregnation Method.* Chinese Journal of Chemical Physics, 2009. **22**(4): p. 429-434.
140. Asamoto, M., et al., *Improvement of Ni/SDC anode by alkaline earth metal oxide addition for direct methane-solid oxide fuel cells.* Electrochemistry Communications, 2009. **11**(7): p. 1508-1511.
141. McIntosh, S. and R.J. Gorte, *Direct hydrocarbon solid oxide fuel cells.* Chemical Reviews, 2004. **104**(10): p. 4845-4865.
142. Lin, Y., Z. Zhan, and S.A. Barnett, *Improving the stability of direct-methane solid oxide fuel cells using anode barrier layers.* Journal of Power Sources, 2006. **158**(2): p. 1313-1316.
143. Zhan, Z. and S.A. Barnett, *Use of a catalyst layer for propane partial oxidation in solid oxide fuel cells.* Solid State Ionics, 2005. **176**(9-10): p. 871-879.
144. Yoon, S.P., et al. *Mixed-fuels fuel cell running on methane-air mixture*. in *3rd International Conference on Fuel Cell Science, Engineering and Technology*. 2005. Ypsilanti, MI: Amer Soc Mechanical Engineers.
145. Mallon, C. and K. Kendall, *Sensitivity of nickel cermet anodes to reduction conditions.* Journal of Power Sources, 2005. **145**(2): p. 154-160.
146. Ahmed, K. and K. Foger, *Kinetics of internal steam reforming of methane on Ni/YSZ-based anodes for solid oxide fuel cells.* Catalysis Today, 2000. **63**(2-4): p. 479-487.
147. McIntosh, S., J.M. Vohs, and R.J. Gorte, *An examination of lanthanide additives on the performance of Cu-YSZ cermet anodes.* Electrochimica Acta, 2002. **47**(22-23): p. 3815-3821.
148. McIntosh, S., J.M. Vohs, and R.J. Gorte, *Impedance Spectroscopy for the Characterization of Cu-Ceria-YSZ Anodes for SOFCs.* Journal of the Electrochemical Society, 2003. **150**(10): p. A1305-A1312.
149. Jiang, S.P. and S.H. Chan, *A review of anode materials development in solid oxide fuel cells.* Journal of Materials Science, 2004. **39**(14): p. 4405-4439.
150. Latz, J., C. Mallon, and K. Kendall. *Operation of SOFCs with Nickel Cermet Anodes on Methane*. in *Sixth European Solid Oxide Fuel Cell Forum*. 2004. Lucerne, Switzerland: Solid Oxide Fuel Cell Forum
151. McIntosh, S., J.M. Vohs, and R.J. Gorte, *Role of Hydrocarbon Deposits in the Enhanced Performance of Direct-Oxidation SOFCs.* Journal of the Electrochemical Society, 2003. **150**(4): p. A470-A476.
152. Liu, J.A. and S.A. Barnett, *Operation of anode-supported solid oxide fuel cells on methane and natural gas.* Solid State Ionics, 2003. **158**(1-2): p. 11-16.
153. Murray, E.P. and S.A. Barnett, *Operation of low-temperature SOFCs on pure methane and ethane without carbon deposition*, in *Solid Oxide Fuel Cells*, S.C. Singhal and M. Dokiya, Editors. 1999, Electrochemical Society Inc: Pennington. p. 1001-1009.

154. Kendall, K., et al., *Effects of dilution on methane entering an SOFC anode.* Journal of Power Sources, 2002. **106**(1-2): p. 323-327.
155. Dikwal, C.M., W. Bujalski, and K. Kendall, *The effect of temperature gradients on thermal cycling and isothermal ageing of micro-tubular solid oxide fuel cells.* Journal of Power Sources, 2009. **193**(1): p. 241-248.
156. Atkinson, A. *http://www.real-sofc.org/*. Real-SOFC 2009 [cited 2009 06/10/2009]; Real-SOFC project homepage]. Available from: http://www.real-sofc.org/.
157. Atkinson, A. and B. Sun, *Residual stress and thermal cycling of planar solid oxide fuel cells.* Materials Science and Technology, 2007. **23**(10): p. 1135-1143.
158. Lawlor, V., et al., *Review of the micro-tubular solid oxide fuel cell Part I. Stack design issues and research activities.* Journal of Power Sources, 2009. **193**(2): p. 387-399.
159. Du, Y.H., C. Finnerty, and J. Jiang, *Thermal stability of portable microtubular SOFCs and stacks.* Journal of the Electrochemical Society, 2008. **155**(9): p. B972-B977.
160. Dikwal, C.M., W. Bujalski, and K. Kendall. *Characterization of the electrochemical performance of micro-tubular SOFC in partial reduction and oxidation conditions*. in *10th Grove Fuel Cell Symposium*. 2007. London, England: Elsevier Science Bv.
161. Larminie, J. and A. Dicks, *Fuel Cell Systems Explained - Second Edition, pp. 30-35*2003: Wiley.
162. Ramani, V., *Fuel Cells*, in *Interface*2006, The Electrochemical Society. p. 41-44.
163. Roy, B.R., et al., *Mechanical properties of micro-tubular solid oxide fuel cell anodes.* Journal of Power Sources, 2009. **188**(1): p. 220-224.
164. Wang, F.Y., et al., *Porous Ag-Ce0.8Sm0.2O1.9 cermets as anode materials for intermediate temperature solid oxide fuel cells using CO fuel.* Journal of Power Sources, 2008. **185**(2): p. 862-866.
165. Hu, J., et al., *Effect of composite pore-former on the fabrication and performance of anode-supported membranes for SOFCs.* Journal of Membrane Science, 2008. **318**(1-2): p. 445-451.
166. Cui, D., et al., *Comparison of different current collecting modes of anode supported micro-tubular SOFC through mathematical modeling.* Journal of Power Sources, 2007. **174**(1): p. 246-254.
167. Suzuki, T., et al., *Current collecting efficiency of micro tubular SOFCs.* Journal of Power Sources, 2007. **163**(2): p. 737-742.
168. Thompson, G., *Improving the Consistency of Microtubular Solid Oxide Fuel Cells for Methane Fuelled Stacks*, in *Chemical Engineering*2010, University of Birmingham.
169. Suzuki, T., et al., *Anode-supported micro tubular SOFCs for advanced ceramic reactor system.* Journal of Power Sources, 2007. **171**(1): p. 92-95.
170. Zhu, H.Y. and R.J. Kee, *The influence of current collection on the performance of tubular anode-supported SOFC cells.* Journal of Power Sources, 2007. **169**(2): p. 315-326.
171. Nicolas, D.D., et al., *Co-Extrusion / Phase Inversion / Co-Sintering for Fabrication of Hollow Fiber Solid Oxide Fuel Cells.* ECS Transactions, 2009. **25**(2): p. 665-672.
172. Dal Grande, F., et al., *Microstructure and performance of novel Ni anode for hollow fibre solid oxide fuel cells.* Solid State Ionics, 2009. **180**(11-13): p. 800-804.
173. Droushiotis, N., et al., *Characterization of NiO-yttria stabilised zirconia (YSZ) hollow fibres for use as SOFC anodes.* Solid State Ionics, 2009. **180**(17-19): p. 1091-1099.
174. Suzuki, T., et al., *Performance of the Micro-SOFC Module Using Submillimeter Tubular Cells.* Journal of the Electrochemical Society, 2009. **156**(3): p. B318-B321.
175. Droushiotis, N., et al., *Novel co-extruded electrolyte-anode hollow fibres for solid oxide fuel cells.* Electrochemistry Communications, 2009. **11**(9): p. 1799-1802.
176. Ouweltjes, J.P., et al., *Redox Tolerant SOFC Anodes with High Electrochemical Performance.* Fuel Cells, 2009. **9**(6): p. 873-882.

177. Lockett, M., M.J.H. Simmons, and K. Kendall. *CFD to predict temperature profile for scale up of micro-tubular SOFC stacks*. in *8th Grove Fuel Cell Symposium*. 2003. London, England: Elsevier Science Bv.
178. Yamaguchi, T., et al., *Fabrication and evaluation of a novel cathode-supported honeycomb SOFC stack.* Materials Letters, 2009. **63**(29): p. 2577-2580.
179. Funahashi, Y., et al., *New Fabrication Technique for Series-Connected Stack With Micro Tubular SOFCs.* Fuel Cells, 2009. **9**(5): p. 711-716.
180. Suzuki, T., et al., *New Stack Design of Micro-tubular SOFCs for Portable Power Sources.* Fuel Cells, 2008. **8**(6): p. 381-384.
181. Kakac, S., A. Pramuanjaroenkij, and X.Y. Zhou, *A review of numerical modeling of solid oxide fuel cells.* International Journal of Hydrogen Energy, 2007. **32**(7): p. 761-786.
182. Cui, D.A. and M.J. Cheng, *Thermal stress modeling of anode supported micro-tubular solid oxide fuel cell.* Journal of Power Sources, 2009. **192**(2): p. 400-407.
183. Serincan, M.F., U. Pasaogullari, and N.M. Sammes, *Effects of operating conditions on the performance of a micro-tubular solid oxide fuel cell (SOFC).* Journal of Power Sources, 2009. **192**(2): p. 414-422.
184. Izzo, J.R., A.A. Peracchio, and W.K.S. Chiu, *Modeling of gas transport through a tubular solid oxide fuel cell and the porous anode layer.* Journal of Power Sources, 2008. **176**(1): p. 200-206.
185. Funahashi, Y., et al., *Simulation Study for the Optimization of Microtubular Solid Oxide Fuel Cell Bundles.* Journal of Fuel Cell Science and Technology, 2010. **7**(2): p. 4.
186. Kattke, K.J., et al., *High-fidelity stack and system modeling for tubular solid oxide fuel cell system design and thermal management.* Journal of Power Sources, 2011. **196**(8): p. 3790-3802.
187. Mulone, V., S. Cordiner, and A. Mariani, *CFD-Based Design of Microtubular Solid Oxide Fuel Cells.* Journal of Heat Transfer-Transactions of the Asme, 2010. **132**(6): p. 15.
188. Yang, J., et al., *Parameter optimization for tubular solid oxide fuel cell stack based on the dynamic model and an improved genetic algorithm.* International Journal of Hydrogen Energy, 2011. **36**(10): p. 6160-6174.
189. Tade, M.O., V.A. Danilov, and P. Vijay, *Improved Tank in Series Reactor Model for Tubular Solid Oxide Fuel Cell Stacks.* Chemical Engineering & Technology, 2011. **34**(5): p. 737-745.
190. Suzuki, T., et al., *Development of Bundle/Stack Fabrication Technology for Micro-SOFCs*, in *Ceramic Materials and Components for Energy and Environmental Applications*, D.L. Jiang, et al., Editors. 2010, Amer Ceramic Soc: Westerville. p. 179-184.
191. Wetzko, M., et al., *Solid oxide fuel cell stacks using extruded honeycomb type elements.* Journal of Power Sources, 1999. **83**(1-2): p. 148-155.
192. Yamaguchi, T., et al., *Fabrication and Evaluation of Micro-Tubular SOFC Stack.* ECS Transactions, 2012. **45**(1): p. 531-534.
193. Funahashi, Y., et al., *Optimization of Configuration for Cube-Shaped SOFC Bundles*, in *Solid Oxide Fuel Cells 10*, K. Eguchi, et al., Editors. 2007, Electrochemical Society Inc: Pennington. p. 643-649.
194. Suzuki, T., et al., *Recent Development of Microceramic Reactors for Advanced Ceramic Reactor System.* Journal of Fuel Cell Science and Technology, 2010. **7**(3): p. 5.
195. Sammes, N.M., R. Bove, and Y.H. Du, *Assembling single cells to create a stack: The case of a 100 W microtubular anode-supported solid oxide fuel cell stack.* Journal of Materials Engineering and Performance, 2006. **15**(4): p. 463-467.
196. Sammes, N.M., Y. Du, and R. Bove, *Design and fabrication of a 100 W anode supported micro-tubular SOFC stack.* Journal of Power Sources, 2005. **145**(2): p. 428-434.
197. Lee, S.-B., et al., *Development of a 700 W anode-supported micro-tubular SOFC stack for APU applications.* International Journal of Hydrogen Energy, 2008. **33**(9): p. 2330-2336.

198. Wang, S.R., et al., *Performance of an anode-supported tubular solid oxide fuel cells stack with two single cells connected by a co-sintered ceramic interconnector.* International Journal of Hydrogen Energy, 2011. **36**(10): p. 6194-6198.
199. Liu, J.A., J.A. Ding, and G.Q. Yin, *Fabrication and characterization of low-temperature SOFC stack based on GDC electrolyte membrane.* Journal of Membrane Science, 2011. **371**(1-2): p. 219-225.
200. Mizutani, Y. *Current state of R&D on micro tubular solid oxide fuel cells in Japan*. in *Conference of the NATO-Advanced-Study-Institute on Mini-Micro Fuel Cells - Fundamentals and Applications*. 2007. Cesme Izmir, Turkey: Springer.
201. Nesaraj, A.S., *Recent developments in solid oxide fuel cell technology - a review.* Journal of Scientific & Industrial Research, 2010. **69**(3): p. 169-176.
202. Shaigan, N., et al., *A review of recent progress in coatings, surface modifications and alloy developments for solid oxide fuel cell ferritic stainless steel interconnects.* Journal of Power Sources, 2010. **195**(6): p. 1529-1542.
203. Dhir, A., *Improved Microtubular Solid Oxide Fuel Cells*, in *Chemical Engineering*2008, University of Birmingham: Birmingham.
204. Preece, J., *Oxygenated Hydrocarbon Fuels*

For Solid Oxide Fuel Cells, in *Chemical Engineering PhD Thesis*2005, University of Birmingham.
205. Kim, P., D.J.L. Brett, and N.P. Brandon, *The effect of water content on the electrochemical impedance response and microstructure of Ni-CGO anodes for solid oxide fuel cells.* Journal of Power Sources, 2009. **189**(2): p. 1060-1065.
206. Bertoldi, M., et al., *Demonstration of a 4-Cells SOFC Stack Under Different Experimental Conditions.* Journal of Fuel Cell Science and Technology, 2008. **5**(1): p. 11004.
207. Suzuki, T., et al., *Fabrication and characterization of micro tubular SOFCs for operation in the intermediate temperature.* Journal of Power Sources, 2006. **160**(1): p. 73-77.
208. Shao, Z. and S.M. Haile, *A high-performance cathode for the next generation of solid-oxide fuel cells.* Nature, 2004. **431**(7005): p. 170-173.
209. Ramakrishna, P.A., S. Yang, and C.H. Sohn, *Innovative design to improve the power density of a solid oxide fuel cell.* Journal of Power Sources, 2006. **158**(1): p. 378-384.
210. Roth, C., et al., *Characterization of Differently Synthesized Pt-Ru Fuel Cell Catalysts by Cyclic Voltammetry, FTIR Spectroscopy, and in Single Cells.* Journal of the Electrochemical Society, 2002. **149**(11): p. E433-E439.
211. Jasinski, P., et al., *Impedance spectroscopy of single chamber SOFC.* Solid State Ionics, 2004. **175**(1-4): p. 35-38.
212. Barbucci, A., et al., *Characterisation of composite SOFC cathodes using electrochemical impedance spectroscopy. Analysis of Pt/YSZ and LSM/YSZ electrodes.* Electrochimica Acta, 2002. **47**(13-14): p. 2183-2188.
213. Orazem, M.E. and B. Tribollet, *Electrochemical impedance spectroscopy*. The Electrochemical Society Series2008, The Electrochemical Society Series: Wiley Interscience.
214. Shi, Y.X. and N.S. Cai. *Modeling & Simulation of Solid Oxide Fuel Cell Using COMSOL MultiPhysics*. in *COMSOL Users Conferences*. 2006. Shanghai & Beijing: COMSOL MULTIPHYSICS.
215. Curnick, O. *Theory of AC Impedance Spectroscopy*. in *Electrochemistry and Electrochemical Engineering Module*. 2010. University of Birmingham.
216. Leonide, A., et al., *Evaluation and modeling of the cell resistance in anode-supported solid oxide fuel cells.* Journal of the Electrochemical Society, 2008. **155**(1): p. B36-B41.
217. Nam, J.H. and D.H. Jeon, *A comprehensive micro-scale model for transport and reaction in intermediate temperature solid oxide fuel cells.* Electrochimica Acta, 2006. **51**(17): p. 3446-3460.

218. KLATencor, *MicroXAM-100 Optical Profiler*, in *Product Overview - Development Series*2010.
219. Dikwal, C.M., *Cycling Studies of Micro-tubular Solid Oxide Fuel Cells*, in *Chemical Engineering*2009, University of Birmingham.
220. Huber, A.-K., et al., *In situ study of activation and de-activation of LSM fuel cell cathodes–Electrochemistry and surface analysis of thin-film electrodes.* Journal of Catalysis, 2012.
221. Lee, T.J., *Characterisation of Anode Supported Microtubular SOFC Process on Pure Methane Reduction and Operation*, in *Department of Chemical Engineering*2009, University of Birmingham.
222. Wang, S.-G., et al., *Kinetic aspect of CO2 reforming of CH4 on Ni(1 1 1): A density functional theory calculation.* Surface Science, 2007. **601**(5): p. 1271-1284.
223. Zhou, L., et al., *Performance of an anode-supported tubular solid oxide fuel cell (SOFC) under pressurized conditions.* Electrochimica Acta, 2008. **53**(16): p. 5195-5198.
224. Nehter, P., *Two-dimensional transient model of a cascaded micro-tubular solid oxide fuel cell fed with methane.* Journal of Power Sources, 2006. **157**(1): p. 325-334.
225. Hajimolana, S.A. and M. Soroush, *Dynamics and Control of a Tubular Solid-Oxide Fuel Cell.* Industrial & Engineering Chemistry Research, 2009. **48**(13): p. 6112-6125.
226. Bhattacharyya, D. and R. Rengaswamy, *A Review of Solid Oxide Fuel Cell (SOFC) Dynamic Models.* Industrial & Engineering Chemistry Research, 2009. **48**(13): p. 6068-6086.
227. Achenbach, E., *Response of a solid oxide fuel cell to load change.* Journal of Power Sources, 1995. **57**(1-2): p. 105-109.
228. Serincan, M.F., U. Pasaogullari, and N.M. Sammes, *A transient analysis of a micro-tubular solid oxide fuel cell (SOFC).* Journal of Power Sources, 2009. **194**(2): p. 864-872.
229. Bhattacharyya, D., R. Rengaswamy, and C. Finnerty, *Dynamic modeling and validation studies of a tubular solid oxide fuel cell.* Chemical Engineering Science, 2009. **64**(9): p. 2158-2172.
230. Achenbach, E., *Three-dimensional and time-dependent simulation of a planar solid oxide fuel cell stack.* Journal of Power Sources, 1994. **49**(1–3): p. 333-348.
231. Welty, J.R., et al., *Fundamentals of momentum, heat, and mass transfer*2009: John Wiley & Sons.
232. Crane, *Flow of fluids through valves, fittings, and pipe.* , in *Technical Paper No. 410 (TP 410)*1988.
233. Yokokawa, H., et al., *Fundamental mechanisms limiting solid oxide fuel cell durability.* Journal of Power Sources, 2008. **182**(2): p. 400-412.
234. Virkar, A.V., F.F. Lange, and M.A. Homel, *A simple analysis of current collection in tubular solid oxide fuel cells.* Journal of Power Sources, 2010. **195**(15): p. 4816-4825.
235. Sutton, T.G., *Wire mesh current collector, solid state electrochemical devices including the same, and methods of making the same*, Patent, Editor 2011, UT-Battelle LLC.
236. Homel, M., et al., *Carbon monoxide-fueled solid oxide fuel cell.* Journal of Power Sources, 2010. **195**(19): p. 6367-6372.
237. Leonide, A., et al., *Performance simulation of current/voltage-characteristics for SOFC single cell by means of detailed impedance analysis.* Journal of Power Sources, 2011. **196**(17): p. 7343-7346.
238. Jiang, S.P., *A comparison of O2 reduction reactions on porous (La,Sr)MnO3 and (La,Sr)(Co,Fe)O3 electrodes.* Solid State Ionics, 2002. **146**(1–2): p. 1-22.
239. Waller, D., et al., *The effect of thermal treatment on the resistance of LSCF electrodes on gadolinia doped ceria electrolytes.* Solid State Ionics, 1996. **86–88, Part 2**(0): p. 767-772.
240. Lee, J.H., et al., *Quantitative analysis of microstructure and its related electrical property of SOFC anode, Ni–YSZ cermet.* Solid State Ionics, 2002. **148**(1–2): p. 15-26.
241. Zhao, H., et al., *Preparation, chemical stability and electrochemical properties of LSCF–CBO composite cathodes.* Materials chemistry and physics, 2004. **88**(1): p. 160-166.

242. Kim, H.S., et al., *A Study of LSCF Cathode Material Prepared by Pechini Process for IT-SOFCs*, in *2012 International Conference on Power and Energy Systems*2012.
243. Bessette, N., et al., *Program Area of Interest: Fuel Transformer Solid Oxide Fuel Cell*, in *Technical Progress Report; Semi Annual*2005, Acumentrics. p. 45-46.
244. Kikuta, K., et al., *Fabrication and characterization of microtubular and flattened ribbed SOFCs prepared by the multi-dip coating and co-firing.* Journal of the European Ceramic Society, 2009. **30**(4): p. 927-931.
245. Siau, S., et al., *Dip coating of dielectric and solder mask epoxy polymer layers for build-up purposes.* Applied surface science, 2005. **245**(1): p. 353-368.
246. Arregui, A., et al., *Stability of ferritic perovskite cathodes in anode-supported solid oxide fuel cells under different processing and operation parameters.* Electrochimica Acta, 2011. **58**: p. 312-321.
247. Xie, Z., et al., *Fuel cell cathode catalyst layers from "green" catalyst inks.* Energy & Environmental Science, 2008. **1**(1): p. 184-193.
248. Yashiro, N., T. Usui, and K. Kikuta, *Application of a thin intermediate cathode layer prepared by inkjet printing for SOFCs.* Journal of the European Ceramic Society, 2010. **30**(10): p. 2093-2098.
249. Luebbe, H., et al. *Microtubular SOFC on nickelate cathode support: Dip-Coating of GDC interlayers*. in *9th European Solid Oxide Fuel Cell Forum*. 2010. Lucerne, Switzerland.
250. Manthiram, A., et al., *(Y0.5In0.5)Ba(Co,Zn)4O7 cathodes with superior high-temperature phase stability for solid oxide fuel cells.* Journal of Power Sources, 2012. **214**(0): p. 7-14.
251. Mahoney, F.M., *Reduction-Oxidation-Tolerant Electrodes for Solid Oxide Fuel Cells*, 2010, Saint-Gobain Ceramics and Plastics Inc.: US.
252. Raichur, A.M., S.P. Rao, and S.S. Tripathy, *Dispersion studies of sub-micron zirconia using Dolapix CE 64.* Colloids and Surfaces A: Physicochemical and Engineering Aspects, 2007. **302**(1-3): p. 553-558.
253. Wheatley, A.E.H., et al., *Nanoparticulate copper--routes towards oxidative stability.* Dalton Trans, 2010. **39**(28): p. 6496-502.
254. Wheatley, A.E.H., et al., *Cu-Based Nanoalloys in the Base-Free Ullmann Heterocyle-Aryl Ether Synthesis.* Organic Process Research & Development, 2010. **14**(3): p. 644-649.
255. Miyake, M., et al., *Size control of monodispersed Pt nanoparticles and their 2D organization by electrophoretic deposition.* Journal of Physical Chemistry B, 1999. **103**(19): p. 3818-3827.
256. Kim, S.I., et al., *Thermal characteristics of poly(vinyl alcohol) and poly(vinylpyrrolidone) IPNs.* Journal of Applied Polymer Science, 2002. **86**(8): p. 1844-1847.
257. Howe, K.S. and E.R. Clark, *GB2490869 - Ink: A Novel Water-Based Cathode Ink Formulation for Solid Oxide Fuel Cells - UK Patent Application Number: 1107672.6*, T.U.o. Birmingham, Editor 2012: UK.
258. Xia, X., et al., *Quantitative Analysis of the Role Played by Poly(vinylpyrrolidone) in Seed-Mediated Growth of Ag Nanocrystals.* Journal of the American Chemical Society, 2012. **134**(3): p. 1793-1801.
259. Barnett, S.A. and T. Tsai, *Effect of LSM-YSZ cathode on thin-electrolyte solid oxide fuel cell performance.* Solid State Ionics, 1997. **93**(3-4): p. 207-217.
260. Kim, J.H., H. Schlegl, and J.T.S. Irvine, *In press, corrected proof: "The catalytic effect of impregnated (La, Sr)(Ti, Mn)O3±delta with CeO2 and Pd as potential anode materials in high temperature solid oxide fuel cells".* International Journal of Hydrogen Energy, 2012(0).
261. Nishimoto, S., et al., *Properties of La2-xPrxNiO4 cathode for intermediate-temperature solid oxide fuel cells.* Journal of the Ceramic Society of Japan, 2011. **119**(1387): p. 246-250.
262. Harris, J.M., *Poly (ethylene glycol) chemistry: biotechnical and biomedical applications*1992: Plenum Publishing Corporation.

263. Yang, T.-H., et al., *Fabrication of a thin catalyst layer using organic solvents.* Journal of Power Sources, 2004. **127**(1–2): p. 230-233.
264. Zhang, X., et al., *Ni-SDC cermet anode for medium-temperature solid oxide fuel cell with lanthanum gallate electrolyte.* Journal of Power Sources, 1999. **83**(1–2): p. 170-177.
265. Wang, F.-Y., S. Chen, and S. Cheng, *Gd3+ and Sm3+ co-doped ceria based electrolytes for intermediate temperature solid oxide fuel cells.* Electrochemistry Communications, 2004. **6**(8): p. 743-746.
266. Zhu, Q. and B. Fan, *Low temperature sintering of 8YSZ electrolyte film for intermediate temperature solid oxide fuel cells.* Solid State Ionics, 2005. **176**(9–10): p. 889-894.
267. Sammes, N.M. and Y. Du, *Fabrication and Characterization of Tubular Solid Oxide Fuel Cells.* International Journal of Applied Ceramic Technology, 2007. **4**(2): p. 89-102.
268. Howe, K.S., et al., *A novel water-based cathode ink formulation.* International Journal of Hydrogen Energy, 2013. **38**(3): p. 1731-1736.
269. McCoppin, J., et al., *Solid oxide fuel cell with compositionally graded cathode functional layer deposited by pressure assisted dual-suspension spraying.* Journal of Power Sources, 2011. **196**(8): p. 3761-3765.
270. Hanifi, A.R., et al., *Improved Redox and Thermal Cycling Resistant Tubular Ceramic Fuel Cells.* ECS Transactions, 2011. **35**(1): p. 409-418.
271. Torabi, A., et al., *Effects of Porous Support Microstructure on Performance of Infiltrated Electrodes in Solid Oxide Fuel Cells.* Journal of the Electrochemical Society, 2011. **159**(2): p. B201-B210.
272. Sholklapper, T.Z., et al., *LSM-infiltrated solid oxide fuel cell cathodes.* Electrochemical and Solid State Letters, 2006. **9**(8): p. A376-A378.
273. Vohs, J.M. and R.J. Gorte, *High-Performance SOFC Cathodes Prepared by Infiltration.* Advanced materials, 2009. **21**(9): p. 943-956.
274. He, H., et al., *Low-Temperature Fabrication of Oxide Composites for Solid Oxide Fuel Cells.* Journal of the American Ceramic Society, 2004. **87**(3): p. 331-336.
275. Dees, D.W., et al., *Conductivity of Porous NI/ZRO2-Y2O3 Cermets.* Journal of the Electrochemical Society, 1987. **134**(9): p. 2141-2146.
276. Klemenso, T., et al., *Stability of Ni-yttria stabilized zirconia anodes based on Ni-impregnation.* Journal of Power Sources, 2010. **195**(21): p. 7295-7301.
277. Jiang, S.P., Y.Y. Duan, and J.G. Love, *Fabrication of high-performance NiOY2O3-ZrO2 cermet anodes of solid oxide fuel cells by ion impregnation.* Journal of the Electrochemical Society, 2002. **149**(9): p. A1175-A1183.
278. Steele, B.C.H., K.M. Hori, and S. Uchino, *Kinetic parameters influencing the performance of IT-SOFC composite electrodes.* Solid State Ionics, 2000. **135**(1-4): p. 445-450.
279. Jiang, S.P., et al., *Fabrication and performance of impregnated Ni anodes of solid oxide fuel cells.* Journal of the American Ceramic Society, 2005. **88**(7): p. 1779-1785.
280. Qiao, J., et al., *Ni/YSZ and Ni-CeO2/YSZ anodes prepared by impregnation for solid oxide fuel cells.* Journal of Power Sources, 2007. **169**(2): p. 253-258.
281. Sholklapper, T.Z., et al., *Synthesis of Dispersed and Contiguous Nanoparticles in Solid Oxide Fuel Cell Electrodes.* Fuel Cells, 2008. **8**(5): p. 303-312.
282. Jiang, S.P., *A review of wet impregnation - An alternative method for the fabrication of high performance and nano-structured electrodes of solid oxide fuel cells.* Materials Science and Engineering a-Structural Materials Properties Microstructure and Processing, 2006. **418**(1-2): p. 199-210.
283. Hanifi, A.R., et al., *Development of Monolithic YSZ Porous and Dense Layers through Multiple Slip Casting for Ceramic Fuel Cell Applications.* International Journal of Applied Ceramic Technology, 2011. **9**(6): p. 1011-1021.

284. Virkar, A.V., et al., *The role of electrode microstructure on activation and concentration polarizations in solid oxide fuel cells.* Solid State Ionics, 2000. **131**(1): p. 189-198.
285. Yonekura, T., et al., *Exchange Current Density of Solid Oxide Fuel Cell Electrodes.* ECS Transactions, 2011. **35**(1): p. 1007-1014.
286. Tanner, C.W., K.Z. Fung, and A.V. Virkar, *The effect of porous composite electrode structure on solid oxide fuel cell performance .1. Theoretical analysis.* Journal of the Electrochemical Society, 1997. **144**(1): p. 21-30.
287. Leng, Y.J., et al., *Performance evaluation of anode-supported solid oxide fuel cells with thin film YSZ electrolyte.* International Journal of Hydrogen Energy, 2004. **29**(10): p. 1025-1033.
288. Sholklapper, T.Z., et al., *Nanostructured solid oxide fuel cell electrodes.* nano letters, 2007. **7**(7): p. 2136-2141.
289. Howe, K.S. and K. Kendall, *Transient Performance of Micro-Tubular Solid Oxide Fuel Cells.* Journal of Fuel Cell Science and Technology, 2011. **8**(3): p. 034502.
290. Howe, K.S., et al., *Performance of microtubular SOFCs with infiltrated electrodes under thermal cycling.* International Journal of Hydrogen Energy, 2013. **38**(2): p. 1058-1067.
291. AeroVironment. *UAS Advanced Development: Hornet, 2003*. 2003; Available from: http://www.avinc.com/uas/adc/hornet/.
292. NASA. *Helios Energy Storage System Passes Major Functional Test - Press Release*. 2002; Available from: http://www.nasa.gov/centers/dryden/news/NewsReleases/2002/02-24_prt.htm.
293. NASA. *"NASA Sets Second Helios Fuel Cell Checkput Flight for Thursday" - Press release*. 2003; Available from: http://www.spaceref.com/news/viewpr.html?pid=11938.
294. FuelCells.org. *Chart of Fuel Cell Vehicles*. Information Resources - Fuel Cell Library October 12th, 2011]; Available from: http://www.fuelcells.org/info/fclib.html.old.
295. FHWiesbaden, *"Betriebsanleitung fur das brennstoffzellenbetriebene Modellflugzeug".* 2005.
296. Moffitt, B.A., *A Methodology for the Validated Design Space Exploration of Fuel Cell Powered Unmanned Aerial Vehicles - PhD Thesis*, in *School of Aerospace Engineering*2010, Georgia Institute of Technology.
297. NavalResearchLaboratory, *Surveillance Vehicles Soar on Fuel Cell Power*, in *Spectra*2010. p. 2-5.
298. Foch, R.J., J.F. MacKrell, and W.W. Schultz. *"XFC - Fuel Cell Powered Long Endurance Tactical UAS", Naval Research Laboratory*. in *AUVSI Unmanned Systems North America*. 2011. Walter E. Washington Convention Center, Washington, DC, USA.
299. *"AeroVironment Flies World's First Hydrogen Powered Plane"*, in *Fuel Cells*

*Bulletin*2005. p. 2-3.
300. Black, R. *First hydrogen plane tested in US - BBC News*. 2005 October 14th, 2011]; Available from: http://news.bbc.co.uk/2/hi/americas/4643575.stm.
301. LaBreche, T. *"Solid Oxide Fuel Cell Power Systems for Small UAVs" , AMI*

in *Joint Service Power Expo - "Power & Energy Independence for Warfighters"*. 2007. San Diego, CA.
302. Bradley, T.H., Moffitt, B., Thomas, R. W., Mavris, D. and Parekh, D. E. *Test Results for a Fuel Cell-Powered Demonstration Aircraft*. in *Society of Automotive Engineers Power System Conference*. 2006.
303. Bradley, T.H., et al., *Development and experimental characterization of a fuel cell powered aircraft.* Journal of Power Sources, 2007. **171**(2): p. 793-801.
304. Bradley, T.H., Moffitt, B., Thomas, R., Parekh, D. E. and Mavris, D., *Flight Test Results for a Fuel Cell-Powered Demonstration Aircraft.* AIAA, 2007(2007-0032).

305. MFDCLab. *Fuel Cell Powered UAV - Environmentally Friendly, Cal State LA*. 2006 [cited 2011 October 12th, 2011]; Available from: http://www.calstatela.edu/centers/mfdclab/research/fcuav.htm.
306. Horizon. *"Horizon Fuel Cell Powers New World Record in UAV Flight", Press Release*. 2007; Available from: http://www.horizonfuelcell.com/file/Pterosoardistancerecord.pdf.
307. Chiang, C., *Email communication with K.S. Howe - Pterosaur flight time*, 2011.
308. Herwerth, C., et al., *Development of a Small Long Endurance Hybrid PEM Fuel Cell Powered UAV*, in *Society of Automotive Engineers*2007, California and Oklahoma State Universities and Horizon Fuel Cell.
309. Horizon. *World's first zero emission, hydrogen fuel cell jet* 2007; Available from: http://www.horizonfuelcell.com/hyfish.htm.
310. Howard, C.E., *Hydrogen fuel-cell technology takes off, powering Hyfish UAV*, in *Military and Aerospace Electronics*2007, Aerospace and Defence Media Group.
311. ChosunNews. *Korean Scientists Build Fuel Cell-Powered UAV*. 2007 October 12th, 2011]; Available from: http://english.chosun.com/site/data/html_dir/2007/10/10/2007101061024.html.
312. Shephard. *"Adaptive Materials and Michigan students set record fuel-cell-powered UAV flight", November 2008.* 2008; Available from: http://www.shephard.co.uk/news/uvonline/adaptive-materials-and-michigan-students-set-record-fuel-cell-powered-uav-flight/761/.
313. FlugRevue. *News in Brief*. 2008 October 12th 2011]; Available from: http://www.flugrevue.de/de/militaer/fluggeraet-hersteller/news-in-brief.3812.htm.
314. Coppinger, R. *"Protonex fuel cell gives Aerovironment Puma over 7h endurance", FlightGlobal*. FlightGlobal 2008; Available from: http://www.flightglobal.com/articles/2008/01/08/220690/protonex-fuel-cell-gives-aerovironment-puma-over-7h.html.
315. Mortimer, G., *AeroVironment Puma Small UAS Achieves Record Flight of Over Nine Hours Using Fuel Cell Battery Hybrid System*, in *sUAS News*2008.
316. EnergyOr. *UAV Fuel Cell Systems.* . 2008 October 13th, 2011]; Available from: http://www.energyor.com/energyor/business.cfm.
317. Ward, T.A. and N. Jenal, *Design and Initial Flight Tests of a Hydrogen Fuel Cell Powered Unmanned Air Vehicle (UAV).* ECS Transactions, 2009. **26**(1): p. 433-444.
318. Egozi, A. *"Bluebird aims for 10h endurance fuel cell for Thunderbird ", FlightGlobal*. FlightGlobal 2008 October 12th, 2011]; Available from: http://www.flightglobal.com/news/articles/bluebird-aims-for-10h-endurance-fuel-cell-for-thunderbird-319528/.
319. BlueBird, *Boomerang - Long Endurance, Fuel Cell Powered mini UAV*, 2009, BlueBird Aero Systems.
320. FuelCellWorks. *The Mako, A Class 2 Unmanned Aerial Vehicle, Soars With a Jadoo Power Fuel Cell System*. Industry News & Information Leader 2009 October 12th, 2011]; Available from: http://fuelcellsworks.com/news/2009/10/13/the-mako-a-class-2-unmanned-aerial-vehicle-soars-with-a-jadoo-power-fuel-cell-system/.
321. Jadoo. *Post-Flight Analysis of the Navier Mako Unmanned Aerial Vehicle with Jadoo Power Systems Fuel Cell - Press Release*. 2010 October 12th, 2011]; Available from: http://www.jadoopower.com/uploads/2010-10-18_Mako-Successful-In-house-Test.pdf.
322. ScienceDaily. *Hydrogen-Powered Fuel Cell Unmanned Air Vehicle Sets 26-Hour Flight Endurance Record*. Your Source for the Latest Research News 2009 October 14th, 2011]; Available from: http://www.sciencedaily.com/releases/2009/11/091130131324.htm.
323. Christodoulou, J. *Naval Research for Energy Efficiency*. in *Summit on Energy Efficiency*. 2011. University of California, Santa Barbara.

324. DefenseUpdate. *Horizon Fuel Cell Tested on Elbit Systems' Skylark I-LE Mini UAV*. 2010; Available from: http://defense-update.com/20101207_aeropak_skylark.html.
325. Horizon. *"IAI MALAT equips BE650-LE Unmanned Aircraft with Horizon's AEROPAK fuel cell system", Press Release*. 2010.
326. DefenseUpdate. *BirdEye 650LE Mini-UAV Uses Fuel Cell to Fly Six Hour Missions*. 2010 [cited 2011 October 12th, 2011]; Available from: http://defense-update.com/20100823_birdeye-650le.html.
327. Horizon. *"Russia's First AEROPAK Fuel Cell Flight Re-Opens Research in Hydrogen in Aviation", Press Release*. 2010; Available from: http://www.hes.sg/files/AEROPAKCIAMfinal.pdf.
328. EVworld. *"Taiwan's NCK University Flies First Fuel Cell UAV", Press Release*. The Future in Motion 2010 October 12th, 2011]; Available from: http://www.evworld.com/news.cfm?newsid=23345.
329. Akbaba, R., et al., *Design and Manufacture of a Fuel Cell Powered Unmanned Air Vehicle*, in *International UAV Workshop, UVW2010*2010: Istanbul.
330. *"An overview of Turkish UAV R&D and production" - Discussion Forum Thread*. 2011 October 12th, 2011]; Available from: http://www.trdefence.com/forum/viewtopic.php?f=17&t=375.
331. Dalton, M., *Lockheed Martin Introduces Ruggedized Extreme Endurance UAS*, in *Press Release*2011.
332. FuelCellToday. *"EnergyOr Fuel Cell UAV Achieves 10 Hour Flight Endurance"*. 2011; Available from: http://www.fuelcelltoday.com/news-events/news-archive/2011/august/energyor-fuel-cell-uav-achieves-10-hour-flight-endurance.
333. Robota. *"Robota Breaks 10 Hour Mark" - Press Release*. 2011; Available from: http://robota.us/2011-08-12/news/robota-breakes-10-hour-mark/.
334. Kim, K., et al., *Fuel cell system with sodium borohydride as hydrogen source for unmanned aerial vehicles.* Journal of Power Sources, 2011. **196**(21): p. 9069-9075.
335. Kim, T. and S. Kwon, *Design and development of a fuel cell-powered small unmanned aircraft.* International Journal of Hydrogen Energy, 2012. **37**(1): p. 615-622.
336. FuelCellToday. *"EnergyOr Demonstrates its Fuel Cell Unmanned Aircraft Systems in Canada"*. 2011 November 18th, 2011]; Available from: http://www.fuelcelltoday.com/news-events/news-archive/2011/november/energyor-demonstrates-its-fuel-cell-unmanned-aircraft-systems-in-canada.
337. http://www.suasnews.com/2012/08/18346/thunderbirds-are-go-chinese-fuel-cell-powered-uav-first-flight/. *Thunderbirds are GO! Chinese fuel cell powered UAV first flight*. sUAS News 2012 [cited 2013 June].
338. http://www.nrl.navy.mil/media/news-releases/2013/nrl-shatters-endurance-record-for-small-electric-uav. *NRL Shatters Endurance Record for Small Electric UAV*. NRL Press releases 2013 [cited 2013 June]; Available from: http://www.nrl.navy.mil/media/news-releases/2013/nrl-shatters-endurance-record-for-small-electric-uav.
339. Swider-Lyons, K., et al., *Liquid Hydrogen Fuel System for Small Unmanned Air Vehicles*, in *51st AIAA Aerospace Sciences Meeting including the New Horizons Forum and Aerospace Exposition*2013, American Institute of Aeronautics and Astronautics.
340. FuelCellToday. *EnergyOr Conducts First Fuel Cell UAV Flights in India* News 2013 [cited 2013 June]; Available from: http://www.fuelcelltoday.com/news-events/news-archive/2013/february/energyor-conducts-first-fuel-cell-uav-flights-in-india.
341. Coppinger, R., *PICTURE: United Technologies claims fuel cell helicopter first* in *Flight Global*2009.
342. Bouabdallah, S., et al., *Towards Palm-Size Autonomous Helicopters.* Journal of Intelligent & Robotic Systems, 2011. **61**(1-4): p. 445-471.

343. Jackson, R. and C. Haddox. *Boeing Feature Story: Phantom Eye High Altitude Long Endurance Aircraft Unveiled*. 2010 October 21st, 2011]; Available from: http://www.boeing.com/Features/2010/07/bds_feat_phantom_eye_07_12_10.html.
344. Warwick, G. *Hydrogen-Powered UAV Begins Flight Tests - Aviation Week*. 2010 October 21st, 2011]; Available from: http://www.aviationweek.com/aw/generic/story.jsp?id=news/awst/2010/08/16/AW_08_16_2010_p42-246255.xml&headline=Hydrogen-Fueled%20UAV%20Begins%20Flight%20Test&channel=awst.
345. Egozi, A. *Bluebird aims for 10h endurance fuel cell for Thunderbird - Press Release, BlueBird Aero Systems*. BlueBird Aero Systems 2008 October 21st, 2011]; Available from: http://www.bluebird-uav.com/Press_FuelCell.html.
346. Roediger, P., et al., *Evaluation of chamber contamination in a scanning electron microscope.* Journal of Vacuum Science & Technology B, 2009. **27**(6): p. 2711-2717.
347. Howe, K.S. and K. Kendall. *Microtubular SOFCs - Review of Properties and Performance*. in *9th European Solid Oxide Fuel Cell Forum*. 2010. Lucerne: Fuel Cell Forum.